Investigation of the bond coat microstructure and interface topography importance on thermal barrier coatings

A thesis submitted to The University of Manchester for the degree of
Doctor of Philosophy
in the Faculty of Engineering and Physical Sciences

2021

João Pedro Martins

Materials Science Centre
School of Materials

List of contents

List of contents 2

List of figures 5

List of tables 10

Nomenclature 14

List of publications 17

Abstract 18

Declaration 20

Copyright statement 21

Chapter 1. Introduction 23

  1.1. Development of gas-turbine engines 23

  1.2. Evolution of thermal barrier coating technology 26

  1.3. Scope of the dissertation 27

Chapter 2. Literature review 29

  2.1. The thermal barrier coating system 29

  2.2. Ceramic topcoat 30

    2.2.1 Functional requirements 30

    2.2.2 Materials 31

    2.2.3 Deposition methods 36

  2.3. Bond coat 39

    2.3.1 Functional requirements 39

    2.3.2 Fabrication methods and materials 40

      2.3.2.1 Diffusion coatings 41

      2.3.2.1 Overlay coatings 44

  2.4. Thermally grown oxide 49

    2.4.1 Functional requirements and formation process 49

    2.4.2 TGO stress and failure 52

  2.5. Failure mechanisms of TBC systems 54

    2.5.1 Predictive lifetime models and failure mechanism categories 54

    2.5.2 Failure modes 57

    2.5.3 Failure mechanisms of EB-PVD TBCs 59

    2.5.4 Failure mechanisms of plasma-sprayed TBCs 61

Chapter 3. Experimental methodology 65

  3.1. Specimen fabrication and preparation 65

  3.2. High-temperature thermal treatment 67

3.3. Characterisation techniques ... 69
3.3.2 Microscopy characterisation ... 72
3.3.3.1 Scanning electron microscopy ... 72
3.3.3.2 Focused ion-beam ... 73
3.3.3 Mechanical testing ... 74
3.3.3.1 Depth-instrumented micro-indentation ... 74
3.3.3.2 Three-point bending ... 75
3.3.3.3 Modified four-point bending ... 76
3.3.4 Grazing incidence-ray diffraction ... 78
3.3.5 Photoluminescence piezospectroscopy (PLPS) ... 80
Chapter 4. Investigation of the bond coat interface topography effect on lifetime, microstructure and mechanical properties of air-plasma sprayed thermal barrier coatings ... 82
4.1. Introduction ... 82
4.2. Materials and methods ... 83
4.2.1 Sample fabrication and preparation ... 83
4.2.2 Bond coat topography characterisation ... 85
4.3. Results and discussion ... 87
4.3.1 TBC system lifetime and oxidation kinetics evolution ... 87
4.3.2 Impact of BC topography on the TBC lifetime ... 92
4.3.3 BC topography-induced microstructural changes in the TBC ... 96
4.3.4 Effect of TBC local and global in-plane elastic modulus ... 98
4.3.5 Effect of BC topography on fracture mechanics ... 102
4.4. Conclusions ... 104
Chapter 5. Effect of bond coat topography on the fracture mechanics and lifetime of air-plasma sprayed thermal barrier coatings ... 106
5.1. Introduction ... 106
5.2. Materials and methods ... 107
5.2.1 Sample fabrication and preparation ... 107
5.2.2 Bond coat topography characterisation ... 108
5.2.3 Modified four-point bending test ... 109
5.2.3.1 Analytical considerations ... 109
5.2.3.2 Crack propagation velocity ... 111
5.2.4 Inter-splat separation frequency ... 112
5.3. Results ... 113
5.3.1 Pre-bending microstructure ... 113
5.3.2 Post-bending microstructure ... 115

5.3.3 Effect of BC topography and TBC microstructure fracture mechanics 117
5.3.4 Crack propagation behaviour 120
5.3.5 Correlation with TCF lifetime results 121
5.4. Discussion 123
5.4.1 Effect of intra-splat cohesion on fracture mechanics 123
5.4.2 Impact of inter-splat separation tortuosity on fracture mechanics 124
5.4.3 Impact on TCF lifetime 126
5.5. Conclusion 127
Appendix A 129
Appendix B 132
Chapter 6. Effect of bond coat microstructure of CoNiCrAlY coatings on the oxide scale formation 134
6.1. Introduction 134
6.2. Materials and methods 135
6.2.1 Sample fabrication and preparation 135
6.2.2 Sample characterisation 136
6.3. Results 137
6.3.1 Pre-oxidation microstructure 137
6.3.2 Oxide growth correlation with the BC microstructure 139
6.3.3 Oxide scale structure and composition 140
6.3.4 Evolution of the oxide scale with oxidation time 144
6.3.5 Cationic diffusion across the oxide scale 147
6.3.6 PLPS analysis of the oxide scale 149
6.3.7 Oxide scale failure 150
6.4. Discussion 152
6.4.1 Current understanding of the outer scale formation mechanism 153
6.4.2 Effect of BC microstructure on the early oxidation behaviour 155
6.4.3 Effect of Cr^{3+} incorporation in the oxide scale 161
6.5. Conclusion 164
Chapter 7. Conclusions and future work 165
7.1. Conclusions 165
7.2. Future work 166
References 168

List of figures

Chapter 1

Fig. 1. 1 (a) Cut-out profile view of a Rolls-Royce Trent 1000 engine where the main constituent sections are highlighted and a typical cross-sectional microstructure of an air-plasma sprayed (APS) TBC used in the internal lining of a combustion chamber is presented (Edited from [11]); (b) Representation of an open Brayton cycle and respective pressure-volume (P-V) diagram displaying the isentropic (i.e. segments 1→2 and 3→4) and isobaric (i.e. segments 2→3 and 4→1) processes performed by an operating gas-turbine engine; (c) Graph displaying the specific core power evolution as a function of turbine rotor inlet temperature for idealised and industrial engine development trends (Edited from [6]). 24

Fig. 1. 2 Evolution of Ni-based superalloy design and TBC temperature capabilities since from 1965 to 2015. The continuous lines connected the data points constitute the maximum allowable temperature for Ni-based superalloys (brown line), TBCs with film cooling (red line) and without (green line) [4].25

Chapter 2

Fig. 2. 1 Schematic illustration of a modern multi-layered TBC system structure wherein the main desirable features are presented alongside the typical surrounding environmental conditions [4]. .. 29

Fig. 2. 2 (a) Schematic representation of the phase transformation of ZrO2 as a function of temperature [32]. 31

Fig. 2. 3 Schematic illustration of the YSZ crystal structure highlighting the addition of Y2O3, edited from [36]. 32

Fig. 2. 4 *A* plot of the thermal expansion coefficient as a function of the thermal conductivity for a range of metal and ceramics materials typically utilised in TBC systems [12]. 34

Fig. 2. 5 (a) Variation of thermal conductivity with thermal exposure temperature for emerging ceramic TBC materials and (b) thermal conductivity values for emerging ceramic TBC materials of temperature-independent materials [24]. Please note that the ordinate axis scaling used in the figures above is not the same. 35

Fig. 2. 6 (a) Schematic illustration of the air-plasma spray (APS) deposition process edited from [70, 71] and respective microstructural details observed from (b) polished and (c) fractured cross-sectional views [72]. 37

Fig. 2. 7 (a) Schematic illustration of the electron beam physical vapour deposition method (EB-PVD) and respective (b) cross-sectional microstructure [31] and (c) characteristic columnar texture [73]. 38

Fig. 2. 8 (a) Binary phase diagram of a Ni-Al system as a function of temperature where the compositional ranges corresponding to β-NiAl (green region) and γ'–Ni_3Al (red region) phases are highlighted [9]; (b) Ternary phase diagram of a Ni-Pt-Al system at 1100 °C where the compositional ranges that originate the β-(Pt,Ni)Al (green region) and γ'–$(Pt,Ni)_3Al$ (red region) phases are highlighted [86]; (c) Ternary phase diagram of a Ni-Cr-Al system at 1050 °C [87] 40

Fig. 2. 9 Backscatted-electron (BSE) micrographs depicting the as-fabricated microstructure of (a) a non-modified β-NiAl bond coat layer deposited via pack-cementation over a Udimet 700 substrate [90] and (b) a Pt-modified nickel aluminide (β-(Ni,PT)Al) bond coat deposited over a second generation single crystal superalloy (CMSX-4) via chemical vapour deposition (CVD) [101]. 43

Fig. 2. 10 BSE micrograph depicting the as-fabricated microstructure of a Pt-diffused γ/γ' bond coat layer formed over a Rene N5 superalloy substrate [104]. 44

Fig. 2. 11 (a) BSE micrograph depicting the as-fabricated cross-sectional microstructure of a NiCoCrAlY-HfSi APS bond coat deposited over a Nimonic 263 alloy substrate and (b) secondary electron (SE) micrograph from a top view perspective of the bond coat surface. 45

Fig. 2. 12 (a) Schematic illustration of the high velocity oxygen fuel (HVOF) processing set up (Edited from [117]) and (b) respective top view secondary SE micrograph of a bond coat surface with high roughness (S_a = 10.6 µm); (c) BSE micrograph depicting the as-fabricated cross-sectional microstructure of a NiCoCrAlY-HfSi HVOF bond coat deposited over a Nimonic 263 alloy substrate, where the dual-phase structure and volumetric defects are highlighted in the inset image. 46

Fig. 2. 13 BSD micrographs illustrating the microstructural evolution of a NiCoCrAl-HfSi bond coat with thermal exposure for the (a) as-deposited state, (b) 88 hours, (c) 166 hours and (d) 241 hours. The decomposition of the β–NiAl phase into solid solution is reflected by the gradually decreasing dual-phase zone. 49

Fig. 2. 14 TGO scale evolutionary stages with thermal exposure progression where (a) transmission electron microscopy (TEM) cross-section depicting a transient TGO scale grown on a NiCoCrAlY bond coat oxidised for 0.5 h at 1000°C with pO_2 of 20kPa [81]; (b) In-lens SEM image of a stable growth TGO scale that formed over a NiCoCrAlY bond coat and an APS topcoat after 400 hours of thermal cyclic oxidation in air at 1050 °C [84] and (c) backscatted-electron SEM micrograph depicting a TGO scale in the accelerated oxidation stage that formed over a CoNiCrAlY bond coat after 550 hours of thermal cyclic oxidation in air at 1135 °C 51

Fig. 2. 15 Schematic illustration of the main intrinsic and extrinsic failure mechanisms contributing to TBC system failure via the edge delamination, interfacial rumpling, sustained-peak low cycle fatigue, impact damage and chemical attack failure modes. Image edited from [1]. 55

Fig. 2. 16 Schematic illustration of the (a) buckling- and (c) edge-driven delamination failure modes for compressed scales with a pre-existent flaw of length L [185], alongside a (b) top view depiction of buckling on an EB-PVD TBC viewed under reflected light [9] and (d) SEM cross-sectional representation of edge delamination on a PS TBC [186]. 58

Fig. 2. 17 (a) Schematic illustration of the EB-PVD main crack nucleation mechanisms and respective cross-sectional SEM observation where failure mechanisms (b) I, II_b and (c) II_a are highlighted [23]. 60

Fig. 2. 18 (a) Schematic illustration of the four crack nucleation mechanisms proposed for plasma-sprayed TBCs and (b) respective cross-sectional SEM observation in a heat treated specimen that has incurred complete delamination[23]. 62

Chapter 3

Figure 3.1 Photograph of the thermal spray chamber experimental setup used to fabricate the button-shaped TBC specimens in the present work (left) and respective specimen holder configuration prior to TBC deposition (right). 65

Figure 3.2 (a) Photograph of the Struers accutom-10 precision cut-off cutting machine and (b) respective setup used to section the TBC specimens. 66

Figure 3.3 (a) Photograph of an as-fabricated button-shaped TBC specimen and (b) respective encapsulated as-polished cross-section. 66

Figure 3.4 Photograph of the Carbolite Gero box RHF 14/15 used for thermal cycling of large batches of TBC specimens and respective arrangement inside the chamber. 68

Figure 3.5 Photograph of the CM^{TM} furnace used for thermal cycling of the polished MCrAlY specimens for early oxidation studies and respective arrangement inside the automatic lifting platform. 69

Figure 3. 6 (a) Post-processed 16-bit colour heightmap of a high tortuosity bond coat topography and resulting (b) 3-D reconstruction. 71

Figure 3. 7 Cross-sectional FIB micrograph of an isothermally aged oxide scale after 240 min taken at 5 keV. 74

Figure 3. 8 Schematic illustration of the three-point bending experimental setup implemented on an Instron 3344 universal testing system. 76

Figure 3. 9 (a) Schematic of the four-point bending experimental setup and specimen geometry used in this experiment (b) Representative load-displacement curve obtained from the four-point bending test along with an inset image depicting of the experimental setup implementation in an Instron 5569 universal testing machine. 77

Figure 3. 10 (a) Bragg-Brentano geometry typically adopted for grazing incidence X-ray diffraction where, α_i denotes the incident beam angle and 2θ the angle between the transmitted and diffracted

beams [219]; (b) Grazing incidence X-ray diffraction experimental setup implemented on a PANalytical X'Pert diffractometer following the Bragg-Brentano geometry. 79
Figure 3. 11 Luminescence spectra of an Al_2O_3 scale showing the characteristic peaks for the α and θ polymorphs. 81

Chapter 4

Figure 4.1 (a) Cross sectional representation of the summit thresholding procedure using an extended maxima transform with equivalent thresholded height *h*; (b) A post-processed 8-bit grayscale heightmap of a high lifetime specimen and (c) respective thresholded heightmap revealing the morphology and projected area of the digitally sectioned summits. 87
Figure 4.2 (a) Normalised TBC lifetime for the different MCrAlY systems as a function of specimen ID; (b) equivalent TGO thicknesses plotted as a function of oxidation time. 88
Figure 4.3 Backscattered-electron (BSE) micrograph of a Ni-based (a) and Co-based (b) specimens where the as-deposited microstructure is depicted; the inset in Fig. 4.3-a) shows a region where the incorporation of Y and Hf in the NiCoCrAlY-HfSi TGO scale was detected whereas, the inset in Fig.4. 3-b) illustrates the presence of a mixed oxide cluster and Cr-rich outer scale in the CoNiCrAlY system. 90
Figure 4. 4 Cross-sectional SEM micrograph of the microstructure of a Co-based BC (a) and a Ni-based BC (d) medium lifetime specimens after 0.22 L_f. Representative micrograph of the Co-based (b) and Ni-based BC (e) failure plane morphology and composition of the major isostructural species found for each composition determined by GIXRD (c) and (f), respectively. 91
Figure 4. 5 Representative BC interface topography heightmaps for low (a), medium (b) and high (c) performance samples and respective cross-sectional SEM micrographs (d) (e) and (f) depicting and highlighting the different topographical features amongst lifetime categories; Three-dimensional reconstruction of a high (g) and medium (h) lifetime specimen post-processed 16 bit colour heightmap with similar S_a values yet very different BC topographies that originated contrastingly different L_f. . 93
Figure 4. 6 Plot of TBC lifetime fraction as a function of (a) arithmetic mean roughness, (b) summit density, (c) arithmetic mean peak curvature and (d) total thresholded summit area of the BC interface. Higher lifetime specimens were correlated with tortuous BC topographies that displayed high roughness, lower summit density, lower peak curvature and higher total thresholded summit areas. 95
Figure 4. 7 Representative SEM micrographs of the microstructural features of a (a) low, (b) medium and (c) high performance specimens in the as-deposited condition, where the different splat morphologies configurations obtained are highlighted; (d) Plot showing the positive correlation between TBC lifetime and average splat curvature (κ_{splat}). 97

Figure 4. 8 (a) Representative load-displacement compliance curves for the low, medium and high lifetime specimen categories; (b) Plot displaying the correlation of local in-plane elastic modulus with TCF lifetime for all different BC-topographies; (c) Plot showing the evolution of the indentation modulus with oxidation time, wherein the TBC sintering rate is described by a logarithmic least squares regression fit; (d) SEM micrograph showing a representative indentation of the TBC in the vicinity of the interface. 99

Figure 4.9 (a) Plot displaying negative correlation between the global in-plane elastic modulus and TCF lifetime for all different BC-topographies; (b) Representative load-displacement curves measured on the underside and topside of the specimens. 101

Figure 4.10 BSE SEM micrographs of the post-failure cross-section of a low (a) and high (b) lifetime specimens, wherein the main failure mechanisms are highlighted; Top view of the failure plane of a the (c) low and (d) high lifetime specimens displaying the BSE SEM image contrast that allowed for the (e) quantification of the different species found at the failure plane. 103

Chapter 5

Figure 5.1 SEM micrograph of the TBC microstructure generated by deposition over (a) low tortuosity, (b) medium tortuosity and (c) high tortuosity BC topographies; Colour heightmaps of the BC surface topography for the (d) low tortuosity, (e) medium tortuosity and (f) high tortuosity specimens and respective total thresholded heightmaps in the order g) to i). 109

Figure 5.2 Optical frame micrograph sequence depicting the crack growth evolution with time for a low tortuosity specimen. 112

Figure 5.3 Representation of the line scan methodology used in the determination of the inter-splat separation frequency by unit of TBC length (v_{IS}) across the TBC layer thickness. 113

Figure 5.4 (a) Backscattered-electron (BSE) micrograph of the pre-bending microstructure at the beam centre-point; Secondary electron (SE) micrograph illustrating a single splat impact over a (b) low and (e) high tortuosity BC surface; Cross-sectional BSE micrographs of the characteristic interfacial features and TBC splat morphology of the (c, d) low and (f, g) high tortuosity specimens, where the indent locations used to determine E_{TBC} and the average splat curvature of potential crack paths (k_{splat}) are highlighted. The k_{splat} values obtained (kappa plugin, ImageJ) represent the summation of the radius of curvature of each point along the Bézier curve defined by the potential crack path. 114

Figure 5.5 Plot of the TBC in-plane elastic modulus as a function of the inter-splat separation frequency. 115

Figure 5.6 (a) Post-bending microstructure of a high tortuosity specimen and respective pre-crack initiation site at the notch root; (c) Near-horizontal crack propagation in low tortuosity specimens (d)

Microstructural evidence of crack deflection and intra-splat cracking mechanisms contribution to crack propagation in regions of high splat curvature. 116

Figure 5.7 (a) Plot of the strain energy release rate as a function of the total thresholded summit area (solid black pattern) and the TBC in-plane elastic modulus in the vicinity of the interface (orange stripe pattern); (b) Plot of the critical energy release rate as a function of the tensile, (K_I) and shear (K_{II}) components of the stress intensity factor, represented by solid black and dashed orange markers respectively. It is important to note that despite gradient observed herein being indicative of an approximately constant phase angle amongst all specimens, this is only a global average based on the model assumption of the planar interface. 118

Figure 5.8 Plot of the mode I and II stress intensity factor components as a function of (a) the total thresholded summit area and (b) the TBC in-plane elastic modulus in the vicinity of the interface. 119

Figure 5.9 Compilation of inversed optical frame micrographs depicting the crack propagation discrepancies observed during the four-point bending test for a high and low tortuosity specimen. 120

Figure 5.10 Plot of the crack propagation velocity as a function of (a) G_c and (b) the total thresholded summit area and local TBC in-plane elastic modulus. 121

Figure 5.11 Normalised TBC lifetime for the different types of CoNiCrAlY and NiCoCrAlY-HfSi specimens as a function of (a) specimen ID and (b) critical strain energy release rate. 122

Figure 5. 12 Plot of the critical strain energy release rate as a function of the inter-splat separation frequency across the TBC thickness. 124

Chapter 6

Figure 6.1 (a) Cross-sectional and (b) top view surface BSE micrographs depicting the as-polished microstructure of the HVOF coatings; (c) EBSD phase map contrast map of the same region represented in the (b), where the red areas were indexed as β-phase, the blue areas as γ-phase and black areas as unindexed; Representative EDS spectra and chemical composition of the (d) β and (f) γ-phases obtained from area analysis. 138

Figure 6.2 (a) BSE micrograph displaying the as-polished BC surface morphology and the respective (b) SE and (c) BSE mode imagery of the oxide scale growing atop; (d) EDS map overlay displaying the distribution of Al+O and Co+Ni ($EHT = 10keV$). The green, yellow and red areas delineated by a dashed line indicate regions of the BC where larger, small and no β grains are found. 140

Figure 6.3 (a) Top view SE micrograph ($EHT = 10keV$) of an oxide scale formed after 120 min of isothermal thermal exposure and (b-e) respective EDS maps alongside a (f) high magnification oblique view of a mixed oxide ridge formation; EDS spectra obtained from area analysis of (g) the inner scale (region 1) and (h) mixed oxide formations (region 2). 141

Figure 6.4 (a) FIB cross-section of the TGO scale after 120 min oxidation and (b) representative depiction of the microstructural features found at the inner/outer scale boundary obtained from STEM-HAADF; EDS map analysis of the framed area (c-f) and linescan analysis displaying the element across the near-interface BC and TGO segments in regions (g) 1 and (h) 2. 143

Figure 6. 5 Evolution of the atomic fraction of (a) Cr in the inner and outer scales and (b) Co and Ni in the outer scale, obtained from EDS point analysis at 10 keV. Each data point corresponds to the average of 10 measurements performed in three different FIB cross-sections. The abscissa axis of both plots is shown in a logarithmic scale of base 10 to improve the visual perception of the overall trend. 144

Figure 6.6 Evolution of the oxide scale morphology from a top view perspective for isothermally heat treated specimens after (a-c) 10, (d-f) 60, (g-i) 240, (j-l) 600 and (m-o) 3000 min. The left column includes a low magnification overview of the oxide scale depicting the overall frequency and distribution of the mixed oxide formations (region 2) with increasing oxidation time. The high magnification SE and BSD micrographs included in the middle and right columns, respectively, illustrate the growth location and morphology of the mixed oxide formations. 146

Figure 6.7 Plots of the (a) percentage of area covered by mixed oxide formations and (b) oxide scale surface roughness as a function of the oxidation time (t_o). It is noteworthy that the abscissa axis of both plots is shown in a logarithmic scale of base 10 to improve the visual perception of the overall trend.. 147

Figure 6.8 (a) SE micrograph of a cross-sectional lamella of an oxide scale prepared by FIB milling after 240 min oxidation and (b) a STEM-HAADF micrograph of the highlighted segment (white dashed area) containing a mixed oxide formation; Linescan compositional analysis across grain boundary segments of inner scale columnar grains confirming the segregation of (c) Cr and (d) Co. 148

Figure 6. 9 PLPS spectra of the oxide scale obtained after 5 (black), 30 (green), 120 (blue) and 3000 (red) min of oxidation. The only peaks observed in the spectra are the R-lines associated with the presence of α-Al_2O_3.. 149

Figure 6. 10 Evolution of the residual stress as a function of oxidation time. The abscissa axis is shown in a logarithmic scale of base 10 to improve the visual perception of the overall trend. 150

Figure 6.11 (a) Depiction of a non-spalled segment of the oxide scale displaying the characteristic features of small-scale bucking (SSB) and (b) a schematic illustration of the respective failure mechanisms; (c) Oblique view of the failure plane of a 3000 min specimen where the two main cracking mechanisms are highlighted (i.e. BC interface and intra-scale cracking) alongside (b) a higher magnification of the inner/outer scale delamination boundary; 152

Figure 6.12 Schematic illustration of the outer scale formation mechanism presented in three stages, mixed oxide nucleation (stage 1), mixed oxide coarsening (stage 2) and outer scale merger (stage 3). The relevant diffusion fluxes and microstructural features that impact the outer scale formation are included.. 153

Figure 6.13 Cross-sectional FIB micrographs and respective schematic illustration of Al flux across the interface during oxidation for a β grain with (a,c) smaller and (b,d) larger phase boundary distance. The BC and oxide scale microstructure and compositions are superimposed on the schematic. The representative Al flux profile over each surface (red line) and the minimum Al flux to maintain the exclusive formation of Al_2O_3 are also represented. 156

Figure 6.14 Plot of the normalised diffusion flux as a function of the position along the bare BC surface for a phase boundary distance of 1 µm and 0.3 µm region of influence. The green and red dashed line represent the normalised Al diffusion flux of across phase boundary and, respectively, whereas the solid blue profile represents the overlap profile of both phase boundaries 158

Figure 6.15 Plot of the normalised overlap diffusion flux as a function of the phase boundary region of influence measured. Each colour line profile represents a different phase boundary distance, ranging from 0.6 to 1.6 µm. 159

Figure 6.16 High magnification BSE micrograph of the as-polished BC microstructure and respective oxide alongside the respective (b) SE and (c) BSE mode images of the oxide scale growing atop where brighter contrast indicates the presence of mixed oxide formations. 160

List of tables

Chapter 3

Table 3.1 Summary of all the techniques used in the characterisation of the TBC specimens. 69

Table 3. 2 Penetration depths of a CuKα 8.04 KeV X-ray beam (α = 1.54 Å) on the major isostructural species identified at the failure plane for an incidence angle α_i = 3°. 80

Chapter 4

Table 4.1 Parameters utilised for the thermal spraying of the BC flashcoat layer. 84

Table 4. 2 Parabolic rate constant determined for all the specimen types. 89

Chapter 5

Table 5. 1 Parameters utilised for the thermal spraying process of the bond coat layer. 108

Appendix A

Table A1 Experimental data used in the calculation of the strain energy release rate and respective results for the Hofinger and the Suo-Hutchinson methods. The elastic modulus for materials 1 and 2 have been calculated according to equations A1. 131

Chapter 6

Table 6. 1 Representative average grain size, aspect ratio and phase fractions of the as-polished HVOF BC specimens. 139

Table 6. 2 Gibbs free energy of formation ($\Delta G0$) for the most common oxide and spinel formations in MCrAlY systems at 727 °C and 1227 °C [290]. 162

Nomenclature

Acronyms

APS	Air-plasma spray
BC	Bond coat
BSE	Backscattered electron
CGDS	Cold gas dynamic spraying
CLSM	Confocal laser microscopy
CMAS	Calcium-magnesium-alumino-silicate)
CVD	Chemical vapour deposition
CTE	Coefficient of thermal expansion
EB-PVD	Electron beam physical vapour deposition
EBSD	Electron backscatter diffraction
EDS	Energy dispersive X-ray spectroscopy
FE	Finite element
FEM	Finite element modelling
FIB	Focused Ion beam
FOD	Foreign object damage
GIXRD	Grazing incidence X-ray diffraction
VPA	Vapour-phase aluminising
HVAF	High velocity air fuel
HVOF	High velocity oxygen fuel
LPPS	Low-pressure plasma spray
OM	Optical microscopy
PLPS	Photoluminescence piezospectroscopy
PS	Plasma spray
PVD	Physical vapour deposition
RE	Reactive element
SE	Secondary electron
SEM	Scanning electron microscopy
STEM	Scanning transmission electron microscope
TBC	Thermal barrier coating
TGO	Thermally grown oxide
XRD	X-ray diffraction
YAG	Yttrium aluminium garnet
EHT	Electron high tension
IDZ	Inter-diffusion zone

Symbols

K_{IC}^{TBC}	Mode I TBC fracture toughness
h_2	Substrate thickness
h_{TBC}	TBC thickness
h_c	Critical excitation energy
h_c	Critical TGO thickness
h_s	Stiffener thickness
κ_{splat}	Inter-splat separation curvature
A_{TGO}	Equivalent thickness

A_{indent}	Area of indent
A_m	Atomic mass
D_{Al}^{PB}	Al diffusion flux at phase boundary
D_{Al}^{γ}	Al diffusion flux on γ grain
D_{Al}^{β}	Al diffusion flux on β grain
G_C	Critical strain energy release rate
G_{SS}	Steady-state strain energy release rate
I_0	Incident beam intensity
I_b	Diffracted beam intensity
I_{max}	Maximum intensity
K_{IC}	Tensile component of stress intensity factor
K_{IIC}	Shear component of stress intensity factor
K_{eff}	Inter-splat separation curvature
L_{TGO}	Equivalent thickness
L_c	Critical flaw size
L_{in}	Inner support span length
L_{out}	Outer support span length
M_r	Relative proportion of Lorentizian character
O_O^x	Lattice oxygen
S_a	Arithmetic mean roughness
S_{ds}	Areal summit density
S_{pc}	Arithmetic mean peak curvature
S_{sth}	Total thresholded summit area
T_0	TBC surface temperature
T_{dep}	Stress-free temperature
T_i	TBC interface temperature
V_0	Acceleration voltage
V_O	Positive bivalent oxygen vacancy
V_k	Critical excitation energy
Y'_{Zr}	Substitution of Zr^{4+} by the Y^{3+}
Z_m	Photon generation depth
d_{RI}	Phase boundary radius of influence
k_p	Parabolic constant
l_{crack}	Crack length
t_f	Critical failure time
t_o	Oxidation time
v_m	Frequency at maximum intensity
w_0	Displacement at beam centre-point
w_{hf}	Width at half maximum
x_{Cr}	Cr concentration in wt.%
x_{PB}	Phase boundary distance
x_{PB}^{crit}	Critical phase boundary distance
x_{cp}	Centre-point distance
x_{pb}	Phase boundary distance
$\Delta\nu^{Cr}$	Peak shift for Cr atoms
Π_c	Critical buckling index
α_{TBC}	Thermal expansion TBC

α_i	Angle of incidence
δ_{eq}	Equivalent thickness
θ_{av}	Average deflection angle
ν_{IS}	Inter-splat separation frequency
ρ_e	Electron density
σ_C	Critical residual stress
υ_{prop}	Critical strain energy release rate
$\lvert K \rvert$	Complex stress intensity factor
$\Delta\alpha_C$	Thermal expansion mismatch
A	Area
c_1	Compliance parameter top layer
c_2	Compliance parameter substrate
E_{gi}	Global in-plane elastic modulus
E_{ind}	In-plane indentation modulus
E_{TBC}	Elastic modulus of the TBC
h	Thickness
I	Second moment of inertia
K_I	Applied mode I stress intensity factor
K_{II}	Applied mode II stress intensity factor
K_{tip}	Crack driving force
L_f	Life fraction
M	Moment per unit thickness
m	Growth strain
Ø	Diameter
P_c	Critical loadR Peak radius
x	Penetration depth
Z	Atomic number
ε	*B*imaterial constant
κ	Thermal conductivity
μ	Attenuation coefficient
Π	Buckling index
K	Magnitude wave vector
P	Applied load
U	Elastic energy
W	Beam length
b	Beam thickness
n	Refractive index
t	Time
$\Delta\nu$	Peak shift
$\Phi(\upsilon)$	Gaussian-Lorentzian function
γ	Characteristic angle
θ	Deflection angle
λ	Loading combination measurement
ρ	Density
σ	Residual stress
υ	Poisson’s ratio
ψ	Phase angle
ω	Real angular quantity

List of publications

Martins, João P., et al., Investigation of the bond coat surface topography effect on TBC lifetime - ICACCS2-015-2019, Oral presentation in the 43ª International Conference and Exposition on Advanced Ceramics and Composites ICACC 2019, United States of America - Daytona Beach, Florida

Martins, João P., et al., Investigation of the bond coat interface topography effect on lifetime, microstructure and mechanical properties of air-plasma sprayed thermal barrier coatings. *Journal of the European Ceramic Society,* 2020. 40(15): p.5719-5730

Brewster, G., **Martins, João P.**, Bond coating for thermal barrier coating system with improved durability. United Kingdom Intellectual Property Office, GB1916269.2, Submitted on November 2019, Pending

Martins, João P., et al., Effect of bond coat topography on the fracture mechanics and lifetime of air-plasma sprayed thermal barrier coatings, Surface & Coatings Technology, 2021, June

Abstract

Investigation of the bond coat microstructure and interface topography importance on thermal barrier coatings

João Pedro Martins

The University of Manchester for the degree of Doctor of Philosophy in the Faculty of Engineering and Physical

MCrAlY bond coatings typically used in thermal barrier coatings (TBC) systems for gas-turbine engines are studied in this thesis, with special focus on microstructural, topographical and oxidation behaviour.

The effect of bond coat/thermal barrier coating (BC/TBC) interface topography on the lifetime of air-plasma sprayed (APS) TBCs has been comprehensively investigated in the present work. A quantitative description of the interface topography was achieved by utilising multiple surface texture parameters obtained from confocal microscopy, including a newly formulated parameter, denominated as total thresholded summit area, S_{sth}. Thermal cycling fatigue (TCF) testing showed a clear correlation between the TBC lifetime and the interface topography, especially for the newly proposed S_{sth} parameter. The topographical and microstructural analysis revealed that deposition of a TBC over tortuous BC topographies leads to a highly curved TBC splat morphology that influences the crack path configuration. Microindentation and three-point bending conducted on as-deposited and heat-treated specimens have showed that the aforementioned microstructural changes lead to a reduced local and global elastic moduli. These features were later associated with more beneficial fracture mechanics behaviours and higher TCF lifetimes.

A modified four-point bending experiment is subsequently conducted on air-plasma sprayed (APS) TBC to gain further insight into the impact of bond coat (BC) topography tortuosity on the TBC fracture mechanics. The degree of BC tortuosity was quantified by the S_{sth} metric and was found to influence the crack path configuration, critical energy release rate (G_c) and crack propagation velocity (v_{prop}). Specimens with higher BC interface tortuosity and more compliant TBC microstructures ere associated with reduced strain energy release rates ($\mathrm{G}_c \leq 79.9\ \mathrm{J}.m^{-2}$) and crack propagation velocities ($v_{prop} \leq 0.9\ \mathrm{mm.s}^{-1}$). These observations seem to indicate that TBC failure is primarily governed by the degree of inter-splat cohesion and intra-splat segmentation, although the topography-induced inter-splat tortuosity still had a relevant impact on fracture mechanics. These findings suggest that despite TBC systems with higher tortuosity specimens and more compliant microstructures tending to show a premature propensity for crack nucleation, the lower strain energy release rates observed induce a

slower crack propagation rate and may delay failure. The correlation observed with the lifetime of analogous thermally cycled specimens tested herein seemed to confirm this, as more compliant TBC microstructures were correlate with longer TBC lifetimes.

The oxidation behaviour of CoNiCrAlY coatings deposited by high velocity oxygen fuel are studied via a combination of correlative microscopy and spectroscopy techniques. The dual-phase BC microstructure was found to promote a site-specific oxidation behaviour that had significant implications in the formation and composition of the oxide scale during the early stages. Oxide growth over the β-phase grains was faster due to accelerated diffusion of cations along the γ/β grain boundaries. It was found that this effect was more prominent in smaller grains with reduced γ/β grain boundary distance ($0.8 \leq x_{PB} \leq 1.2\ \mu m$), as the resulting interaction between fluxes resulted in the undesirable nucleation of mixed oxide formations in the outer scale. The evolution of the oxide scale with oxidation time further revealed that the outer scale undergoes a notable thermo-chemical transformation via outward diffusion of non-Al cations across the inner scale. The high residual stresses and premature failure suggest that the outer scale has an adverse effect on the durability of the oxide scale. Furthermore, the incorporation of large quantities of Cr in the oxide scale (~4 at.%) and subsequent segregation to the outer scale is detrimental for the early oxidation behaviour, overall stress state and durability.

Declaration

No portion of the work referred to in this thesis has been submitted in support of an application for another degree or qualification of this or any other university or other institute of learning.

Copyright statement

i. The author of this thesis (including any appendices and/or schedules to this thesis) owns certain copyright or related rights in it (the “Copyright”) and he has given The University of Manchester certain rights to use such Copyright, including for administrative purposes.

ii. ii. Copies of this thesis, either in full or in extracts and whether in hard or electronic copy, may be made only in accordance with the Copyright, Designs and Patents Act 1988 (as amended) and regulations issued under it or, where appropriate, in accordance with licensing agreements which the University has from time to time. This page must form part of any such copies made.

iii. iii. The ownership of certain Copyright, patents, designs, trademarks and other intellectual property (the “Intellectual Property”) and any reproductions of copyright works in the thesis, for example graphs and tables (“Reproductions”), which may be described in this thesis, may not be owned by the author and may be owned by third parties. Such Intellectual Property and Reproductions cannot and must not be made available for use without the prior written permission of the owner(s) of relevant Intellectual Property and/or Reproductions.

iv. iv. Further information on the conditions under which disclosure, publication and commercialization of this thesis, the Copyright and any Intellectual Property and/or Reproduction described in it may take place is available in the University IP Policy (See http://www.campus.manchester.ac.uk/medialibrary/poilcies/intellectual-property.pdf), in any relevant Thesis restriction declarations deposited in the University Library, The University Library’s regulations (see http://www.manchester.ac.uk/library/aboutus/regulations) and in The University’s policy on presentation of Theses.

Acknowledgements

Firstly, I would like to start by expressing my deep appreciation and gratitude for all the advice, teachings and support provided by my main supervisor, Prof. Ping Xiao. His guidance was instrumental for the development of my research and critical thinking skills in the field of materials for demanding environments and will certainly be crucial throughout my career. Secondly, I would like express my sincere gratitude to Rolls-Royce plc. for their financial support throughout the PhD project, and to Dr. Gyaneshwara Brewster and Mr. Roy McIntyre for their industrial supervision and guidance in sample fabrication. I would also like to extend my sincere appreciation to Dr. Ying Chen for his insightful scientific advice, experimental guidance and discussions that played an important role in major decisions involving research direction.

I would like to thank all the colleagues in my group for their everyday companionship and good disposition during the long lab hours we have worked together. I would also like to thank the multiple experimental officers, Mr. Andy Wallwork, Dr. Patrick Hill, Mr. Gary Harrison, Mr. Stuart Morse, Mr. Kenneth Gyves, Dr. John Warren, Dr. Xiangli Zhong, Dr. Teruo Hashimoto, Mr. Andy Forrest, Mr. Andrij Zadoroshnyj, Mrs. Julia Cheung, Mr. Gary Ingham and Mr. Michael Faulkner for their invaluable technical support, scientific advice, assistance with social inclusion and friendly discussions.

I would like to thank my dear wife, Diana Martins and son, Afonso Martins for their unconditional love, support and companionship throughout this challenging endeavour. Lastly, I would like to thank my parents, sibling and sister-in-law, João Martins, Fátima Freitas, Francisco Martins and Leonor Duque for laying down the foundations that allowed me to explore my inquisitive and curious nature. My parents-in-law, Almerino Gonçalves and Ana Gonçalves also provided important family and personal support throughout my PhD project.

Chapter 1. Introduction

1.1. Development of gas-turbine engines

Over the last few decades, the continuous development of gas-turbine engine technology has been motivated by an increased global demand in commercial air travel, a trend that is expected to double over the next couple of decades according to the International Air Transport Association (IATA)[2]. As a result, the global market value of gas-turbine engines for aviation has been experiencing a period of sustained growth, displaying a total production value of $641 billion over the last ten years and a forecasted $887 billion for the next ten years [3]. In the year of 2019 alone, the production of 14,375 gas-turbine engines for aerospace applications equated to a production value of $75 billion, a metric that is forecasted to increase to $105 billion in 2029 as a result of the production 17,374 engines [3]. These reports and forecasts can be seen as an indicator for the increasing importance of gas-turbine technology to the aerospace sector.

Gas-turbine engines comprise an air intake system, fan, compressors, combustor, turbine and exhaust components distributed across cold or hot sections of the engine, as depicted in the Rolls-Royce Trent 1000 engine schematic presented in Fig 1.1-a). Modern gas-turbine engines convert chemical energy from combustible fuel sources to mechanical energy according to the thermodynamic processes described by the open Brayton cycle operating principle represented in Fig. 1.1-b). In turn, the mechanical energy resulting from the rotation of the high- and low-pressure turbines is converted into electricity by power generators. This means that the operational efficiency of these engines can be improved by increasing the gas stream temperatures, as illustrated by Fig. 1.1-c) [4-6]. Consequently, the development process of gas-turbine engines has been predominantly driven by continuously pushing the operational limits further to achieve enhanced fuel consumption profiles, increased thrust to weight ratio, reduced air cooling needs and greenhouse gas emissions [4, 6, 7]. However, the maximum operating temperature allowed for a gas-turbine engine is determined by limitations of the engine components' design and high-temperature capability of the constituent materials. The standard material that has been typically used in gas-turbine engine components is a Ni-based superalloy due to meeting the functional requirements in terms of chemical (oxidation and hot corrosion resistance), physical (high melting point, elastic modulus, thermal expansion) and mechanical properties (high-temperature strength, creep resistance). However, the limited evolution in temperature capability of Ni-based superalloys over the last five decades (Fig. 1.2) caused by thermo-chemical and mechanical degradation issues at temperatures over 850°C evidenced a growing difficulty in keeping up with the increasingly demanding operational temperature requirements [8]. Up until three decades ago, these limitations were primarily being addressed by improvements in alloy design, development of single crystal engine turbine blades and highly complex internal cooling channel systems incorporated into these components [4, 9, 10]. However, the gap between the desired operational temperatures of gas-turbine engines and the Ni-based superalloys maximum allowable temperature has grown by a few hundred degrees during this time (Fig 1.2). This shifted the research focus to the improvement of the high-temperature capabilities of other TBC system constituents (i.e. the bond coat and TBC layers) and respective inter-layer mechanical and chemical interactions [4, 6, 8]

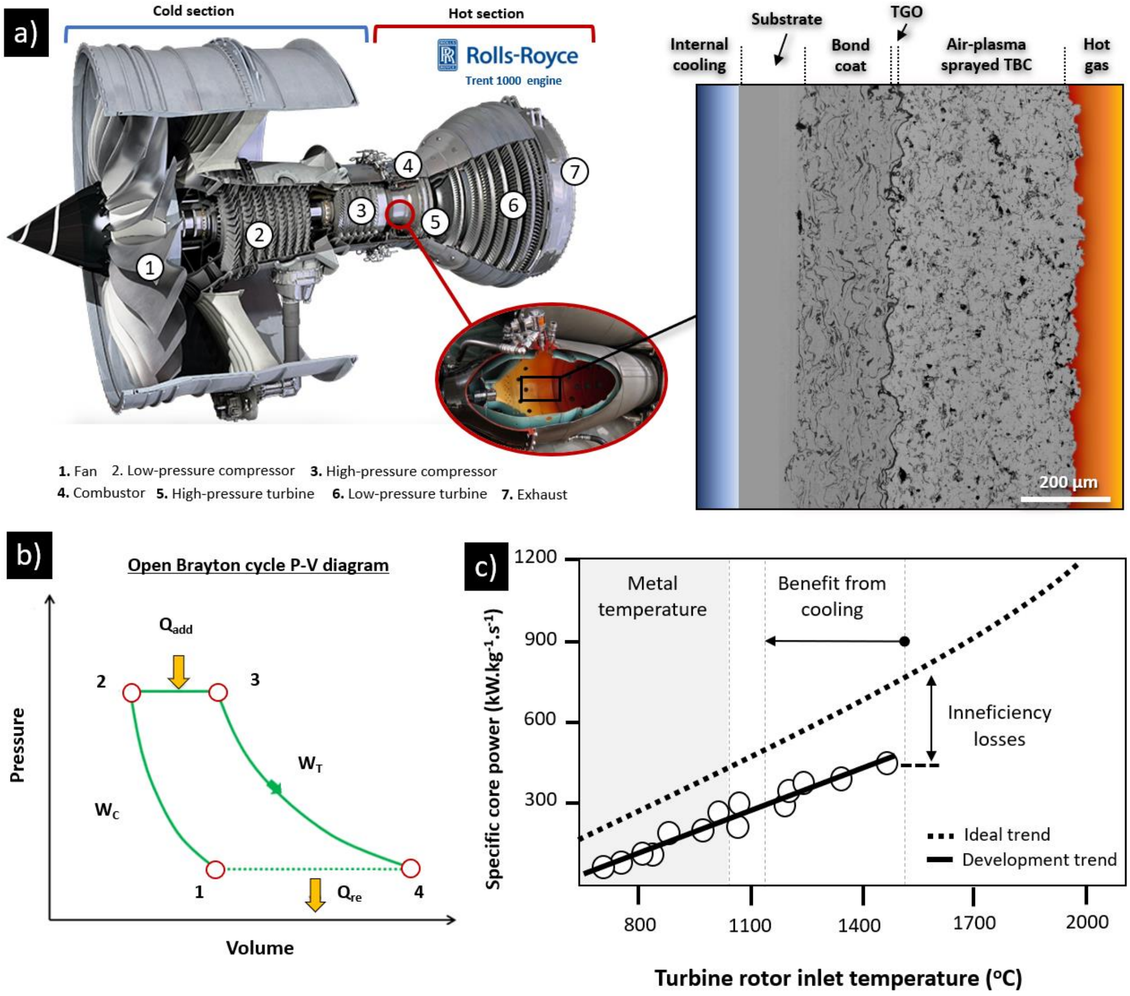
a)
Cold section
Hot section
Rolls-Royce
Trent 1000 engine
1
2
3
4
5
6
7
1. Fan 2. Low-pressure compressor 3. High-pressure compressor
4. Combustor 5. High-pressure turbine 6. Low-pressure turbine 7. Exhaust
Internal cooling
Substrate
Bond coat
TGO
Air-plasma sprayed TBC
Hot gas
200 μm
b)
Open Brayton cycle P-V diagram
Pressure
Volume
Q_add
Q_re
W_C
W_T
1
2
3
4
c)
Specific core power (kW.kg⁻¹.s⁻¹)
1200
900
600
300
Metal temperature
Benefit from cooling
Inneficiency losses
Ideal trend
Development trend
800
1100
1400
1700
2000
Turbine rotor inlet temperature (°C)

Fig. 1. 1 (a) Cut-out profile view of a Rolls-Royce Trent 1000 engine where the main constituent sections are highlighted and a typical cross-sectional microstructure of an air-plasma sprayed (APS) TBC used in the internal lining of a combustion chamber is presented (Edited from [11]); (b) Representation of an open Brayton cycle and respective pressure-volume (P-V) diagram displaying the isentropic (i.e. segments 1→2 and 3→4) and isobaric (i.e. segments 2→3 and 4→1) processes performed by an operating gas-turbine engine; (c) Graph displaying the specific core power evolution as a function of turbine rotor inlet temperature for idealised and industrial engine development trends (Edited from [6]).

The resulting research efforts were instrumental in identifying the most desirable physical, chemical, microstructural, mechanical and thermal properties of each individual layer and subsequently establishing an idealised set of functional requirements for the design and development of TBC systems. The continuous experimentation with multiple TBC system internal structures (i.e. functionally graded TBCs, multi-layer bond coat, Al_2O_3 interlayers, interface topography, etc.), layer composition (e.g. new materials, doping) and processing methods was instrumental in building a solid understanding of this technology. Ultimately, this culminated in the definition of the reference TBC system architecture represented in Fig. 2.1 and commonly adopted by the industrial and scientific communities.

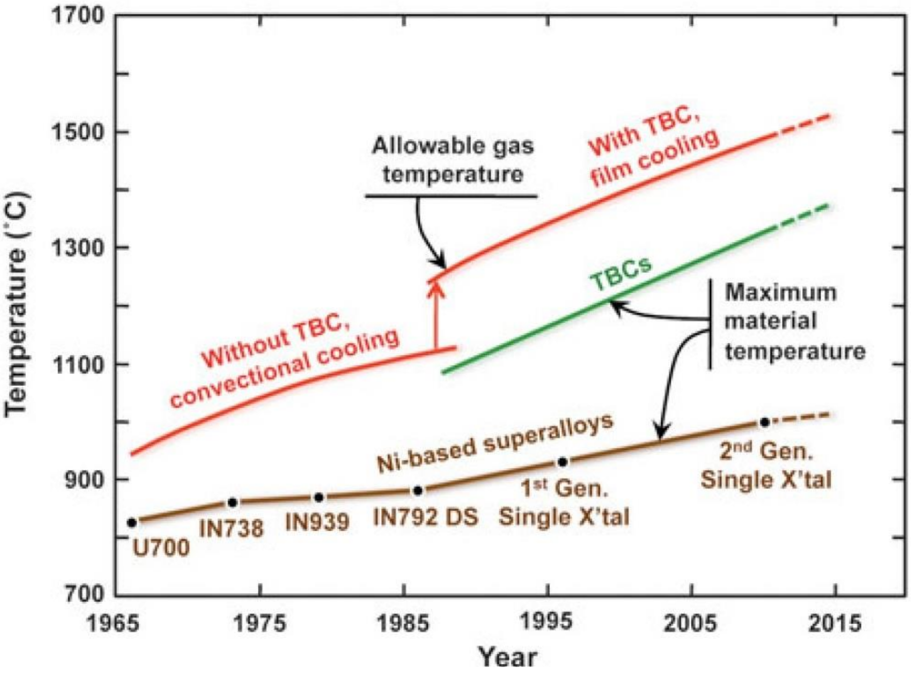

Fig. 1. 2 Evolution of Ni-based superalloy design and TBC temperature capabilities since from 1965 to 2015. The continuous lines connected the data points constitute the maximum allowable temperature for Ni-based superalloys (brown line), TBCs with film cooling (red line) and without (green line) [4].

Although gas-turbine engine technology has seen tremendous improvement in efficiency and power output over the last five decades, as shown in Fig. 1.1-c), the continuous demand for improved engine efficiency, durability and enhanced reliability has pushed current Yttria-Stabilised Zirconia (YSZ)-based TBC systems imminently close to their operational limit [12, 13]. Under these conditions, thermally-induced phenomena that are dependent on the engine operating conditions (i.e. radiative heat transport, sintering, oxidation, diffusion, and inter-layer mechanical interactions) accelerate the degradation of the TBC systems and reduce the TBC durability significantly [1]. Therefore, current research trends are predominantly focused on transitioning from YSZ-based systems deposited over high flame temperature processed bond coats (BC) to lower thermal conductivity (i.e. low-κ)

pyrochlore or perovskite-based systems deposited over lower flame temperature BCs. All these concerted efforts will eventually culminate in the development of more advanced TBC systems with superior performance, potentially facilitating the transition from a continuous lifetime extension approach to a prime reliance stage.

1.2. Evolution of thermal barrier coating technology

Thermal barrier coatings are refractory-oxide ceramic coatings of variable thickness (0.1 to 3 mm) that are typically applied on metallic components of gas-turbine engines with the intent of providing efficient thermal insulation at high temperatures in demanding environments [6]. These ceramic coatings were initially developed in the late 1940s by the National Advisory Committee for Aeronautics (NACA) as a part of a thermal protection system for military aircraft engine components [14, 15]. The first frit enamel coatings used showed some durability issues and therefore flame-sprayed ceramic coatings were investigated in the mid-1950s as an alternative. Zirconia-calcia coatings emerged as a viable material candidate for high-temperature protection of engine parts but the lack of phase stability and relatively high thermal conductivity at temperatures over 1000°C limited their widespread application significantly [14, 16].

It was not until the mid-1960s that the TBC field was revolutionised by the emergence of plasma jet technology for high-temperature spraying of ceramics, when porous dual-layered APS zirconia-yttria (ZrO_2-Y_2O_3) TBC systems were introduced for the first time [17]. In 1970, APS TBC systems comprised of 12 wt.% YSZ TBC and Ni-16Cr-6Al-0.6Y wt.% bond coat (BC) were finally integrated into several components of commercial gas-turbine engines, a milestone that marked the beginning of the modern era of TBCs. In the late 1970s, it was discovered that lowering the yttria content required for the stabilisation of zirconia to the 6-8% range presented enormous benefits for the TBC system durability [18], effectively contributing to the establishment of 7-8 wt% YSZ as the reference TBC material. Around the same time, the first electron beam-physical vapour deposition (EB-PVD) YSZ coatings were manufactured and displayed a comparable performance with the APS YSZ coatings used at that time [14, 19]. EB-PVD coatings finally surpassed the performance of their APS counterparts by the early 1980's but poor processing reproducibility prevented immediate widespread application. However, these issues were mitigated by mid-decade and engine tests indicated that EB-PVD coatings were suitable for thermal protection of subsonic engines aerofoils due to enhanced substrate adhesion and excellent strain tolerance. The well-known improvement in TBC efficiency observed during this decade resulted in the widespread incorporation of TBC systems into commercial engine vane platforms and rotating blades [14, 20], further reasserting the importance of a thermal protection layer in providing efficient thermal protection to the underlying superalloy substrates used in gas-turbine engine parts [4, 12].

Nowadays, TBCs are considered critical components in thermal protection systems of gas-turbine engines and are widely applied to a variety of components such as combustors, nozzles, rotating blades, stationary guide vanes, shrouds and afterburners [4, 7]. The standard reference TBC material is still the 7-8 wt.% Yttria-stabilised-Zirconia (i.e. 7-8YSZ), as it displays a unique set of highly desirable properties (i.e. low thermal conductivity, high strain tolerance, phase stability, high fracture toughness) that have not been fully met by alternative materials so far [4, 12, 20-23]. However, recent trends show that efforts have been carried out over the last decade to slowly migrate towards higher complexity crystal structures and compositions (i.e. pyrochlores, perovskite-structured oxides and lanthanide orthophosphates/silicates) that can accommodate higher operational temperatures (≥ 1400°C) [24, 25]. Nevertheless, such a transition is expected to take some time as the emerging materials still display critical issues that need to be addressed before widespread application in gas-turbine engines can be considered (i.e. thermal expansion mismatch and high reactivity incompatibilities with adjacent layers, low toughness, increased processing complexity, reliability and reproducibility issues) [25]. These topics will be further explored in chapter 2.

1.3. Scope of the dissertation

The main objective of this dissertation is to promote an improved understanding on how the bond BC/TBC interface topography affects the microstructural and mechanical properties of the TBC, ultimately focusing on how these changes affect the TBC fracture mechanics and its durability. The role of the bond coat microstructure on the early oxidation behaviour of MCrAlY coatings was also investigated to gain new insight into how the initial stages of oxidation affect the oxide scale formation and evolution. The thesis follows the following structure:

Chapter 2 consists of a comprehensive literature review on the TBC system, wherein the individual layers are introduced and contextualised in terms of material requirements, properties and processing methods. The main failure mechanisms and degradation processes identified in TBCs to this date are also reviewed. Special regard has been given to the effects of the intrinsic failure mechanisms of APS coating architectures since they are the main focus of study of this dissertation.

Chapter 3 consists of a description of the multiple experimental techniques utilised in the fabrication, preparation, testing and analysis of the APS TBC systems. This is complemented by a justification of why these techniques were selected and an explanation of the methodology implemented in each case.

Chapter 4 consists of a comprehensive study into how the bond coat interface topography affects the durability of APS TBC systems. The interface topography is one of the most important microstructural features in the design of a TBC system as it plays a key role in the generation of the interfacial stresses responsible for the nucleation and propagation of cracks. A combination of several surface texture parameters were used to characterise the different bond coat interface topographies, including a newly proposed metric denoted *total thresholded summit area* (S_{sth}). The topography-induced alterations to the microstructural and mechanical properties of the TBC coatings were quantified in terms of the splat curvature and elastic modulus. The TCF failure mechanisms and overall crack configuration were also discussed and contextualised with other studies in the literature. All these results are then evaluated in terms of their impact on the TBC thermal cycling fatigue lifetime (TCF) results.

Chapter 5 is a natural continuation of the work done in the previous chapter, focusing on the mechanistic understanding of how bond coat topography affects the APS TBC fracture mechanics. This is achieved by conducting an in-situ modified four-point bending test under controlled atmospheric conditions to determine the intrinsic critical energy release rate and stress intensity factor of each different BC topography. Although a significant amount of studies have been carried out on the fracture toughness of APS TBCs, most have focused on investigating the effects of sintering or oxidation kinetics and have overlooked the contribution of the BC interface topography. In the present study, the degree of BC tortuosity was quantified for each TBC system using the S_{sth} metric and its impact on the crack path configuration, fracture toughness (K_i), critical energy release rate (G_c) and crack propagation velocity (v_{prop}) is studied. The effect of splat morphology on fracture mechanics is evaluated in terms of curvature and inter-splat cohesion.

Chapter 6 consists of an investigation into the early stage formation and evolution of Al-rich oxide scales growing over HVOF CoNiCrAlY coatings at high temperatures. The formation of a continuous and thermodynamically stable Al_2O_3 oxide scale with minimal formation of non-Al oxides is an important functional requirement in TBC systems. While many studies have been conducted on the oxidation of MCrAlY coatings, only a small fraction have focused specifically on how the early stages of oxidation behaviour lead to the formation of a spinel-rich outer layer. The oxide scale formation and evolution with oxidation time is studied herein by a correlative microscopy and spectroscopy approach. The mechanisms enabling the gradual transformation of the oxide scale are examined and discussed in terms of their impact on stress generation and failure mechanisms. Special consideration is given to the concentration and distribution of Cr within the scale.

In chapter 7, all the main conclusions are summarised and an outlook on future research is provided with basis on the current findings.

Chapter 2. Literature review

2.1. The thermal barrier coating system

A TBC system is a multi-layered thermal protection system that can be utilised in moving or stationary parts of gas-turbine engines in order to provide efficient thermal insulation in high-temperature oxidising environments. These systems have evolved considerably over the last few decades into a modern TBC architecture typically comprised of four primary constituents, a ceramic thermal barrier coating, a Ni-based superalloy substrate, a metallic bond coat (BC) and a thermally grown oxide (TGO), as illustrated in Fig. 2.1. [4, 12, 22, 23].

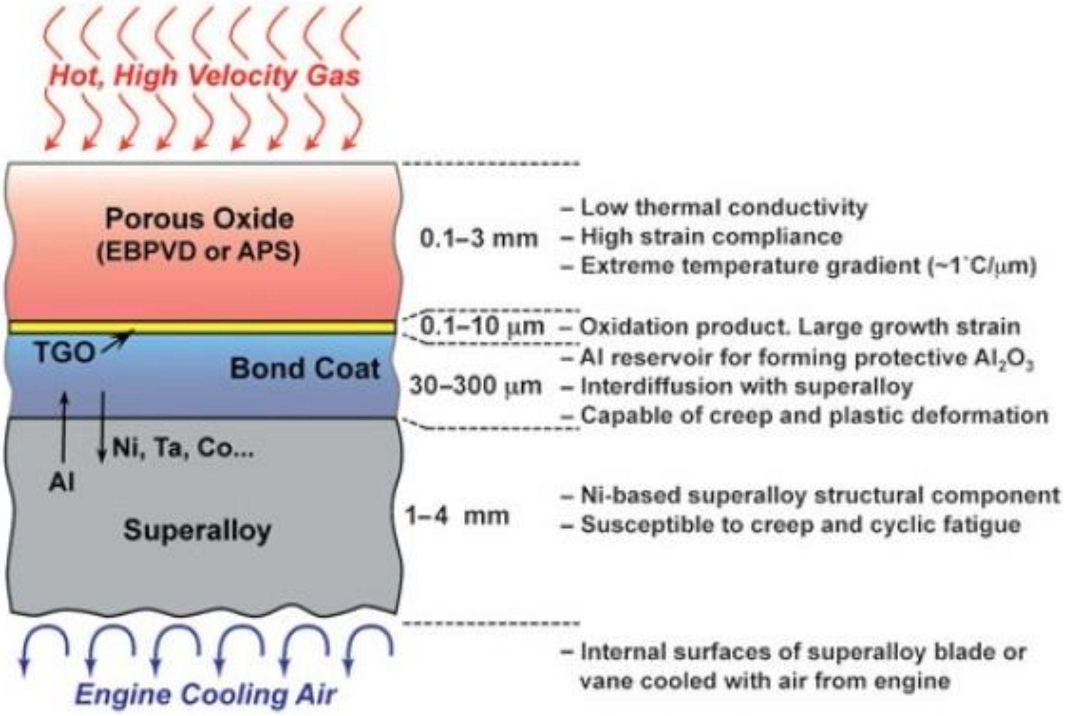
Hot, High Velocity Gas
Porous Oxide
(EBPVD or APS)
0.1–3 mm
– Low thermal conductivity
– High strain compliance
– Extreme temperature gradient (~1°C/μm)
0.1–10 μm
– Oxidation product. Large growth strain
TGO
Bond Coat
30–300 μm
– Al reservoir for forming protective Al2O3
– Interdiffusion with superalloy
– Capable of creep and plastic deformation
Ni, Ta, Co...
Al
Superalloy
1–4 mm
– Ni-based superalloy structural component
– Susceptible to creep and cyclic fatigue
– Internal surfaces of superalloy blade or vane cooled with air from engine
Engine Cooling Air

Fig. 2. 1 Schematic illustration of a modern multi-layered TBC system structure wherein the main desirable features are presented alongside the typical surrounding environmental conditions [4].

Each one of these layers has been carefully designed, developed and continuously optimised with the purpose of fulfilling a specific set of functional requirement criteria and addressing the main degradation mechanisms identified in TBC systems. A very succinct description of their primary functions and properties is outlined below [4, 12, 22, 23]:

- Topcoat – a ceramic layer with low thermal conductivity and high strain tolerance that is responsible for providing efficient thermal insulation to the underlying structure via thermal transport scattering mechanisms;

- Bond coat – a metallic alloy layer that is engineered to promote the formation of a thermally grown oxide scale via selective oxidation of Al^{3+} and provides oxidation/hot corrosion protection to the underlying substrate;
- TGO – a thermodynamically-stable oxide protective scale that forms between the topcoat and the bond coat upon exposure to high temperature oxidising environments;
- Substrate – a Ni-based superalloy with a high melting point, high-temperature strength, good oxidation and hot corrosion resistance that is typically utilised as a structural component in gas-turbine engines.

The multi-layer and multi-material nature of the TBC system leads to an unavoidable complexity that can be simultaneously regarded as beneficial and detrimental to its performance. On one hand, it allows for a high degree of versatility in the design and manufacturing processes of the thermal protection system, which contributes to an adequate applicability on components with different in-service requirements due to their location in the engine. On the other hand, it also leads to undesirable inter-layer interactions (i.e. thermo-mechanical and -chemical) that are responsible for most of the limitations and issues that limit the TBC systems durability [12, 26, 27]. Taking this into consideration, the TBC system cannot be viewed as an isolated set of stacked layers but rather as a complex, dynamic and highly interactive system [22, 23]. In order to better understand its constituent layers and respective interactions, the TBC system will be virtually de-constructed and analysed over the following sections with special focus on their individual requirements, materials, processing methods and stress development. This is followed by an overarching analysis of the main mechanisms that lead to the failure of TBC systems.

2.2. Ceramic topcoat

2.2.1 Functional requirements

A topcoat layer needs to incorporate a certain set of intrinsic properties in order to accommodate all the structural and physical requirements of TBC systems operating in demanding environments. First and foremost, the selected material for the topcoat layer must have low thermal conductivity with minimal temperature sensitivity to provide efficient thermal insulation under exposure to high temperatures [12, 22]. Concurrently, it should also exhibit good structural stability and durability when exposed to high-temperature oxidising environments for a long period of time [28, 29]. Secondly, it must also be strain compliant to mitigate the effects of thermal mismatch stresses arising between the topcoat and the underlying layers during the TBC cooling process [4, 12]. Thirdly, it should present good phase stability and thermo-chemical compatibility with the adjacent layers to avoid the formation of undesirable interphases and phase transformations that induce significant volume changes and generate stresses that are detrimental to the TBC durability [4, 29, 30]. Lastly, the selected material must also be able to resist plastic deformation and fracture from external environmental sources like foreign object damage (FOD), erosion, corrosion and Calcium-Magnesium-Alumino-Silicate (CMAS) attack [1, 31]. These requirements have gradually emerged from extensive research carried out over several decades and are now used as a guideline for developing new TBC architectures, materials and even processing methods.

2.2.2 Materials

Numerous ceramic materials have been studied for application in TBC systems, but none has been able to match the performance and wide acceptance of zirconia-based ceramic topcoats so far, especially the most commonly used material in TBC systems, the 7-8wt.% yttria-stabilised zirconia (7-8YSZ) [4, 24]. This can be primarily attributed to the unique match between the aforementioned requirements for high temperature thermal protection coatings and the inherent properties of zirconia-based ceramic materials described in this section. However, the development of such a material lasted a couple of decades and started with the selection of pure zirconium dioxide (ZrO_2) as a candidate material. This was mostly because ZrO_2 incorporated a considerable amount of desirable properties for application in high-temperature demanding environments (i.e. low thermal conductivity, high temperature toughness and strength, high melting point and chemical inertness) [32]. Under equilibrium conditions, ZrO_2 can assume three different crystallographic phases depending on the temperature, as shown in Fig. 2.2 [32]:

$$Monoclinic - ZrO_2 \underset{950^{o}C}{\overset{1170^{o}C}{\rightleftharpoons}} tetragonal - ZrO_2 \underset{\square}{\overset{2370^{o}C}{\rightleftharpoons}} cubic - ZrO_2 \underset{\square}{\overset{2680^{o}C}{\rightleftharpoons}} liquid$$

Fig. 2. 2 (a) Schematic representation of the phase transformation of ZrO2 as a function of temperature [32].

The in issue with this material is that the phase transformation from tetragonal to monoclinic ($t \longrightarrow m$) is martensitic and therefore, is accompanied by a disruptive volume change ($\sim 4 - 5\%$) that leads to a low thermal shock resistivity and therefore higher propensity for stress-induced cracking [32, 33]. This issue was solved by partial stabilisation of ZrO_2 with oxide dopants (i.e. Y_2O_3, MgO, Sc_2O_3, In_2O_3 and CeO_2), as their inclusion in the lattice stabilised the tetragonal-prime (t') phase and suppressed the $t \longrightarrow m$ martensitic phase transformation altogether. Even though most of these oxides stabilised ZrO_2 to some extent, Y_2O_3 emerged as the preferred stabiliser since it showed increased potential for extended thermal cycling fatigue (TCF) lifetime, effectively marking the discovery of yttria-stabilised zirconia (YSZ) [23]. The optimal level of Y_2O_3 required to stabilise ZrO_2 was subsequently investigated, culminating in the conclusion that 7-8wt.% was ideal for TBC application due to showing longer thermal cycling lifetime and easier deposition features [22, 23]. This unique material also showed other desirable properties such as low thermal conductivity ($2.0 - 2.3\ W.m^{-1}K^{-1}\ at\ 1000^oC$ for fully dense YSZ), high melting point ($\sim 2800^o\mathrm{C}$), mutual low solubility with adjacent layers, good morphological phase stability and inter-layer thermodynamic compatibility [4, 23, 34]. The remarkable low thermal conductivity displayed by the YSZ material results from the high concentration of phonon scattering point defects incorporated into the YSZ lattice by the doping process, such as oxygen vacancies and substitutional solute aliovalent cations (i.e. Y^{3+}, La^{3+}, Ca^{2+} and Mg^{2+}) [35]. More specifically, it is the addition of these cations with lower valence than Zr^{4+} that generate the oxygen vacancies in the sublattice structure due to the need for charge neutrality compensation [35]. In the specific case of Y_2O_3 addition, the substitution of Zr^{4+} by Y^{3+} results in a negative lattice net charge that is compensated by the formation of a positive bivalent oxygen vacancy, as described by equation 2.1 in Kröger-Vink notation [35] and illustrated in Fig. 2.3 [36].

$$Y_2O_3 \longrightarrow 2Y'_{Zr} + 3O_{\ddot{O}}^x + V_{\ddot{O}} \quad \text{with} \quad [V_{\ddot{O}}] = 2[Y'_{Zr}] \tag{2.1}$$

where Y'_{Zr} represents the substitution of Zr^{4+} by the Y^{3+} ion, $O_{\ddot{O}}^x$ the lattice oxygen and $V_O$the positive bivalent oxygen vacancy.

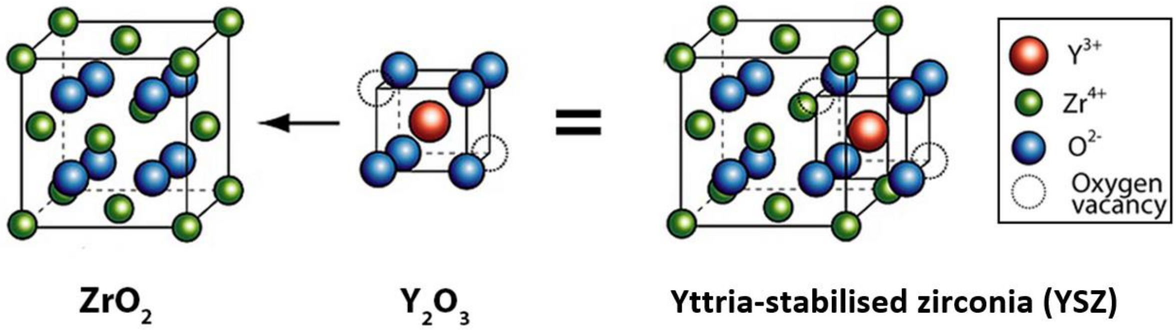

Fig. 2. 3 Schematic illustration of the YSZ crystal structure highlighting the addition of Y2O3, edited from [36].

Another advantageous consequence of the t' phase stabilisation of YSZ is the high fracture toughness that arises from a reversible ferroelastic domain switching. This toughening phenomenon is insensitive to temperature and allows the material to retain its high toughness at elevated temperatures, significantly improving its fracture resistance and making it useful for TBC applications [37, 38]. However, fully dense YSZ exhibits a wide range of toughness values ($6 \leq G_C \leq 210\ J.m^{-2}$) that are dependent on Y_2O_3 content, crystal structure, deposition technique and phase content [38].

Moreover, the TBC processing method can also originate significantly different toughness values for identical YSZ compositions ($45 \leq G_C \leq 150\, J.m^{-2}$ for 7YSZ [38]). This effect is often explored to obtain an adequate microstructural balance between fracture toughness and TBC compliance that is extremely beneficial to TBC durability [39-41].

Another intrinsic property of YSZ that is crucial for TBC application is a high coefficient of thermal expansion ($CTE\ {\sim}10.7 - 11.5 \times 10^{-6}\ C^{-1}\ up\ to\ 1000^oC$) that approximates the magnitude of typical Ni-based alloys ($13 - 16 \times 10^{-6}\ C^{-1}$), TGO (${\sim}8 - 9 \times 10^{-6}\ C^{-1}$) and bond coat ($16 \times 10^{-6}\ C^{-1}$) materials under the same environmental conditions [12, 23, 24, 42], as illustrated by Fig. 2.4. However, even though the CTE mismatch between the YSZ coating and adjacent materials is within the acceptable range for application in TBC systems, the continuous exposure to thermal cycling conditions generates high thermal stresses ($2.5 \leq \sigma_{CTE\ mismatch} \leq 4.5\ GPa$) that gradually lead to the TBC degradation [12]. Consequently, three-dimensional (3-D) defects of various sizes and morphologies are intentionally introduced into the TBC structure during the manufacturing process (i.e. globular pores, inter-splat discontinuities and intra-splat cracks) in order to increase its compliance and strain tolerance [21, 23, 34]. An advantageous side effect arises from this, as the introduction of these microstructural defects (i.e. porosity) further reduces the TBC thermal conductivity due to a decrease in the phonon net section propagation area [23, 24]. Depending on the extent of the TBC porosity network, which can range from 10 to 30% depending on the TBC deposition method and system structure [43], thermal conductivity can be reduced to the $0.5\text{–}\ 1.8\ \mathrm{W}.m^{-1}K^{-1}$ range [12, 24]. Typically, a reduction to $45 - 65\%$ of the fully dense YSZ thermal conductivity can be achieved when using an electron-beam physical vapour deposition (EB-PVD) deposition technique and up to 80% for the APS counterparts. This difference is primarily originated by the distinct microstructures generated by EB-PVD (i.e. columnar) and APS (i.e. laminated) deposition methods.

Although YSZ still remains the preferred material for thermal protection of gas-turbine engines in the current range of surface operational temperatures ($\leq 1200^oC$), it faces significant challenges to meet the long-term engine operational requirements of more demanding engine atmospheric conditions ($\geq 1350^oC$) [1, 16]. Under such conditions, compositional and microstructural changes such as sintering, phase decomposition and CMAS attack are significantly exacerbated, becoming serious limitations for TBC durability. More specifically, the t' phase undergoes a detrimental phase partition by diffusion into a mixture of low-yttria tetragonal (*t*) and high-yttria cubic (*c*) phases after long-term thermal exposure at elevated temperatures [44, 45]. In turn, the former undergoes a detrimental $t \longrightarrow m$ phase transformation during cool-down to ambient temperatures that leads to cracking and disintegration of the TBC [44, 45]. Adding to this, the increased ionic mobility at higher operation temperatures also promotes a faster TBC sintering rate, simultaneously decreasing the TBC compliance and increasing radiative heat transfer due to a large reduction in microstructural defects [46, 47]. As most siliceous build-up mixtures found in gas-turbine engines melt at approximately 1200°C, CMAS penetration via cyclic dissolution/infiltration/re-precipitation process is another factor that contributes to the t' phase de-stabilisation [1]. All these limitations have created a need for the development of new TBC materials with lower thermal conductivities and sintering tendencies together with improved phase stability and resistance to CMAS attack.

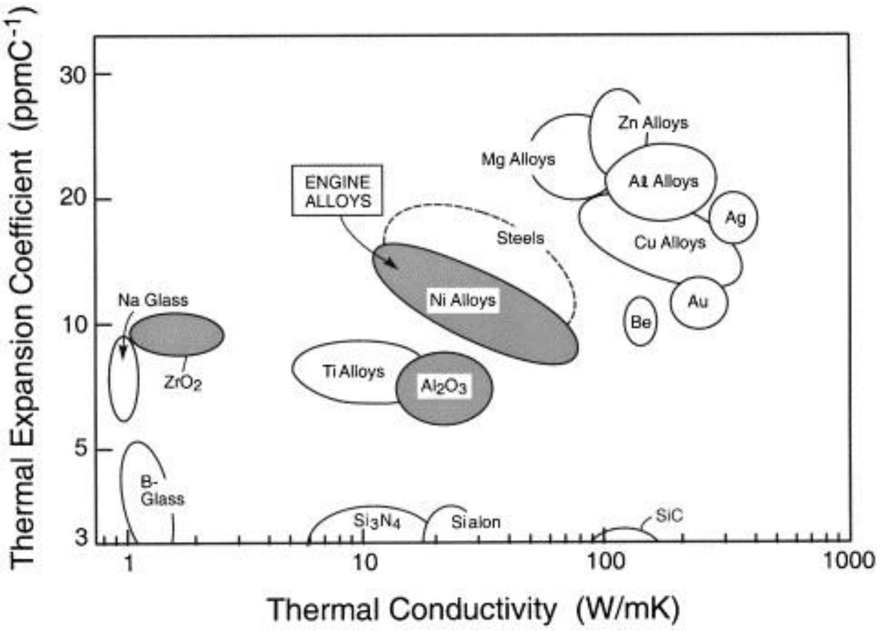

Fig. 2. 4 *A* plot of the thermal expansion coefficient as a function of the thermal conductivity for a range of metal and ceramics materials typically utilised in TBC systems [12].

Accruing from these limitations, scientific and industrial efforts are now being combined to slowly effect a move towards higher complexity crystal structures and compositions that can withstand significantly higher surface temperatures ($\geq 1350^{o}C$), i.e. low-κ TBC materials. Fig. 2.5 shows a compilation of the thermal conductivity values for the most promising emerging low-κ TBC materials, indicating that there might be multiple alternatives to YSZ. Pyrochlore structured materials ($A_2B_2O_7$, where A= rare-earth zirconates and B= Zr) and perovskite structured oxides (ABO_3, where A= La, Pr, Nd, Sm, Eu, Gd, Y, Er, Lu and B can be Ti, Mo Sn, Zr, Pb) are currently amongst the most promising alternatives to YSZ [24, 25], as they exhibit lower thermal conductivities ($\sim$ 1-2 W.m^{-1}.K^{-1} up to $1200^{o}C$ for fully dense microstructures), improved sintering resistance, higher thermal stability and improved resistance to CMAS attack. However, the change from YSZ to alternate materials is likely to be gradual and lengthy as these materials display other limitations associated with other physical (i.e. CTE) and mechanical properties (i.e. fracture toughness). Most pyrochlore and perovskite-based materials show lower CTEs (i.e. $\sim 8.5 - 10 \times 10^{-6}.m^{-1}.K^{-1}$ [24, 42, 48]) in comparison to YSZ, with exception of a few materials such as $Gd_2Zr_2O_7$ ($\sim 10.4 \times 10^{-6}.m^{-1}.K^{-1}$ up to $1000^{o}C$), $SrZrO_3$ ($\sim 10.9 \times$

$10^{-6}.m^{-1}.K^{-1}$ up to 1000^oC) and Ba($Mg_{0.33}Ta_{0.66}$)O_3 ($\sim 10.9 \times 10^{-6}.m^{-1}.K^{-1}$ up to 1000^oC). The lower CTEs lead to higher thermal stresses upon cooling down to ambient temperature due to the larger mismatch with the other TBC system layers. Adding to this, the complete absence of toughening mechanisms results in an intrinsically lower fracture toughness that leads to weak thermal shock resistance and lower thermal cycling durability [48, 49]. To further complicate matters, some pyrochlore materials are also not thermo-chemically compatible with the TGO layer, resulting in the formation of porous and brittle interphases that lead to compromised inter-layer adhesion and lower durability [50]. In an attempt to circumvent the higher temperature limitations of single-layer YSZ and reduced thermal shock resistance of alternate TBC materials, a double-layer TBC system concept materials has been introduced with some success [42, 49]. Their structure encompasses an YSZ under-layer that provides enhanced thermo-chemical and –mechanical compatibility with the underlying TBC layers, and a pyrochlore over-layer that offers superior thermo-physical capabilities at temperatures above 1300°C. In fact, experimental studies focused on thermal cycling lifetime have demonstrated that these structures display superior thermal cycling durability at temperatures in the 1300-1450°C temperature range, effectively emerging as promising alternatives for commercial TBC applications [49, 51].

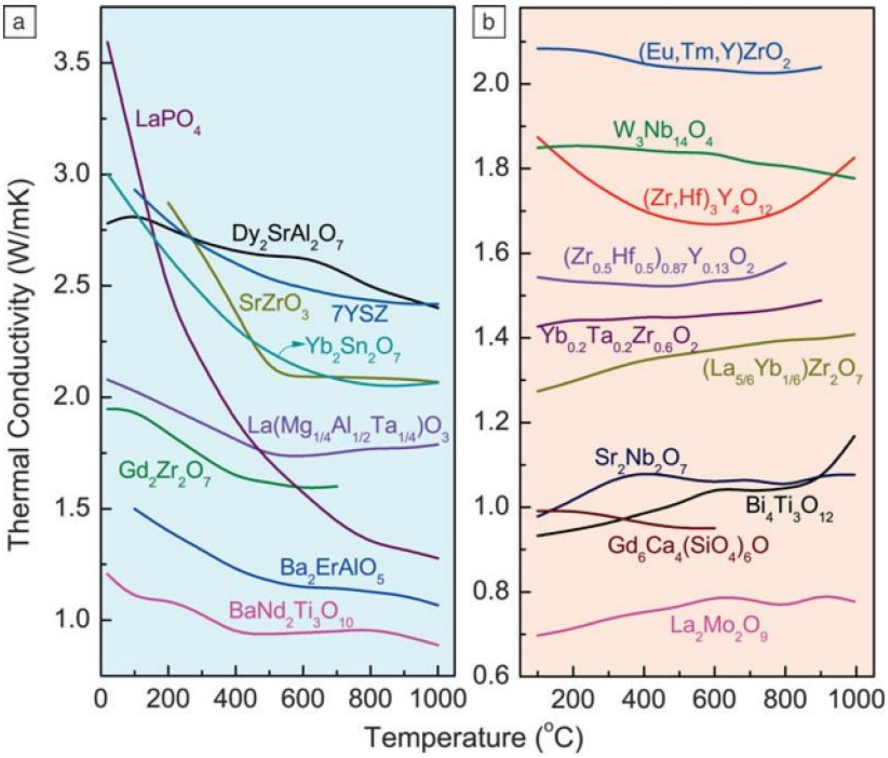

Fig. 2. 5 (a) Variation of thermal conductivity with thermal exposure temperature for emerging ceramic TBC materials and (b) thermal conductivity values for emerging ceramic TBC materials of temperature-independent materials [24]. Please note that the ordinate axis scaling used in the figures above is not the same.

2.2.3 Deposition methods

TBC materials are refractory oxides with extraordinary high melting points (≥ 2300ºC) that require ultra-high temperature processing methods to achieve an effective deposition profile and the desirable microstructural and mechanical properties [34]. The main processing methods selected to fabricate these coatings are APS and EB-PVD due to their ability to produce high-quality ceramic coatings. The specific use of one method over another is often dictated by their adequacy to satisfy the in-service functional requirements of task-specific engine components [22, 23]. On one hand, APS is a technologically less complex method that is typically used to coat stationary engine components (i.e. combustor, vanes and shrouds) due to better thermal insulation efficiency and lower fabrication cost. On the other hand, EB-PVD is a technologically complex and costly method that is typically used to coat non-stationary engine parts (i.e. turbine blades and vanes), as it imparts the TBCs with superior strain tolerance and increased durability [12, 22, 34].

The APS processing method consists of the injection of micrometre-sized powder particles into a hot plasma jet stream (~10000 K) that melts, accelerates and directs the particles toward the intended substrate to form the coating, as illustrated in Fig 2.6-a) [34, 52]. Upon impact, these particles spread radially and establish a good thermal contact with the substrate that leads to rapid solidification and formation of an elongated splat morphology with internal columnar grain microstructure, as depicted in Fig 2.6-c) [52-56]. The subsequent inter-splat stacking assemblage results in a highly complex microstructure that incorporates a vast network of connected inter-splat discontinuities, globular pores and intra-splat segmentation cracks (Figs. 2.6-b) and 2.6-c)) that may comprise between 10 to 25% of the total volume of the ceramic coating [23, 25]. This large network of defects is actually one of the most important characteristics of APS coatings, as it imparts them with the lower thermal conductivity (0.8-1.1 $W.m^{-1}K^{-1}$ for YSZ) [57-59] and improved strain compliance [59-61] required for application in gas-turbine engines. In addition to this, APS TBCs are typically deposited over tortuous BC surfaces in order to promote enhanced adhesion with the underlying substrate [62, 63]. Although mechanical interlocking is considered to be the primary source of interfacial adhesion in these coatings due to superior lateral constraint, the high temperature involved in the plasma spray deposition process and high pressure upon substrate impact are also believed to contribute to the development of chemical and diffusive interfacial bonds [54, 64]. These combined contributions amount to an interfacial adhesion strength in the order of 10 to 50 MPa, which is governed by the processing conditions selected and the degree of BC interfacial tortuosity [16, 60, 63, 65]. In addition, this also illustrates how the microstructural and mechanical properties of these coatings can be optimised via manipulation of deposition parameters like the plasma jet stream characteristics (i.e. spraying distance, particle trajectory, spraying velocity, grain size distribution, thermal/kinetic energy and melting state), substrate condition (i.e. roughness, temperature, position, geometry), atmospheric spraying conditions (i.e. air or vacuum) and the plasma gun settings (i.e. current, voltage) [34, 52, 66-69].

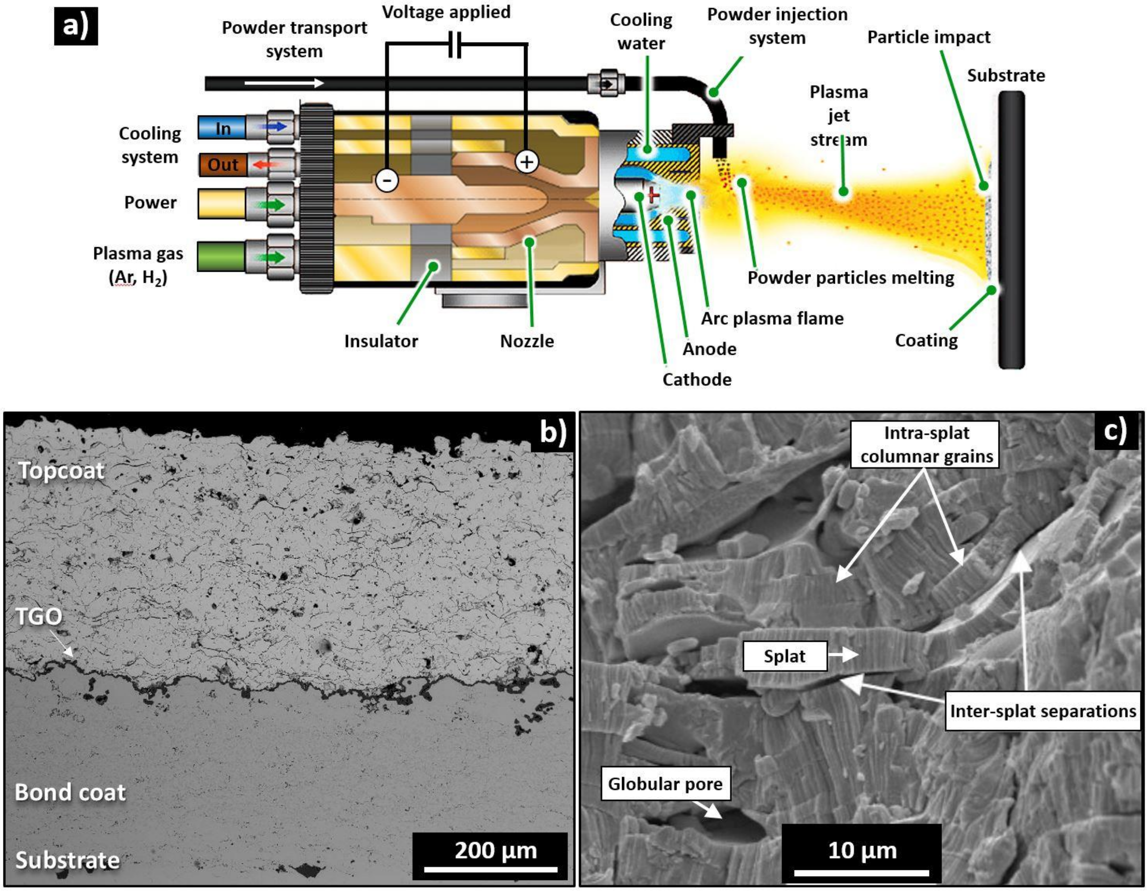
a)
Powder transport system
Voltage applied
Cooling water
Powder injection system
Particle impact
Substrate
Plasma jet stream
Cooling system
In
Out
Power
Plasma gas (Ar, H₂)
Insulator
Nozzle
Powder particles melting
Arc plasma flame
Anode
Cathode
Coating
b)
Topcoat
TGO
Bond coat
Substrate
200 µm
c)
Intra-splat columnar grains
Splat
Inter-splat separations
Globular pore
10 µm

Fig. 2. 6 (a) Schematic illustration of the air-plasma spray (APS) deposition process edited from [70, 71] and respective microstructural details observed from (b) polished and (c) fractured cross-sectional views [72].

On the other hand, the EB-PVD processing method consists of the deposition of a TBC via sublimation of fully-dense ceramic ingots with a high-energy focused electron beam, as depicted in Fig. 2.7-a). Firstly, the beam vaporises the surface of the ingot at a pre-specified rate into a vapour cloud of overheated molten material (i.e. pink oval shape in figure 2.7-a)) that is in suspension inside the vacuum chamber. Then, a radial high vapour pressure directs the suspended molten particles into the centre of the vacuum chamber where the rotating pre-heated substrate is located [34]. At this point, vapour condensation initiates the crystal nucleation and growth process at a rate of a few microns per minute[58]. This process promotes the formation of a typical thin columnar microstructure that grows perpendicularly to the BC/TBC interface to an approximate thickness of 120-150 µm [34, 73], as depicted in Fig. 2.7-b), and shows high interfacial adhesive strength ($\sim 64\ to\ 76$ MPa) [74, 75] . The individual columns are separated by narrow inter-columnar gaps [73] that impart the coating with a superior strain compliance, accruing from their freedom to expand and contract to accommodate the inter-layer thermal mismatch stress. Additionally, the textured nature of these columns displayed in Fig. 2.7-c) originates from an energetically favoured crystallographic growth preference along the $\{111\}$ plane, which is induced by the unique pattern of vapour and macroscopic shadowing resulting from the rotation of the component during deposition [12, 34]. As a result, intra-columnar porosity is introduced into the columns microstructure, a crucial feature that is behind the advantageous reduction in thermal conductivity observed for these coatings (1.5-1.9 W.m^{-1}K^{-1} for YSZ) [58, 73]. Lastly, all these features are strongly dependent on the processing conditions and parameters such as substrate temperature, bond coat interface roughness, rotation rate from the component and vapour flux from the evaporator [76].

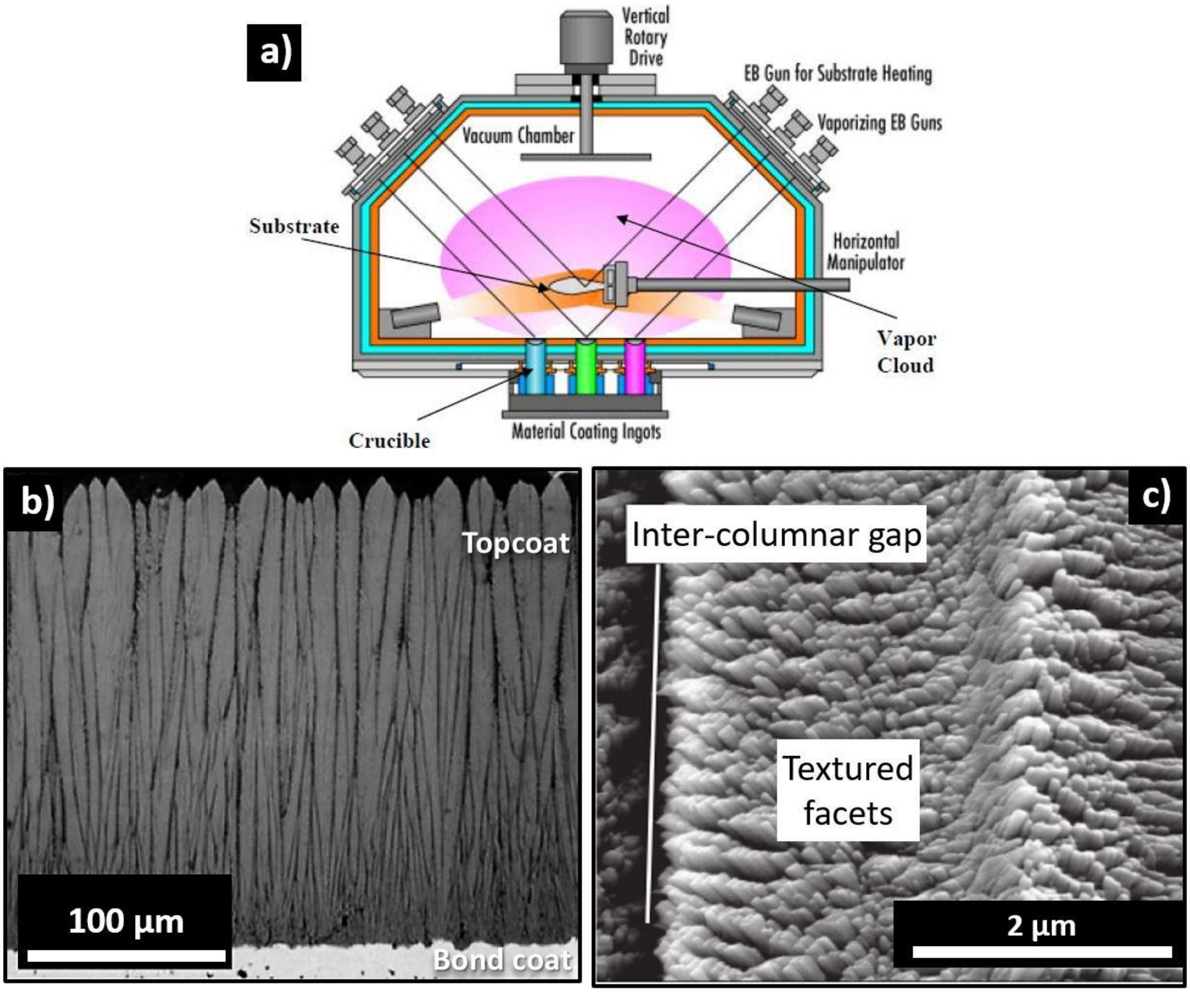
a)
Vertical Rotary Drive
EB Gun for Substrate Heating
Vaporizing EB Guns
Vacuum Chamber
Substrate
Horizontal Manipulator
Vapor Cloud
Crucible
Material Coating Ingots
b)
Topcoat
100 µm
Bond coat
c)
Inter-columnar gap
Textured facets
2 µm

Fig. 2. 7 (a) Schematic illustration of the electron beam physical vapour deposition method (EB-PVD) and respective (b) cross-sectional microstructure [31] and (c) characteristic columnar texture [73].

2.3. Bond coat

2.3.1 Functional requirements

The infiltration and diffusion of molecular oxygen through the permeable topcoat layer is a significant problem for the integrity of bare Ni-based superalloy substrates exposed to high temperatures, as the porous microstructure and the fast ion oxygen conductor nature of the YSZ topcoat facilitate the continuous ingress of oxygen [4, 77]. Although the Ni-based substrate materials are engineered to possess good thermo-mechanical properties (i.e. high strength, good fatigue and creep resistance at high-temperature), their corrosion and oxidation resistance capabilities are not suitable to withstand the effects of long-term exposure to high temperatures [11, 12, 78, 79]. Under these conditions, a bare Ni-based superalloy would promote the formation of a fast-growing, unstable and compositionally complex oxide scale (e.g. NiO, Cr_2O_3, TiO_2, RuO_2, HfO_2 and $Ni(Cr, Al, Ta)_2O_4$ spinels) that is thermodynamically incompatible with the adjacent topcoat layer and therefore, highly detrimental to the TBC system durability [78].

The most efficient way of addressing this issue is the addition of an intermetallic layer (thickness ~ 30-300 μm) between the substrate and the topcoat, commonly referred to as the bond coat. The bond coat is a multi-functional and compositionally elaborate layer that is specifically engineered to meet a certain set of physical, thermo-mechanical and –chemical criteria [80, 81]. Its primary function is to provide high temperature oxidation and corrosion protection to the underlying substrate, by promoting the formation of a thin, dense, stable and slow-growing oxide layer (i.e. TGO) that acts as an oxygen diffusion barrier [12, 80]. As a result, bond coat materials need to be enriched with aluminium to promote the formation and maintenance of an α-Al_2O_3 oxide scale. These scales have to be compatible with the adjacent layers and simultaneously display good mechanical integrity and thermodynamic stability [82, 83]. It is also crucial for the bond coat to maintain adequate adhesion with the adjacent layers during long-term thermal exposure, so as to prevent premature interfacial delamination induced by the detrimental inter-layer mechanical (i.e. CTE mismatch stresses) and chemical interactions (i.e. embrittlement of bond coat/TGO interface by segregation of impurities) [12]. A good resistance to thermo-chemical degradation is also important to mitigate the microstructural (i.e. phase transformations, internal oxide formation) and compositional changes (i.e. aluminium depletion, impurity segregation) induced by inter-diffusion with the substrate and long-term aluminium consumption [81, 84]. In addition to this, the bond coat should also display a high creep strength so as to minimise the bond coat/TGO interfacial plastic deformation (i.e. rumpling) induced by phase transformations and thermal stresses, as this may lead to premature interfacial de-cohesion [12, 84].

2.3.2 Fabrication methods and materials

As the bond coat layer is directly deposited over Ni-based superalloy substrates and is primarily engineered to promote the formation of Al-based oxide scales upon exposure to high-temperatures, the thermo-mechanical and –chemical compatibility between these layers is of crucial importance for the selection of adequate bond coat materials [80, 83, 85]. As a result, the development and research of new bond coat materials has been primarily focused on compatible intermetallic chemistries containing Ni and Al, starting from the simpler Ni-Al binary system displayed in Fig. 2.8-a) to the more advanced ternary systems (i.e. Ni-Al-Cr, NiCo-Al-Cr and Ni-Pt-Al) presented in Figs. 2.8-b) and c) [80].

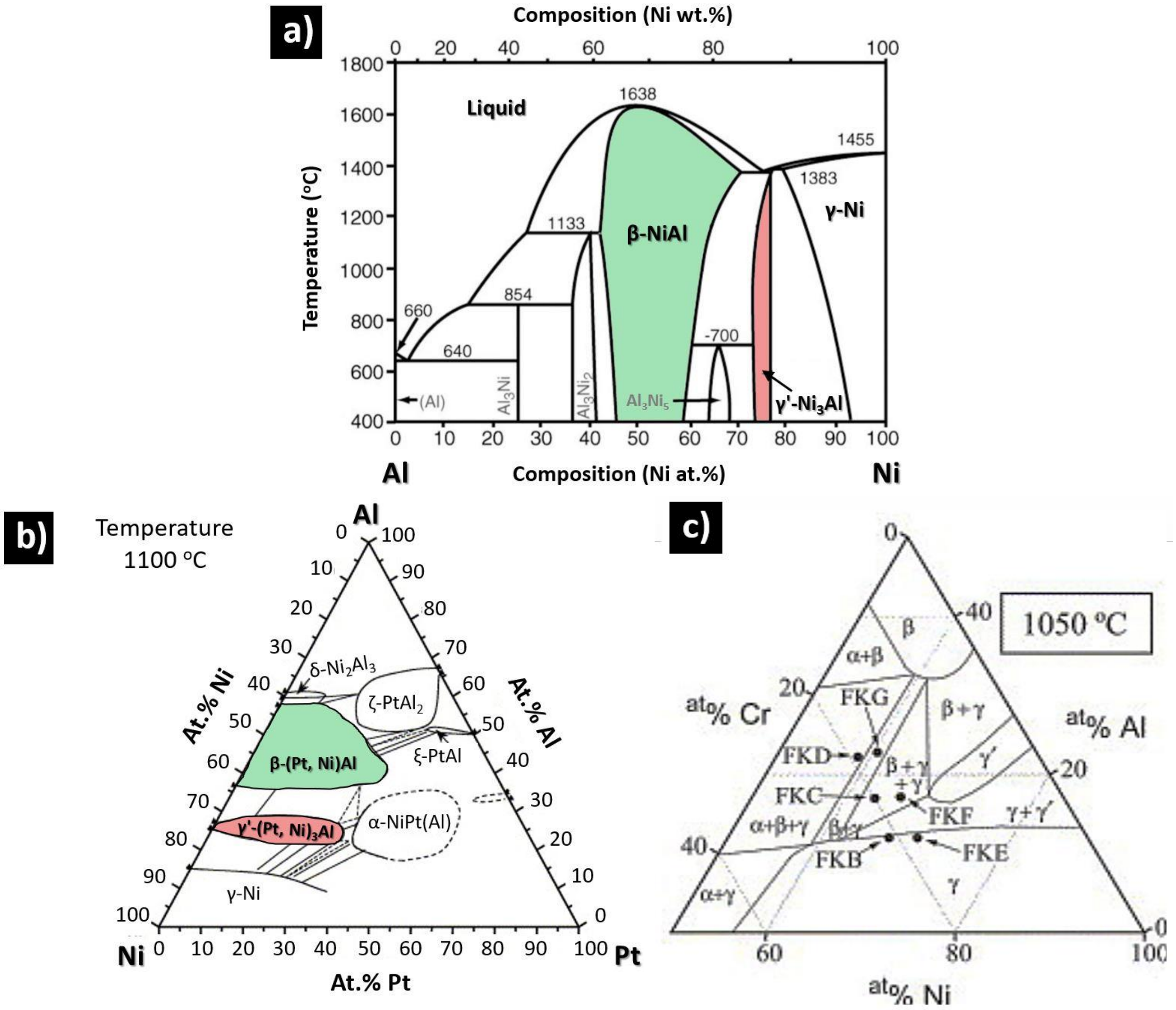

Fig. 2. 8 (a) Binary phase diagram of a Ni-Al system as a function of temperature where the compositional ranges corresponding to β-NiAl (green region) and γ‘–Ni_3Al (red region) phases are highlighted [9]; (b) Ternary phase diagram of a Ni-Pt-Al system at 1100 °C where the compositional ranges that originate the β-(Pt,Ni)Al (green region) and γ‘–$(Pt,Ni)_3Al$ (red region) phases are highlighted [86]; (c) Ternary phase diagram of a Ni-Cr-Al system at 1050 °C [87] .

Modern bond coat materials are predominantly based on the Ni-Pt-Al, Ni-Cr-Al and Co-Cr-Al ternary systems and can be divided into two main categories according to the respective processing methods, diffusion (i.e. β-(Ni, Pt)Al, γ-Ni/ γ-Ni_3Al) and overlay coatings (i.e. M-Cr-Al-X where M=Co, Ni, Co-Ni, Ni-Co and X = Y, Hf, Mo, Si, Re, Zr, Nb and Ta) [4, 22, 80, 83, 88]. Their distinct composition and fabrication methods impart the coatings with different microstructural, physical, chemical and mechanical properties that make them more suitable for application in specific components of the gas-turbine engine [80, 81]. Regardless of their differences, both types of coatings are still able to satisfy the majority of requirements mentioned in the previous section, although the formation of an α-Al_2O_3 protective scale via selective oxidation of aluminium at high temperatures is still the primary concern during their design and development.

2.3.2.1 Diffusion coatings

Diffusion coatings are high-temperature reaction products resulting from an inter-diffusion process between a Ni-based superalloy substrate and an aluminium or platinum external source (donor) [80]. Over the years, these coatings have gone through a long evolutionary process to improve their high-temperature performance and durability that led to a differentiation in coating architecture and properties. As such, these coatings can be divided into two main subcategories, the nickel-aluminide depicted in Fig. 2.9 (i.e. β-NiAl and β-(Ni,Pt)Al) and the platinum-diffused γ/γ' coatings in Fig. 2.10 [80, 81]. Diffusion coatings are typically fabricated via chemical vapour deposition (CVD), vapour-phase aluminising (VPA), slurry aluminising or pack cementation, although the latter is often preferred due its simplicity, versatility and reduced cost [89-91]. Regardless of the method utilised, they all promote the desired high-temperature chemical reaction between nickel diffusing outwards from the substrate and the aluminium/platinum diffusing into the alloy (i.e. aluminising process). This process is typically conducted on surfaces with very low roughness and leads to the formation of coatings that can vary significantly in terms of thickness (i.e. 40-80 µm), microstructure and mechanical properties.

Nickel-aluminide coatings (β-NiAl) were introduced during the 1960's for environmental protection of Ni-based engine components [80, 81] due to their adequate oxidation and corrosion resistance, low density and ability to retain their strength and stiffness at elevated temperatures [92, 93]. Structurally, these coatings can be divided into two separate sub-layers, a chemically complex inner inter-diffusion zone (IDZ) and a more homogeneous β-NiAl outer layer, as shown in Fig. 2.9-a) [90, 93]. The IDZ zone is a chemically diverse region that undergoes significant microstructural and compositional changes during the aluminising process such as severe loss of Ni and concomitant diffusion of Al into this region. These diffusional mechanisms yield a multi-phase microstructure that incorporates numerous intermetallic precipitates hosted in a β-NiAl phase matrix [90]. On the other hand, the β-NiAl phase that comprises the outer scale is arranged according to an ordered B2 cubic crystal structure (CsCl, $Pm\overline{3}m$ space group) comprised of two interpenetrating primitive cubic sublattices, one occupied by Ni atoms and the other by Al atoms [93]. This specific arrangement promotes good phase stability over a wide range of compositions and temperatures, as can be seen in the Ni-Al binary phase diagram in Fig. 2.8-a), effectively contributing to an increased resistance to undesirable phase transformations arising from thermo-chemical degradation processes (i.e. aluminium depletion and substrate inter-diffusion) [94]. Further to this, the high aluminium content of the β-NiAl phase ($\sim 41 \leq Al\ at.\% \leq 55$ [94]) can be regarded as a reservoir that enables the formation and long-term maintenance of a stable α–Al_2O_3 TGO scale [90, 93]. However, these oxide scales often display an undesirable tendency for recurrent cracking and partial spallation under thermal cycling conditions that is detrimental for the TBC system durability, as it facilitates oxygen diffusion into the bond coat and accelerates the aluminium consumption rate. Eventually, it leads to premature aluminium depletion and formation of disruptive non-Al_2O_3 oxides that further compromise oxidation resistance and inter-layer adhesion [81, 91, 93]. To complicate matters further, the β-NiAl phase also undergoes a ductile to brittle transition at 600°C that reduces its high-temperature yield strength (~ 25 MPa at 1150°C [95]) and makes the coating more susceptible to thermo-mechanical fatigue [12, 96].

These limitations motivated the development of more advanced nickel-aluminide coatings that were modified with additional alloying elements such as platinum, yttrium, hafnium, zirconium and dysprosium [88, 91, 97-99]. Platinum addition was more effective in enhancing the bond coat resistance to cyclic oxidation and hot corrosion [91, 100]. These improvements resulted in a significant performance increase over the non-modified counterparts, making Pt-modified nickel-aluminide coatings (i.e. β-(Ni,PT)Al) the modern industrial standard [91]. In terms of fabrication, these coatings can be produced by the same methods as their non-modified counterparts, as long as a thin layer of platinum (~ 5-7 µm) is electroplated onto the substrate and subjected to a vacuum heat treatment prior to the aluminising process [91]. The resulting microstructure (Fig. 2.9-b)) is fundamentally similar to their non-modified counterparts, displaying a Pt-enriched β–NiAl outer layer and a chemically diverse IDZ (Fig. 2.9-b) [90, 91]. Nonetheless, variations in the processing conditions utilised (i.e. Pt layer thickness, vacuum heat treatment temperature and duration, aluminising process) often lead to different microstructures with specific thermo-chemical and –mechanical properties.

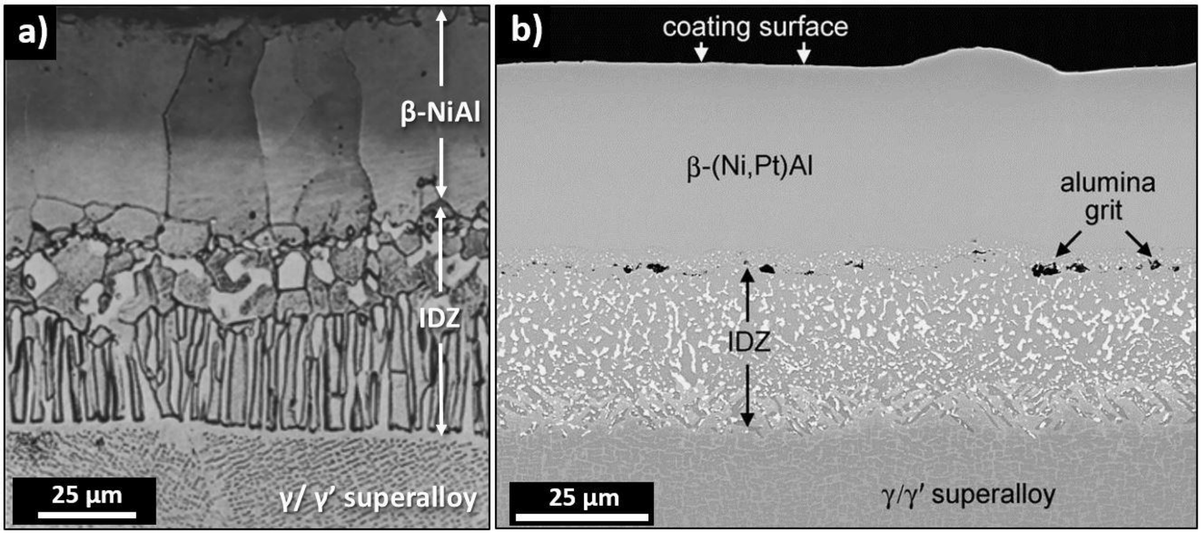

Fig. 2. 9 Backscatted-electron (BSE) micrographs depicting the as-fabricated microstructure of (a) a non-modified β-NiAl bond coat layer deposited via pack-cementation over a Udimet 700 substrate [90] and (b) a Pt-modified nickel aluminide (β-(Ni,PT)Al) bond coat deposited over a second generation single crystal superalloy (CMSX-4) via chemical vapour deposition (CVD) [101].

The other type of diffusion coatings are referred to as Pt-diffused γ/γ′ bond coats and have been developed in the late 1990's by Rolls-Royce plc. as a more cost-effective alternative to the nickel-aluminide coatings [91, 102, 103]. The fabrication process of Pt-diffused γ/γ′ coatings consists of electroplating a thin platinum layer (~ 7 – 12 µm) onto the surface of a single-crystal Ni-based superalloy substrate containing aluminium (e.g. René N5, CMSX-4), followed by a short vacuum heat treatment at high temperatures to promote inter-diffusion with the substrate (i.e. 1100 – 1200°C for one or two hours) [103, 104]. During this process, platinum diffuses into the lattice of the γ-Ni and γ′-Ni_3Al phases of the superalloy and expands the respective unit cell volumes due to its larger atomic radius [105]. This process introduces a strain in the lattice that leads to a process of recrystallization in the vicinity of the superalloy surface and precipitation of the Pt-enriched γ-Ni and γ′-Ni_3Al phases that constitute the Pt-diffused γ/γ′ bond coat layer, as seen in Fig. 2.10 [105]. The presence of platinum solid solution in the γ and γ′ phases is of crucial importance for the oxide scale formation, as it facilitates the diffusion of aluminium from the substrate to the surface [106] and increases the aluminium to nickel atomic ratio via occupation of nickel sites in the γ-Ni and γ′-Ni_3Al lattices [107]. In practical terms, Pt-diffused γ/γ′ coatings offer substantial advantages over the conventional aluminide coatings, as the elimination of the aluminising process lowers the fabrication cost, improves the thermo-chemical compatibility with the substrate and generates a microstructure with enhanced creep resistance [96, 102, 104]. However, this also means that the formation of the oxide scale is entirely reliant on the relatively low aluminium content of the substrate (~ 25 at.%), effectively leading to concerns over the long-term oxidation resistance and impact on the TBC system durability.

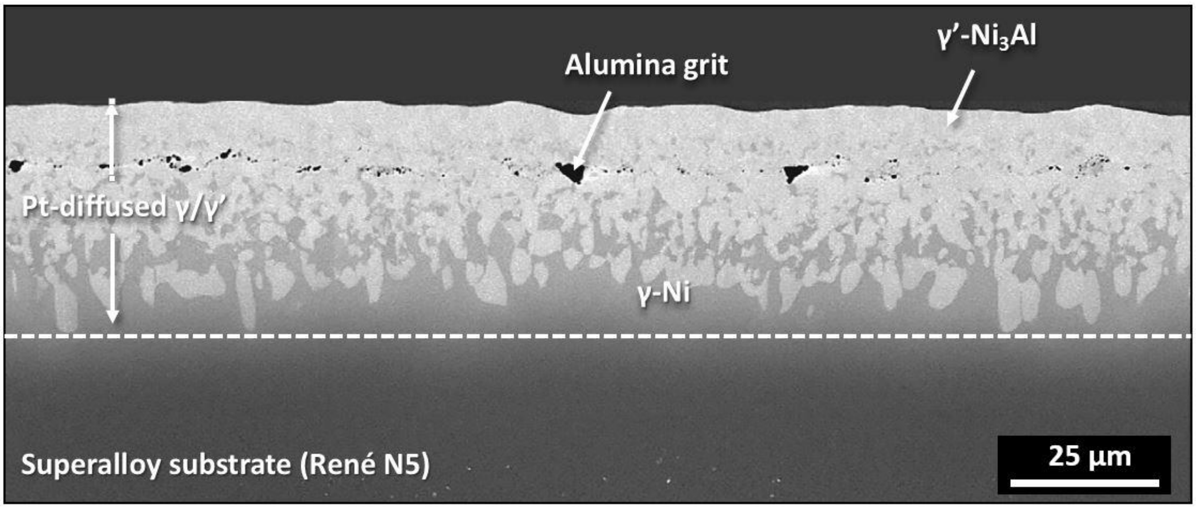

Fig. 2. 10 BSE micrograph depicting the as-fabricated microstructure of a Pt-diffused γ/γ’ bond coat layer formed over a Rene N5 superalloy substrate [104].

2.3.2.1 Overlay coatings

Overlay bond coats are metallic alloy coatings deposited or grown over Ni-based superalloy substrates by means of thermal spray or physical vapour deposition (PVD) [4, 80, 81]. Both methods can produce high-quality overlay coatings but the manufacturing cost, process duration and infrastructure associated with the latter is prohibitive for wide scale implementation purposes [80]. Consequently, less complex and more cost-effective thermal spray methods, such as APS, cold-gas dynamic spraying (CGDS), high velocity oxygen fuel (HVOF) and the novel high velocity air fuel (HVAF), are more commonly utilised in the fabrication of modern overlay coatings [80, 81]. Although there is a good variety of deposition methods available, their use is always considered in terms of cost, pre-existent infrastructure, component geometry, scalability and efficacy in achieving the desired microstructural and mechanical properties [80]. As such, methods that can produce fairly dense and chemically homogeneous coatings with the desired thickness, low porosity and minimal internal oxidation are often favoured by the industrial and scientific communities.

Ideally, thermal spraying under low-oxygen atmospheric conditions would be the preferred choice of engine manufacturers, as the inert processing atmosphere enables the fabrication of coatings that satisfy the aforementioned functional requirements [80]. However, the high cost of acquisition and maintenance of specialised equipment (i.e. vacuum chamber, gas system, vacuum pumps, etc.) makes wide-scale implementation economically impractical, restricting its use to strictly necessary applications [80, 108]. As a consequence, thermal spray under atmospheric conditions has been long established as the most viable solution for scalable, expedient and cost-effective deposition of overlay coatings [109]. The APS method described in section 2.2.3 has been the primary deposition method of commercial overlay coatings for the last few decades due to its capability of generating fairly dense coatings with enhanced substrate adhesion, high surface tortuosity and roughness, as depicted in Fig. 2.11 [81, 109]. However, the oxygen-rich atmospheric conditions, high flame temperature (~ 10000 K) and low particle velocity (~ 170 m.s^{-1} [110]) involved in the deposition process promote undesirable in-flight oxidation of certain metallic elements (i.e. aluminium and reactive elements). These conditions originate a splat-based microstructure with considerable internal oxidation, reduced post-deposition concentrations of aluminium and reactive elements as well as a lower β–NiAl phase ratio, as depicted in Fig. 2.11-a) [39, 110, 111]. These features have a detrimental impact on the long-term oxidation kinetics of TBC systems, as they accelerate the thermo-chemical degradation of the bond coat, leading to premature aluminium depletion and subsequent morphological/chemical instability of the TGO scale [12, 110, 112]. Although these limitations have been tolerated at lower operational temperatures, the current pursuit of improved engine efficiency at higher operation temperatures and extended durability makes them an impediment for the technological evolution of gas-turbine engines.

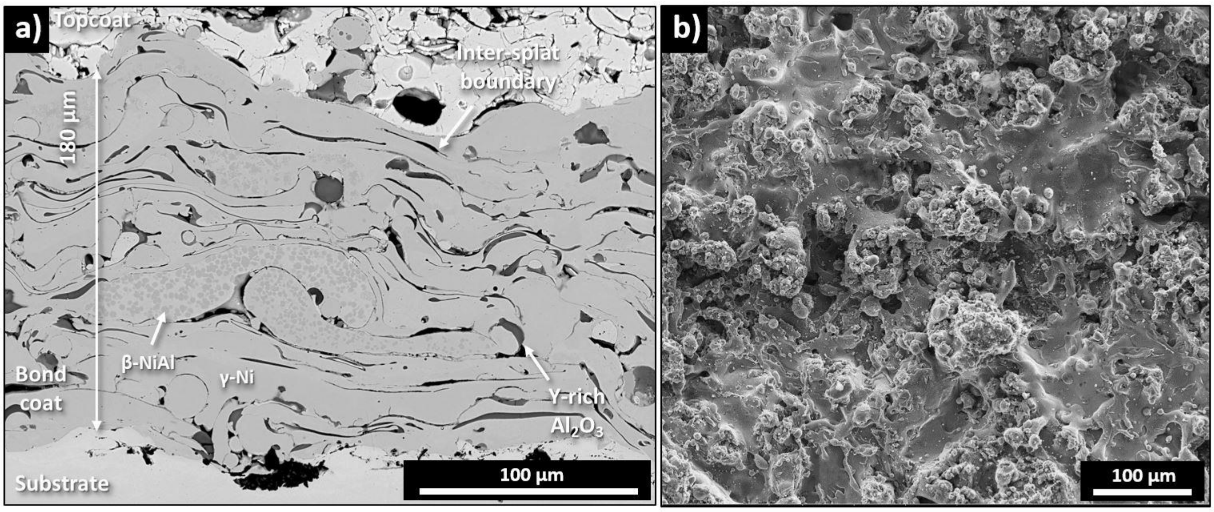

Fig. 2. 11 (a) BSE micrograph depicting the as-fabricated cross-sectional microstructure of a NiCoCrAlY-HfSi APS bond coat deposited over a Nimonic 263 alloy substrate and (b) secondary electron (SE) micrograph from a top view perspective of the bond coat surface.

Inexorably, this has motived a gradual shift towards lower temperature deposition methods (~ 1000-3400 K) that are capable of achieving higher particle velocities (500 - 2000 m.s^{-1}), such as HVOF and CGDS [80, 113, 114]. However, even though both methods can reduce in-flight time and particle oxidation substantially, CGDS is still not entirely suitable for spraying overlay coatings due to low as-deposited ductility, inadequacy for spraying geometrically complex components, and requirement of expensive gas additives (i.e. helium) to successfully spray MCrAlY alloys [114]. On the other hand, as the HVOF method presents less technical and functional limitations, it has gradually emerged as the most reliable alternative to conventional high-temperature thermal spray deposition methods [63, 108, 115]. This technique uses a mixture of oxygen with flammable gases or liquid fuel (i.e. propane, propylene, hydrogen or kerosene) to generate a controlled combustion within the combustion chamber and produce a stable flame [113, 116]. The powder particles are then transported through an inert gas carrier system and injected into the initial section of the nozzle, where they are heated up to the melting point and accelerated through a long nozzle at supersonic velocities towards the surface of the substrate, as illustrated by the schematic in Fig. 2.12-a) [113, 116].

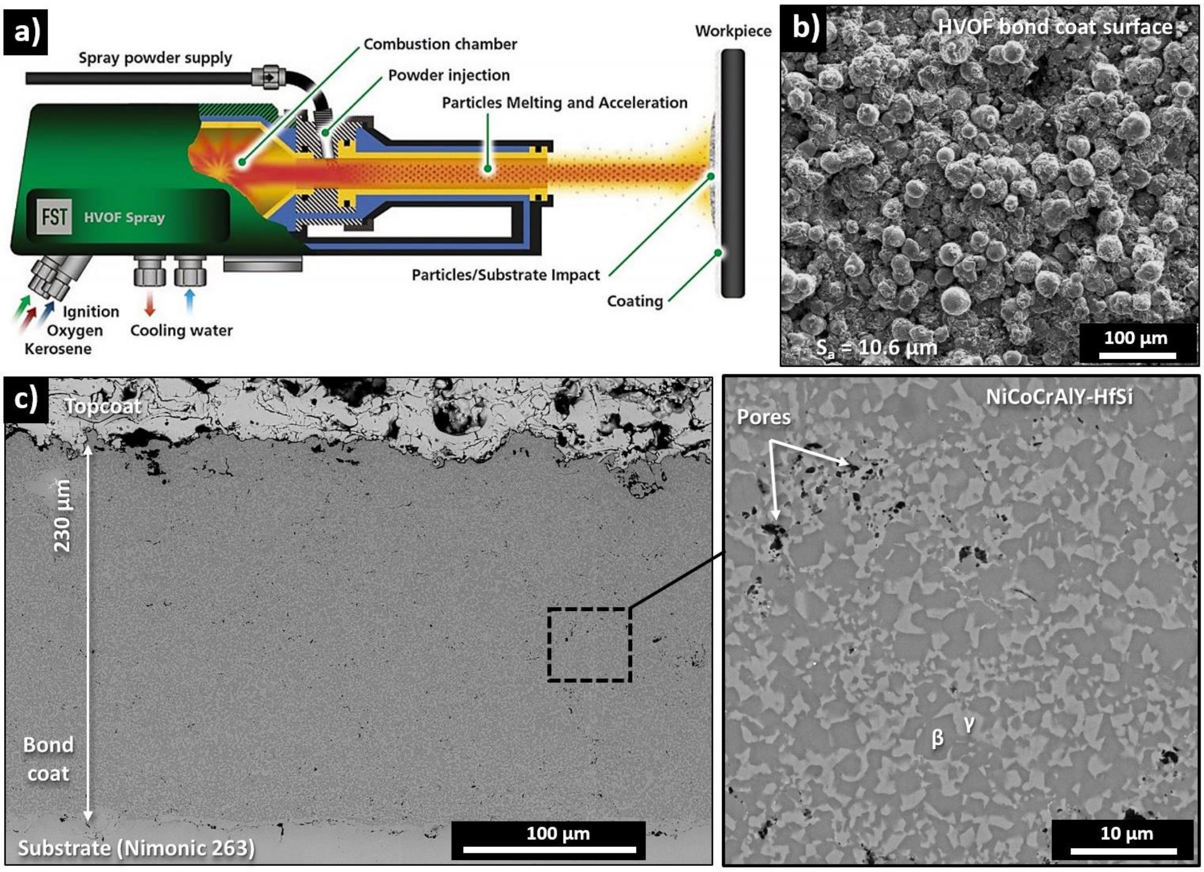
a)
Spray powder supply
Combustion chamber
Powder injection
Particles Melting and Acceleration
Workpiece
FST
HVOF Spray
Particles/Substrate Impact
Coating
Ignition
Oxygen
Kerosene
Cooling water
b)
HVOF bond coat surface
S_a = 10.6 µm
100 µm
c)
Topcoat
230 µm
Bond coat
Substrate (Nimonic 263)
100 µm
NiCoCrAlY-HfSi
Pores
β
γ
10 µm

Fig. 2. 12 (a) Schematic illustration of the high velocity oxygen fuel (HVOF) processing set up (Edited from [117]) and (b) respective top view secondary SE micrograph of a bond coat surface with high roughness (S_a = 10.6 µm); (c) BSE micrograph depicting the as-fabricated cross-sectional microstructure of a NiCoCrAlY-HfSi HVOF bond coat deposited over a Nimonic 263 alloy substrate, where the dual-phase structure and volumetric defects are highlighted in the inset image.

Typically, this process is closely controlled to provide just enough thermal energy to bring the particles into a semi-molten malleable state and enough kinetic energy to ensure the densification of the coating [116]. The resulting microstructure is fairly homogeneous and displays a very low concentration of oxides and porosity ($< 1\%$), good inter-layer adhesion and increased β-phase ratio, as depicted in Fig. 2.12-c) [115]. However, the high kinetic energy imparted on the particles leads to a high degree of flattening upon impact with the substrate that reduces the bond coat surface roughness and surface tortuosity [39, 115]. This limitation is detrimental for the TBC system durability as the reduced interfacial adhesion between the bond coat and the TBC often leads to premature failure [60, 118-120]. However, it can be easily and economically overcome by spraying a thin flashcoat layer on top of the dense and thick base layer, resulting in a dual-layer bond coat that satisfies the requirements described in section 2.3.1. Furthermore, the fact that the flashcoat layer can be deposited by other methods capable of generating enhanced surface roughness (e.g. HVAF, APS or even HVOF with modified processing parameters) opens up the possibility for precise manipulation and optimisation of the bond coat surface topography to improve the TBC system durability [39, 60, 121]. An example of such modification is displayed in Fig. 2.12-b), where a high surface roughness ($S_a = 10.6\ \mu m$) and tortuous bond coat surface topography was formed by deposition of a HVOF flashcoat layer with modified processing parameters (i.e. lower flame temperature and high particle velocity).

The nature of the thermal spray methods discussed above allows for a high degree of versatility and flexibility during the deposition process, as they can be manipulated and optimised to produce coatings with the desirable thickness, density, microstructure and internal oxide contents [80, 115]. This aspect is further reinforced by the compositional diversity of bond coat materials, as they can be specifically tailored to include a wide range of metallic elements and generate multiple alloy combinations based on the Ni-Cr-Al ternary system (Fig. 2.8-c) [81, 83, 122]. Modern overlay bond coat materials are based on Ni- or Co-based alloys (i.e. MCrAlY where M=Co, Ni or CoNi) containing 18-22 wt.% of chromium, 8-12 wt.% of aluminium and minute quantities of reactive elements such as Y, Hf, Mo, Si, Re, Zr, Nb and Ta (0.2-1 wt.%) [81, 123, 124]. Cobalt is added to these alloys to suppress the undesirable $\gamma - \mathrm{Ni} \rightarrow \gamma' - \mathrm{Ni_3Al}$ phase transformation via stabilisation of the γ-Ni and β-NiAl phases at high-temperatures [87]. The concomitant addition of Cr promotes the formation and maintenance of a stable α–Al_2O_3 TGO layer whilst reducing the bond coat Al content requirements to form and maintain a protective homogenous scale [83]. It has been proposed that this is due to Cr reducing oxygen solubility in the alloy and acting as a getter for any impurities diffusing from the substrate, effectively preventing internal oxidation of Al [83, 111, 125]. The supplementary addition of small quantities of reactive elements is aimed at improving the TGO scale adhesion via suppression of impurities diffusing into the interface (e.g. sulphur) [81, 126, 127] and reduction of the TGO growth rate due to slowing down ionic transport kinetics across the scale grain boundaries [83, 128]. Further to this, the presence of reactive elements in the alloy also reduces the grain size and/or increases the dislocation or sub-grain boundary densities, effectively increasing the flux of scale-forming elements into the interface and resulting in the selective oxidation of Al [125]. The most commonly used reactive element is Yttrium, as its concentration and distribution in the bond coat have an instrumental role in TGO scale transport processes, stress generation and inhibition of impurities segregation to the interface [126, 129]. Hafnium and silicon are also used concomitantly in MCrAlY coatings (e.g. NiCoCrAlY-HfSi) to provide enhanced scale adhesion, reduction in TGO growth rates and increased capability for post-spallation scale regeneration [122].

In terms of microstructure, overlay coatings are predominantly comprised of two main phases, a brittle Al-rich β-phase (b.c.c.) that functions as a reservoir for the formation of an α–Al_2O_3 TGO scale and a ductile Al-poor γ-Ni (f.c.c.) phase that serves as a host matrix. However, these coatings may also contain additional equilibrium phases that may affect the bond coat oxidation kinetics, depending on their chemistry and thermal exposure temperatures [81]. For instance, a high concentration of Cr (15-22 wt.%) causes the formation of Cr-rich precipitates (i.e. α-Cr phase) within the β-NiAl phase due to an analogous crystal structure similarity and perfect lattice coherency with the β-phase [87, 130, 131]. Although the α-Cr phase decomposes completely into the γ-Ni solid solution within a few hours of thermal exposure at 1135°C in conventional MCrAlY coatings ($\sim$ 20 hours), the addition of rhenium (1-3 at.%) can stabilise the α-Cr phase and form a protective thin sub-scale that improves the bond coat oxidation resistance [132]. The formation of a tetragonal σ–CoCr phase has been also predicted up to 10 vol.% at temperatures of 950°C via thermodynamic calculation conducted by Achar et al. [87] and has been reported in commercial Co-rich MCrAlY bond coats (i.e. CoCrAlY, CoNiCrAlY or even NiCoCrAlY) used under high-cylcle/low-temperature conditions [133, 134]. Mendis et al. [134] have suggested that large concentrations of this brittle phase in the vicinity of the interface can be detrimental to the interfacial toughness. However, the most significant microstructural changes undergone by the bond coat are attributed to thermally-induced long-term diffusional processes. Diffusion of Al into the interface and inter-diffusion of other metallic elements with the substrate lead to the dissolution of the β-NiAl and any additional phases into solid solution, eventually transforming the bond coat into a single γ–Ni phase bond coat layer, as sequentially depicted in Fig. 2.13 [135].

The most frequently used compositions in overlay TBC systems correspond to CoNiCrAlY and NiCoCrAlY, as these alloys display enhanced high-temperature capabilities such as oxidation and hot corrosion resistance as well as ductility and creep resistance [80, 123]. The latter has better oxidation resistance at elevated temperatures (> 900°C), a fact that is reflected by the lower TGO growth rates and slower thermo-chemical degradation reported in the literature [60, 133, 136]. In addition to this, TGO scales growing over CoNiCrAlY coatings have a higher propensity to form Cr- and Ni-based oxides with faster growth rates and different CTEs, yielding less favourable stress states in the vicinity of the interface that are often associated with premature TBC failure [133, 137]. As such, NiCoCrAlY coatings tend to be applied on components exposed to high-temperature oxidising environments whereas the latter tends to be applied on components where type II hot corrosion predominates [123]. Further to this, as-processed NiCoCrAlY coatings also exhibit a high elastic modulus (~ 231 GPa), high tensile strength (~ 1.2 GPa) and considerable plasticity (~ 0.75 %) at ambient temperatures. These properties have a positive contribution to the enhancement of interfacial toughness and resistance to morphologic instability degradation (i.e. rumpling) [138, 139].

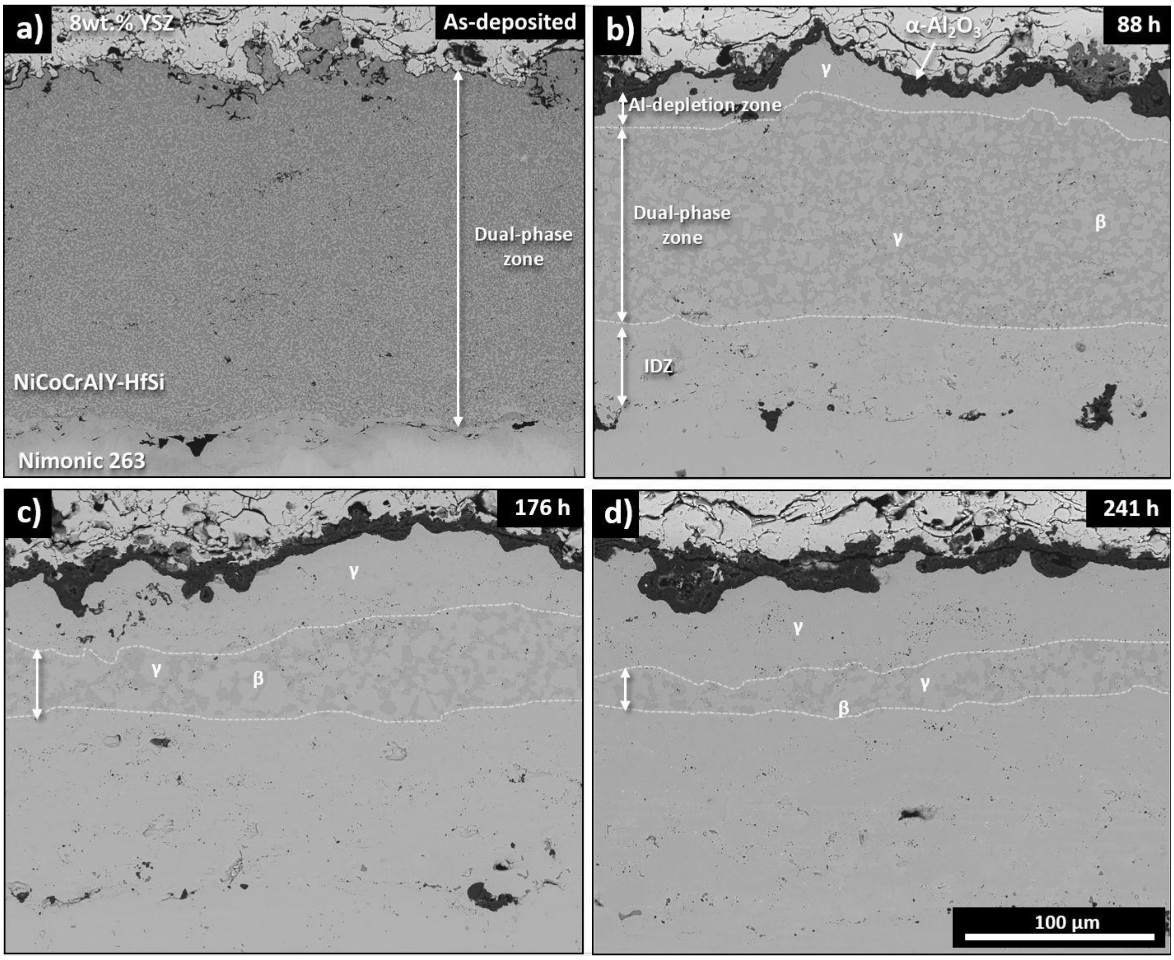
a)
8wt.% YSZ
As-deposited
Dual-phase zone
NiCoCrAlY-HfSi
Nimonic 263
b)
α-Al₂O₃
88 h
γ
Al-depletion zone
Dual-phase zone
γ
β
IDZ
c)
176 h
γ
γ
β
d)
241 h
γ
γ
β
100 μm

Fig. 2. 13 BSD micrographs illustrating the microstructural evolution of a NiCoCrAl-HfSi bond coat with thermal exposure for the (a) as-deposited state, (b) 88 hours, (c) 166 hours and (d) 241 hours. The decomposition of the β–NiAl phase into solid solution is reflected by the gradually decreasing dual-phase zone.

2.4. Thermally grown oxide

2.4.1 Functional requirements and formation process

The thermally grown oxide (TGO) is a thin oxide layer (thickness ≤ 15 μm) that forms between the bond coat and topcoat due to oxidation of the former at elevated temperatures (> 900°C) [140]. The primary function of the TGO is to provide environmental protection to the underlying TBC system constituents when exposed to high temperature oxidising and corroding atmospheres [81, 83]. In order to achieve this, the protective scale should be a continuous, dense, slow-growing and thermodynamically stable diffusion barrier with the ability of maintaining good adhesion and thermo-chemical compatibility with the adjacent layers [50, 81, 83, 141]. Fundamentally, the TGO scale is the by-product of a chemical reaction between the molecular oxygen (O_2^-) diffusing inward through the topcoat and several metallic cations (i.e. Al^{3+}, Cr^{3+}, Ni^{2+}, Co^{2+}, Y^{3+}, Hf^{4+}, Si^{4+}) diffusing outward from the bond coat [81, 83, 140]. However, as mentioned in section 2.3.2, the bond coat layer is compositionally engineered to promote the selective oxidation of Al^{3+} and form an Al-rich oxide scale that is predominantly comprised of α-Al_2O_3. This preference can be primarily attributed to the fact that this material meets the majority of the aforementioned requirements for a stable high-temperature protective scale [83, 84, 140, 142, 143]. Nevertheless, the inevitable diffusion of other metallic elements into the interface and/or across the scale during its formation and growth leads to the incorporation of alternative oxide species into the scale (i.e. NiO, CoO, Cr_2O_3, Y_2O_3, HfO_2, TiO_2, $Ni,Co[Al,Cr]_2O_4$), as illustrated in Fig. 2.14 [12, 81, 83, 144]. This phenomenon is often considered detrimental for the long-term durability of the TBC system since the accelerated oxide growth rate, high-temperature instability and larger CTE mismatch with the adjacent layers increases the propensity for stress-induced crack nucleation and propagation [112, 137, 145].

The oxide scale growth in TBC systems is a slow, long and complex evolutionary process that can be divided into three major regimes and arranged by chronological order, transient oxidation, stable growth and accelerated oxidation [81, 146]. These regimes are typically characterised by the distinct morphological and compositional properties of the TGO scale during specific stages of the thermal exposure process, as illustrated by Fig. 2.14. These properties are primarily dependent on the bond coat microstructure (i.e. size and composition of main phases) [146, 147], distribution and chemical state of reactive elements in the alloy (i.e. metallic or oxidised) [88, 126], bond coat topography (i.e. roughness, peak curvature and density) [120, 135], annealing conditions (i.e. oxygen partial pressure, time and temperature) [148, 149] and thermal exposure parameters (i.e. temperature, atmosphere, time) [81].

The transient oxidation stage depicted in Fig. 2.14-a) is a short-duration oxidation stage that takes place in the very early stages of thermal exposure and is instrumental for the formation of the primordial TGO scale [142]. In the very initial stages of this regime, there is an accelerated consumption and temporary reduction in Al concentration at the surface of the bare bond coat alloy that leads to the formation of a layered and compositionally diverse TGO scale [142, 146, 150]. The outer subscale is formed first and comprises a mixture of fast growing brittle oxides such as NiO, Cr_2O_3, CoO, $(Ni,Co)(Cr,Al)_2O_4$. Once this subscale has been established and covers the entirety of the bare alloy surface, an inner subscale comprised of a mixture of α-Al_2O_3 with metastable Al_2O_3 polymorphs (e.g. θ-Al_2O_3, γ-Al_2O_3) starts to form, as illustrated in Fig. 2.14-a). This stage is often critical for the evolutionary growth process of the TGO scale, as the excessive presence of non-α-Al_2O_3 oxides or fast-growing Al_2O_3 polymorphs at this stage leads to a morphological heterogeneity that hinders inter-layer adhesion, long-term stability and the protection effectiveness of the scale [9, 144, 146].

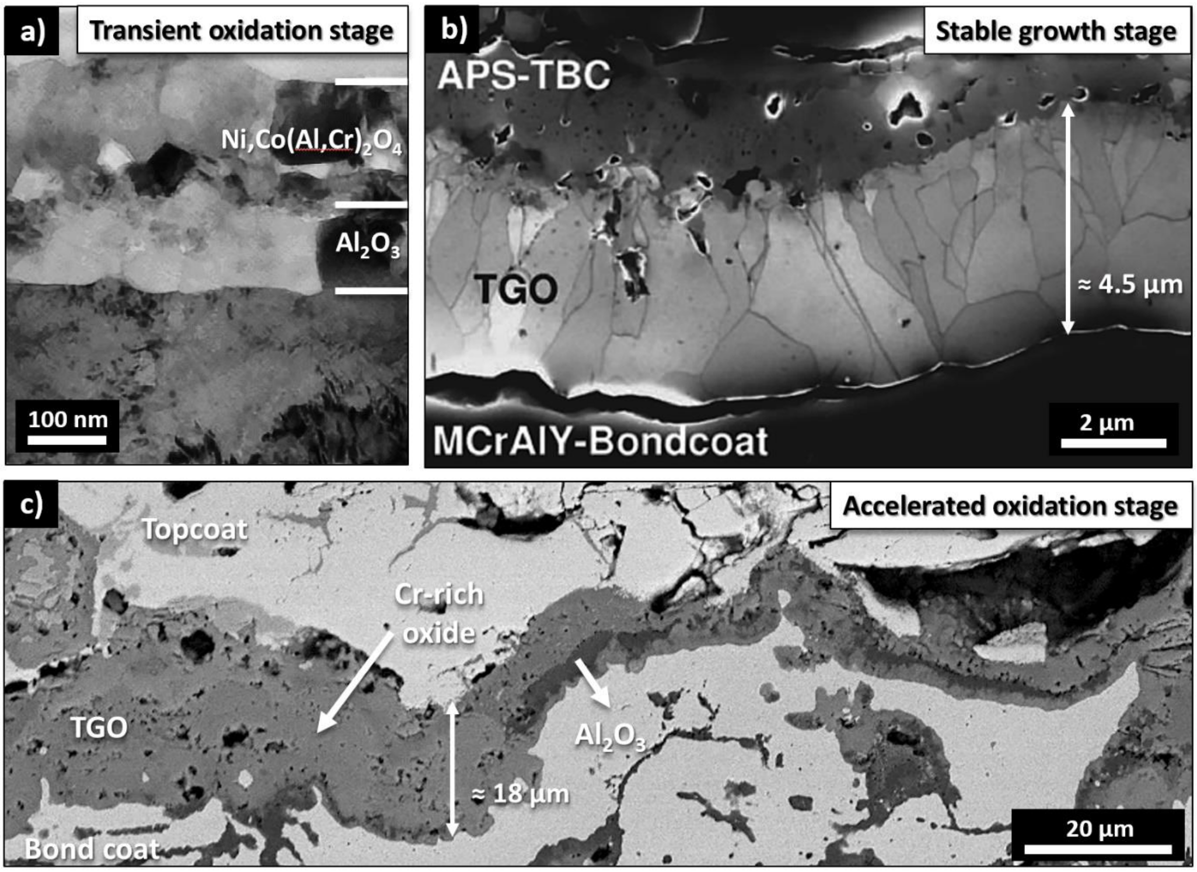
a)
Transient oxidation stage
Ni,Co(Al,Cr)₂O₄
Al₂O₃
100 nm
b)
Stable growth stage
APS-TBC
TGO
≈ 4.5 µm
2 µm
MCrAlY-Bondcoat
c)
Accelerated oxidation stage
Topcoat
Cr-rich oxide
TGO
Al₂O₃
≈ 18 µm
20 µm
Bond coat

Fig. 2. 14 TGO scale evolutionary stages with thermal exposure progression where (a) transmission electron microscopy (TEM) cross-section depicting a transient TGO scale grown on a NiCoCrAlY bond coat oxidised for 0.5 h at 1000°C with pO_2 of 20kPa [81]; (b) In-lens SEM image of a stable growth TGO scale that formed over a NiCoCrAlY bond coat and an APS topcoat after 400 hours of thermal cyclic oxidation in air at 1050 °C [84] and (c) backscatted-electron SEM micrograph depicting a TGO scale in the accelerated oxidation stage that formed over a CoNiCrAlY bond coat after 550 hours of thermal cyclic oxidation in air at 1135 °C .

Once a continuous TGO scale has been established and the oxygen activity at the interface is too low to promote the formation of non-Al_2O_3 oxides at the inner subscale, the TGO has entered the stable growth stage shown in Fig.2.14-b) [12]. This stage is characterised by a much slower TGO growth rate that is controlled by the ionic transport processes across the scale and can be analytically described by a parabolic or sub-parabolic growth function given in eq. 2.2 [12, 81, 83].

$$\delta^2 = 2k_p t \tag{2.2}$$

where δ is the thickness, k_p the parabolic rate constant and t the time.As the growth kinetics are dominated by ionic diffusivity along the grain boundaries and presence of impurity effects [140, 151], both the grain size and presence of reactive elements at the grain boundaries are instrumental in dictating the oxide scale growth rate [88, 140, 152]. During this stage, the polycrystalline TGO scale displays two distinct microstructural domains, an outer section comprised of smaller-sized equiaxed grains and an inner section comprised of a columnar grain structure, as illustrated in Fig. 2.14-b) [81, 84, 151]. The outer scale is compositionally rich in oxidised metallic species such as NiO, CoO, Cr_2O_3, Y_2O_3, $CoCr_2O_4$, $NiCo_2O_4$ and $CoAl_2O_4$ that have formed primarily during the initial stages of oxidation. These oxide species continue to grow with the progression of thermal exposure due to diffusion of metallic elements through the TGO scale and often lead to its degradation and failure [153]. On the other hand, the inner scale is predominantly formed by inward diffusion of oxygen along the grain boundaries and selective oxidation of aluminium at the BC/TGO interface, leading to the preferential formation of the stable α-Al_2O_3 polymoprh [81].

As thermal exposure progresses, the bond coat undergoes detrimental changes of compositional nature that bring the aluminium activity coefficient beyond the minimum threshold required to continuously promote the exclusive formation of α-Al_2O_3 ($\alpha_{Al} \leq 10^{-17}$) [12, 81]. This marks the onset of the accelerated oxidation stage depicted in Fig. 2.14-c) and is reflected by a sharp reduction in the sub-scale aluminium concentration, thereby enabling the diffusion of other metallic elements through the TGO scale grain boundaries. This leads to the chemical decomposition of the TGO scale into a mixture of brittle, non-protective and thermodynamically incompatible oxides (e.g. NiO, Cr_2O_3, TiO_2, $Co(Cr, Al)_2O_4$, $Ni(Cr, Co, Al, Y, Ti)_2O_4$ and $Y_3A_5O_{12}$) [12, 81]. From this point onward, the thermo-chemical degradation of the bond coat and TGO are dramatically accelerated, resulting in a faster non-parabolic TGO growth rates and remarkably thicker scales, as depicted in Fig. 2.14-c). The CTE mismatch and resulting volumetric strains of TGO generate large out-of-plane tensile stresses in the near-interface TBC region (up to 4.5 GPa [154]) that are conducive to accelerated crack propagation and premature failure [112].

2.4.2 TGO stress and failure

As a result of its formation process and location in the TBC system, the TGO is subjected to inter-layer thermo-mechanical interactions and internal growth processes that lead to the development of large residual stresses of compressive nature within the scale (~ 3 – 6 GPa) [12, 77, 155]. These stresses are primarily generated by the thermal expansion mismatch with the underlying substrate (~ 3-5 GPa) and to a lesser extent by the oxide scale growth process (~ 100 MPa – 1.3GPa [140, 156]) [12, 156].

The overall magnitude of these stresses is different for each TGO scale as it is governed by the dynamic interplay between the intrinsic stress generation and relaxation mechanisms at high temperatures (i.e. TGO creep and cyclic yielding of the bond coat) [156, 157].

Residual stresses originating from the thermal expansion mismatch with the underlying substrate are generated by the thermally-induced volumetric strains resulting from the different rates of contraction between the substrate and TGO upon cool-down to ambient temperature [12]. As a consequence, the overall TBC thickness [155] and the degree of CTE dissimilarity between the TGO and the substrate [158] have an instrumental role in dictating the residual stress magnitude. In addition to this, the amplitude and morphology of the BC interfacial asperities also contribute to the redistribution of stresses at the TGO interface as it affects the thermal expansion behaviour of adjacent layers in the interface regions [158-160].

On the other hand, the TGO growth stress contribution to the overall residual stress state is cumulatively generated by the growth strains associated with continuous scale thickening and lateral growth processes [12, 161]. These strains occur predominantly at one of the TGO interfaces, depending on the predominant diffusion mechanism [162]. The origins of the growth strains have remained elusive until recently, when Heuer et al. [140] demonstrated that the formation of new Al_2O_3 crystallites along the TGO scale grain boundaries originates an electrochemically driven strain that generates localised lateral stresses [140, 161]. These growth stresses are generated at the BC/TGO interface if the oxide scale growth is controlled by inwards anionic diffusion (e.g. O_2^-) and at the TGO/TBC interface when controlled by outwards cationic diffusion (i.e. Al^{3+}, Ni^{2+}, Co^{2+}, Cr^{3+}, Y^{3+},etc.) [83, 162]. When oxide growth occurs over planar segments of the interface, the TGO thickening volume change can be accommodated by a rigid body displacement perpendicular to the interface and therefore, the only contribution to the growth stresses comes from the lateral growth component, i.e. lengthening [77]. Conversely, in the case where oxide growth occurs in non-planar segments of the interface, both the thickening and lateral components contribute to the stress generation [77, 161]. The resulting TGO growth stresses are strongly dependent on the underlying bond coat alloy composition [163], presence of embedded reactive elements within the scale [129, 164], thermal exposure conditions [165], substrate constraint [77, 161] and interfacial topography [159, 166]. A good example of how one of these features affect the stress magnitude is the discrepancy observed between Ni- and Fe-based systems, where TGO growth stresses range from a 100-200 MPa in the former to about 1.3 GPa in the latter [12, 140]. Another example is the addition of Y and Dy to MCrAlY alloys resulting in a reduction of the TGO growth stresses [164].

The morphological and compositional evolution of the TGO layer during thermal exposure are known to affect the degradation of the metal/ceramic interface adhesion and subsequent failure via spallation. This is mostly because the gradual TGO thickening and lateral expansion (i.e. lengthening) have an increasingly relevant role on the overall interfacial stress development, redistribution and relaxation mechanisms [12, 155, 162, 167]. As thermal exposure progresses, the TGO scale experiences large in-plane compressions (~ 3-6 GPa) due to the substrate/TGO CTE mismatch during cool-down to ambient temperatures. In an attempt to relax the stresses generated, the TGO scale lengthens itself via out-of-plane displacements (i.e. buckling of the scale) or visco-plastic deformation of the BC [12]. These displacements induce out-of-plane tensile stresses at the TGO interfaces that contribute to a gradual increase in the scale's strain energy density [168]. Once this value reaches the critical energy requirements to produce localised de-cohesion (i.e. critical energy release rate, G_c), crack nucleation and propagation ensue [168-170]. Ultimately, the rate at which these cracks propagate and coalesce will determine the size of the detached sections and dictate how fast TBC spallation occurs [12, 162]. This process is typically accelerated by the presence of low-amplitude imperfections (i.e. oxide pegs, rumpling) or higher-amplitude asperities (i.e. peaks and summits) at the bond coat/topcoat interface, as their amplitude is intrinsically related to the magnitude and redistribution of the tensile stresses generated [12, 159, 162], especially in thicker thermally aged scales [165, 171]. Conversely, it can also be slowed-down by TGO creep, as the associated stress relaxation at high temperatures ($> 1050^oC$) contributes to the reduction of the strain energy density within the scale, effectively delaying crack propagation and delamination of the TBC system [12, 165, 172]. For instance, TGO scales with smaller grain size show improved stress relaxation efficiency and resistance to delamination due to having higher creep rates [172].

2.5. Failure mechanisms of TBC systems

2.5.1 Predictive lifetime models and failure mechanism categories

TBC systems have been regarded as a viable technology for the last four decades and their widespread implementation in gas-turbine engines has been instrumental for the evolution of the aviation and energy production sectors [4]. However, the inherent complexity of the TBC system, the variety of possible failure mechanisms and their dependence on the engine operating conditions has made it difficult to develop an accurate lifetime prediction model [4]. This inability to predict when the integrity will be compromised has forced manufacturers to adopt conservative durability estimations in order to address safety concerns. As a consequence, the interest in developing reliable lifetime prediction models for in-service engine components has grown over time, with empirical and theoretical frameworks being proposed [162, 173-175]. However, challenges associated with lack of fabrication reproducibility and the complexity of in-service failure mechanisms (i.e. intrinsic and extrinsic) required some oversimplifications that compromises the predictive model's accuracy. As such, achieving TBC prime-reliance in the near future is forecasted to rely predominantly in monitoring of in-service operational temperatures, preventive detection of manufacturing flaws and sub-critical crack evolution [27].

From a macroscopic point of view, TBC system failure is always perceived as the spallation of the ceramic topcoat from the underlying substrate, resulting in partial or complete exposure of the underlying superalloy to the harsh atmospheric engine conditions [7, 12, 176]. As spallation typically occurs at or in close proximity of the bond coat/topcoat interface upon cooling from high to ambient temperatures, the TBC system thermal insulation capabilities and protection against external aggressive factors are irreparably compromised [4, 12, 20]. The failure mechanisms leading to spallation can be divided into intrinsic and extrinsic categories, depending on whether they are related to inherent degradation processes of the TBC system (i.e. oxidation kinetics, stress development, bond coat chemical degradation, and inter-diffusion with the substrate) or external aggression factors related to engine degradation phenomena (i.e. FOD, erosion, CMAS and hot corrosion). [20, 80], as schematically depicted in Fig. 2.15.

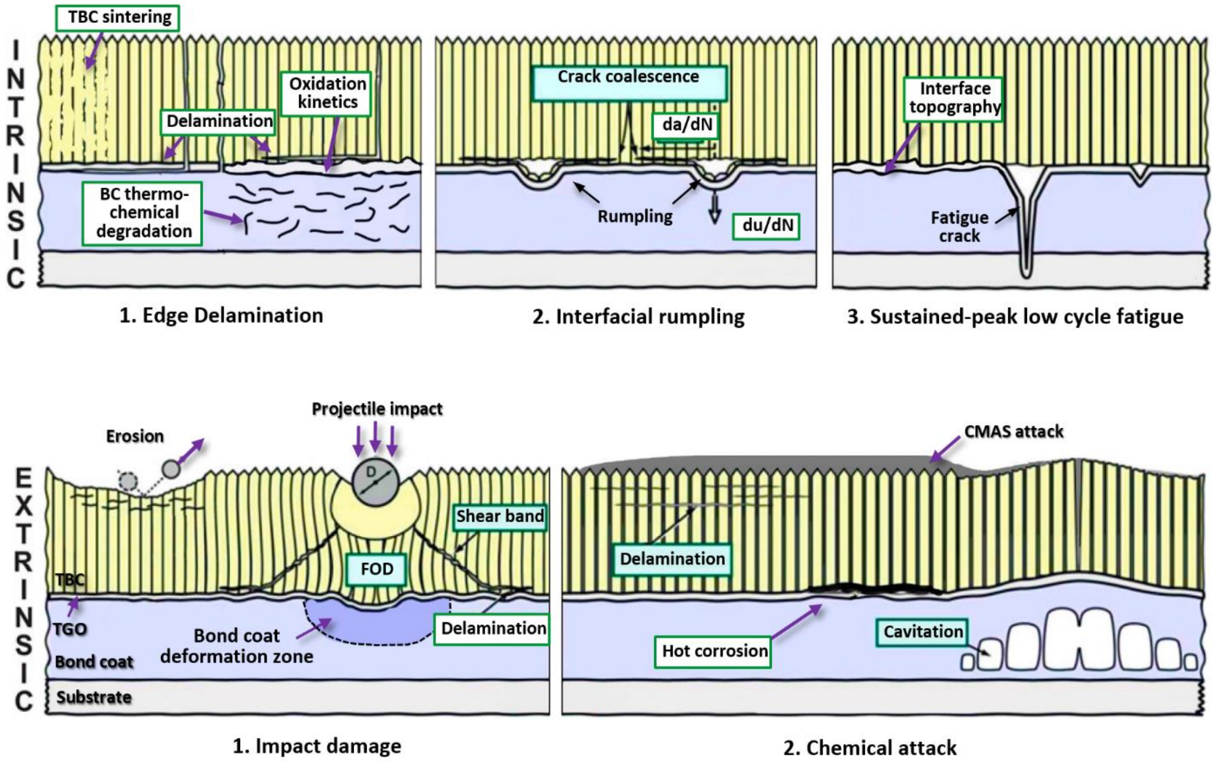
INTRINSIC
TBC sintering
Delamination
Oxidation kinetics
BC thermo-chemical degradation
1. Edge Delamination
Crack coalescence
da/dN
Rumpling
du/dN
2. Interfacial rumpling
Interface topography
Fatigue crack
3. Sustained-peak low cycle fatigue
EXTRINSIC
Erosion
Projectile impact
D
Shear band
FOD
TBC
TGO
Bond coat
Substrate
Bond coat deformation zone
Delamination
1. Impact damage
CMAS attack
Delamination
Hot corrosion
Cavitation
2. Chemical attack

Fig. 2. 15 Schematic illustration of the main intrinsic and extrinsic failure mechanisms contributing to TBC system failure via the edge delamination, interfacial rumpling, sustained-peak low cycle fatigue, impact damage and chemical attack failure modes. Image edited from [1].

Although failure is typically caused by the concomitant contributions of multiple failure mechanisms, there is a generalised consensus amongst the scientific community that oxidation kinetics is one of the more prominent mechanisms affecting the TBC system lifetime [12, 46, 60, 159, 162, 177, 178]. Consequently, a large number of studies aimed at studying the fundamental role of bond coat oxidation in TBC failure have been conducted over time on EB-PVD and PS coatings [83, 110, 111, 133, 135, 142, 146, 177, 179, 180]. Most studies have focused on how the oxide scale formation, interfacial roughness and morphological/compositional evolution affect the interfacial stress state (i.e. distribution, magnitude) and fracture mechanics [77, 83, 143, 161, 163, 164]. Some of these studies showed that the TGO thickness had a significant influence on the TBC lifetime and therefore, the concept of a critical TGO thickness (h_c) as a failure criterion for TBC systems was eventually proposed by Evans et al. [162]. In this model, the critical thickness was estimated as a function of the TGO growth strain, some TBC mechanical properties (i.e. elastic modulus, fracture toughness) and interfacial topography features (i.e. peak spacing and radius), as shown in eq. 2.3. Its dependence on the thermal exposure time allowed it to be re-expressed in terms of a failure time in eq. 2.4, thereby emerging as a possible lifetime prediction tool [12, 29, 162].

$$h_c = 2\pi(1 - \upsilon^2)\, md^{\frac{3}{2}}\, K_{IC}^{TBC}(m-1)RE_{TBC} \tag{2.3}$$

And it can be expressed in terms of failure time (t_f)

$$t_f = \, {h_c}^2 2k_p \tag{2.4}$$

where υ is the Poisson's ratio, m is the growth strain, $2d$ is the peak spacing, K_{IC}^{TBC} is the fracture toughness of the TBC, R is the peak radius, E_{TBC} is the TBC elastic modulus and k_p is the parabolic constant.

However, even though some studies reported a good degree of correlation in TBC systems with relatively flat interfaces exposed to isothermal or minimal thermal cycling conditions [158, 177, 179], the same trend was not verified in systems with tortuous interfaces exposed to long-term TCF conditions [60, 120, 159]. Such discordance in the experimental results motivated additional studies focused on the contributions of bond coat interface topography [60, 118, 120, 159], TBC sintering [46, 59, 181] and bond coat thermo-chemical degradation [153, 182] to TBC lifetime. These studies have shown that other intrinsic mechanisms or features can also become predominant factors in governing TBC failure regardless of the TGO thickness.

Around the same time, a more advanced micromechanical model that accounted for the concomitant contributions of oxidation kinetics, BC roughness, substrate curvature and TGO/BC creep to the overall interfacial stress state was proposed by Vaβen et al. for plasma sprayed TBCs [183]. This model combined a finite element modelling (FEM) with a crack propagation analytical model to simultaneously estimate the overall interfacial stress state during thermal loading and the theoretical crack development. Although this model was able to explain the overall results trend, certain geometrical, physical and mechanical assumptions were made based on literature data (i.e. sinusoidal interface topography, CTE, creep rate and stress intensity factor) and other factors such as sintering and BC thermo-chemical degradation were excluded [183]. This is a good example of how even more advanced models that account for multiple factors simultaneously are still limited by the sheer complexity of the TBC system. It also highlights the need for a deeper understanding of how the individual failure mechanisms can concomitantly lead to the large-scale failure modes introduced in the next section.

2.5.2 Failure modes

Buckle- and edge-driven delamination mechanisms are presently regarded as the most prevalent large scale failure modes observed in thin films or thermally grown oxide scales subjected to compressive lateral stresses [184, 185]. Buckling mechanisms are more predominant in TBC systems with low interfacial roughness and homogeneous TGO scales that show a relatively low concentration of morphological heterogeneities, such as EB-PVD TBCs [84, 185]. In contrast, edge delamination is more likely to occur in TBC systems with thicker and inhomogeneous TGO scales that incorporate a higher concentration of interfacial defects and multiple oxide species, such as PS TBCs [84].

Buckle-driven delamination (Fig. 2.16-a)) is a well understood mechanism that originates from the generation of equi-biaxial compressive stresses, σ_0, induced by the CTE misfit between the TBC and the underlying layer during cooling down from high temperatures to ambient [184, 185]. Physically, the onset of buckling is initiated when the buckling index (Π) exceeds a critical value ($\Pi \geq \Pi_c$), defined as $\Pi_c = \pi^2/3 = 3.29$ for plain strain buckle and $\Pi_c = 4.89$ for an axisymmetric buckle [185]. This index is described in eq. 2.5 as a function of a given coating thickness (h), elastic modulus (E) and residual stress (σ_0), whilst assuming a pre-existent flaw of width L at the interface between the scale and the substrate [185].

$$\Pi = (1 - \upsilon^2)\left(\frac{\sigma_0}{E}\right)\left(\frac{L}{h}\right)^2 \tag{2.5}$$

The buckling condition can be re-expressed in terms of the length of the delamination width L by equating it to a critical flaw size width required to trigger the onset of buckling, L_b, and Π to the critical buckling index Π_c mentioned above. The resulting rearranged equations are shown below for a plane strain and axisymmetric buckle.

$$\frac{L_b}{h} = 1.81\ \frac{\bar{E}}{\sigma_0}\ \text{(plane strain)} \tag{2.6}$$

$$\frac{L_b}{h} = 2.21\ \frac{\bar{E}}{\sigma_0}\ \text{(axisymmetric)} \tag{2.7}$$

Where $\bar{E}$ is the in-plane elastic modulus of the scale determined by $\bar{E} = E/(1-\upsilon^2)$.

If equations 2.6 and 2.7 are solved for a TBC system with a flat interface, typical TBC elastic moduli (i.e. 50-100 GPa [59, 60]) and compression magnitudes in the order of 3-5 GPa [12, 163], the critical flaw length required to trigger spallation surpasses the TBC thickness by at least 20 times. As the TBC thickness typically ranges between 0.1 mm to 1 mm, these equations predict that a flaw size of 2 to 20 mm would have to be present for large scale buckling (LSB) to occur. However, such flaws are not typically observed until the later stages of thermal exposure and therefore, LSB must originate from other processes during thermal exposure [52, 73]. It is currently accepted that the generation of a critical size flaw required to initiate LSB ensues from the development of smaller interfacial local flaws that gradually propagate and coalesce to form large detached segments, as depicted in Figs. 2.16-a) and b) [13, 156, 162, 165]. This process is accelerated by the presence of prototypical imperfections at the interface (i.e. undulations or morphological heterogeneities) that facilitate the nucleation of these local flaws, eventually contributing to a reduction of the critical flaw size required to trigger buckling [185].

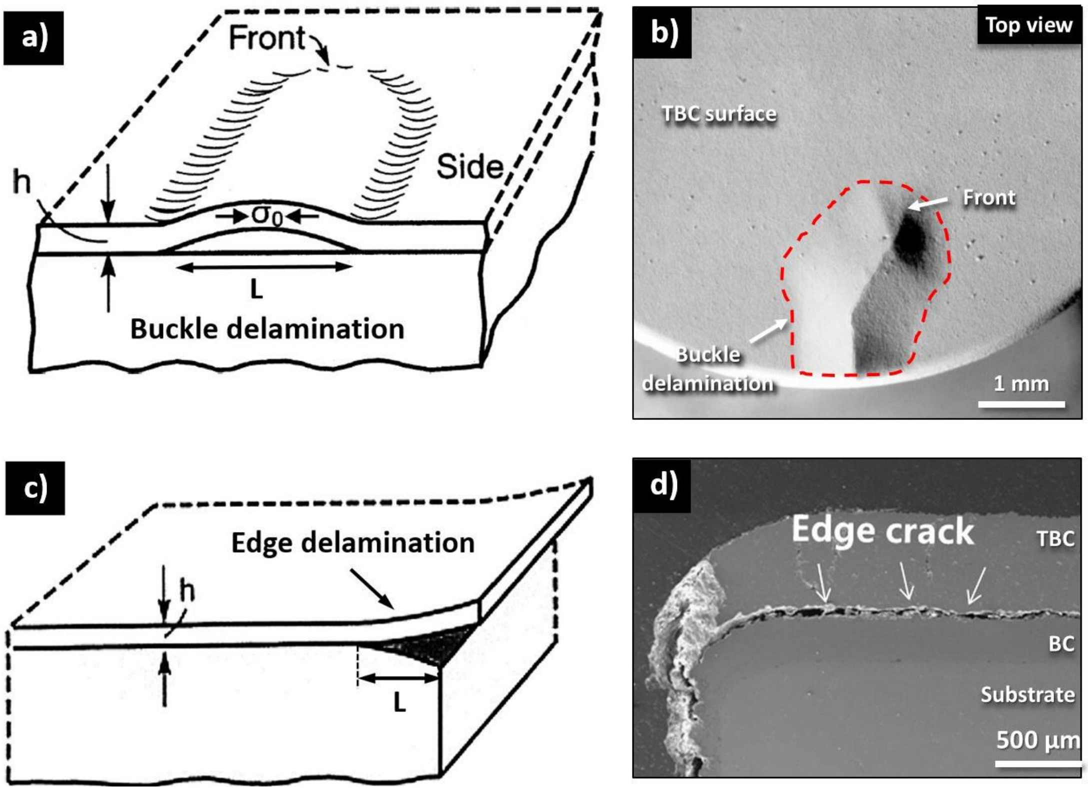

Fig. 2. 16 Schematic illustration of the (a) buckling- and (c) edge-driven delamination failure modes for compressed scales with a pre-existent flaw of length L [185], alongside a (b) top view depiction of buckling on an EB-PVD TBC viewed under reflected light [9] and (d) SEM cross-sectional representation of edge delamination on a PS TBC [186].

On the other hand, edge delamination occurs when an internal flaw located near the interface between the thin scale and the adjacent layers acts as the nucleation point for a plane strain crack propagation along the interface, as illustrated in Figs. 2.16-c) and -d) [185]. Multiple studies have concluded that this failure mode is more likely to occur in systems under large thermal gradients and with higher TBC in-plane stiffness [60, 145, 182, 187-189]. Under such conditions, the inter-layer thermal expansion misfit generates large residual stresses that translate into a higher strain energy density in the vicinity of the BC interface and eventually into cracking events [12, 185]. The strain energy release rate associated with an edge delamination event (G_{SS}) can be estimated by eq. 2.8 and is primarily dependent on the TBC elastic modulus (E_{TBC}) and the difference between the stress free temperature (T_{dep}) and TBC surface temperature (T_0) [190]. As E_{TBC} is intrinsically related to the frequency of microstructural features such as globular porosity, inter- and intra-splat porosity [61, 69, 191] in the TBC, this means that the fracture mechanics behaviour can be affected by the processing parameters and feedstock materials. Another factor influencing the magnitude of the G_{SS} is the BC interface topography [40, 167, 192] and respective near-interface TBC splat morphology [69, 191, 193], as they have the potential to alter the crack propagation direction and affect the overall crack propagation path (i.e. crack configuration) [188, 192].

$$G_{SS} = \left(E_{TBC}\, h_{TBC}\, {\alpha_{TBC}}^2\, 2T_0\right) + T_i - 2{T_{dep}}^2 \tag{2.8}$$

where ${G_{SS}}^{edge}$ is the steady-state energy release rate, E_{TBC} the TBC elastic modulus, h is the TBC thickness, α_{TBC} the TBC thermal expansion coefficient, T_0 the temperature at the TBC surface, T_i the temperature at the interface and T_{dep} the TBC stress-free temperature.

2.5.3 Failure mechanisms of EB-PVD TBCs

EB-PVD TBCs are typically deposited over smooth and homogeneous bond coat surfaces with low interfacial roughness ($R_a \leq 2$ µm) in order to maximise the verticality of the columnar grain microstructure, reduce the TGO growth rate and the formation of heterogeneities [194, 195]. In addition to this, EB-PVD deposition over these surfaces also promotes the formation of strong chemical bonds with the underlying substrate that impart superior interfacial adhesion (~ 64 to 76 MPa) [74, 75]. Although these features have been shown to be effective in delaying crack nucleation and improving the TBC system lifetime, TBC delamination still occurs in the vicinity of the interface due to the concomitant effects of cyclic oxidation with low interfacial roughness, presence of heterogeneities (i.e. pegs) and thermally-induced TGO morphological instability [12, 196, 197].

The morphological instability of the TGO, also referred to as “rumpling” or “ratcheting”, is a generalised phenomenon that takes place all across the interface and originates from the progressive displacement of the TGO into the bond coat during cyclic oxidation,. This displacement is driven by the lateral growth strain in the TGO and accommodated by creep of the bond coat, effectively allowing the compressively stressed scale to lengthen itself via out-of-plane displacements, as highlighted as an outward displacement in Fig. 2.17-a) [12, 185]. As cyclic oxidation progresses, this mechanism becomes increasingly more pronounced and induces larger tensile strains at one of the TGO interfaces, which in turn generate interfacial tensile stresses that lead to local de-cohesion at one of the TGO interfaces, as illustrated in Fig. 2.17 [12, 179, 185]. The detachment of the TGO from the BC shown in Figs. 2.17-a) and –b) (mechanism I) is primarily driven by tensile stresses arising from TGO thickening and occurs predominantly in outward displacement segments of the TGO. On the other hand, the separation of the TGO from the TBC depicted in Fig. 2.17 can occur either by inward (mechanism $\mathrm{II_a}$) or outward (mechanisms $\mathrm{II_b}$) displaced segments of the TGO. These two nucleating mechanisms can originate from three different processes, where the first is caused by the aforementioned TGO rumpling process and the second is related to the formation and widening of cavities in the bond coat that are partially filled by oxides [74].

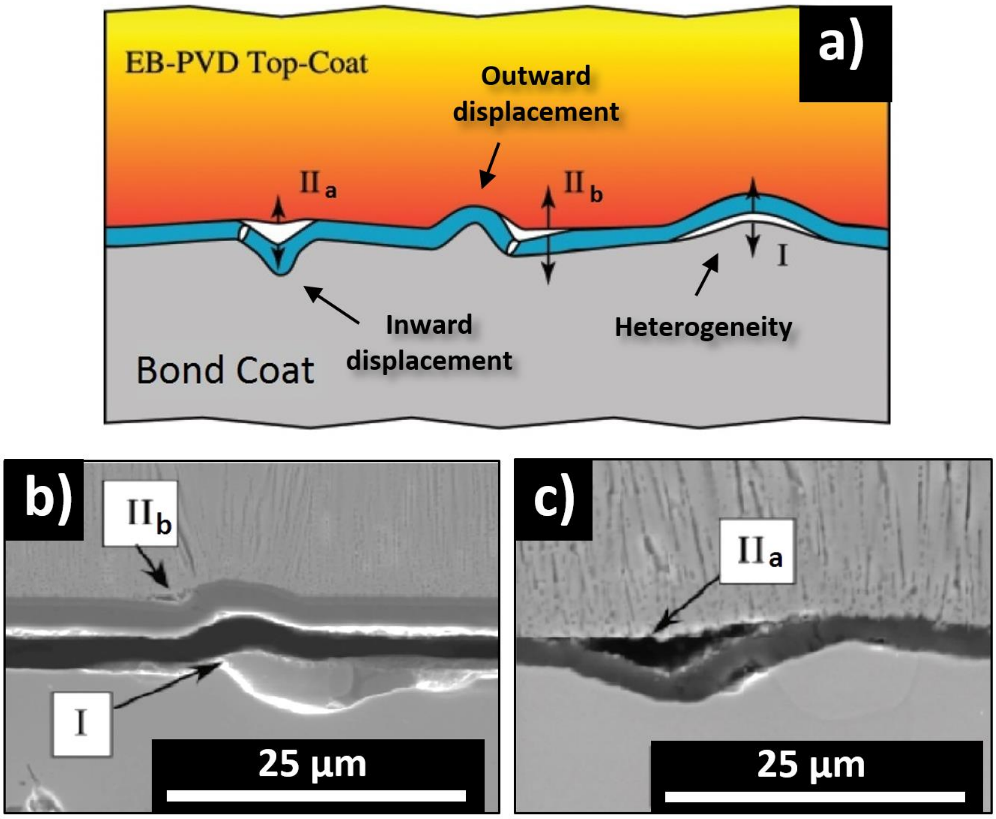

Fig. 2. 17 (a) Schematic illustration of the EB-PVD main crack nucleation mechanisms and respective cross-sectional SEM observation where failure mechanisms (b) I, $\mathrm{II_b}$ and (c) $\mathrm{II_a}$ are highlighted [23].

The third process is the formation of localised TGO thickness heterogeneities (i.e. oxide pegs) that can develop at the interface and contribute to its cyclic degradation [197]. These heterogeneities are typically formed in TGO regions with accelerated O_2^- diffusion, such as yttrium aluminium garnet

(YAG), and contribute to the nucleation of BC/TGO cracks after reaching a critical size [185, 197]. The cracks resulting from the combined rumpling and oxide peg formation effects then propagate across the interface and coalesce to satisfy the requirements of one of the large-scale failure modes mentioned in section 2.5.2 [75]. However, TBC spallation via large-scale buckling is more likely to occur due to the combination of large interfacial stresses ($\sim 3\ to\ 4\ GPa$ [155]), low interfacial roughness [12] and lateral compliance of the columnar microstructure.

2.5.4 Failure mechanisms of plasma-sprayed TBCs

Plasma sprayed TBCs are typically deposited over tortuous bond coat surfaces with peak-to-trough amplitudes in the order of tens of microns to ensure adequate inter-layer adhesion ($\sim 20\ to\ 40$ MPa [16]) via mechanical interlocking with the TBC [12, 60, 118]. The presence of these high-amplitude convex asperities originates a tortuous BC/TBC interface that affects the TBC microstructural and mechanical properties, as well as the overall crack configuration [60, 120, 188]. In addition to this, the growth of a TGO scale over such topographies promotes a local redistribution of the interfacial stresses [112, 159, 160, 166] that is very relevant to the TBC system durability [60, 119, 171]. The nature of these stresses is intimately related with the local curvature of the interface asperities, as out-of-plane tensile stresses are generated around the crests of convex asperities (i.e. peaks) and compressive stresses in the concave regions (i.e. troughs) [159, 166, 173]. The generation of these stresses over the course of cyclic oxidation is the main reason behind the progressive degradation of the interfacial adhesion and/or inter-splat cohesion in the vicinity of the interface [12, 27, 118, 188].

Experimental observations have shown that spallation of plasma-sprayed TBCs is generally driven by the combined delamination of interfacial and inter-splat segments of the coating [188, 198]. These local de-cohesions are usually nucleated by a combination of the four distinct types of failure mechanisms identified up to this date, which are schematically illustrated in Fig. 2.18-a) and illustrated in Fig. 2.18-b) [23]. The type I cracking mechanism highlighted in Figs. 2.18-a) and -b) occurs at the peak crests between the BC/TGO interface and is caused by CTE misfit tensile stresses generated upon cooling down from ambient temperatures. This type of de-cohesion is typically observed in thicker TGO scales, as the combination of a pronounced peak curvature with the radial volumetric growth and expansion of the TGO induce interfacial stresses capable of overcoming the interfacial adhesion strength. In cases where the local inter-splat cohesion strength at the crests of the convex asperities exceeds the TGO/TBC adhesion strength, de-cohesion takes place at the TGO/TBC interface (type II cracking mechanism in 2.17-a) and -b)). This is motivated by analogous inter-layer CTE mismatch tensile stresses generated at the TGO/TBC interface. In contrast, if the inter-splat cohesion is weaker than interfacial adhesion of both TGO interfaces, the CTE mismatch tensile stresses generated in TBC will promote the opening of pre-existent inter-splat separations and lead to the type III cracking mechanism highlighted in Figs. 2.18-a) and -b) [12, 23].

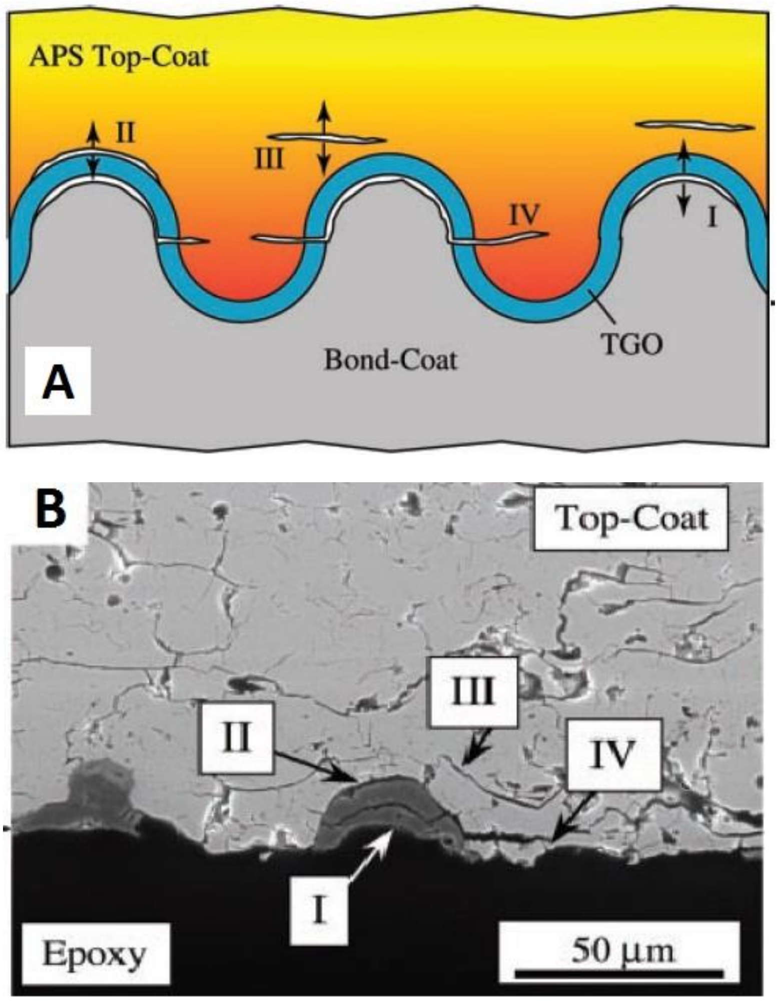

Fig. 2. 18 (a) Schematic illustration of the four crack nucleation mechanisms proposed for plasma-sprayed TBCs and (b) respective cross-sectional SEM observation in a heat treated specimen that has incurred complete delamination[23].

Lastly, the mechanism responsible for type IV cracking is more complex and is still not fully understood up to this date, despite a couple of theories having been proposed. On one hand, Schlichting et al. [199] have proposed that cracking arises from the radial tensile stresses generated around the convex interfacial asperities by the thermal expansion mismatch between the TBC and the underlying BC/TGO composite [199]. In essence, it was proposed that as the TGO grows and starts to constitute a significant fraction of the bond coat asperity, the thermal stresses generated are governed locally by the CTE mismatch between the topcoat and the bond coat/TGO composite. Once the TGO surpasses a critical thickness, the CTE of the BC/TGO composite will be lower than the TBC's CTE, thus inverting the initial nature of the interfacial stresses to compressive around the peaks and to tensile around the troughs. This allows for the newly nucleated cracks in the trough regions to slowly coalesce with pre-stress inversion nucleated cracks at the crests [199], thereby originating the wave-like crack configuration that is often observed in delaminated TBCs (Fig. 2.17-b)). This explanation has continuously gained credence as subsequent studies have reported results that are consistent with the stress inversion theory [159, 171, 178]. On the other hand, Evans et al. [12] have proposed that the volumetric variations associated with the TGO growth around convex asperities cannot be fully accommodated by a rigid body displacement and therefore induces tangential tensile stresses in the surrounding TBC. This leads to radial cracking in the trough regions surrounding the convex asperities, which is intensified by the thermal expansion misfit as the TGO thickens and exceeds a certain critical thickness [12, 162].

Understanding delamination in plasma-sprayed TBCs goes beyond the identification and comprehension of the local crack nucleating mechanisms, as the complex propagation and coalescence behaviours can originate a multitude of different crack configuration paths, as shown in Fig. 2.18 [188]. Nevertheless, the overall crack configuration is still dependent on the ratio of one nucleating mechanism to another, which in turn is dictated by the microstructural (i.e. splat morphology, internal oxidation, porosity, grain morphology/composition, phases and surface topography) and mechanical properties (i.e. elastic modulus, adhesion/cohesion strength, fracture toughness, creep rate) of the bond coat and TBC layers. These relationships have deep implications on the TBC system fracture mechanics, as the geometry and location of the crack path in the TBC system affect the crack tip energy balance (i.e. strain energy storage vs relaxation) and rate of crack propagation significantly [188, 200-202]. This is mostly predicated on the fact that some of the aforementioned microstructural features can alter the crack propagation behaviour via activation of certain extrinsic toughening mechanisms (i.e. crack deflection, zone and contact shielding) [203] or stress relaxation mechanisms (i.e. splat sliding, intra-splat crack closure, microcracking), directly affecting the crack driving force and critical strain energy release rate [200, 201]. This has major implications on the TBC durability since delamination in plasma-sprayed TBCs is driven by the release of elastic strain energy stored in the TBC layer and concomitantly resisted by the inherent TBC fracture toughness and interfacial adhesion strength [12, 204].

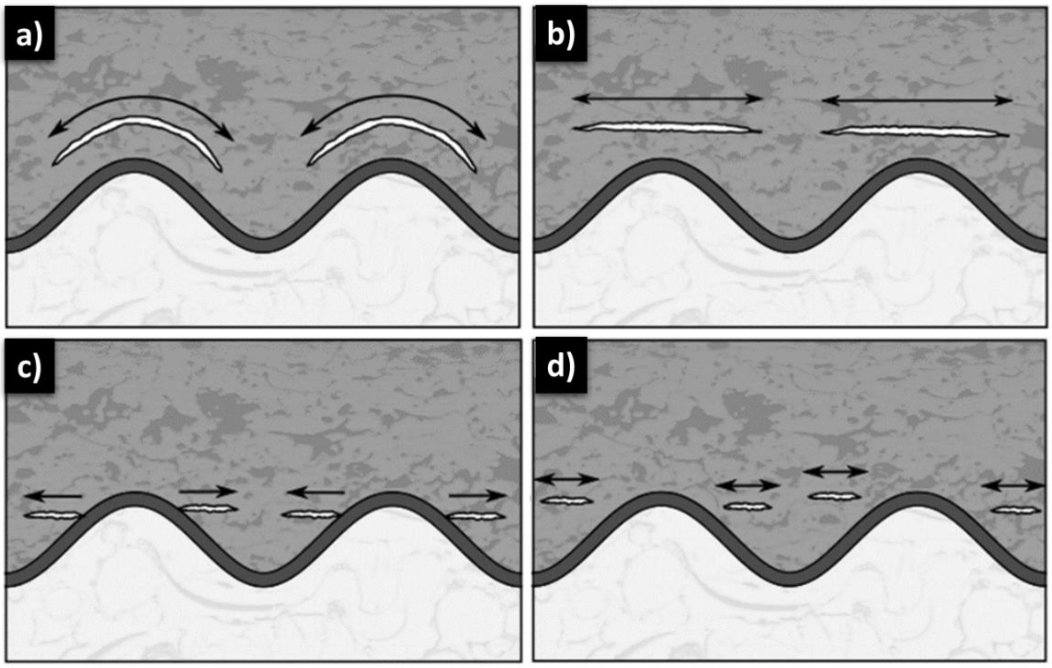

Figure 2.18 Depiction of multiple crack configuration identified by Eriksson et al. [188] that nucleate from a similar local failure mechanism, inter-splat de-cohesion (type III cracking in Fig. 2.13).

Chapter 3. Experimental methodology

3.1. Specimen fabrication and preparation

Specimen fabrication was carried out at Rolls-Royce facilities (Annesley, United Kingdom) using a combination of Diamond Jet 2600 and 3MB thermal spray guns (Oerlikon Metco) mounted on a six-axis robotic arm, as displayed in Fig. 3.1-a). The general fabrication process started by degreasing the as-received button-shaped Nimonic Alloy 263 substrates (Ø=25 mm, height=6mm) with acetone to eliminate any contaminants prior to deposition. The substrate was then grit blasted with 20 µm diameter alumina particles using a Guyson Euroblast cabinet to intentionally roughen the substrate surface and provide adequate adhesion with the bond coat layer. The substrate was then cleaned with compressed air and heated to approximately 200ºC prior to the immediate deposition of the bond coat. A MCrAlY bond coat layer of approximately 180-250 µm was deposited over the substrate at a spraying distance of 200 mm with a vertical step of 4 mm and a raster velocity between 500 and 1000 mm.s^{-1}, depending on the target properties. This resulted in an average deposition rate of approximately 80 µm per cycle, thereby requiring 3 complete passes to achieve the intended bond coat thickness. A standard 8 wt.% YSZ topcoat layer (Metco 204B-NS) was then deposited over the bond coat surface using an APS technique. The same spraying distance and vertical step of the BC were used with a constant raster velocity of 1000 mm.s^{-1}. This resulted in a deposition rate of approximately 14 µm per cycle, which after 25 complete passes yielded a TBC in the 300-350 µm thickness range. Both the MCrAlY and YSZ powders were transported across the gas injection system by Argon using a pressure differential and injected into the flame at a rate of 54 g/min. A representative photograph of an as-fabricated button-shaped specimen is shown in Fig. 3.3-a).

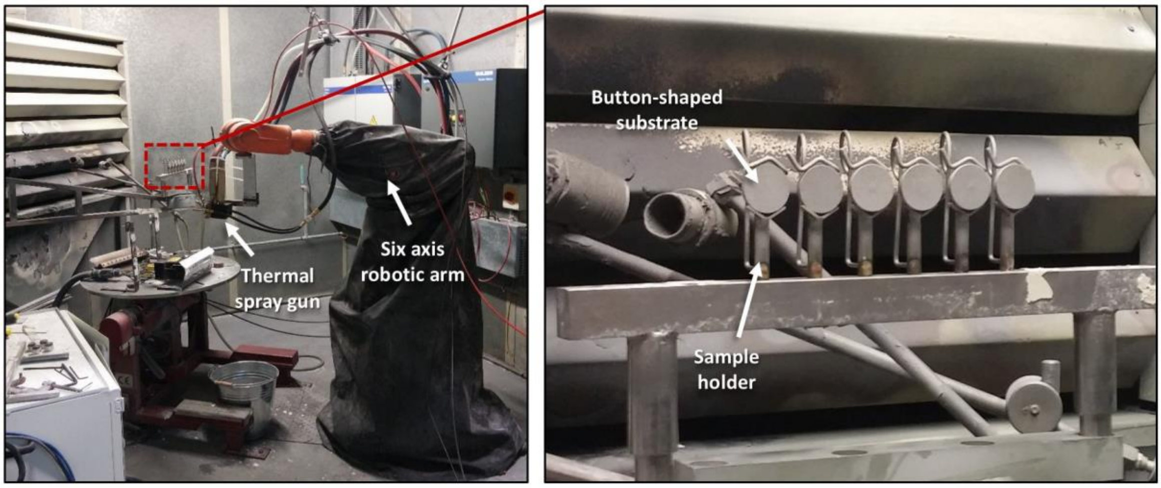

Figure 3.1 Photograph of the thermal spray chamber experimental setup used to fabricate the button-shaped TBC specimens in the present work (left) and respective specimen holder configuration prior to TBC deposition (right).

The standard metallographic preparation procedure used on these specimens was defined as the process required to transform the specimen from an as-fabricated and as-tested state to an analysis-ready state. The multiple iterative steps involved in this process are described in more detail below:

- Sectioning – specimens were sectioned into the desired shape using a precision cut-off machine Struers Accutom-10 equipped with a SiC abrasive blade, as illustrated in Fig 3.2. A slow cutting speed was selected (0.010 mm.s^{-1}) to minimise any mechanical damage arising from the machining process. Heat-treated specimens were preventively encapsulated before sectioning to minimise the alteration of microstructural features (i.e. crack extension) associated with the failure mechanisms;

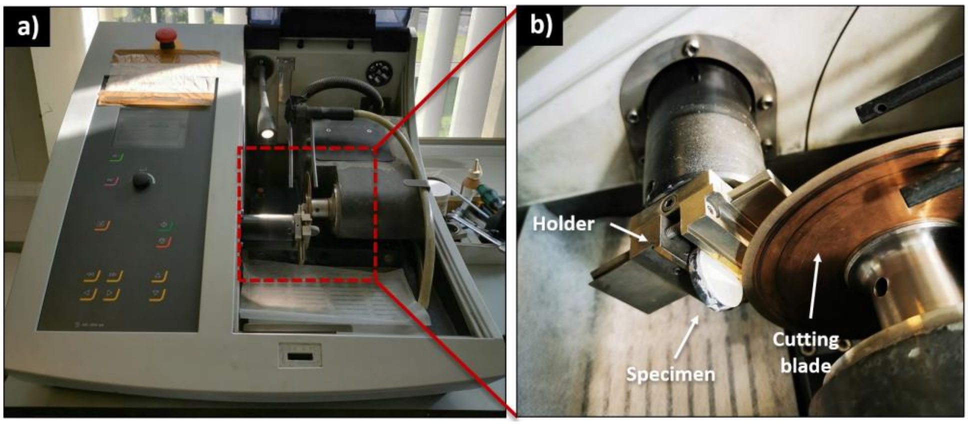

Figure 3.2 (a) Photograph of the Struers accutom-10 precision cut-off cutting machine and (b) respective setup used to section the TBC specimens.

- Encapsulation – specimens were encapsulated using a cold mounting technique, as the porous TBC microstructure and the metallic nature of the MCrAlY bond coat make them sensitive to high-pressure and higher temperature encapsulation methods, respectively. The transparent epoxy resin EpoThin2 was cured inside a vacuum-impregnation chamber for 8 hours;

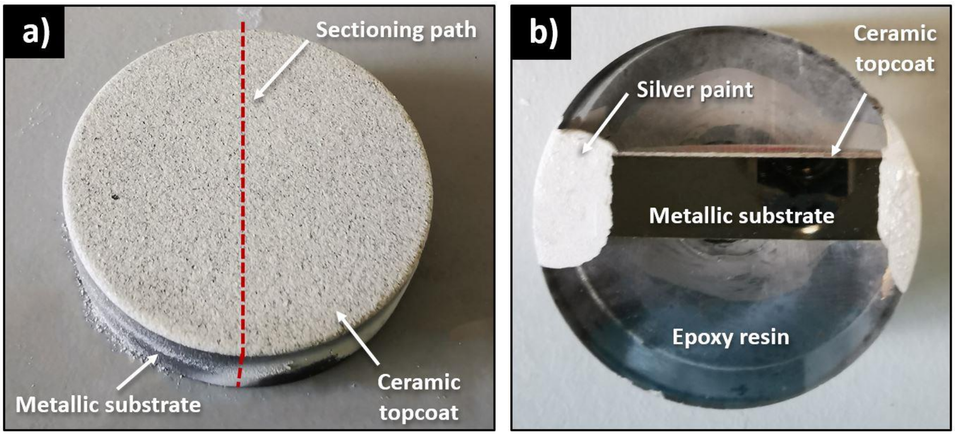

Figure 3.3 (a) Photograph of an as-fabricated button-shaped TBC specimen and (b) respective encapsulated as-polished cross-section.

- Rotary grinding and polishing – The specimens were ground on a water-cooled rotary grinding machine at 300 RPM, iteratively moving from coarser to finer papers (P240, P400, P800, P1200, P2400, P4000). The specimen was rotated by 90° between steps and analysed under the optical microscope to ensure homogeneous scratch profiles were achieved and traces of cutting damage were removed. The specimens were then polished using a lubricant impregnated 6 µm diamond abrasive cloth followed by 1 µm and 0.25 µm cloths. The specimens were thoroughly washed with soap in warm water and degreased with an ethanol solution between each polishing step;
- Electron microscopy sample preparation - a thin homogeneous conductive layer (≈ 3-5 nm) was deposited using a Quorum Q150T carbon coater to make the as-polished specimen surface conductive. Carbon was selected as the material for the conductive layer since it does not interfere with the relevant energy-dispersive X-ray spectroscopy (EDS) spectrum pattern. Lastly, silver paint (Agar Scientific AGG3790) was utilised to establish a conductive path from the sample surface to the metallic stub, as illustrated in Fig. 3.3-b), in order to prevent electron build-up during electron microscopy analysis.

3.2. High-temperature thermal treatment

Thermal cycling fatigue (TCF) is a testing method used for studying the behaviour of TBC system test pieces or engine component parts under high-temperature oxidising and corroding environments that are partially representative of the atmospheric conditions in gas-turbine engines. TCF testing consists of exposing these parts to a thermal cycle comprised of heating, dwell and cooling segments [4, 205]. However, engine-analogous atmospheric conditions are difficult to reproduce in laboratory settings (i.e. high-pressure, mechanical loading, temperature gradients and transients) and therefore, TCF testing is typically used to investigate the TBC system progression with thermal exposure and durability [27]. This is mostly due to the fact that this procedure can satisfactorily induce thermo-chemical (i.e. oxidation, corrosion, inter-layer element diffusion) and -mechanical (i.e. thermal expansion/contraction) degradation behaviours that are analogous to the ones responsible for the failure of TBC systems [26, 76, 84].

In the present work, TCF testing of the button-shaped YSZ-coated CoNiCrAlY and NiCoCrAlY-HfSi TBC systems was carried out in a Carbolite GERO RHF 14/15 box furnace shown in Fig. 3.4 due to its large chamber capacity. The specimens were placed in the central region of the furnace on top of an alumina plate, as displayed in Fig. 3.4. Each TCF cycle consisted of a 30 °C.min^{-1} ramping up rate until the target temperature of 1135°C, followed by an 11 hour dwell and a controlled slow cooling to room temperature at a rate of 1.6°C.min^{-1}. The selection of this dwell temperature was based on trying to test the specimens at a service-analogous temperature. In addition to this, the selection of a slow cooling rate allowed for a considerable oxidation-induced degradation of the TBC system prior to thermal shock induced delamination. This methodology enabled a more accurate evaluation of how the bond coat surface topography and long-term thermally oxide growth behaviour contributed to the failure mechanisms. One specimen of each type being was removed periodically after 2, 4, 16, 22 and 41 cycles in order to study the evolution of the TBC system oxidation kinetics, inter-diffusion with the substrate and thermo-chemical degradation of the bond coat. The remaining samples were left inside the furnace to intentionally undergo spallation of the topcoat, which was defined as the removal of more than 50% of topcoat. This thermal treatment procedure was used in the specimens studied in chapters 4 and 5.

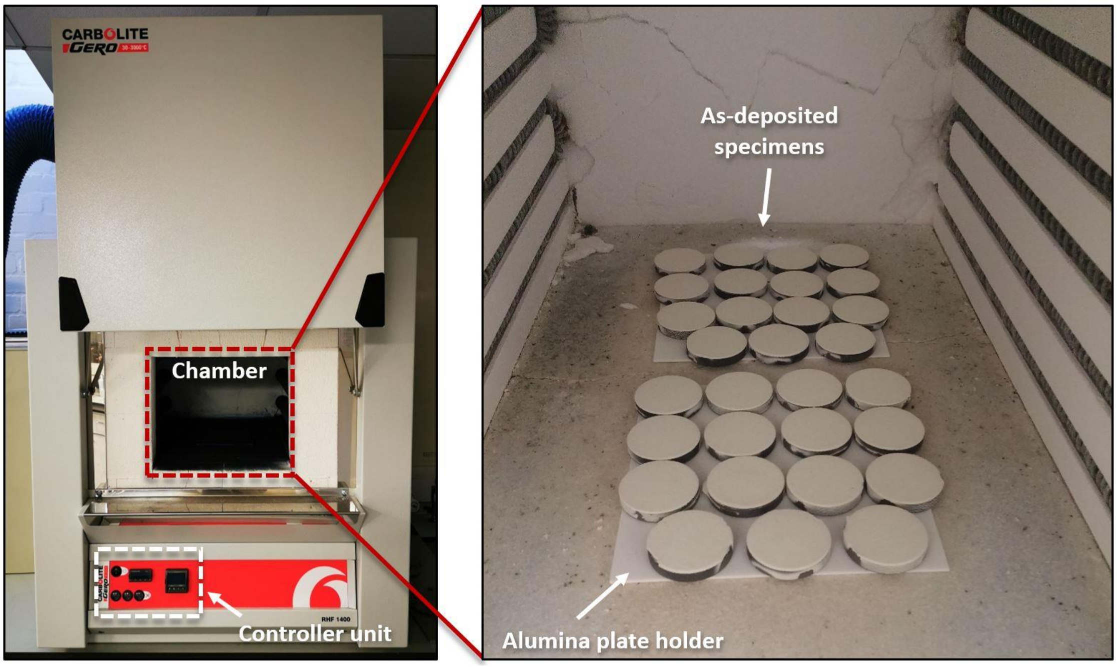

Figure 3.4 Photograph of the Carbolite Gero box RHF 14/15 used for thermal cycling of large batches of TBC specimens and respective arrangement inside the chamber.

On the other hand, the isothermal exposure of as-polished bare MCrAlY bond coat specimens (i.e. no TBC coating deposition) was performed in a CM^{TM} TCF furnace (Fig. 3.5) to investigate the formation of the TGO layer in the early stages of oxidation and how this affects its long-term stability. The samples were placed in the central region of the alumina stage at equidistant positions from the centre point where the thermocouple is located, to ensure atmospheric homogeneity amongst specimens during heat-treatment. The heat treatment profile consisted of a 50°C.min^{-1} ramping up rate until reaching the target temperature of 1135°C, followed by a unique dwell time for each specimen ranging from 5, 10, 30, 60, 120, 240, 600 and 3000 minutes, and a fan-assisted rapid cool down to room temperature.

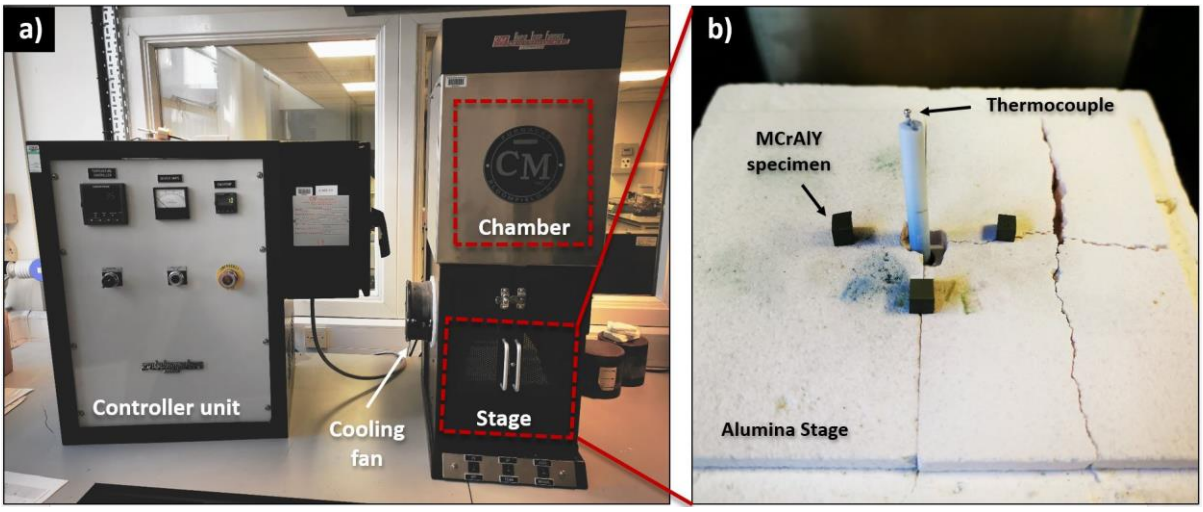

Figure 3.5 Photograph of the CM™ furnace used for thermal cycling of the polished MCrAlY specimens for early oxidation studies and respective arrangement inside the automatic lifting platform.

3.3. Characterisation techniques

In order to carry out a comprehensive investigation of the chemical, physical, microstructural and mechanical properties of the TBC systems studied throughout this PhD project (i.e. MCrAlY alloys, thermally grown oxides and porous ceramic coatings), a complementary combination of experimental techniques was used. All the techniques utilised and respective purposes have been compiled in table 3.1, followed by a description of the respective experimental setups and conditions in the following subsections.

Table 3.1 Summary of all the techniques used in the characterisation of the TBC specimens.

Field	Technique	Purpose
Microscopy	Optical (OM)	Preliminary inspection of the cross-sectioned microstructure during sample preparation
	Scanning electron (SEM)	Observation of surface and cross-sectional microstructural features
	Confocal laser scanning (CLSM)	Characterisation of the surface topography of bond coat and TGO layers
	Focused Ion-beam / EDS	Milling of cross-sections for morphology/compositional analysis of thin oxide scales and preparation of TEM specimens.

	Transmission electron (TEM)	Analysis of the TGO scale structure and grain boundary diffusion
Spectroscopy	X-ray diffraction and electron backscatter diffraction (EBSD)	Composition and phase identification of APS TBCs and metallic alloys
	Energy-dispersive X-ray (EDS)	Chemical characterisation TBCs and bond coat (i.e. composition)
	Photoluminescence piezospectroscopy (PLPS)	Phase identification and measurement of residual stresses
Mechanical testing	Microindentation	Determination of the local in-plane elastic modulus of APS TBCs and metallic alloys
	Three-point bending	Determination of the global in-plane elastic modulus of free standing APS TBCs
	Modified four-point bending	Evaluation of the interfacial fracture toughness of APS TBCs
Diffraction	Grazing incidence X-ray diffraction (GIXRD)	Determine the structure and composition of the chemical species found at the failure plane

3.3.1 Surface characterisation

The characterisation of the bond coat interface topography was conducted on a high-resolution three-dimensional (3-D) laser microscope system (VK-X200K, Keyence) prior to deposition of the TBC. This technique was selected in preference to the two-dimensional cross-sectional analysis, as the topographical data obtained along a third spatial dimension improves the topographical analysis statistics and provides a more accurate description of the BC topography [62, 120, 159]. This line-of-sight and non-destructive technique uses a computer controlled XY-axis motorised stage with a step-based Z-axis scanning system and limited depth of focus optical lens to acquire a matrix of points that represents the 3-D height profile data within a user-selected region of interest (ROI). This equipment uses a focused beam of laser light ($\lambda = 403\ nm$) to scan the surface of the specimen. The incident light reflected from each matrix point (pixel) is then recorded and coupled with the respective coordinates to produce a heightmap and a 3-D reconstruction of the specimen's surface topography, as respectively depicted in Figs. 3.6-a) and –b). The selection of an adequate region of interest and optical lens is instrumental and depends on the size of the microstructural features being studied and resolution required. In the case of the bond coat surface topography measurements, the selection of a 20x magnification lens yielded an image resolution of 0.06 μm^2 per pixel and 2.76 mm^2 field of view, thus ensuring that enough BC surface area is scanned in adequate detail to yield a statistically relevant analysis. In contrast, the analysis of the TGO scale surface topography formed over flat HVOF interface topographies required a 150x magnification (image resolution of 2.1x10^{-3} μm^2 per pixel and 0.05 mm^2 field of view per measurement) to capture the desired small-scale topographical features.

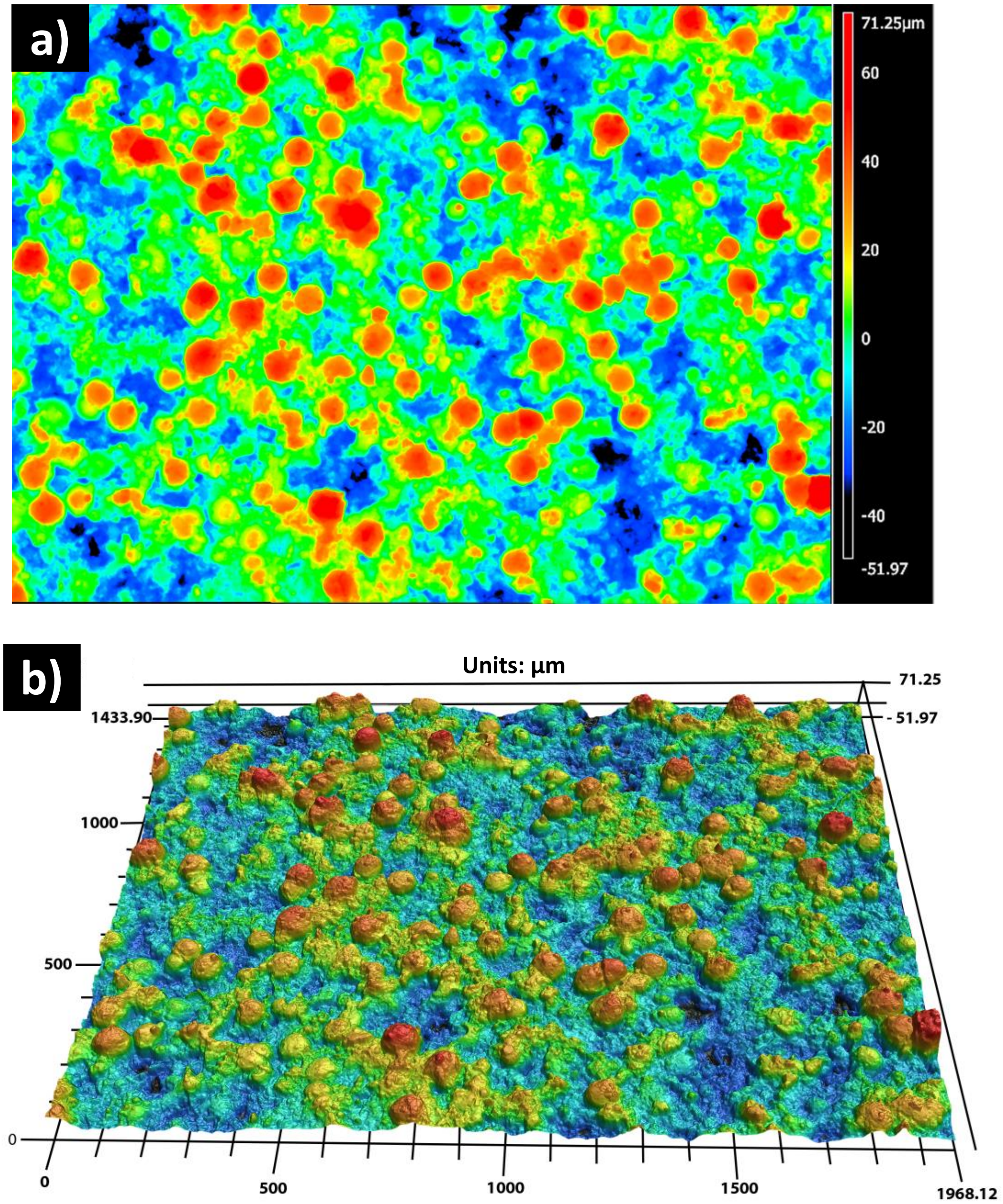

Figure 3. 6 (a) Post-processed 16-bit colour heightmap of a high tortuosity bond coat topography and resulting (b) 3-D reconstruction.

Each sample was randomly scanned in ten areas within a 10 mm radius of the specimen centre-point in order to avoid factoring in any edge related topographical anomalies. All datasets were subjected to the same post-processing procedure (i.e. reference plane tilt correction, 7 square pixel median smoothing filter, height cut level threshold and dark/bright cut level corrections) in order to minimise the impact of experimental error sources such as noise, surface contamination and specimen geometry defects on the results. Lastly, a 5 µm low-pass filter (i.e. S-filter) was applied on bond coat specimens to exclude low-amplitude interfacial features that have been shown to have a negligible contribution to the overall interfacial stress state and fracture mechanics from the quantitative analysis [120]. An example of a 16-bit colour post-processed heightmap of a high tortuosity bond coat topography and respective 3-D reconstruction are displayed in Figs. 3.6-a) and b), wherein a colour gradient represents the variable height of the topography.

3.3.2 Microscopy characterisation

3.3.3.1 Scanning electron microscopy

Scanning electron microscopy was the main technique used for the microstructural analysis of the as-deposited and heat-treated TBC systems. The combination with other complementary techniques such as energy-dispersive X-ray spectroscopy (EDS) and electron-backscatter diffraction (EBSD) was used to obtain additional information regarding the chemical composition, element distribution, phase identification, grain size and orientation. Microstructural features such as layer structure, porosity and surface morphology were investigated under secondary emission mode (SE) due to the low generation depth (≤ 10 nm from the surface) of secondary electrons (≤ 100 eV), thus providing better surface resolution [206]. On the other hand, backscattering emission mode (BSE) mode was used to analyse the bond coat phase evolution with thermal exposure time (e.g. β-phase decomposition) and identify regions of interest within the oxide scale (i.e. oxide clusters, embedded precipitates) for EDS analysis. The penetration depth of the backscattered electrons ranged from a few tens to a few hundreds of nanometres, depending on the density of the target materials and accelerating voltage selected (EHT) [206].

The experimental microscopy work was carried out on multiple electron microscope systems (FEI Quanta 650, FEI Quanta 250, Zeiss Sigma VP and Tescan Mira3 LC) equipped with EDS and EBSD capabilities. The specimens were prepared according to the methodology in section 3.1 and imaged under high vacuum conditions ($\approx 3 - 5 \times 10^{-4}\ mbar$) at a nominal working distance (WD) between 8 to 13 mm, depending on the SEM equipment, mode and complementary techniques used. A 5-10 keV and 20-30 µm aperture diameter were selected for SE mode, in contrast to the 20 kV EHT and 40-50 µm aperture diameter used for BSE mode and EDS data acquisition. The EDS X-max systems utilised

(Oxford Instruments) were comprised of either a 80 or 150 mm^2 detector that provided adequate spatial resolution (≤10 nm) and element detection threshold (0.1 wt.%). Adding to this, the average photon generation depth was determined for each acquisition mode using eq. 3.1 in order to ensure that the measurements were limited to the region of interest [207].

$$Z_m = \frac{0.033\left(V_0^{1.7} - V_k^{1.7}\right)A}{\rho Z} \qquad \text{(eq. 3.1)}$$

Where Z_m is the photon generation depth (µm), V_0 the acceleration voltage (keV), V_k the critical excitation energy for the element of interest (keV), A the atomic mass (amu), ρ the density of the material (g/cm^3) and Z the atomic number.

A count-based acquisition mode with a 1x10^6 counts imposition was selected for the point and areal analysis in order to yield a statistically relevant analysis and ensure the minimal element detection threshold was achieved. In addition to this, a resolution of 2048x2048 and 400 µs pixel dwell time was selected for EDS mapping to improve the signal-to-noise ratio per unit of area.

EBSD mapping was carried out on a Nordlys Nano detector with high spatial resolution (∼100 nm) and low beam current (∼100 pA) acquisition capabilities. The analytical configuration consisted of a pre-tilted specimens (70°) imaged at a WD of 13 mm under a 20 keV accelerating voltage and 10 nA probe current. A binning mode of 2x2 was combined with an acquisition frequency of 75 Hz and a scanning step of 0.145 µm to yield an adequate resolution for the BC submicron grain microstructure. These conditions have additionally provided a good balance between the pattern signal intensity and the electron interaction volume within the material whilst avoiding Kikuchi pattern overlap in dual-phase microstructures.

3.3.3.2 Focused ion-beam milling

Focused ion beam (FIB) was the main specimen preparation technique used for site specific analysis of the thermally grown oxide scales and transmission electron microscopy (TEM). This technique was purposefully selected to avoid introducing any microstructural artefacts typically associated with other metallographic techniques (i.e. grain pull-out, microcracking, pore size enhancement). FIB cross-sectioning was conducted on a FEI Helios Nanolab 660 system equipped with a liquid Ga$^+$ ion source and a X-Max 150 mm^2 EDS system. The oxide scale surface and cross-sectional microstructure of the oxides were analysed under SE mode at low incident beam energy (5 keV) to maximise the surface sensitivity and highlight the morphological/topographical differences, as established in the current literature [208]. On the other hand, all EDS analysis was conducted under the same conditions described in section 3.3.3.1 to ensure that the main K_α and K_β lines of the elements relevant to the analysis (Co, Cr, Ni, Al, O) could be accurately quantified and still maintain a minimal photon generation depth. This is important to minimise the contribution of the underlying layers of material to the EDS signal, as the oxide scales were thin (< 3 µm). An example of a FIB cross-section performed on the surface of a thermally grown oxide scale after 240 min is presented in Fig. 3.7. A protective Pt layer of ~ 2 µm was deposited in all specimens prior to Ga$^+$ ion milling to avoid any damage to the oxides present at the surface of the scale. In addition to this, the final step of ion milling was performed at low probe currents ($< 300\ pA$) to minimise re-deposition of sputtered material and enhance the surface finish.

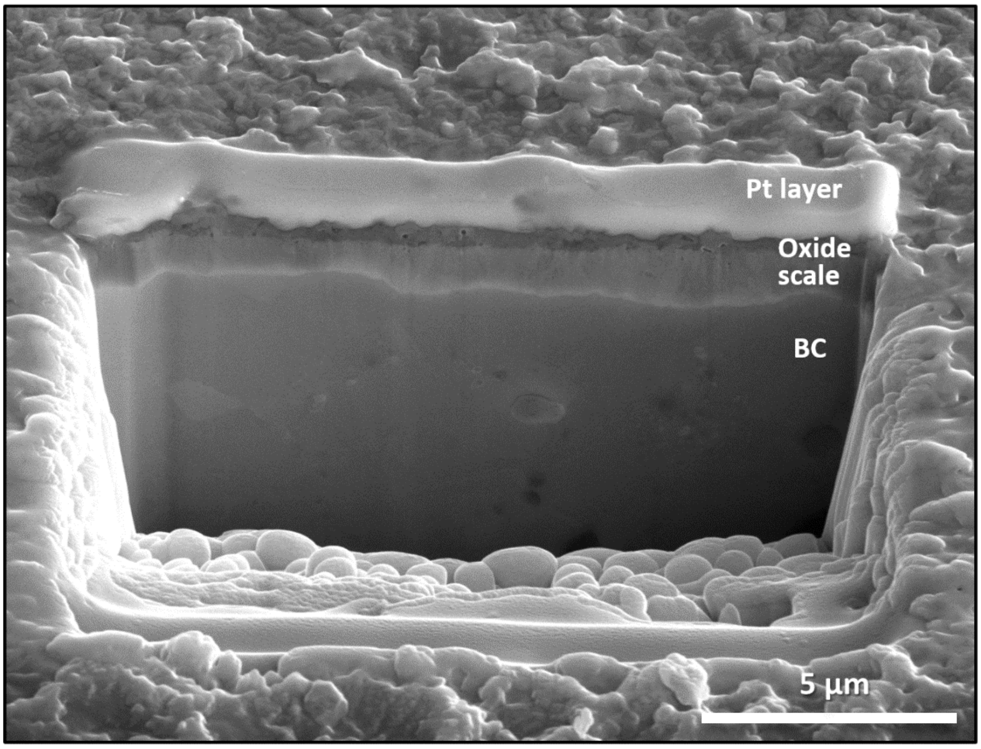

Figure 3. 7 Cross-sectional FIB micrograph of an isothermally aged oxide scale after 240 min taken at 5 keV.

3.3.3 Mechanical testing

3.3.3.1 Depth-instrumented micro-indentation

Depth-instrumented indentation testing was performed on TBC specimens using a micro-indentation tester (MHT^3, Anton Paar) equipped with a square diamond pyramid indenter tip (i.e. Vickers indenter) at room temperature. This indenter geometry was intentionally selected due to its adequacy for use in high stiffness materials such as YSZ ceramics and MCrAlY alloys. The elastic modulus (E_{ind}) was determined from the slope of the unloading section of the load-displacement curve according to the Oliver & Pharr method [209]. A total of twenty measurements were performed on three different specimens of each type of BC topography, both in the as-deposited and thermally cycled conditions. Each measurement was performed on a mirror polished cross-section of the TBC, at an approximate distance of 25 µm from the BC/topcoat interface, as illustrated in Fig. 4.7-d). A loading/unloading rate of 4 N/min was selected along with a hold time of 15 seconds and a 2 N maximum load imposition. These parameters ensured that the resulting indent size was large enough to encompass multiple splats (i.e. approximate diagonal length of 25 µm) and account for the effect of inter-splat sliding, intra-splat closure and microcracking to the deformation behaviour. Each indent was carefully checked under the optical microscope to exclude contributions from pile-up, sink-in, cracking anomalies as well as of excessive proximity to the BC interface. The elastic properties of the TBC were measured in the vicinity of the interface to ensure that the moduli results were representative of the TBC microstructure region where cracks typically nucleate and propagate in APS TBCs [41].

3.3.3.2 Three-point bending

A three-point bending test was conducted on free-standing APS TBC beams (12 x 2 x 0.35 mm^3) machined from standard button-shaped specimens fabricated according to the methodology described in references [210, 211] with the purpose of determining the global in-plane elastic modulus. The as-deposited specimens selected for the experiment were first sliced into rectangular beams using a precision cut-off machine (Accutom-10, Struers) and polished to a 0.25 µm finish in accordance with the procedure described in section 3.1. Complete detachment of the TBC was achieved by immersion of the beams in a HCL solution at room temperature that gradually etched the BC layer. Five measurements of the dimension of each detached TBC strip were carried out with a digital Vernier calliper to ensure a precise determination of the specimens' dimensions.

The three-point bending experiment was conducted on an Instron 3344 universal testing system equipped with a 10 ± 0.001 N load cell and 2 mm diameter support/load roller pins separated by a 5 ± 0.01 mm support span (L_s), as depicted in Fig. 3.8. The fragile nature of the specimen required the use of a reduced width support span to simultaneously minimise the load-displacement curve noise level and maximise the loading force without neglecting the recommended span to thickness ratio to avoid generation of shear stresses (∼20) [210]. Two TBC strips detached from each different BC-topography specimen were loaded at the centre-point of the support span on each side of the coating (i.e. TBC top surface and detached interface) with a constant crosshead speed of 0.1 mm/min up to a displacement of 0.015 mm. Cycling loading was the testing mode selected as it enables the calculation of the global in-plane elastic modulus using elastic unloading data and analysis of the coating recovery behaviour. Each TBC strip was loaded/unloaded ten times. The experimental setup parameters were chosen in order to improve the signal-to-noise ratio and ensure the aforementioned span to thickness ratio that prevents fracture induced by shear forces. The global in-plane elastic modulus of the TBC obtained from the three-point bending test, E_{gil}, was determined by eq. 3.2 [210].

$$E_{gi} = \frac{L^3}{48I}\frac{dP}{dw_0} \qquad \text{(eq. 3.2)}$$

where P is the load applied, L is the support span, w_0 is the displacement at the centre of the beam, $\frac{dP}{dw_0}$ is the slope of the load-displacement curve obtained experimentally, I is the second moment of area defined in a rectangular beam of width a and thickness b, given by $I = \frac{ba^3}{12}$.

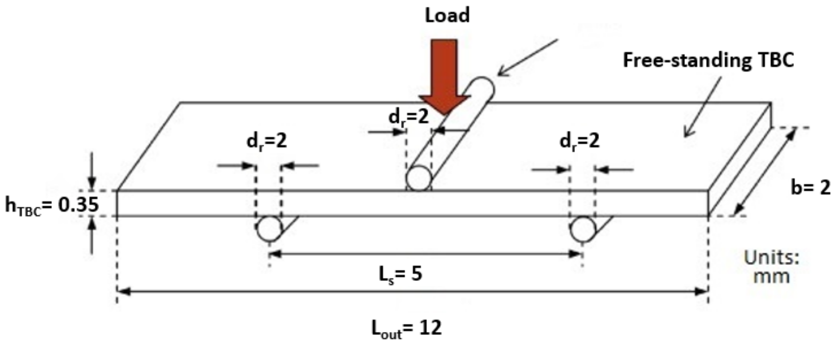

Figure 3. 8 Schematic illustration of the three-point bending experimental setup implemented on an Instron 3344 universal testing system.

3.3.3.3 Modified four-point bending

A modified four-point bending test was conducted on beam-shaped specimens following the modified geometry displayed in Fig. 3.9-a) that was proposed by Hofinger et al. [212]. The minimum beam dimensions recommended by the ASTM C1161-13 standard [213] were also selected for this study, as they are believed to augment the variation of critical load and strain energy release rate magnitude amongst different specimen types. Following the fabrication of the beam-shaped specimens described in section 5.2.1, a Nimonic Alloy 263 stiffener was bonded to the topside of the TBC using an epoxy adhesive (Araldite rapid). The resulting adhesive layer had an approximate thickness of 0.15 mm and displayed a low level of infiltration in the coating, thus minimising its contribution to the experimental results [204, 214]. A vertical notch of approximately 0.45 mm in width was then introduced at the beam centre-point, from the top stiffener surface to the BC/TBC interface using a precision cutting machine (Struers Accutom-10) equipped with a SiC abrasive blade. A slow cutting speed (0.010 mm/s) and low force settings were selected to minimise the mechanical damage introduced by the machining process. The notched region was observed under SEM to confirm that it had reached the interface and no visible cracks had been introduced in the TBC, as depicted in Fig. 5.4-a). In total, five specimens were fabricated for each type shown in table 1, of which, two were used for sacrificial purposes and the remaining three for testing.

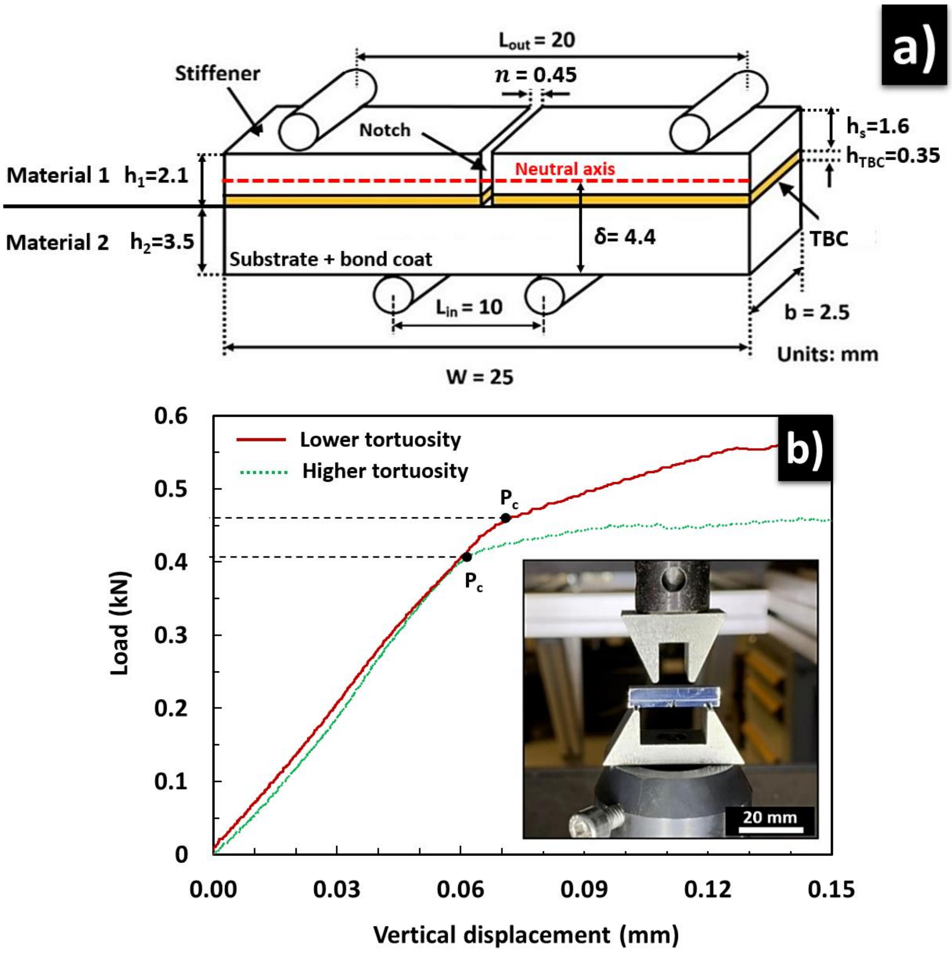
a)
Stiffener
L_{out} = 20
n = 0.45
Notch
h_s=1.6
h_{TBC}=0.35
Material 1 h_1=2.1
Neutral axis
Material 2 h_2=3.5
Substrate + bond coat
δ= 4.4
TBC
L_{in} = 10
b = 2.5
Units: mm
W = 25
b)
Lower tortuosity
Higher tortuosity
P_c
P_c
Load (kN)
0.6
0.5
0.4
0.3
0.2
0.1
0
0.00
0.03
0.06
0.09
0.12
0.15
Vertical displacement (mm)
20 mm

Figure 3. 9 (a) Schematic of the four-point bending experimental setup and specimen geometry used in this experiment (b) Representative load-displacement curve obtained from the four-point bending test along with an inset image depicting of the experimental setup implementation in an Instron 5569 universal testing machine.

The experiment was carried out at room temperature in an Instron 5569 universal testing machine (inset in Fig. 3.9-b) equipped with a 5 kN static load cell, wherein a crosshead velocity of 0.5 mm.min^{-1} and 20/10 mm support and loading spans were selected. The sacrificial specimens were used to determine the elastic limit points for each specimen type. One was loaded until a TBC delamination crack could be observed and the resulting load displacement curve was used to pre-load the other sacrificial specimen and ensure that incipient cracks had formed on both sides of the notch ($\sim 200\ \mu m$). These values were then used to pre-load three specimens of each type shown in table 1 up to their pre-determined elastic limit points and introduce analogous pre-cracks at the notch prior to testing. The testing specimens were then loaded under the aforementioned conditions to obtain a load-displacement curve, such as the one presented in Fig. 3.9-b) for a lower and higher tortuosity specimen. The linear region corresponds to the pre-cracked beam stiffness and the slope change to further crack propagation in the TBC. The critical load (P_c) values obtained were confirmed with direct observation of the crack development during the test and pre-crack formation confirmed via generation of ε_{yy} strain maps. It is noteworthy that although the strain maps were adequate to detect the formation of a pre-crack, the limited optical resolution of the DIC system and lack of surface contrast made this method unsuitable for the determination of the crack propagation velocity, strain measurements and stress determination.

3.3.4 Grazing incidence-ray diffraction

Grazing incidence X-ray diffraction (GIXRD) is a non-destructive and surface-sensitive technique that can be typically used in the characterisation of thin superficial layers [215]. The selection of very low incidence angles ($0.5^{o} \leq \alpha_{i} \leq 5^{o}$) reduces the penetration depth of X-rays by an order of magnitude and improves the surface sensitivity considerably. This is facilitated by the increased X-ray beam path length through the superficial layers of the specimen, simultaneously maximising the signal intensity from the near-surface species and reducing the contribution of any underlying undesired species in the diffraction pattern (e.g. substrate) [216]. The interaction between the incident X-ray beam and the crystalline material produces diffracted X-rays that are collected by a detector moving step-wise along an angular trajectory, as schematically depicted in Fig 3.10-a), effectively scanning an angular region that is equivalent to the angle between the transmitted and diffracted beams (i.e. 2θ) [216]. The number of X-ray photons detected per second is equivalent to the intensity of the signal and is recorded for each angular position within the selected range, producing a diffraction pattern that encompasses all the families of planes of all the chemical species present.

As the TBC system usually fails in the vicinity of the BC/TBC interface and the thin TGO layer is often exposed, there have been a few studies that used this technique to investigate the failure plane composition [148, 217].Therefore, the GIXRD technique has been used herein to determine the structure and composition of the chemical species found at the failure plane of thermally-exposed TBC systems that have incurred partial or complete spallation of the ceramic topcoat. However, it is important to note that the diffraction pattern is affected by the failure plane roughness, as the low incidence angles combined with the higher-amplitude convex asperities might produce a shadowing effect on certain regions of the surface and affect the penetration depth in non-horizontal segments. Nevertheless, the experimental results are considered viable and representative of the specimen's failure plane, as the area analysed (i.e. 100 mm^2) has enough statistical relevance to compensate for aforementioned limitations.

The GIXRD measurements were conducted on a PANalytical X'Pert diffractometer with a proportional point detector in a Bragg-Brentano geometry employing a Copper Line Focus X-ray tube with Ni kβ absorber (0.02 mm; Kβ = 1.39 Å) and Kα radiation (λ=1.54 Å). The incident angle selected was $\alpha_i = 3^{o}$

in order to achieve an adequate balance between signal intensity and surface sensitivity. The range selected for the angle between the transmitted and diffracted beams was $20^{o} \leq 2\theta \leq 110^{o}$ to ensure that the most relevant crystallographic planes were detected and an angular step of 0.05^{o} with hold time of 7 seconds to improve the spectrum resolution. The sample height and tilt were calibrated as shown in Fig. 3.10-b) to maximise the intensity of the signal and reflect the geometry presented in Fig. 3.10-a). Further to this, the penetration depth was calculated beforehand for the most common chemical species detected at the failure plane using eq. 3.3, so as to ensure that it was within the acceptable range for this experiment. The results obtained were compiled in table 3.2 and since the penetration depths obtained were lower than the measured thickness of the TGO after prolonged thermal exposure, the viability and reliability of the technique were confirmed. All densities used in the calculations were from fully dense materials, with exception of the 8YSZ and NiCoCrAlY materials, whose APS-processed density values were obtained from reference [218].

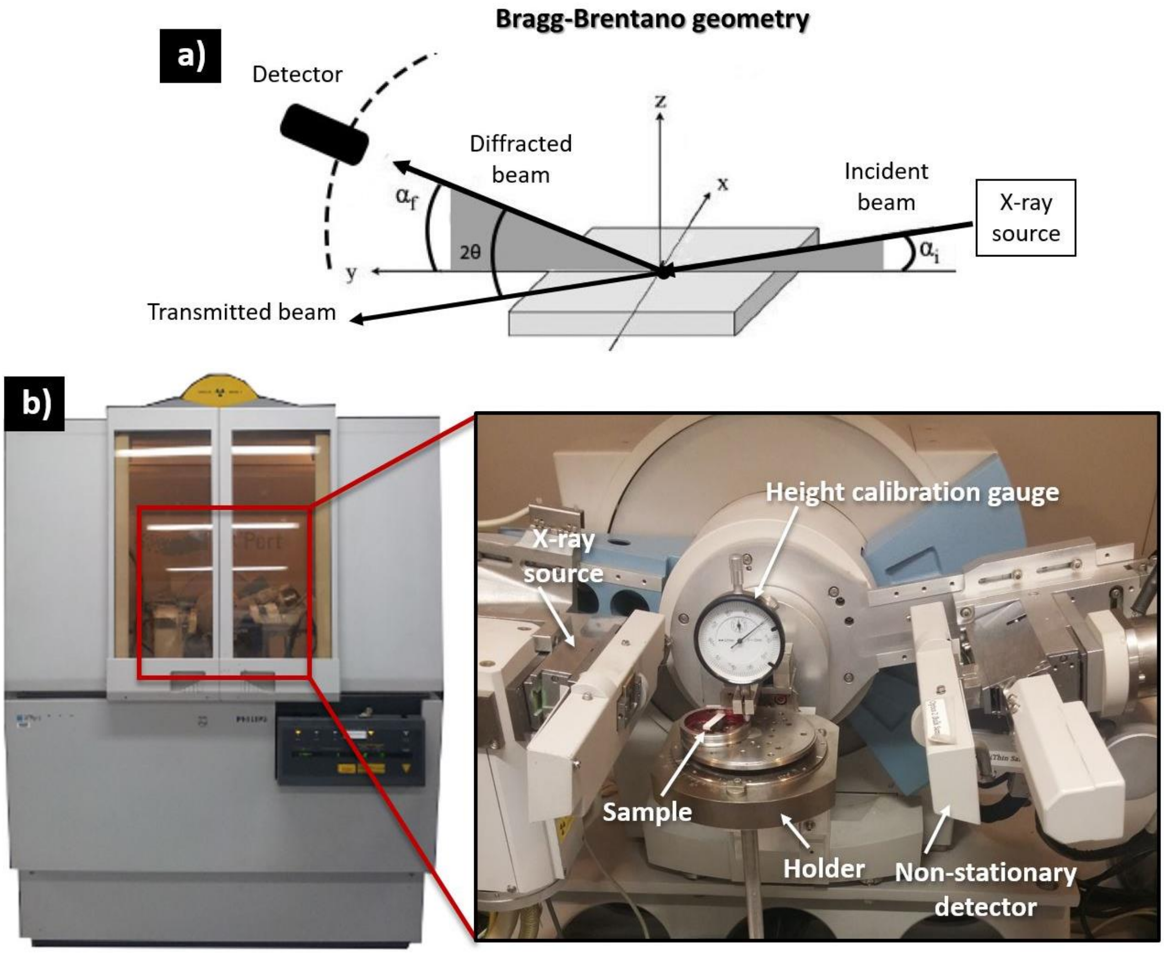
Bragg-Brentano geometry
a)
Detector
Diffracted beam
z
x
Incident beam
X-ray source
α_f
2θ
α_i
y
Transmitted beam
b)
Height calibration gauge
X-ray source
Sample
Holder
Non-stationary detector

Figure 3. 10 (a) Bragg-Brentano geometry typically adopted for grazing incidence X-ray diffraction where, α_i denotes the incident beam angle and 2θ the angle between the transmitted and diffracted beams [219]; (b) Grazing incidence X-ray diffraction experimental setup implemented on a PANalytical X'Pert diffractometer following the Bragg-Brentano geometry.

$$I = I_0 e^{(-2xKB)} \quad \text{(eq. 3.3)}$$

where $$B = \sqrt{\frac{1}{2}\sqrt{(\alpha_i{}^2 - 2\delta)^2 + 4\beta^2} - (\alpha_i{}^2 - 2\delta)^2} \quad \text{(eq. 3.4)}$$

Where I_0 is the incident beam intensity, x the penetration depth coordinate, $K = \frac{2\pi}{\lambda}$ is the magnitude of the wave vector, α is the angle of incidence, δ and β are derived from the refractive index $n = 1 - \delta - i\beta$ and are dependent on the attenuation coefficient μ *and* electron density ρ_e of the target material.

Table 3. 2 Penetration depths of a CuKα 8.04 KeV X-ray beam (α = 1.54 Å) on the major isostructural species identified at the failure plane for an incidence angle $\alpha_i = 3°$.

Material	Penetration depth (μm)
Al_2O_3	4.27
Cr_2O_3	0.58
Y_2O_3	1.14
NiO	1.95
TiO_2	0.89
$CoCr_2O_4$	0.50
$CoAl_2O_4$	0.95
$NiCo_2O_4$	0.51
$AlCo_2O_4$	0.53
8wt.% YSZ	1.01
NiCoCrAlY (APS)	0.48

3.3.5 Photoluminescence piezospectroscopy (PLPS)

Photoluminescence piezospectroscopy (PLPS) is a non-destructive analytical technique commonly used in the measurement of residual stresses in Al_2O_3 scales such as the TGO layer. This technique uses a laser light of adequate wavelength to excite the R- and/or T-line luminescence of substitutional Cr^{3+} impurities present in the Al_2O_3 scale and obtain the respective luminescence spectrum [150, 156]. A typical spectrum of an unstrained single crystal sapphire with trace amounts of Cr^{3+} atoms (0.05 wt.%) displays R-line luminescence peaks at ~14400 cm^{-1} (R1) and ~14434 cm^{-1} (R2) if the α- Al_2O_3 polymorph is present in the sample [220] and T-line luminescence peaks at ~14546 cm^{-1} (T1), ~14626 cm^{-1} (T2) and ~14330 cm^{-1} (T1) if the θ-Al_2O_3 polymorph is present [150]. An example of such a spectrum is given in Fig. 3.11. The R2 line shows a linear dependence on the mean stress of the scanned region and therefore, the resulting peak shift ($\Delta\nu$) in relation to the aforementioned stress-free R2 line can be used to determine the residual stress, as shown in equation 3.5.

$$\Delta\nu \;=\; 5.07\;(cm^{-1}GPa^{-1})\;\sigma \qquad \text{(eq. 3.5)}$$

where $\Delta\nu$ is the frequency shift of the R2 line and σ the residual stresses arising from CTE mismatch and growth stresses assuming an equi-biaxial plane stress in the scale.

The residual stress measurements were performed at room temperature on a Renishaw InVia Raman equipped with a He-Ne laser source (λ=633 nm) with a wavelength within the absorption band of the Cr-doped Al_2O_3 scales. The laser was focused to a spot size of ~1.5 μm on the sample surface and the spectrometer was calibrated before each measurement using a pure silicon sample to obtain a reference spectrum. Each measurement covered a square grid area of 100 x 100 μm with an acquisition time of 1 second. The peak positions of the R1 and R2 lines in the heat treated specimens were determined by deconvoluting the Al_2O_3 luminescence spectra in GRAMS AI software (Thermo Fisher^{TM}) using an automatic fitting algorithm based on the Gaussian-Lorentzian function ($\Phi(\nu)$) given below [221]:

$$\Phi(\nu) = (1-M)I_{max}e^{\left[-\left(\frac{\nu-\nu_m}{w}\right)^2(4\ln(2))\right]} + M\left[\frac{I_{max}}{1+4\left(\frac{\nu-\nu_m}{w}\right)^2}\right] \qquad \text{(eq. 3.6)}$$

where the first term is the Gaussian component and the second is the Lorentzian component. M is the relative proportion of the Lorentzian character, I_{max} is the maximum intensity, ν_m the frequency at maximum intensity, w the full width at half maximum.

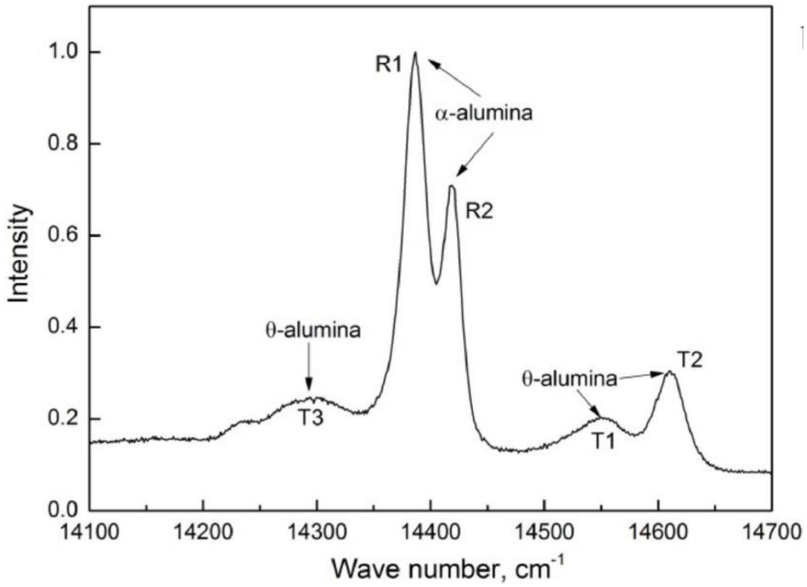

Figure 3. 11 Luminescence spectra of an Al_2O_3 scale showing the characteristic peaks for the α and θ polymorphs.

Chapter 4. Investigation of the bond coat interface topography effect on lifetime, microstructure and mechanical properties of air-plasma sprayed thermal barrier coatings

Statement: *The contents of this chapter are based on the work published in the Journal of the European Ceramic Society, Volume 40, Issue 15.*

Contributions: Ying Chen, G. Brewster, R. McIntyre, Ping Xiao

4.1. Introduction

Numerous studies focused on the stress generation mechanisms responsible for failure in overlay TBC systems [84, 118, 166, 183, 222, 223] have shown that they are mainly generated by the thermal expansion mismatch between the ceramic topcoat and the metallic substrate [84, 118, 166, 183, 222, 223]. This is aggravated by the BC/TBC interface tortuosity required to promote enhanced inter-layer adhesion in overlay systems, as it exacerbates the magnitude of the out-of-plane tensile stresses generated in the vicinity of the interface. A few studies aimed at investigating the effect of BC interface topography on stress generation and TBC system lifetime [112, 118, 147, 183] were conducted using two-dimensional parameters (e.g. arithmetic mean height, slope distribution, kurtosis) for the characterisation of the topography. Even though this analysis is useful for characterising the general BC interfacial features, the lack of information along a third dimension can affect the interface characterisation and lead to an inaccurate estimation of the parameters true impact on the TBC system properties. In reality, only a couple of studies [120, 159] have ever explored the relationship between BC topography and TBC lifetime using three-dimensional surface texture parameters (e.g. arithmetic mean roughness S_a, root mean square slope S_{dq}, summit density S_{ds} and peak curvature S_{pc}) to establish a correlation with TBC lifetime. Even though these studies were able to show that TBC lifetime can be improved by enhancement of the BC topography, a quantitative analysis of how the BC topography affects the TBC layer properties was not conducted. Therefore, this leaves the link between BC topography and microstructural, mechanical properties and fracture mechanics of TBCs mostly unaddressed.

As the TBC layer is formed by the high-velocity impingement of particles undergoing a rapid solidification process, these coatings are characterised by their elongated splat morphology of variable curvature and porosity [23]. As a result, a large network of inter/intra-splat cracks is formed resulting in a highly variable range of topcoat microstructures that alter the TBC mechanical properties [34, 69, 120, 224]. These features are primarily dependent on the characteristics of the plasma jet stream, the substrate condition and the gun settings [34, 52]. In a scenario where the substrate topography is the only variable in the spraying process, as it is the case of the current study, the effect that BC topography has on the TBC layer formation and properties can be thoroughly investigated. Cedelle et al. [55] demonstrated that the substrate surface topography has a significant impact on the splat formation process, with wettability being inversely proportional to the splat spreading time. Expanding this concept to YSZ plasma sprayed coatings, Salimijazi et al. [225] provided further evidence that manipulation of roughness and other surface topography features had a meaningful impact on improving wettability and splat solidification behaviour. Additionally, Lima et al. [226] were able to link the microstructural features with the APS TBC mechanical properties after reporting an inversely proportional relationship between BC interface roughness and the TBC elastic modulus. A correlation between flat splat morphology and high elastic moduli coatings microstructures was also observed.

Piecing all this information together, it is reasonable to consider that a tortuous BC interface with variable topography features might alter the splat morphology in such a way that ultimately affects the lifetime of a TBC system. Thus, the main aim of the current study is to investigate the effect of BC topography on the microstructure and mechanical properties of the APS TBC coatings, ultimately linking these properties to specific fracture mechanics behaviours and TBC durability. A correlation between the three-dimensional BC interfacial features and splat morphology was established via microstructural analysis of the topcoat and measurement of the respective local and global in-plane elastic moduli in the vicinity of the interface. The relationship between the BC topography and the TBC's fracture mechanics was also investigated and discussed.

4.2. Materials and methods

4.2.1 Sample fabrication and preparation

Sample fabrication was carried out according to the specifications in section 3.1. The resulting TBC system was comprised of a button-shaped Nimonic Alloy 263 substrate (Ø=25 mm, height=6mm), a 200 µm dual-layer MCrAlY bond coat and a 350 µm 8 wt.% YSZ ceramic topcoat (Metco 204B-NS). The BC base layer was deposited by High Velocity Oxygen Fuel (HVOF) and two different BC compositions were utilised, a Co-based chemistry comprised of Bal. Co, 31-33% Ni, 20-22% Cr, 7-9% Al, 0.35-0.65% Y (H.C. Stark, AMPERIT® 405.072) and Ni-based chemistry comprised of Bal. Ni, 21-23% Co, 16-18% Cr, 11.8-13.2% Al, 0.4-0.8% Y, 0.1-0.3 Hf, 0.2-0.6 Si (H.C. Stark, AMPERIT® 415.072). The flashcoat layer was subsequently deposited over the base layer by either HVOF or APS, following the specifications in table 4.1, to generate different BC interface topographies. The MCrAlY coated substrates were then annealed for 1 hour at 1100°C in an Argon atmosphere (1.7×10^{-1} mbar) prior to topcoat deposition in order to reduce porosity, promote homogenisation of the BC internal microstructure and relax the residual stresses arising from deposition. The ceramic topcoat layer was deposited using the same processing parameters and atmospheric conditions in order to ensure that the only variable arising from the deposition process was the BC morphology-induced changes in the splat morphology.

Table 4.1 Parameters utilised for the thermal spraying of the BC flashcoat layer.

Material composition	Deposition method	Powder particle size	Specimen ID
CoNiCrAlY (Bal. Co, 31-33% Ni, 20-22% Cr, 7-9% Al, 0.35-0.65% Y)	HVOF	Small (AMPERIT 415.072)	Co HVOF S
	HVOF	Medium (AMPERIT 415.063)	Co HVOF M
	APS	Medium (AMPERIT 415.063)	Co APS M
	APS	Large (AMPERIT 415.002)	Co APS L
NiCoCrAlY-HfSi (Bal. Ni, 21-23% Co, 16-18% Cr, 11.8-13.2% Al, 0.4-0.8% Y, 0.1-0.3 Hf, 0.2-0.6 Si)	HVOF	Small (AMPERIT 405.072)	Ni HVOF S
	HVOF	Medium (AMPERIT 405.090)	Ni HVOF M
	APS	Medium (AMPERIT 405.090)	Ni APS M
	APS	Large (AMPERIT 405.002)	Ni APS L

Microstructural and chemical characterisation of the as-deposited and heat-treated specimens was carried out by scanning electron microscopy (Quanta 650, FEI) coupled with energy dispersive X-ray spectroscopy (EDS X-max 80mm^2 detector, Oxford Instruments) according to the methodology described in section 3.3.2. The equivalent thickness of the TGO was determined by measuring the area and length of a cross-sectional TGO segment (ImageJ, area tool) of five different micrographs like the ones shown in Figs. 4.3-a) and –b) and calculating the average, as analytically described by eq. 4.1.

$$\delta_{eq} = \frac{\sum_n^i \frac{A_{TGO}}{L_{TGO}}}{n} \qquad \text{(eq. 4.1)}$$

Where A_{TGO} and L_{TGO} are the cross-sectional area and length of the TGO segment, and n is the number of TGO segments analysed.

The local and global in-plane elastic modulus were respectively obtained from depth-instrumented micro-indentation and three point bending according to the methodologies described in sections 3.3.3.1 and 3.3.3.2. The thermal cyclic fatigue testing was conducted in a Carbolite GERO box furnace following the methodology described in section 3.2. In total, sixteen samples of each type were tested, with a few of each type having been removed from the furnace during TCF testing for oxidation kinetics and microstructural investigation purposes. The remaining eight specimens of each type were left inside the furnace for lifetime assessment purposes until spallation of more than 50% of the topcoat was observed. The subsequent characterisation of the failure plane of TBC systems that have incurred complete or partial spallation was performed using the GIXRD technique and methodology described in section 3.3.4.

4.2.2 Bond coat topography characterisation

The BC interface topography was characterised by assessing the impact of four independent surface descriptors on TBC lifetime using the methodology described in section 3.3.1. Three of these parameters were well-established surface texture parameters defined by the ISO 25178 standard (i.e. arithmetic mean roughness S_a, arithmetic mean peak curvature S_{pc}, areal summit density S_{ds}), whereas the fourth parameter was a newly formulated surface descriptor denominated total thresholded summit area, S_{sth}. The proposal of this novel parameter was motivated by the need of quantifying the concomitant impact of summit morphology and tortuosity.

The arithmetic mean roughness is the most commonly used parameter to describe the BC interface roughness and can be defined as a height parameter that expresses the sum of the absolute height difference values between each data point, $z(i,j)$, and the respective arithmetic mean $|\bar{z}|$ for the entire area, as given by eq. 4.2.

$$S_a = \frac{1}{mn}\sum_{i=1}^{m}\sum_{j=1}^{n}|z(i,j) - \bar{z}| \qquad \text{(Eq. 4.2)}$$

The areal summit density represents the number of summits per unit of BC surface area scanned, as described by eq. 4.3. For the purpose of this study, summits were defined as peaks with amplitude over 15% of the maximum height of the distribution (S_z), as illustrated in Fig. 4.1-a). These higher relief regions were specifically selected as they are believed to have a larger impact on the alteration of the topcoat splat morphology and on the redistribution of local stresses.

$$S_{ds} = \frac{number\ of\ summits\ above\ the\ imposed\ \ threshold\ limit}{total\ area\ measured} \qquad \text{(Eq. 4.3)}$$

The arithmetic mean peak curvature represents the arithmetic mean of the principal curvatures of each height element along the X and Y axes, thus allowing for the quantification and comparison of the predominant peak curvature profile for different BC topographies. This parameter is given in its discrete form by eq. 4.4.

$$S_{pc} = -\frac{1}{2n}\sum_{k=1}^{n}\left(\frac{\partial^2 z(i,j)}{\partial x^2} + \frac{\partial^2 z(i,j)}{\partial y^2}\right) \qquad \text{(Eq. 4.4)}$$

where n is the number of summits in the area analysed and z(i,j) the height element for a specific set of (i,j) coordinates.

Lastly, the total thresholded summit area parameter, S_{sth}, is a newly formulated surface descriptor aimed at providing a quantification of the total area of all thresholded summits (white regions in Fig. 4.1-c) within an area scanned by a surface characterisation technique. The first step to determine this parameter is to threshold a grayscale topography heightmap (Fig. 4.1-b) at a pre-defined height (*h)* from the top of the summit in order to reveal the individual area of the thresholded summit (S_{si}) formations relevant to the analysis, as illustrated in Fig. 4.1-a). It is followed by the summation of all S_{si} values and divided by the total area scanned (A), as expressed by eq. 4.5 in its discrete form.

$$S_{sth} = \frac{1}{A}\sum_{i=1}^{n} S_{s_i} \qquad \text{(Eq. 4.5)}$$

where *A* is the total surface area sampled, *n* is the number of thermo-mechanically dominant summits present in the area sampled and S_{s_i} is the area of an individual thresholded summit.

The inhomogeneous and complex nature of the interface topography amongst specimens requires the heightmaps to be thresholded at the same height for all specimens ($i.e. h = nSz\ where\ 0 \leq n \leq 1$), which must be a percentage of the maximum height of the distribution (S_z), using an extended maxima transform (MorphoLibJ plugin, ImageJ). In essence, thresholding the summits in this manner reveals information about the morphology, width and area of each individual summit (S_{s_i}) at the thesholded height. When extrapolated to a larger scale, it can be used as a metric to indirectly assess the degree of BC tortuosity capable of affecting the TBC microstructure since the overall curvature of the summit is associated with its diameter at the thresholded height. It is important to note that the conversion between S_a and the S_{sth} parameters is not possible, as these parameters do not take the same topographical features into account. Nevertheless, both parameters can be used concurrently for a more comprehensive characterisation of the topography, as exemplified herein. It is also noteworthy that the use of the S_{sth} parameter to compare different topographies is limited by the variation amongst the respective S_z values. The work in this chapter has confirmed that S_z variations up to two-fold are still within the acceptable range to establish an effective comparison.

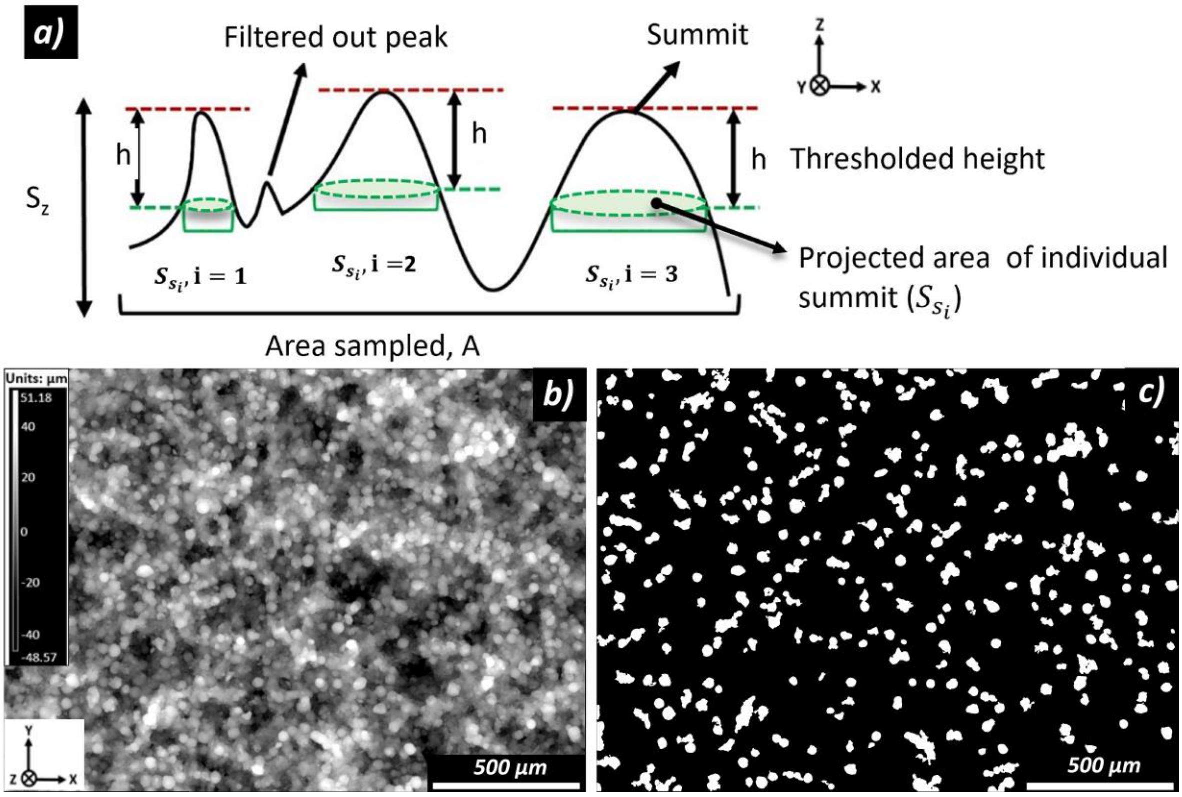
a)
Filtered out peak
Summit
Z
Y
X
h
h
h
Thresholded height
S_z
S_{s_i}, i = 1
S_{s_i}, i =2
S_{s_i}, i = 3
Projected area of individual summit (S_{s_i})
Area sampled, A
Units: µm
51.18
40
20
0
-20
-40
-48.57
b)
Y
Z
X
500 µm
c)
500 µm

Figure 4.1 (a) Cross sectional representation of the summit thresholding procedure using an extended maxima transform with equivalent thresholded height *h*; (b) A post-processed 8-bit grayscale heightmap of a high lifetime specimen and (c) respective thresholded heightmap revealing the morphology and projected area of the digitally sectioned summits.

4.3. Results and discussion

4.3.1 TBC system lifetime and oxidation kinetics evolution

Fig. 4.2-a) shows the experimental TCF lifetime of the TBC specimens, wherein the lifetime was normalised with respect to the highest lifetime (L_f) and plotted as a function of specimen ID. Each data bar represents the average life fraction value of eight specimens and the error bars represent the respective standard deviation. Specimens were categorised according to their lifetimes, with two Co-based HVOF TBC systems showing the highest lifetimes ($L_f \geq 0.8$), one Ni-based HVOF system showing the lowest lifetime ($L_f \leq 0.3$) and all the remaining specimens displaying medium lifetimes ($0.4 \leq L_f \leq 0.6$).

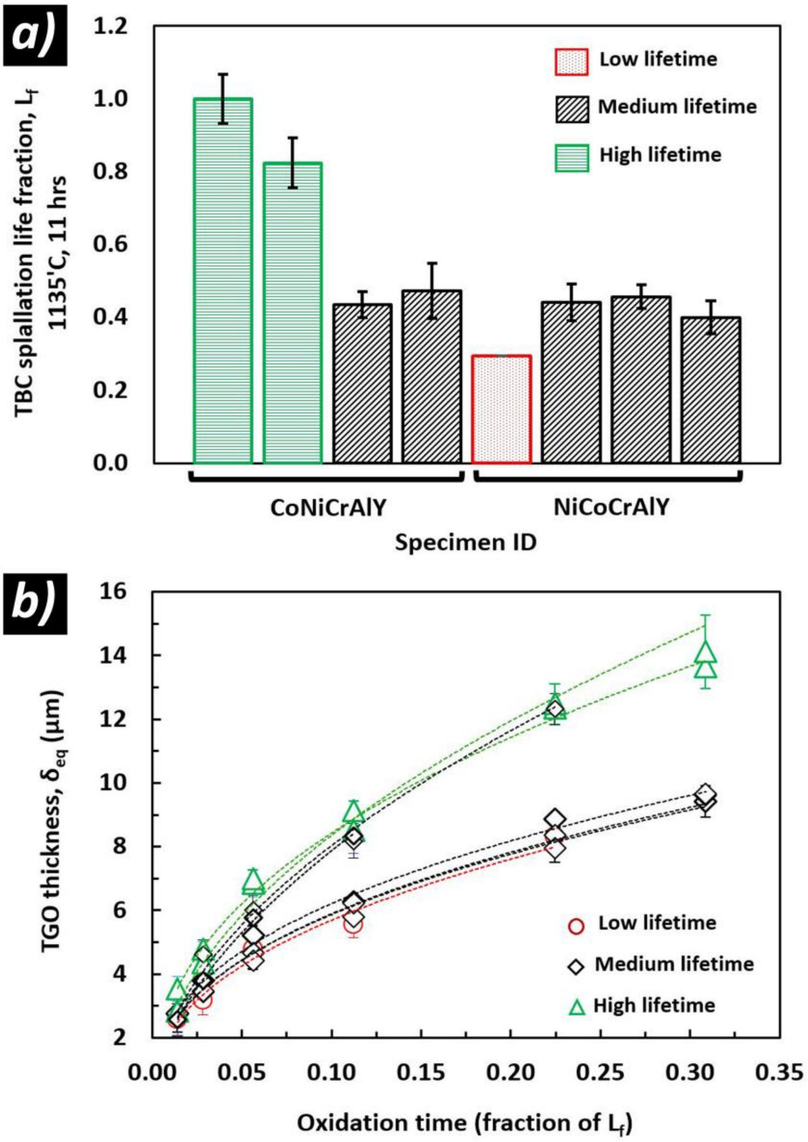

Figure 4.2 (a) Normalised TBC lifetime for the different MCrAlY systems as a function of specimen ID; (b) equivalent TGO thicknesses plotted as a function of oxidation time.

The equivalent TGO thickness (δ_{eq}) for each specimen type was determined according to the methodology described in section 4.2.1 and plotted as a function of oxidation time in Fig. 4.2-b). A least squares power-law fit was performed for each dataset ($R^2 \geq 0.96$) and revealed that the TGO growth follows the typical parabolic function (i.e. $\delta^2 = 2k_pt$) mentioned in the literature for similar TBC systems [12, 141, 180]. The parabolic constant value range obtained for the Ni- ($1.69x10^{-13} \leq k_p \leq 1.76x10^{-13} m^2.h^{-}$) and Co-based ($3.83x10^{-13} \leq k_p \leq 4.28x10^{-13} m^2.h^{-1}$) chemistries are shown in table 4.2 and provided quantitative evidence that specimens with higher lifetime displayed a faster TGO growth rate. This is contrary to the well-established and targeted slower oxide scale growth trend often considered as beneficial for achieving higher TBC lifetime [4, 12, 141, 180].

Table 4. 2 Parabolic rate constant determined for all the specimen types.

Specimen ID	**Parabolic constant, k_p ($m^2.h^{-1}$)**	**TBC spallation life fraction, L_f (a.u.)**
Co HVOF S	3.83 x10^{-13}	1
Co HVOF M	4.13 x10^{-13}	0.83
Co APS M	4.28 x10^{-13}	0.44
Co APS L	4.10 x10^{-13}	0.47
Ni HVOF S	1.69 x10^{-13}	0.29
Ni HVOF M	1.75 x10^{-13}	0.44
Ni APS M	1.76 x10^{-13}	0.46
Ni APS L	1.76 x10^{-13}	0.40

The slow TGO growth rate observed for the Ni-based chemistry was mainly attributed to a higher as-deposited Al-content in the BC (20.3≤ Al at.% ≤22.0%) and to the addition of reactive elements Y and Hf. Such near-interface Al-content promoted the formation of a dual-phase structure with high β-phase content (≈ 51.20%), as depicted in Fig. 4.3-a), that was more conducive to the formation of an almost exclusive and homogeneous Al_2O_3 scale. However, variable quantities of Y (≤ 4.6 at.%) and Hf (≤ 0.8 at.%) were detected in the BC inner oxides and TGO scale, as exemplified in the inset image in Fig. 4.3-a). As Y^{3+} and Hf^{4+} are known to diffuse along phase and grain boundaries of MCrAlY alloys and TGO scales [81, 128], it is highly likely that they have contributed to a reduction in the oxygen transport kinetics through the TGO scale grain boundaries due to a site-blocking mechanism, as proposed by Wu et al. [128] and observed by Unocic et al. [227]. On the other hand, even though the lower Al-content in the Co-based BC (14.3≤ Al at.% ≤16.1%) was still sufficient to form a dual-phase microstructure, this resulted in a much lower content of β-phase (≈ 19.74%), as illustrated by Fig. 4.3-b). The predominance of Al-poor γ-phase at the BC surface combined with a high Al-flux at the *γ/β* grain boundaries during the transient oxidation stage [146] is believed to have resulted in formation of less protective non-Al oxides clusters and outer scale that slowly de-stabilised the TGO scale. This is in good agreement with early microstructural observations shown in the inset image of Fig. 4.3-b), where the formation of mixed oxide clusters and Cr-rich TGO outer scale is already noticeable at around 0.03 L_f, long before Al-depletion is observed.

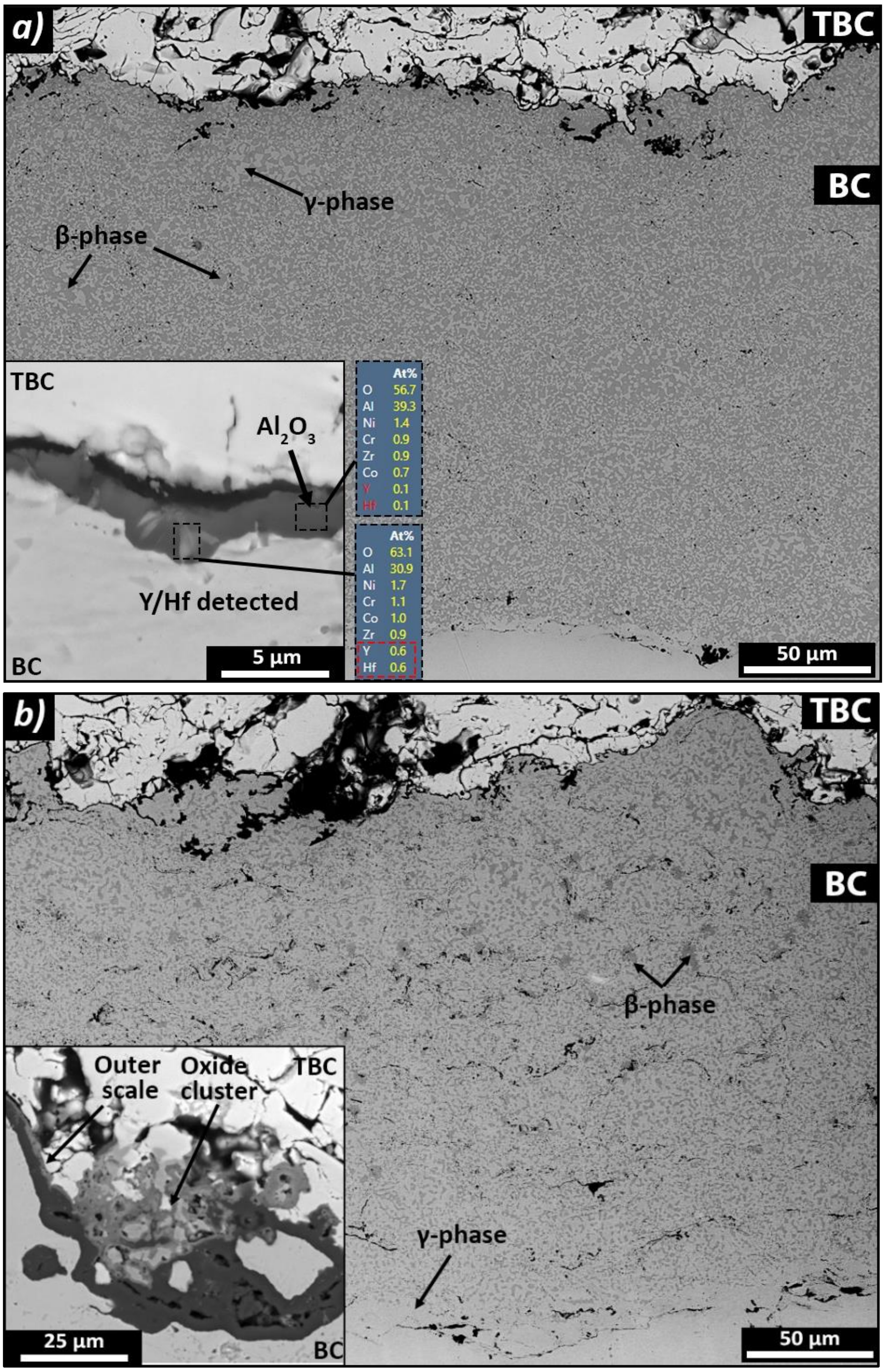
a)
TBC
BC
γ-phase
β-phase
TBC
Al_2O_3
Y/Hf detected
BC
5 µm
50 µm
b)
TBC
BC
β-phase
Outer scale
Oxide cluster
TBC
γ-phase
25 µm
BC
50 µm

	At%
O	56.7
Al	39.3
Ni	1.4
Cr	0.9
Zr	0.9
Co	0.7
Y	0.1
Hf	0.1

	At%
O	63.1
Al	30.9
Ni	1.7
Cr	1.1
Co	1.0
Zr	0.9
Y	0.6
Hf	0.6

Figure 4.3 Backscattered-electron (BSE) micrograph of a Ni-based (a) and Co-based (b) specimens where the as-deposited microstructure is depicted; the inset in Fig. 4.3-a) shows a region where the incorporation of Y and Hf in the NiCoCrAlY-HfSi TGO scale was detected whereas, the inset in Fig.4. 3-b) illustrates the presence of a mixed oxide cluster and Cr-rich outer scale in the CoNiCrAlY system.

A complementary microstructural and compositional analysis of the failure plane was carried out using a combination of GIXRD, SEM and EDS techniques and compiled in Fig. 4.4 with the purpose of understanding the oxide scale morphology and composition at the failure plane.

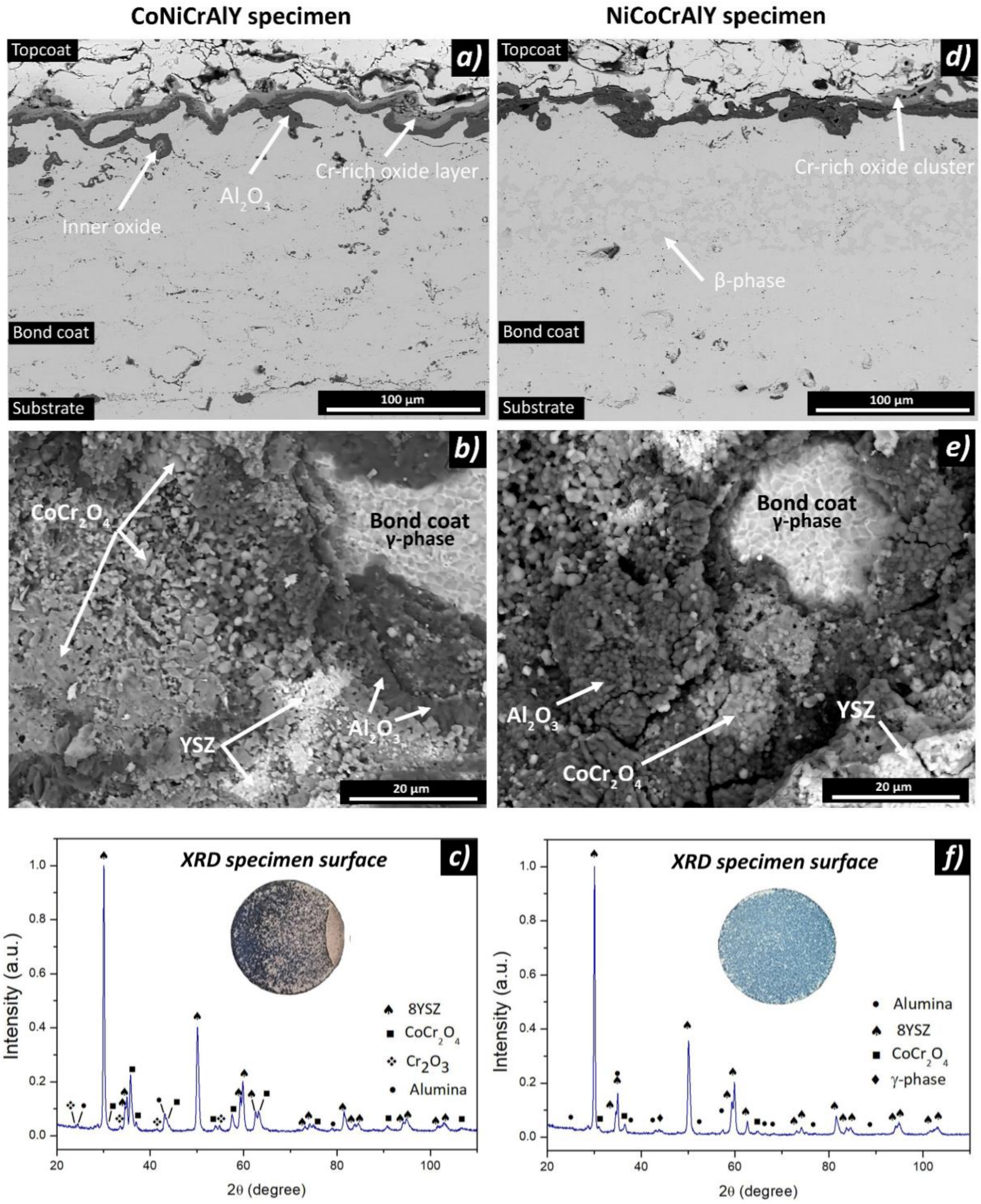
CoNiCrAlY specimen
NiCoCrAlY specimen
Topcoat
a)
Cr-rich oxide layer
Al_2O_3
Inner oxide
Bond coat
Substrate
100 µm
Topcoat
d)
Cr-rich oxide cluster
β-phase
Bond coat
Substrate
100 µm
b)
$CoCr_2O_4$
Bond coat
γ-phase
YSZ
Al_2O_3
20 µm
e)
Bond coat
γ-phase
Al_2O_3
YSZ
$CoCr_2O_4$
20 µm
XRD specimen surface
c)
Intensity (a.u.)
1.0
0.8
0.6
0.4
0.2
0.0
20
40
60
80
100
2θ (degree)
8YSZ
$CoCr_2O_4$
Cr_2O_3
Alumina
XRD specimen surface
f)
Intensity (a.u.)
1.0
0.8
0.6
0.4
0.2
0.0
20
40
60
80
100
2θ (degree)
Alumina
8YSZ
$CoCr_2O_4$
γ-phase

Figure 4. 4 Cross-sectional SEM micrograph of the microstructure of a Co-based BC (a) and a Ni-based BC (d) medium lifetime specimens after 0.22 L_f. Representative micrograph of the Co-based (b) and Ni-based BC (e) failure plane morphology and composition of the major isostructural species found for each composition determined by GIXRD (c) and (f), respectively.

Analysis of Fig. 4.4-b) and c) show that Co-based BC specimens have a larger presence of Cr-rich oxides (i.e. Cr_2O_3, $CoCr_2O_4$) and a minor presence of Al_2O_3 at the failure plane, with thicker oxide clusters typically found in the trough regions. This is in good agreement with the cross-sectional analysis, which revealed the presence of a Cr-rich outer scale in the continuous duplex TGO layer along the interface, as illustrated in Fig. 4.4-a). Conversely, Figs. 4.4-e) and f) show that the Ni-based BC counterparts followed an opposite trend, with the formation of a TGO scale overwhelmingly comprised of Al_2O_3 and occasional presence of clustered Cr-rich oxides around the summit crests, as reported by Chen et al. [135] for an analogous BC composition. As similar oxidation kinetics and oxide scale compositions were observed for specimens of the same BC composition, it was concluded that the variation of deposition method and powder particle size had a less noticeable impact on their oxidation behaviour. This phenomenon might be explained by the fact that the microstructural differences originated by the deposition of a thin flashcoat layer were not enough to significantly limit Al-flux into the interface and alter the oxidation kinetics behaviour amongst similar BC chemistry specimens. Consequently, the oxidation kinetics results obtained for these specimens could not provide a satisfactory explanation for the TCF results shown in Fig. 4.2-a), indicating that the TBC spallation lifetime is being affected by another factor.

4.3.2 Impact of BC topography on the TBC lifetime

Based on the TCF lifetime results presented in section 3.1 and the BC interface characterisation, the specimens were divided into three categories, low ($L_f \leq 0.3$), medium ($0.4 \leq L_f \leq 0.6$) and high ($L_f \geq 0.8$) lifetime. In order to provide a clear visual comparison and highlight the fundamental differences between the BC surface topographies identified in this study, a representative topography heightmap and cross-sectional micrograph of each specimen category are presented in Fig. 4.5.

The BC topography of low lifetime specimens shown in Figs. 4.5-a) and d) is comprised of a low curvature "dune-like" interface with frequent presence of low-amplitude asperities (i.e. microroughness) and rare presence of larger radii summits. These interfacial features were originated by the smaller powder particle size (38/10 µm) used for the BC deposition, which improved the particle melting process and led to a less tortuous topography. According to the topographical quantitative analysis shown in Fig. 4.6, this topography can be analytically described as having low roughness (S_a= 7.1 µm), high summit density (S_{ds} = 157 summits/mm^2), high peak curvature (S_{pc} = 0.51 µm^{-1}) and lower total thresholded area (S_{sth} = 8.5 %). The medium lifetime specimen's topography presented in Figs. 4.5-b) and e) are comprised of a large number of steep and narrow convex asperities, with the occasional presence of wide and round summits. The trough areas are wide, flat and smooth, reflecting a complete absence of microroughness. These features were originated by deposition of an APS flashcoat layer where, the trough regions were formed by heavy splat flattening and the summits by rapid solidification of the splat edges. The formation of larger radii summits was infrequent and resulted from the impact of partially melted BC powder particles on the BC base layer surface. Such interfaces can be analytically described as having a moderate roughness ($8.3 \leq S_a \leq 10.7$ µm), high summit density ($144 \leq S_{ds} \leq 184$ summits/mm^2), high peak curvature ($0.53 \leq S_{pc} \leq 0.61$ µm^{-1}) and moderate total thresholded area ($8.92 \leq S_{sth} \leq 9.82$ %).

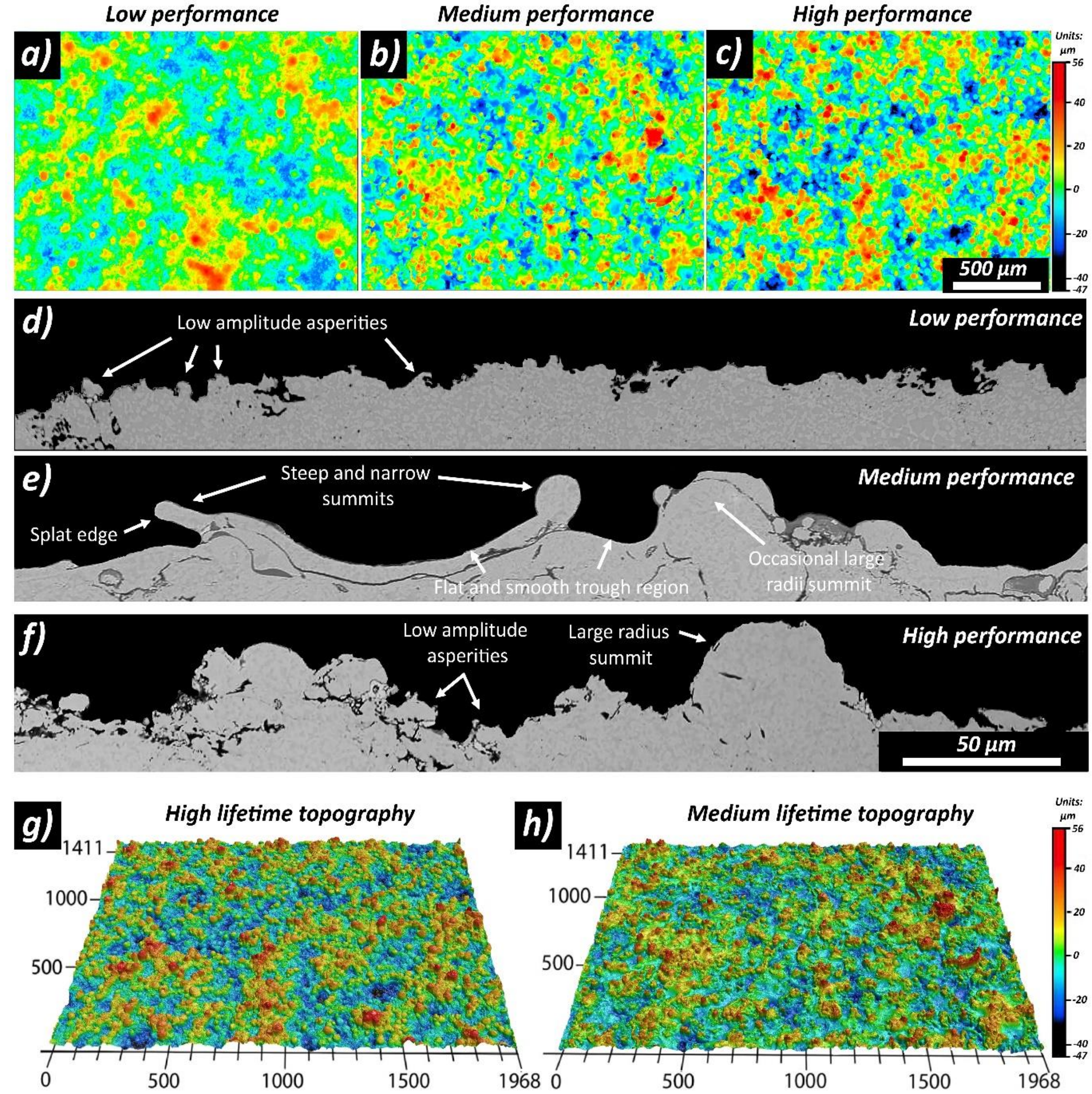
Low performance
Medium performance
High performance
a)
b)
c)
Units: µm
56
40
20
0
-20
-40
-47
500 µm
d)
Low amplitude asperities
Low performance
e)
Steep and narrow summits
Splat edge
Flat and smooth trough region
Occasional large radii summit
Medium performance
f)
Low amplitude asperities
Large radius summit
High performance
50 µm
g)
High lifetime topography
1411
1000
500
0
500
1000
1500
1968
h)
Medium lifetime topography
1411
1000
500
0
500
1000
1500
1968
Units: µm
56
40
20
0
-20
-40
-47

Figure 4. 5 Representative BC interface topography heightmaps for low (a), medium (b) and high (c) performance samples and respective cross-sectional SEM micrographs (d) (e) and (f) depicting and highlighting the different topographical features amongst lifetime categories; Three-dimensional reconstruction of a high (g) and medium (h) lifetime specimen post-processed 16 bit colour heightmap with similar S_a values yet very different BC topographies that originated contrastingly different L_f.

Fig. 4.5-(c) and (f) display an example of the interface topography of a high performance specimen that is predominantly comprised of high amplitude, wide and round convex asperities that originated from a combination of fully and partially melted powder particles. In contrast, the trough regions are considerably less tortuous but consistently populated by low-amplitude asperities. This topography can be representatively described as a high roughness ($10.6 \leq S_a \leq 13.6$ µm), lower summit density ($69 \leq S_{ds} \leq 101$ summits/mm^2), lower peak curvature ($0.23 \leq S_{pc} \leq 0.27$ µm^{-1}) and high total thresholded area ($11.53 \leq S_{sth} \leq 12.70$ %) surface topography.

Fig. 4.6 displays a compilation of all the quantitative topography data obtained in this study, wherein the TBC lifetime is plotted as a function of the (a) arithmetic mean roughness, (b) summit density, (c) arithmetic mean curvature and (d) total thresholded summit area. Fig. 4.6-a) shows a moderate positive correlation between interface roughness and TBC lifetime, in good agreement with previous literature reports [39, 118, 119]. However, when inspecting the dataset more thoroughly, it is clear that even though all medium lifetime specimens displayed very similar lifetimes, their roughness profiles varied significantly (≈23%). A similar trend was also observed amongst high L_f specimens, as a 20% reduction in roughness resulted in a 17% increase in lifetime for the lower roughness specimen. Lastly, the most noticeable discrepancy can be seen with the aid of a 3-D reconstruction of a post-processed colour heightmap of a high and medium L_f specimens displayed in Fig. 4.5-g) and h). Even though these specimens have equivalent roughness profiles analytically (S_a ≈10.3 µm), a simple visual comparison is enough to verify that the topographies are indeed very different, most likely leading to the contrasting L_f results. All these discrepancies provide strong evidence of a significant limitation in using the S_a parameter to investigate or predict the true impact of BC topography on TBC lifetime, thus strengthening similar claims made by Gupta et al. [159] and Weeks et al. [120]. As such, assessing the contribution of other surface descriptors on the TBC lifetime becomes an unavoidable necessity for a better understanding of the interfacial topography effect on lifetime.

Analysis of the of the BC topography summit density results shown in Fig. 4.6-b) revealed that high ($S_{ds} > 144$ summits/mm^2) or very low ($S_{ds} < 70$ summits/mm^2) densities are increasingly detrimental for TBC durability. Notwithstanding, a summit density in the apparent ideal range ($S_{ds} \approx 100 \pm 10$ summits/mm^2) was not sufficient to ensure higher TBC lifetimes, as specimens with similar S_{ds} values showed a significant difference in L_f. These results suggest that other topographical features might be affecting the lifetime results and therefore the arithmetic mean summit curvature was factored in the analysis, as shown in Fig. 4.6-c). Results showed that BC topographies with lower peak curvature values (i.e. wider and rounder summits) were associated with increased TBC lifetime. However, this parameter was only able to differentiate between high L_f specimens and the remaining counterparts since a clear differentiation between low and medium L_f categories was not possible. Even though the combined analysis of all ISO 25178 parameters provided solid evidence in favour of the BC topography impacting TBC lifetime, the BC interface morphological complexity made it harder for a single parameter to provide an optimal correlation with L_f.

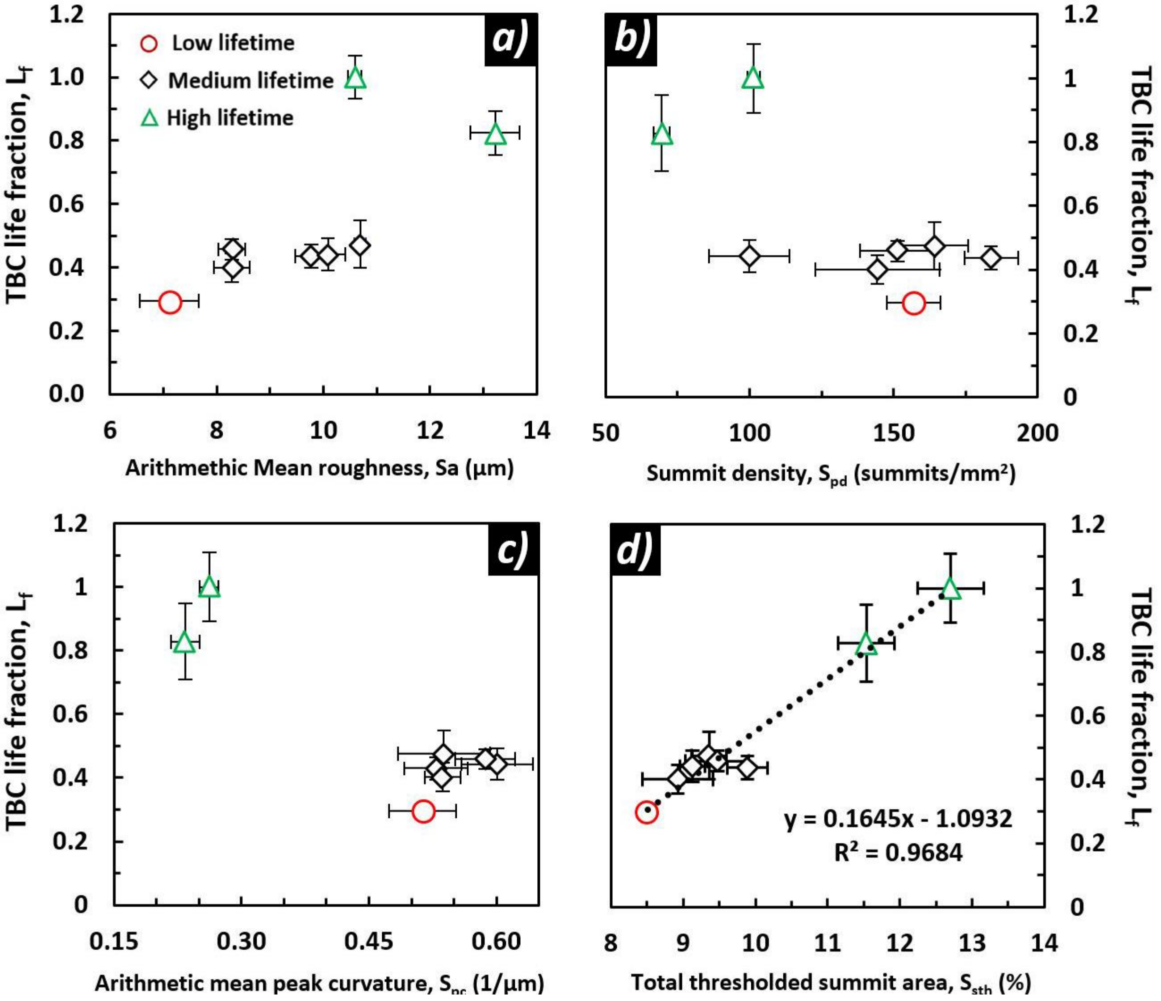

Figure 4. 6 Plot of TBC lifetime fraction as a function of (a) arithmetic mean roughness, (b) summit density, (c) arithmetic mean peak curvature and (d) total thresholded summit area of the BC interface. Higher lifetime specimens were correlated with tortuous BC topographies that displayed high roughness, lower summit density, lower peak curvature and higher total thresholded summit areas.

Since most studies in the literature have emphasised the importance of having a tortuous BC topography for enhanced mechanical interlocking [119, 120, 159], the formulation of the S_{sth} parameter is an attempt of trying to introduce a novel surface texture parameter that provides indirect insight to the degree of tortuosity of the BC surface. When plotting the TBC lifetime as a function of this parameter (Fig. 4.6-d), a least squares linear fit of the dataset revealed a positive correlation (R^2=0.97) between the two variables. The higher S_{sth} values obtained were attributed to a reduction in detrimental topographical features (i.e. steep, narrow and irregularly shaped summits) in favour of an increase in more beneficial features such as broader and more homogeneous summits, as illustrated by Fig. 4.5. Inexorably, these changes in individual summit morphology led to an increase of the individual summit threshold area (S_{si}) and by extension on the overall tortuosity of the BC interface, thus yielding higher S_{sth} values. These changes in the BC interface tortuosity can be further confirmed when comparing figures 4.5-a), -b) and -c) with reference to a common height scale bar, as the noticeable increase in adjacent higher (red) and lower (blue) relief regions is indicative of a sharp height variation over a relative short distance. Moreover, the good correlation between S_{sth} and lifetime also opens up the possibility of using this parameter as an empirical model for lifetime prediction purposes on TBC systems with non-extreme oxidation kinetics behaviour.

The previous analysis made it possible to conclude that interface topographies with a moderate frequency of high-amplitude large radii summits and a persistent presence of microroughness in the trough regions proved to be highly beneficial in achieving improved TBC durability. Therefore, the evidence obtained herein suggests that the TBC lifetime of plasma-sprayed coatings is undeniably associated with the ratio of beneficial to detrimental BC interface morphological features. The means by which these features affect the adjacent TBC microstructure and respective mechanical properties is assessed in the following section.

4.3.3 BC topography-induced microstructural changes in the TBC

The APS topcoat microstructure obtained in this study was comprised of a characteristic splat-like morphology with the presence of frequent microstructural defects (i.e. inter-splat separations, intra-splat cracks and globular pores), as shown in Fig. 4.7. As all the YSZ coatings in this study were deposited under the same processing parameters and atmospheric conditions, no significant differences should be observed in the topcoat microstructure of different specimen types, unless the BC topography played a role in the microstructural alterations of the TBC. However, a very significant variation of the TBC microstructure was observed along the BC interface in the form of altered splat curvature around the summits. Fig. 4.7 shows a representative BC/TBC interface region of a low (a), medium (b) and high (c) lifetime specimen in the as-deposited condition, where the main microstructural differences originated from deposition of the topcoat over different topographies are highlighted. Since splat curvature was qualitatively identified as a feature of interest in the analysis of the splat morphology, its average curvature around the summits was determined (Kappa plugin, ImageJ) and plotted against the TCF lifetime on Fig. 4.7-d). A least squares linear fit of the dataset revealed a positive correlation between splat curvature and TBC lifetime, meaning that TBC coatings with overall higher splat curvature morphology achieved higher TCF lifetimes.

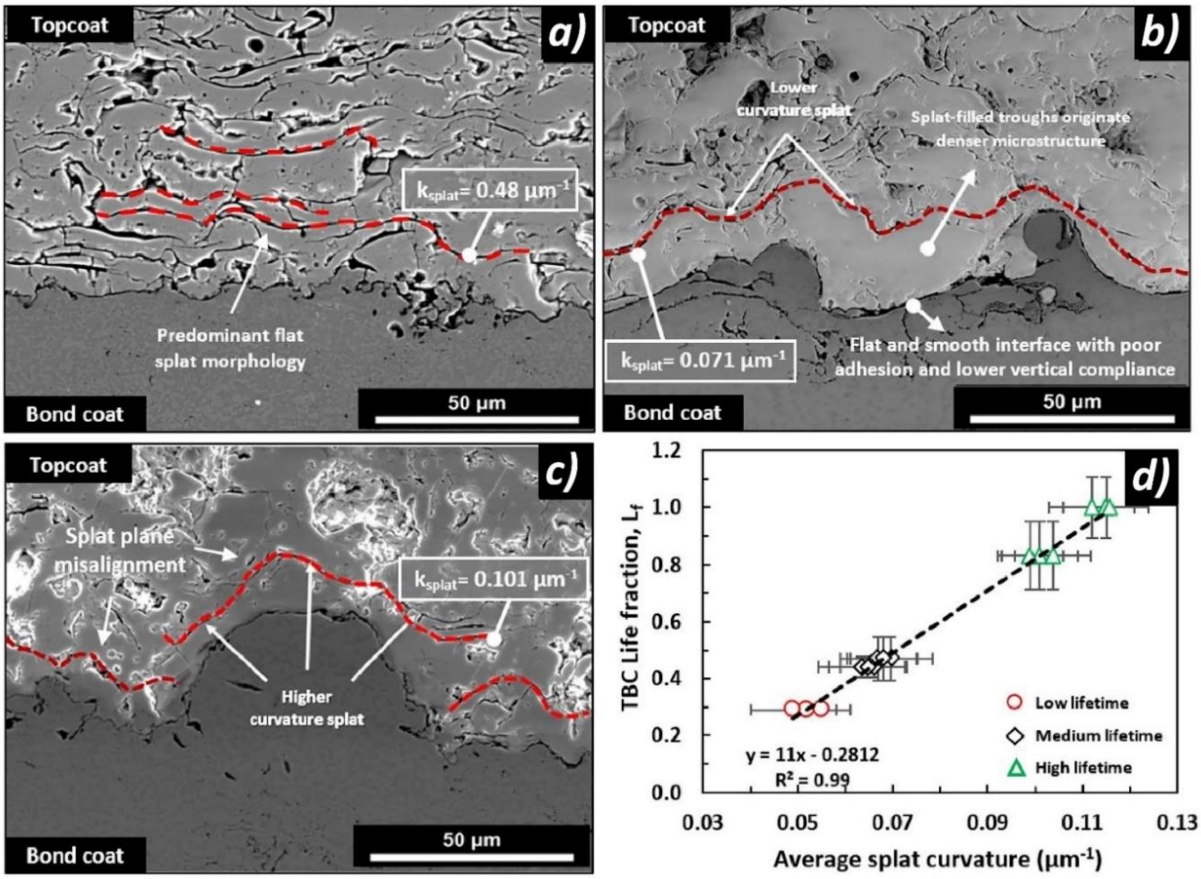

Figure 4. 7 Representative SEM micrographs of the microstructural features of a (a) low, (b) medium and (c) high performance specimens in the as-deposited condition, where the different splat morphologies configurations obtained are highlighted; (d) Plot showing the positive correlation between TBC lifetime and average splat curvature (κ_{splat}).

As can be seen in Fig. 4.7-a), deposition over less tortuous BC topographies resulted in a predominant elongated flat splat morphology with lower curvature ($0.049\pm0.009 \leq \kappa_{splat} \leq 0.055\pm0.006$ µm^{-1}) in the vicinity of the BC/TBC interface. The lack of higher amplitude asperities at the interface reduced the lateral constraint of the impinging droplets, promoting a higher degree of spreading and originating a longer and thinner splat morphology [55, 225, 226]. As the topcoat formation is driven by successive droplet impacts, the resulting morphology originated a stack of low curvature splats. From a fracture mechanics standpoint, the alignment of inter-splat separations in parallel to the BC interface creates a less tortuous crack path that is more conducive to earlier coalescence of cracks and delamination of the TBC [118, 120, 183].

Coatings deposited over medium lifetime topographies (Fig. 4.7-b) displayed an overall similar but slightly higher splat curvature ($0.064\pm0.009 \leq \kappa_{splat} \leq 0.070\pm0.009$ µm^{-1}), ensuing from a different formation mechanism. As the summits observed for these systems were steeper and narrower with large flat trough regions between them, the first wave of impinging droplets filled the trough regions, consequently offsetting the BC topography to the approximate height of the summits and rendering the initial interfacial topography features almost non-existent. The next wave of droplets impacted on relative flat surface formed by a combination of existing splats and summit crests, resulting in a potential crack path alignment within the same plane, similarly to what was reported by Weeks et al. [120]. Notwithstanding, a significant number of higher curvature splats were still observed for these specimens, likely contributing to the slightly higher lifetime observed.

In contrast, the coatings deposited over high lifetime topographies generated a highly tortuous wave-like splat morphology, where splats forming over large radii summits displayed higher curvatures ($\kappa_{splat} \geq 0.099 \pm 0.007\ \mu m^{-1}$). In contrast, splats formed in the trough regions showed a lesser degree of tortuosity and moderately larger spread. The predominant high amplitude and radii summit morphology promoted a misalignment of the overall plane defined by the inter-splat separations between the first and second layer of splats (i.e. potential crack path), thus creating the wave-like morphology seen in Fig. 4.7-c). Inexorably, a tortuous and longer potential crack path was formed, thereby increasing the potential for delayed crack coalescence and theoretically making these coatings more resistant to delamination [120].

4.3.4 Effect of TBC local and global in-plane elastic modulus

Fig. 4.8-a) shows the representative load-displacements curves obtained from micro-indentation for the low, medium and high lifetime topography specimens in the as-deposited condition. This plot illustrates the different deformation behaviours observed for each specimen category, effectively showing that the BC topography-induced changes in TBC microstructure have an impact on the TBC compliance. The higher lifetime specimens showed a larger displacement and therefore a more compliant behaviour. The TBC lifetime was then plotted as a function of the in-plane elastic modulus (E_{ind}) in Fig. 4.8-b) and an inversely proportional relationship ($R^2 = 0.96$) was obtained. The selection of the local in-plane modulus over the global modulus measured by three-point bending was related to being able to measure the local TBC properties whilst under substrate constraint. The trend in Fig. 4.8-b) indicates that a 35% variation in the elastic moduli between the low ($E_{ind} = 95.31 \pm 3.96$ GPa) and high ($60.33 \pm 3.66 \leq E_{ind} \leq 64.40 \pm 2.96$ GPa) lifetime specimens results in a three-fold lifetime increase (≈70%). These findings are in very good agreement with a numerical model proposed and experimentally validated by Vaβen et al.[178], which showed that an increase in the TBC elastic modulus (i.e. 18 to 28 GPa, ≈36%) led to a considerable reduction in lifetime (≈65%). Therein, it was argued that more compliant TBC microstructures showed more efficient stress relaxation mechanisms and therefore achieved higher lifetimes. An analogous phenomenon is believed to have been responsible for our findings, as the enhanced strain compliance observed for the lower moduli specimens in all stages of thermal exposure might have promoted more effective stress relaxation mechanisms that delayed the onset of large scale crack propagation.

Indentation measurements of heat-treated specimens showed that the local in-plane modulus around the interface region increased with oxidation time as a result of sintering of the ceramic topcoat, in good accordance with the literature [228-230]. The rate of increase in the elastic modulus obtained was analogous to the ones in the literature [46, 228, 229, 231] and followed a similar logarithmic trend for all specimens, as shown in Fig. 4.8-c). These results are quite significant as they confirm that TBC sintering occurs predominantly in the earlier stages of thermal exposure and the as-deposited elastic moduli differences measured were maintained as oxidation time increased. This means that the higher lifetime specimens' increased compliance will be playing a differentiating role in the relaxation of the thermal mismatch stresses during the whole thermal exposure time [178]. This is especially relevant in the late stages of oxidation, as TBC sintering exacerbates the magnitude of the thermal mismatch stresses by an estimated factor of two [173].

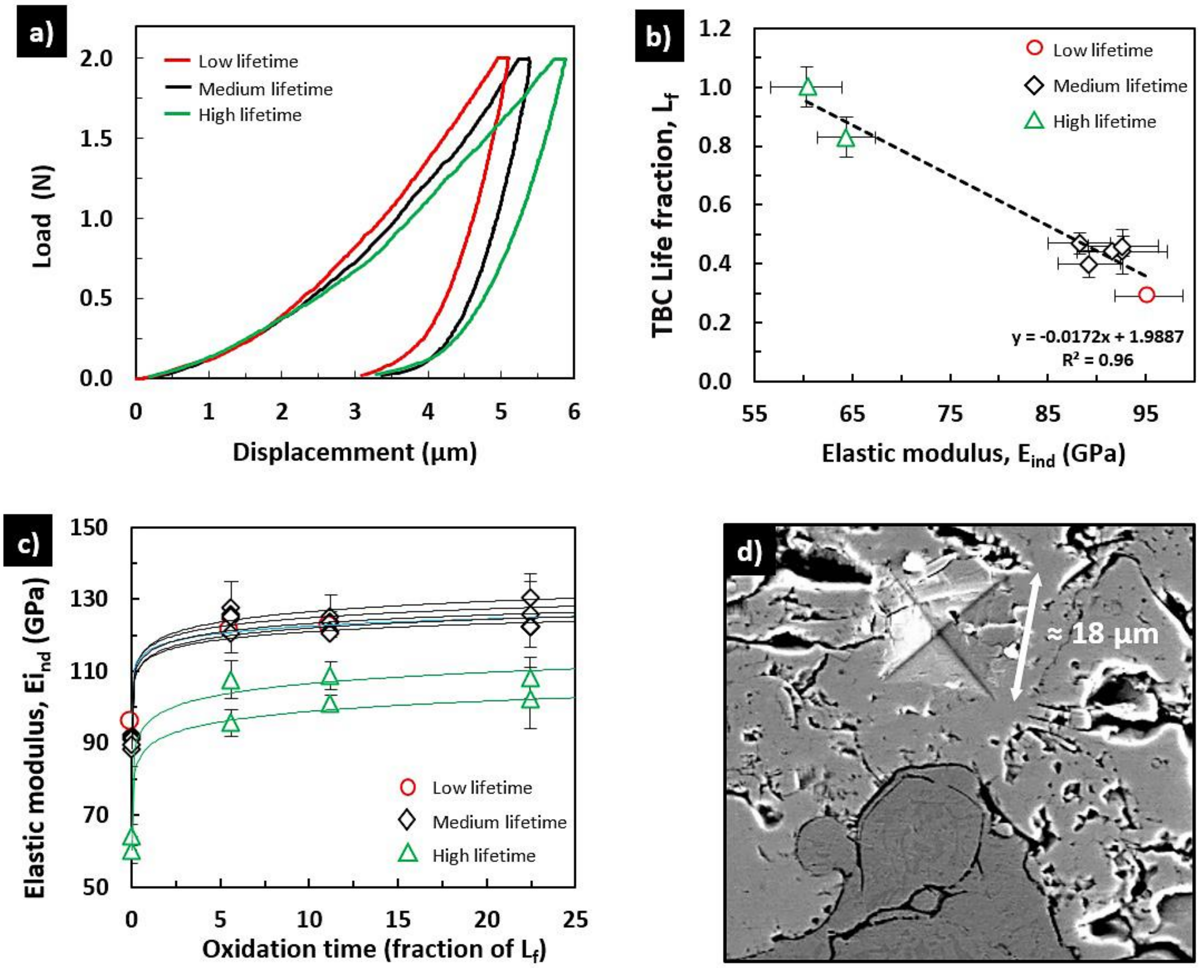

Figure 4. 8 (a) Representative load-displacement compliance curves for the low, medium and high lifetime specimen categories; (b) Plot displaying the correlation of local in-plane elastic modulus with TCF lifetime for all different BC-topographies; (c) Plot showing the evolution of the indentation

modulus with oxidation time, wherein the TBC sintering rate is described by a logarithmic least squares regression fit; (d) SEM micrograph showing a representative indentation of the TBC in the vicinity of the interface.

The as-deposited global in-plane elastic modulus of detached TBC coatings was determined by three-point bending for all specimen types to ascertain if the BC topography also affected the global mechanical properties of the TBC. The cyclic loading results obtained for the underside of the coating (BC/TBC interface in compression) were compiled in Fig. 4.9-a), wherein a negative correlation between the global in-plane elastic modulus (E_{gi}) and TCF lifetime was identified. The E_{gi} values obtained were within the data range reported in the literature [224, 228, 231-233], ranging from 4.05±0.29 $\leq E_{gi} \leq$ 4.41±0.34 GPa on the higher lifetime coatings to 6.92±0.18 GPa $\leq E_{gi} \leq$ 7.77±0.24 GPa on the medium and 9.01±0.29 GPa and lower lifetime counterparts. A comparison between the global and local in-plane elastic moduli trends shows the same inversely proportional relationship with TCF lifetime, thereby providing unambiguous evidence that the global in-plane modulus is also affected by the topography-induced TBC microstructural changes. However, in an effort to investigate if the aforementioned effect extended through the entire coating thickness due to the successive splat stacking nature of the coating formation, the same cyclic loading bending procedure was additionally performed on the topside of the ceramic coating (i.e. TBC surface). The resulting elastic modulus values obtained ranged from 6.06 GPa $\leq E_{g\ \mathrm{topside}} \leq$ 9.76 GPa and were approximately 10 to 33% higher than the respective interface values (4.05±0.29 GPa $\leq E_{gi} \leq$ 9.01±0.29 GPa), with the variation being less apparent for the stiffer coatings. A similar trend was observed for the medium lifetime specimens but the curves were omitted in Fig. 4.9-b) in the interest of visual clarity. The same figure shows that the elastic region slope of the load-displacement curve is steeper when loading on the topside, meaning that when the interface is under tension, the TBC offers more resistance to deformation. This can be interpreted as evidence of a variation in elastic modulus across the TBC thickness that is likely originated by differences in the local microstructure and different degrees of TBC stress relaxation mechanisms (i.e. like inter-splat sliding, intra-splat closure and microcracking). These microstructural and mechanical differences can also be seen as evidence in favour of a gradient across the TBC thickness. In addition to this, all topside load-displacement curves showed a smaller elastic recovery and a higher inelastic stored strain energy upon unloading. This constitutes further evidence that the TBC microstructure is indeed stiffer near the BC/TBC interface than at the top surface. This phenomenon has been previously noted by Eldrige et al. [234] and Choi et al. [233] at NASA Glenn Research Centre but the fracture mechanics implications were not explored.

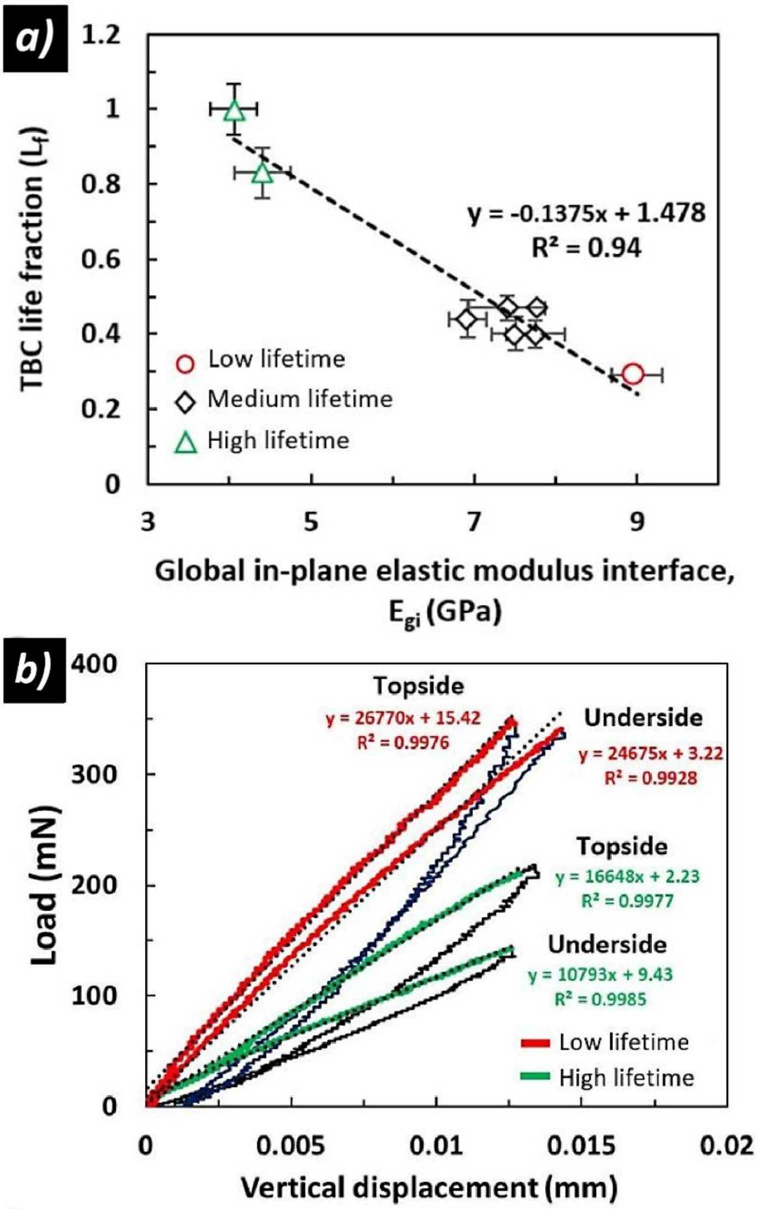

Figure 4.9 (a) Plot displaying negative correlation between the global in-plane elastic modulus and TCF lifetime for all different BC-topographies; (b) Representative load-displacement curves measured on the underside and topside of the specimens.

The experimental findings in this section strongly suggest that the topography-induced alterations of the TBC microstructure are not limited to the interface region, as the TBC coatings do not show the same deformation behaviour when loaded on different sides. The main implication of these results is that the TBC deposition over different BC topographies created distinct near-interface microstructures and resulted in local and global changes in the mechanical properties of the TBC. The impact of the microstructural and mechanical properties on the TCF fracture mechanics is analysed in the next section.

4.3.5 Effect of BC topography on fracture mechanics

As nucleation and propagation of cracks in APS TBCs generally occur in the vicinity of the BC/TBC interface [84, 118, 166, 183, 222, 223], all the BC topography-induced alterations in the topcoat reported herein are expected to have a significant impact on TCF fracture mechanics [183, 231]. A cross-sectional micrograph of the post-failure microstructure of a lower and higher lifetime specimens is presented in Figs. 4.10-a) and b), respectively, wherein the predominant failure mechanisms that led to delamination are highlighted. Complementary to this, a comprehensive top view quantitative image analysis of the delamination surface was conducted on five BSE SEM micrographs for each specimen type in Figs. 4.10-c) and d), effectively covering an overall area of 16.5 mm^2 for statistical significance. The compositional ratios of this analysis were then compiled and presented in Fig. 4.10-e).

Delamination in high lifetime specimens was primarily attributed to the enlargement of pre-existent inter-splat separations (type III cracks), that eventually coalesced with cracks nucleated at the TGO/TBC interface (type II cracks), in good accordance with the mixed failure mechanisms commonly reported in the literature for high roughness APS systems [23, 188, 235]. The cross-sectional analysis revealed that the delamination crack path followed the higher curvature splat morphology as a result of the enhanced mechanical interlocking induced by the BC tortuosity, ultimately shifting the failure plane away from the interface, as shown in Fig. 4.10-b). Additionally, top view image analysis of the delamination surface (Fig. 4.10-d) revealed a larger presence of YSZ ($66.41 \pm 1.25 \leq Area_{TBC} \leq 69.80 \pm 1.71\%$) and a reduced presence of TGO ($29.91 \pm 1.78 \leq Area_{TGO} \leq 33.59 \pm 0.76\%$) at the failure plane, further corroborating that delamination occurred predominantly within the TBC for these specimens. These findings are consistent with the observations of Eriksson et al. [118], who have reported that TBC systems with higher interfacial roughness and TBC durability tend to show a larger fraction of TBC at the failure plane due to enhanced BC/TBC adhesion strength [65]. An explanation for this phenomenon was later proposed by Eriksson et al. [188], who demonstrated via FE crack growth modelling that the effective stress intensity factor (K_{eff}) decreases for cracks propagating within the TBC as the distance from the interface increases. In essence, this means that such crack configuration is conducive to a reduction on the crack driving force and delayed coalescence of pre-existent cracks, effectively delaying the delamination of the TBC and increasing the durability of the system. This could be a direct consequence of the local TBC microstructure alterations observed in the vicinity of the interface that were caused by deposition over tortuous topographies. The extent to which the splat morphology, inter-splat separation and intra-splat segmentation density affect the TBC system fracture mechanics was explored in chapter 5.

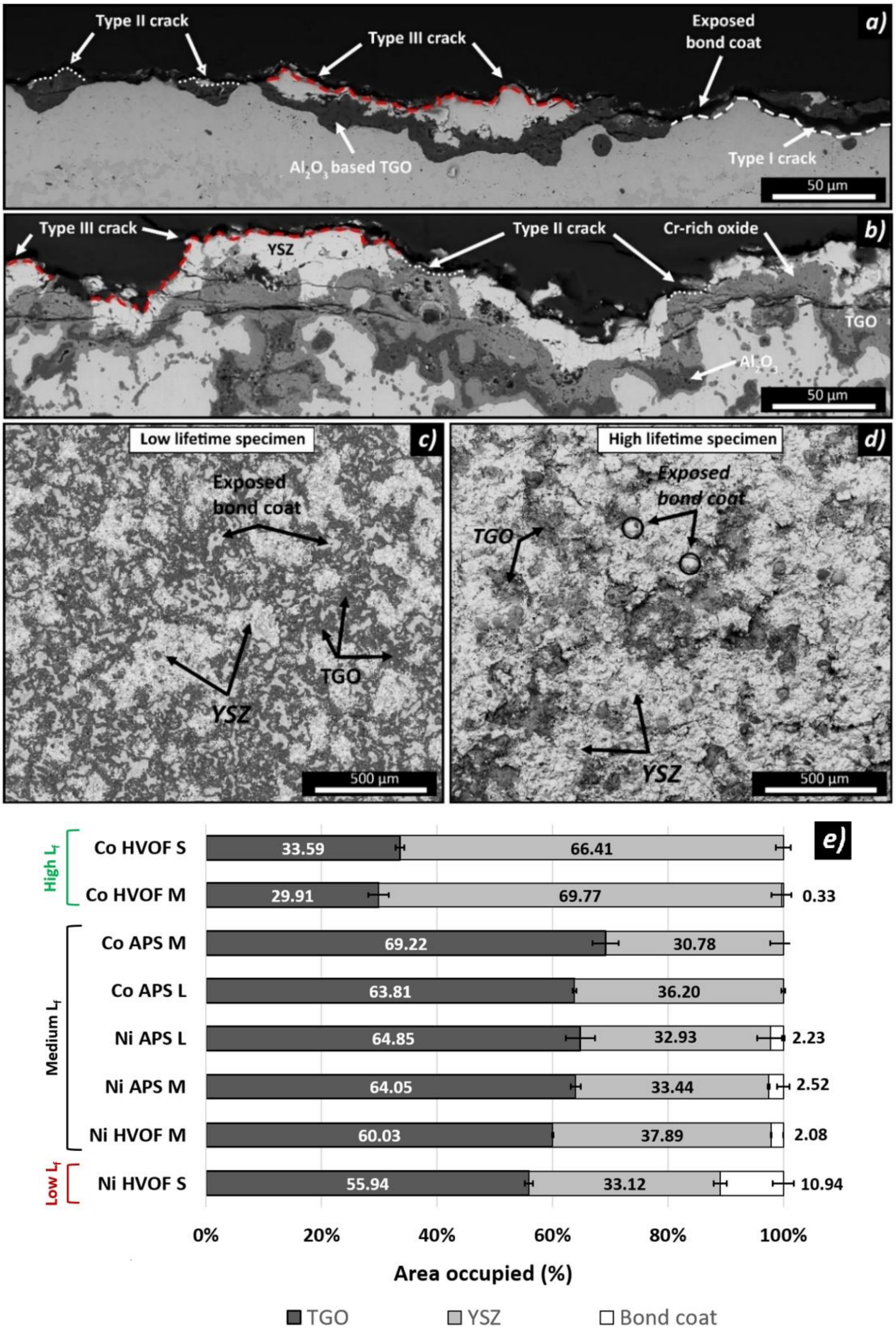
a)
Type II crack
Type III crack
Exposed bond coat
Al$_2$O$_3$ based TGO
Type I crack
50 µm
b)
Type III crack
YSZ
Type II crack
Cr-rich oxide
TGO
Al$_2$O$_3$
50 µm
c)
Low lifetime specimen
Exposed bond coat
YSZ
TGO
500 µm
d)
High lifetime specimen
Exposed bond coat
TGO
YSZ
500 µm
e)
High L$_f$
Co HVOF S 33.59 66.41
Co HVOF M 29.91 69.77 0.33
Medium L$_f$
Co APS M 69.22 30.78
Co APS L 63.81 36.20
Ni APS L 64.85 32.93 2.23
Ni APS M 64.05 33.44 2.52
Ni HVOF M 60.03 37.89 2.08
Low L$_f$
Ni HVOF S 55.94 33.12 10.94
0% 20% 40% 60% 80% 100%
Area occupied (%)
▪ TGO
▨ YSZ
☐ Bond coat

Figure 4.10 BSE SEM micrographs of the post-failure cross-section of a low (a) and high (b) lifetime specimens, wherein the main failure mechanisms are highlighted; Top view of the failure plane of a the (c) low and (d) high lifetime specimens displaying the BSE SEM image contrast that allowed for the (e) quantification of the different species found at the failure plane.

In contrast, the low and medium lifetime specimens displayed a delamination behaviour that was dominated by type II cracking at the low-amplitude summit crests, which exposed a larger fraction of the TGO at the failure plane ($60.03 \pm 0.1 \leq Area_{TGO} \leq 69.22 \pm 2.3$ %), as evidenced by Figs. 4.10-a) and –c). As thermal exposure time progressed, these cracks coalesced with cracks nucleated at the trough regions of the TBC, eventually exposing a significant portion of the TBC at the failure plane ($30.78 \pm 2.3 \leq Area_{TGO} \leq 37.89 \pm 0.1$ %), and leading to the delamination of the TBC, as depicted in Fig. 4.10-a). In addition, as a result of the overall flatness of the BC/TBC interface and gradual TGO thickening, the lower lifetime specimens also saw a significant contribution of cracks nucleated at the BC/TGO interface (type I cracks) to the delamination ($Area_{BC} \approx 10.94\%$). These observations strongly suggest that this crack configuration is associated with higher elastic moduli and a low curvature splat morphology. A comprehensive assessment of crack configurations in TBCs conducted by Eriksson et al. [188] showed that the effective stress intensity factor *(K_{eff})* increases as the delamination crack approximates the interface and the adhesion strength decreases [65], ultimately leading to a faster crack propagation speed and accelerated crack coalescence [188]. This is in good agreement with our observations, as specimens that have displayed this type of crack propagation behaviour have also showed a significantly lower TBC durability.

The observed failure mechanisms provide supporting evidence in favour of the hypothesis that the BC tortuosity has an impact on the fracture mechanics of the TBC system. The BC topography-induced alterations in the TBC microstructure and mechanical properties (i.e. splat morphology curvature, elastic modulus) played an important role in changing the failure mechanisms responsible for delamination of the TBC, ultimately affecting the crack path configuration under TCF conditions. The literature [65, 118, 120, 188] has also emphasised that the region where the cracks propagate is an important factor for TBC durability, as it is intrinsically related to the crack driving force and therefore to the rate of crack coalescence that leads to delamination of the TBC. These results have motivated a deeper investigation into the effect of BC topography on the fracture mechanics of TBC systems, laying the foundational research motivation for pursuing this in the next chapter.

4.4. Conclusions

The BC/TBC interface topography effect on the lifetime of air-plasma sprayed (APS) TBCs has been comprehensively investigated and a positive correlation has been found in the present work. An accurate quantitative description of different BC interface topographies and their correlation with lifetime was achieved when combining multiple ISO 25178 surface texture parameters such as arithmetic mean roughness (S_a), arithmetic mean peak curvature (S_{pc}), summit density (S_{ds}) with a newly proposed total thresholded summit area (S_{sth}). The novel S_{sth} parameter was the most effective surface descriptor in terms of correlation with lifetime, as it was able to quantify the contribution of the most relevant features of individual summit morphology (i.e. summit width, frequency) to the overall BC topography tortuosity. The good correlation obtained with lifetime suggests that the empirical equation obtained from the linear fitting demonstrates potential to be used as a TBC lifetime prediction tool under non-extreme oxidation kinetics conditions. The topographical and microstructural analysis of the BC interface and TBC revealed that the tortuosity of the BC topography is a crucial parameter in defining the near-interface TBC microstructure, especially the inter-splat separation curvature. Mechanical testing of as-deposited and heat-treated specimens evidenced that the aforementioned microstructural changes promoted a reduced local and global elastic moduli, effectively linking the more compliant TBC microstructures with more beneficial fracture mechanics behaviours and higher TCF lifetimes.

Chapter 5. Effect of bond coat topography on the fracture mechanics and lifetime of air-plasma sprayed thermal barrier coatings

Statement: The contents of this chapter are based on the work published in the Surface & Coatings Technology Volume 40, Issue 15.

Contributions: Hanyang Yu, Ying Chen, G. Brewster, R. McIntyre, Ping Xiao

5.1. Introduction

Thermal barrier coating systems are multi-layered thermal protection systems commonly applied to gas-turbine engine components to provide efficient insulation in high temperature oxidising environments [26, 27]. Exposure to such environments originates a variety of thermo-chemical and -mechanical degradation processes that generate large residual stresses and lead to the cyclic accumulation and release of stored strain energy [12, 27, 236]. Inexorably, this process leads to the nucleation and propagation of cracks that compromise the structural integrity and durability of the TBC system [12, 76]. The effect of these degradation mechanisms is generally counteracted by the enhancement the TBC strain compliance via incorporation of TBC microstructural defects (i.e. intra- and inter-splat crack networks) [66, 236] and improvement of the interfacial adhesion via manipulation of the bond coat (BC) topography [65, 118, 202].

Several studies have investigated the adhesion of metal/ceramic interfaces using a myriad of techniques such as tensile [62, 63, 214], compressive [237, 238], indentation [62, 239], barb pull-out [240, 241] and bending tests [176, 212, 242-247]. However, as the crack propagation behaviour in TBCs is highly dependent on the loading conditions at the crack tip, the selection of the test method should be representative of the thermal cycling fatigue (TCF) mixed-mode loading conditions. The four-point bending experiment proposed by Charalambides et al. [248, 249] and modified by Hofinger et al.[212] has proven effective in reproducing such conditions, as the crack segmentation suppression geometry maximises the TBC stored strain energy and promotes near-interface crack propagation [204, 212]. This technique was used by Yamazaki et al. [245, 250] and Théry et al. [176] to investigate the delamination resistance of APS and EB-PVD TBC systems as a function of thermal exposure time, respectively. Zhao et al. [204] conducted a similar investigation on APS TBC interfacial fracture toughness evolution with thermal exposure time and attributed the increase in energy release rate observed (50 to 120 J.m^{-2}) to TBC sintering, in good accordance with previous results from Choi et al. [59].

Most bending studies performed on APS systems [204, 245, 246, 250, 251] have consistently focused on investigating the interfacial delamination resistance under different thermal exposure conditions.

Only a single study conducted by Yamazaki et al. [245] has looked into the effect of the interfacial roughness (R_a) on the TBC fracture toughness but was unable to find sufficient evidence in favour of a correlation. However, these findings can be explained by the lack of bond coat (BC) interfacial roughness variety amongst specimens ($\Delta R_a = 0.8\mu m$), and limitations of the two-dimensional cross-sectional roughness characterisation technique utilised [62]. In contrast, an interfacial indentation test conducted by Hadad et al. [62] showed that increasing the interfacial roughness (R_a) from 2.7 to 5.6 µm on a 0.3 mm Al_2O_3 APS coating resulted in an interfacial toughness reduction. Similarly, Lima et al. [63] also reported that lower interfacial roughness led to enhanced adhesion in porous 8 wt.% YSZ (8YSZ) coatings following a tensile adhesion test. Also, a finite element method (FEM) investigation into the TBC fracture mechanics led by Aktaa et al. [252] demonstrated that an increase from 5 to 10 µm in interfacial roughness amplitude should originate a 60% decrease in the strain energy release rate, even when not accounting for the TBC microstructural features [252]. Another FEM study conducted by Zhang et al. [253] also demonstrated that the interface roughness has a significant impact on the strain energy release rate, interfacial stress distribution and crack propagation patterns.

Although the effect of the BC interface topography on APS coatings fracture mechanics has remained relatively unexplored thus far, the few experiments and FEM simulations conducted are suggestive of a relationship between the near-tip conditions associated with crack propagation and the BC interface topography. In addition to this, the body of work presented in chapter 4 has demonstrated that the manipulation of the BC interface topography alone was sufficient to induce alterations in the TBC microstructure and mechanical properties that had critical implications on the TBC system durability. Therefore, this study aims to evaluate if the manipulation of the BC interface tortuosity can also affect the TBC fracture toughness and the post-critical point fracture behaviour. A modified in-situ four-point bending test was utilised to determine the critical strain energy release rate (G_c) and critical stress intensity factor (K_C) whilst investigating the loading conditions at the crack tip. The resulting optical micrographs enabled the study of the crack propagation behaviour in specimens with different BC topographies. These observations were complemented by a comprehensive characterisation of the BC topography and investigation of pre/post-bending microstructural features under confocal and scanning electron microscopy, respectively. The local microstructural and mechanical properties of the TBC were also determined and correlated with the fracture behaviour observed.

5.2. Materials and methods

5.2.1 Sample fabrication and preparation

Samples were fabricated at Rolls-Royce (Annesley, United Kingdom) using Diamond Jet 2600 and 3MB thermal spray guns (Oerlikon Metco) according to the procedure in section 3.1. Specimens with similar composition and layer structure but with different geometries (i.e. button and elongated beam) were produced for TCF and four-point bending testing purposes, respectively. Both sample types were comprised by a Nimonic Alloy 263 substrate, a 200 µm single layer MCrAlY BC (H.C. Stark, AMPERIT 415/ 405) and a 300 µm 8YSZ TBC (Metco 204B-NS). The TCF specimens presented a standard button geometry ($\emptyset = 25\, mm, height = 6mm$) whereas bending specimens assumed the geometry presented in Fig. 3.8-b). Different BC/TBC interface topographies were generated by varying the BC processing parameters according to table 5.1. All specimens were annealed for 1 hour at 1100°C in an Argon atmosphere ($1.7 \times 10^{-1}\ mbar$) prior to topcoat deposition. The ceramic topcoat layer was deposited by APS under the same atmospheric conditions and processing parameters described in section 3.1 to minimise its impact on the TBC microstructure.

Table 5. 1 Parameters utilised for the thermal spraying process of the bond coat layer.

Material composition	**Deposition method**	**Powder particle size (µm)**	**Combustion conditions (H_2-O_2 content)**	**Specimen ID**
CoNiCrAlY ($Bal. Co, 31-33\%\ Ni, 20-22\%\ Cr, 7-9\%\ Al, 0.35-0.65\%\ Y$)	HVOF	38/10	Nominal value	Group 1/G1
	HVOF	38/10	↓20%	Group 2/G2
	HVOF	38/10	↑10%	Group 3/G3
	HVOF	38/10	↓30%	Group 4/G4
	APS	90/45	N/A	Group 7/G7
NiCoCrAlY-HfSi ($Bal. Ni, 21-23\%\ Co, 16-18\%\ Cr, 11.8-13.2\%\ Al, 0.4-0.8\%\ Y, 0.1-0.3\ Hf, 0.2-0.6\ Si$)	HVOF	38/10	Nominal value	Group 5 /G5
	HVOF	38/10	↑20%	Group 6 / G6
	APS	90/45	N/A	Group 8 /G8

TCF testing of the button-shaped specimens was conducted under atmospheric conditions in a Carbolite GERO box furnace, with each cycle consisting of a 30 °C.min^{-1} ramping-up rate, 11 hour dwell at 1135°C and a slowly controlled cooling (1.6°C.min^{-1}) to room temperature. In total, 12 samples of each type were tested and, as TCF progressed, four samples of each type were removed from the furnace periodically for oxidation kinetics and microstructural analysis. The remaining specimens were left inside the furnace until spallation of more than 50% of the topcoat was observed. Microstructural and compositional analysis of the as-deposited, heat-treated and failed specimens was done by scanning electron microscopy (Quanta 650, FEI) coupled with energy-dispersive X-ray spectroscopy (EDS X-max, Oxford Instruments).

5.2.2 Bond coat topography characterisation

The BC topography of two specimens from each group shown in table 5.1 was characterised prior to TBC deposition following the methodology described in section 3.3.1. The resulting post-processed heightmaps of the low, medium and high tortuosity specimens BC topographies are shown in Figs. 5.1-d) to f), respectively. Following the methodology outlined in section 4.2.2, these heightmaps were then used to obtain the respective total thresholded summit area (S_{sth}) maps presented in Figs. 5.1-g) to i). This parameter was selected as the metric to describe the BC tortuosity in this study since it provided a better correlation with fracture mechanics parameters than the arithmetic mean roughness. The as-deposited TBC microstructure corresponding to deposition over these topographies is presented in Figs. 5.1-a) to c).

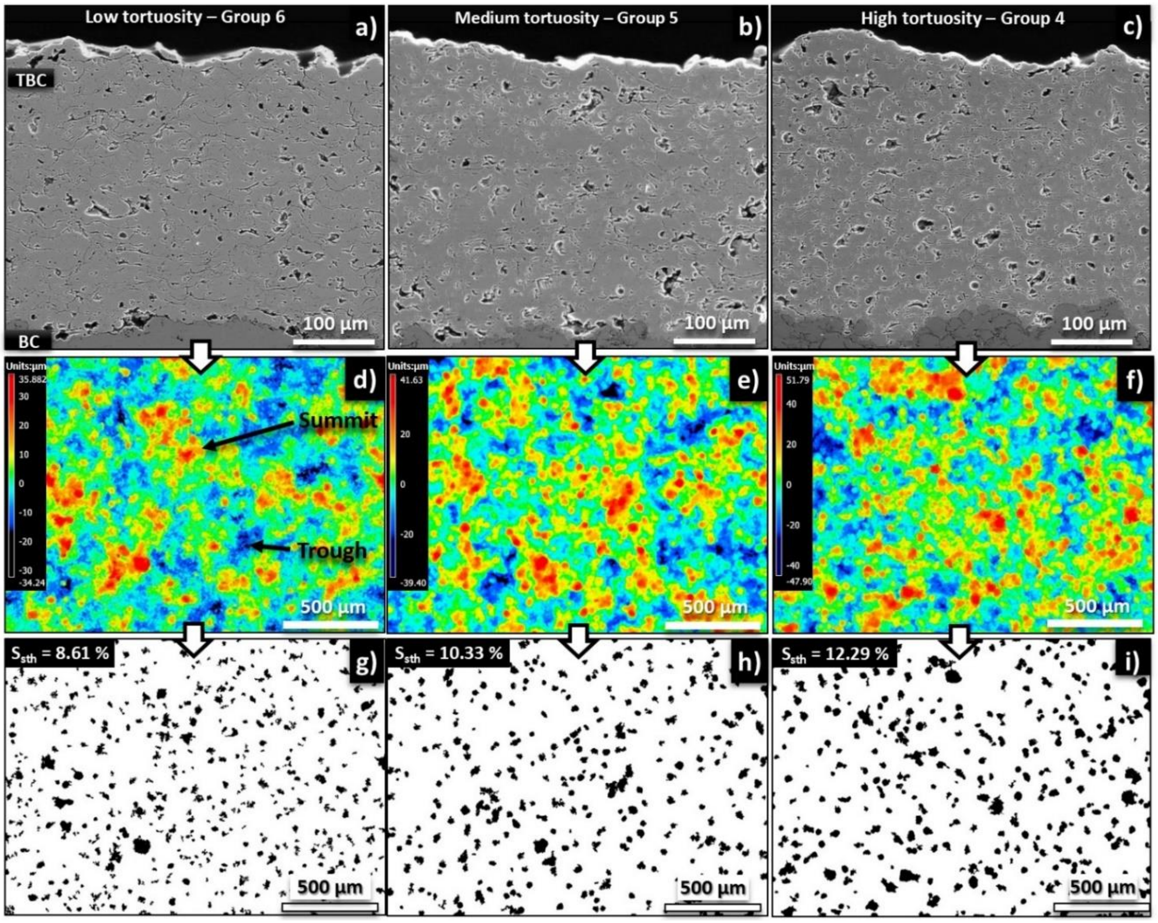
Low tortuosity – Group 6
a)
TBC
BC
100 µm
Medium tortuosity – Group 5
b)
100 µm
High tortuosity – Group 4
c)
100 µm
d)
Units:µm
35.882
30
20
10
0
-10
-20
-30
-34.24
Summit
Trough
500 µm
e)
Units:µm
41.63
20
0
-20
-39.40
500 µm
f)
Units:µm
51.79
40
20
0
-20
-40
-47.90
500 µm
S_sth = 8.61 %
g)
500 µm
S_sth = 10.33 %
h)
500 µm
S_sth = 12.29 %
i)
500 µm

Figure 5.1 SEM micrograph of the TBC microstructure generated by deposition over (a) low tortuosity, (b) medium tortuosity and (c) high tortuosity BC topographies; Colour heightmaps of the BC surface topography for the (d) low tortuosity, (e) medium tortuosity and (f) high tortuosity specimens and respective total thresholded heightmaps in the order g) to i).

5.2.3 Modified four-point bending test

5.2.3.1 Determination of the critical strain energy release rate and stress intensity factor

The preparation of the as-deposited beam-shaped specimens and experimental testing conditions used in the modified four-point bending experiment have been presented in section 3.3.3.3. However, the analytical considerations and assumptions are addressed below. The methodology selected to determine the stress intensity factor (*K*) and the critical strain energy release rate (G_C) was based on the analytical approach proposed by Suo-Hutchinson [254] and later validated by Zhao et al. [204] for thin ceramic brittle layers. This mathematical construct assumes that each material is isotropic and linearly elastic with a neutral axis located at a distance δ from the bottom surface of material 2, as depicted in Fig. 3.9-a). This approach allows for the multi-layer beam geometry adopted herein to be treated as a bi-layer composite beam approximation where the stiffener, TBC and adhesive layers are regarded as material 1 and the BC and substrate are regarded as material 2. As a consequence, the effective elastic modulus of material 1 was calculated according to a rule of mixtures methodology, as previously demonstrated by Vasinonta & Beuth [239] and Zhao et al. [204] in similar studies. The respective calculations and an additional representation of the physical principles associated with the four-point bending experiment are shown in Fig A1 (appendix A) to facilitate their interpretation in the context of a multi-layered beam system. The neutral axis of the present experiment was determined as $\delta = 4.4$ mm, meaning that the section of the beam below the neutral axis is under compression and the section above is under tension (see schematics in Gigs 3.9 and Fig A1 for mechanical contextualisation). As the interface region is still under low compression loads, crack propagation is ensured by the vertical notch introduced due to the stiffener plates keeping their flat geometry during bending and inducing tensile forces at the interface, as illustrated in Fig. A1 (Appendix A). The resulting load at which crack propagation ensues (i.e. critical load, P_c) can then be measured experimentally and used to calculate *K* and G_C from eqs. 5.1 and 5.2, respectively. All these calculations were performed automatically by the python script given in Appendix B.

$$|\mathrm{K}| = \sqrt{\frac{p^2}{2}\left(\frac{P^2}{Ah_1} + \frac{M^2}{Ih_1^3} + 2\frac{PM}{\sqrt{AI}h_1^2}sin\gamma\right)} \tag{5.1}$$

$$G_C = \frac{c_1+c_2}{16\cosh^2(\pi\varepsilon)}|K|^2 \tag{5.2}$$

where c_1 and c_2 are the compliance parameters, ε is the bimaterial constant, *P* is the load per unit thickness, *M* is the moment per unit thickness, γ is the characteristic angle, *A*, *I* and *p* are positive non-dimensional parameters and h_1 is the combined thickness of the stiffener, TBC and adhesive (material 1). The equations used to calculate all these parameters are presented in appendix A. The bi-axial local in-plane elastic moduli values used in these calculations were obtained via depth-instrumented microindentation, following the methodology described in section 3.3.4.1, and are presented in table A1 (Appendix A) [202]. An illustration of the location where the indentation measurements were conducted is shown in Figs. 5.4-c) and –f) for low and high tortuosity specimens respectively.

The phase angle (ψ) is a parameter that describes the ratio between the mode I (K_I) and II (K_{II}) components of the stress intensity factor. It can be determined from eq. 5.3 and be used to determine the tensile (K_I) and shear (K_{II}) components of the stress intensity factor via eqs. 5.4 and 5.5.

$$\psi = tan^{-1}\left[\frac{\lambda\, sin\,\omega - cos(\omega+\gamma)}{\lambda\, cos\,\omega - sin(\omega+\gamma)}\right] = tan^{-1}\left[\frac{K_{II}}{K_I}\right] \tag{5.3}$$

$$K_I = Kcos(\psi) \quad (5.4) \qquad\qquad K_{II} = Ksin(\psi) \quad (5.5)$$

where λ is the loading combination measurement and ω is the real angular quantity. The remaining equations used in the calculation of the phase angle are also presented in appendix A.

Despite the Suo-Hutchinson methodology having been used in TBC systems before, it is noteworthy the results obtained from this approach correspond to interfacial crack propagation between two different materials where the undulating nature of the crack path was not accounted for. This is believed to contribute to an overestimation of the computed K and G_C values herein, as the original Rice [255] & Hutchinson et al. [256] theoretical framework uses a linear traction distance (r) in the calculation of *the* near-tip stresses instead of an arc length traction distance.

5.2.3.2 Crack propagation velocity

The in-situ four-point bending experimental setup enabled the quantitative analysis of the post-critical point crack propagation velocity (v_{prop}) for each specimen type. A difference blending mode function (Photoshop CC 2017, Adobe) highlighted the microstructural differences between the selected and reference frames (i.e. pre-cracked microstructure) in a high contrast black and white colour scheme, as depicted in Fig. 5.2. The resulting micrographs facilitated the pinpointing of the pre-crack location and enabled its use as a reference in the crack propagation analysis. The crack tip progression was then tracked in each frame from the pre-crack tip to the edge of the frame image (≈1 mm) and, Bézier curves representing the established crack path were drawn (Bézier curve tool, ImageJ). Their lengths were then quantified, averaged, and divided by the frame time interval ($\Delta t = 100\ ms$), thereby yielding the crack propagation velocity in eq. 5.6. It is noteworthy the high-speed crosshead velocity selected ($0.5\ \mathrm{mm}.min^{-1}$) is only adequate to investigate the post-critical point crack propagation in the high-speed range ($10^{-4} \leq v_{prop} \leq 10^{-3} m.s^{-1}$), thereby neglecting the contributions of subcritical crack growth.

$$v_{prop} = \frac{l_{crack}}{\Delta t} = \frac{arc\ length\ \overline{AB}}{\Delta t} \tag{5.6}$$

where v_{prop} is the crack propagation velocity and l_{crack} the crack length.

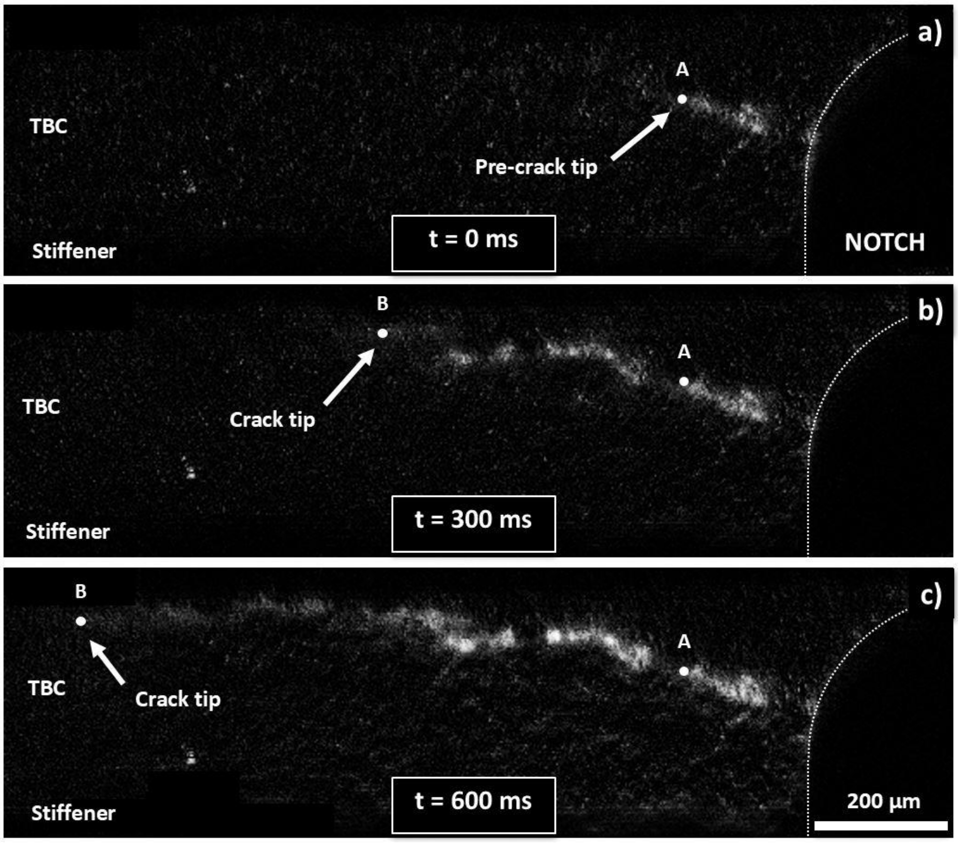

Figure 5.2 Optical frame micrograph sequence depicting the crack growth evolution with time for a low tortuosity specimen.

5.2.4 Inter-splat separation frequency

The inter-splat separation frequency (ν_{IS}) of the near-interface TBC microstructure was determined by a line intersection method (Line Scan analysis, ImageJ) that determines the number of existent discontinuities per unit of scanned line length across the TBC thickness, as described by eq. 5.7.

$$\nu_{IS} = \sum_{j=1}^{n} \frac{n^{\underline{o}}\ of\ discontinuities}{L} \qquad \text{(eq. 5.7)}$$

Where *n* is the total number of line segment scanned and *L* the individual line segment length.

The brightness and contrast of all electron micrographs used in the analysis were homogeneously adjusted using BioVoxxel toolbox plugin (ImageJ) prior to the threshold procedure. A uniform thresholding procedure was then established for all specimens, consisting of a black & white (B&W) mean-based threshold with a minimum threshold value of 0 and a maximum of 127. Following this, a systematic scan of interspersed sequential line segments (length ≈ 70 µm) on multiple cross-sectional thresholded SEM micrographs across a 300 µm segment of the BC/TBC interface, as exemplified in Fig. 5.3. Discontinuities originating grayscale intensity variations greater than 50% were classified as inter/intra-splat separations and recorded according to their position on the segment line. This metric was then used to assess the degree of inter-splat cohesion in the vicinity of the interface in the TBC.

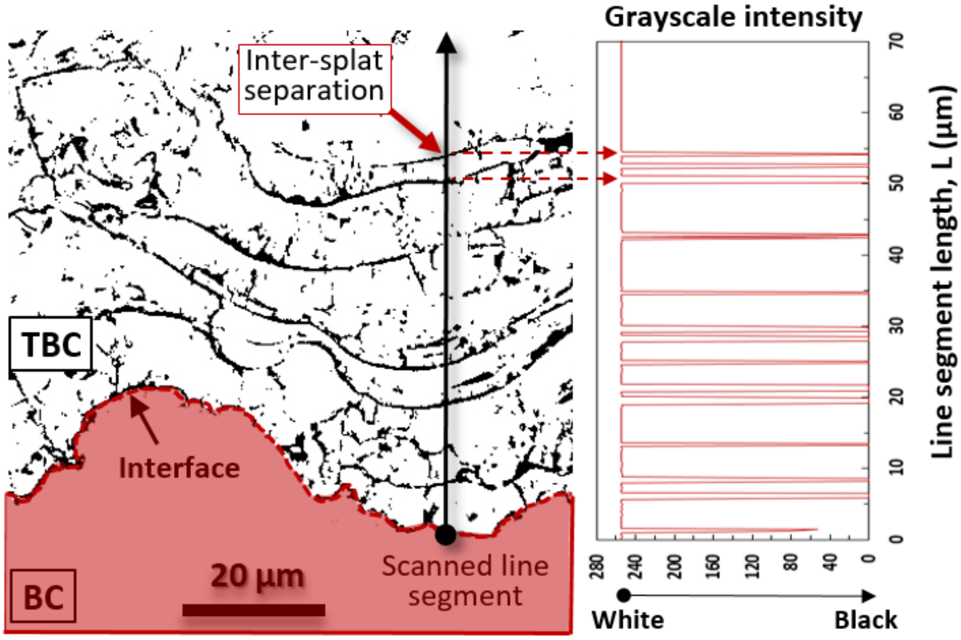

Figure 5.3 Representation of the line scan methodology used in the determination of the inter-splat separation frequency by unit of TBC length (v_{IS}) across the TBC layer thickness.

5.3. Results

5.3.1 Pre-bending microstructure

Fig. 5.4 is a compilation of SEM micrographs displaying the representative pre-bending microstructural features of as-machined low and high tortuosity specimens. A low-magnification overview of the beam centre-point region of a high tortuosity specimen is presented in Fig. 5.4-a), effectively confirming that the stiffener adhered well to the TBC, the notch reached the BC interface and no mechanical damage was introduced during the machining process. Fig. 5.4-b) depicts a representative deformation behaviour of a single 8YSZ particle $(\varnothing = 50\ \mu\mathrm{m})$ upon impact on a low tortuosity BC surface topography. The minimal lateral constraint induced by the BC topography upon impact originated a larger splat spreading ratio and reduced splashing that led to the predominant formation of thinner and larger radii splats, as previously noted in the literature [67]. The successive impingement of YSZ feedstock particles over the pre-formed low-curvature solidified splats led to the formation of a TBC microstructure with reduced intra-splat segmentation and enhanced inter-splat cohesion, as shown in Figs. 4-c) and -d). This is believed to have been caused mostly by epitaxial growth of columnar grains across the narrow inter-splat interfaces [56].

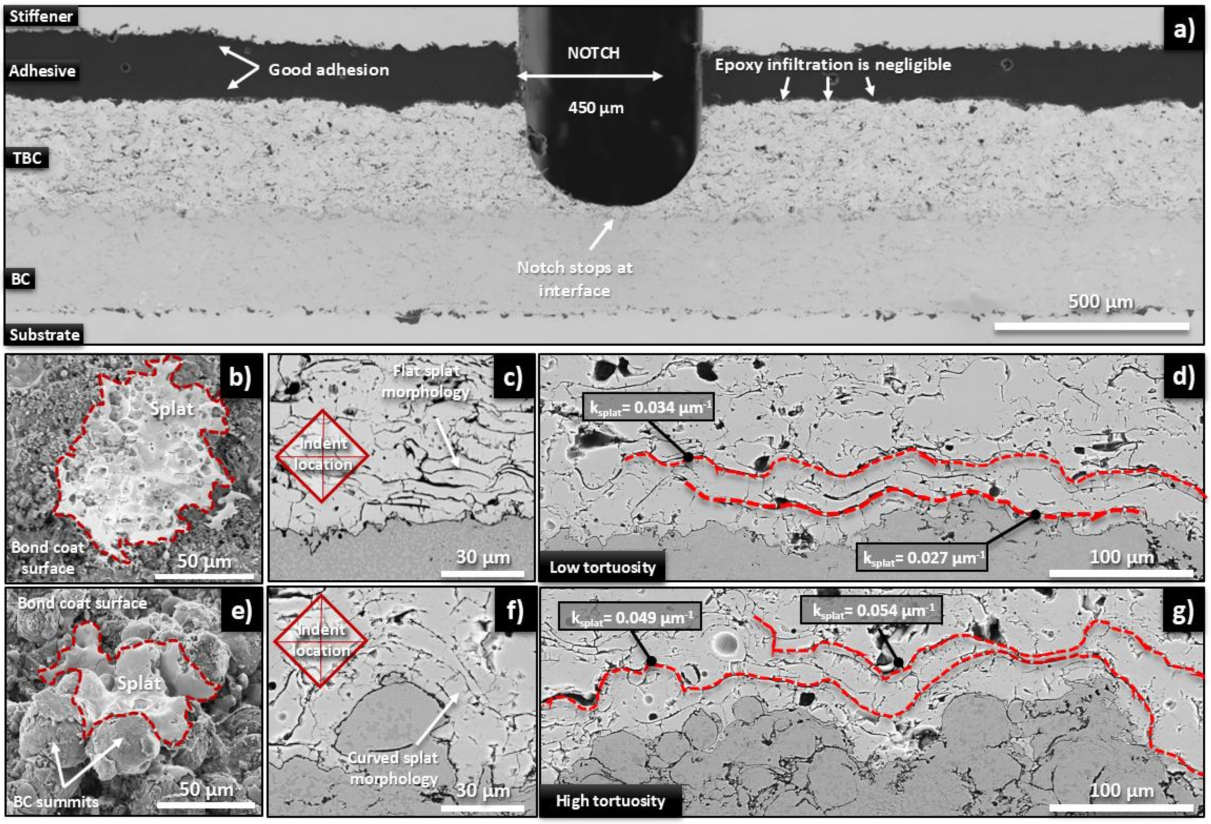
Stiffener
Adhesive
Good adhesion
NOTCH
450 µm
Epoxy infiltration is negligible
a)
TBC
BC
Notch stops at interface
500 µm
Substrate
b)
Splat
Bond coat surface
50 µm
c)
Flat splat morphology
Indent location
30 µm
d)
k_{splat}= 0.034 µm^{-1}
k_{splat}= 0.027 µm^{-1}
Low tortuosity
100 µm
Bond coat surface
e)
Splat
BC summits
50 µm
f)
Indent location
Curved splat morphology
30 µm
k_{splat}= 0.049 µm^{-1}
k_{splat}= 0.054 µm^{-1}
g)
High tortuosity
100 µm

Figure 5.4 (a) Backscattered-electron (BSE) micrograph of the pre-bending microstructure at the beam centre-point; Secondary electron (SE) micrograph illustrating a single splat impact over a (b) low and (e) high tortuosity BC surface; Cross-sectional BSE micrographs of the characteristic interfacial features and TBC splat morphology of the (c, d) low and (f, g) high tortuosity specimens, where the indent locations used to determine E_{TBC} and the average splat curvature of potential crack paths (k_{splat}) are highlighted. The k_{splat} values obtained (kappa plugin, ImageJ) represent the summation of the radius of curvature of each point along the Bézier curve defined by the potential crack path.

The inter-splat separation frequency across the TBC (ν_{IS}) was quantified by using the methodology described in section 5.2.4 and plotted against the local in-plane elastic modulus (E_{TBC}) in Fig. 5.5. Results confirmed that a decreased number of non-bonded splat segments across the TBC ($\nu_{IS} \leq 0.17\ \mathrm{separations.\,\mu m^{-1}}$) was correlated with denser microstructures ($E_{\mathrm{TBC}} \geq 88.6 \pm 1.4\ \mathrm{GPa}$) and less extensive porosity networks $(14.8 \pm 1.0\%)$, as illustrated by Fig. 5.1-a). The resulting splat arrangement originated a low-curvature splat morphology near the interface ($0.027 \leq \mathrm{k_{splat}} \leq 0.034\ \mathrm{\mu m^{-1}}$) that created multiple potential crack paths with near-horizontal configuration, as highlighted in Fig. 5.4-d).

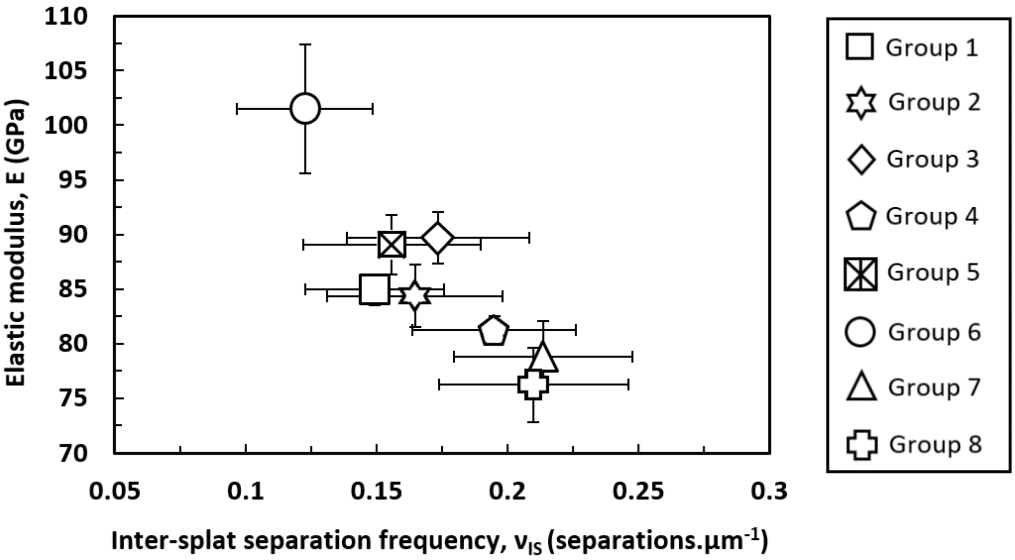

Figure 5.5 Plot of the TBC in-plane elastic modulus as a function of the inter-splat separation frequency.

In contrast, the increased topographical constraint provided by the high-amplitude and radii BC summits of specimens with high BC interface tortuosity promoted a higher degree of splat deformation and limited spreading behaviour upon impact, as shown in Fig. 5.4-e). The tortuosity-induced variations in the flow viscosity and higher quenching stresses during splat formation [257] promoted increased intra-splat segmentation and splashing that resulted in a higher degree of splat fragmentation [258]. Microstructurally, this was reflected by the formation of a highly curved and moderately thicker splat morphology that reduced the overall degree of inter-splat cohesion ($\nu_{IS} \geq 0.19$ separation.µm^{-1}) and resulted in the formation of more compliant TBC microstructures ($E_{TBC} \leq 84.9 \pm 1.1\ GPa$) with increased porosity ($20.1 \pm 0.9\%$), as seen in Fig. 5.1-c). The representative as-deposited interface region of a high tortuosity specimen is presented in Figs. 5.4-f) and g), showing that the periodic presence of higher amplitude asperities induced a higher curvature splat morphology ($0.049 \leq k_{splat} \leq 0.054$ µm^{-1}). This led to the formation of more tortuous and lengthier potential crack paths with reduced inter-splat cohesion.

5.3.2 Post-bending microstructure

Fig. 5.6 shows a representative SEM micrograph compilation of the post-bending microstructure of a high tortuosity specimen where the most important features of the fractured TBC layer are highlighted. Figs. 5.6-a) and b) show that pre-crack initiation occurred within the TBC layer in the curved segment of the notch and propagated towards the interface before stabilising and continuing in parallel to the BC/TBC interface.

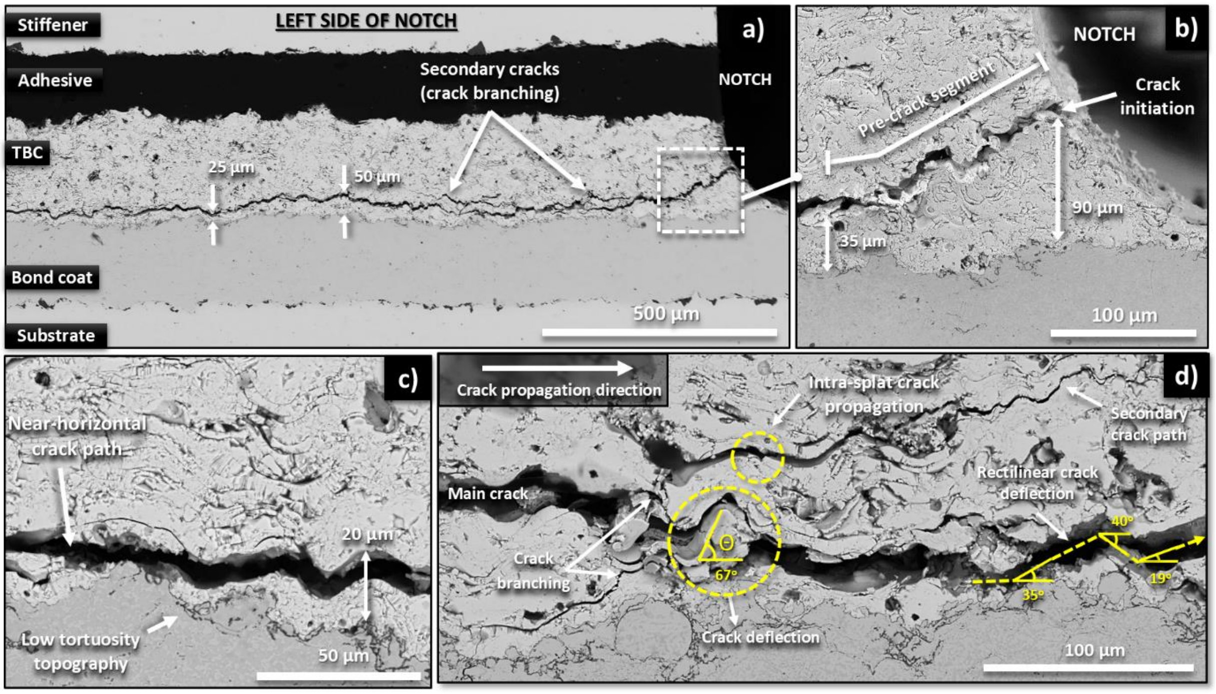
Stiffener
LEFT SIDE OF NOTCH
a)
Adhesive
Secondary cracks
(crack branching)
NOTCH
TBC
25 µm
50 µm
Bond coat
500 µm
Substrate
NOTCH
b)
Pre-crack segment
Crack
initiation
90 µm
35 µm
100 µm
c)
Near-horizontal
crack path
20 µm
Low tortuosity
topography
50 µm
Crack propagation direction
Intra-splat crack
propagation
d)
Secondary
crack path
Main crack
Rectilinear crack
deflection
40°
Θ
Crack
branching
67°
35°
19°
Crack deflection
100 µm

Figure 5.6 (a) Post-bending microstructure of a high tortuosity specimen and respective pre-crack initiation site at the notch root; (c) Near-horizontal crack propagation in low tortuosity specimens (d) Microstructural evidence of crack deflection and intra-splat cracking mechanisms contribution to crack propagation in regions of high splat curvature.

Crack propagation initiated from the pre-crack tip and resulted from a combination of cohesive and adhesive fracture along the inter-splat separations and BC/TBC interface, respectively. The ratio of cohesive to adhesive fracture was dictated by the degree of BC tortuosity and was responsible for defining the overall crack path configuration. In higher BC tortuosity specimens, the enhanced interfacial adhesion and reduced inter-splat cohesion shifted crack propagation away from the interface ($25 \leq d_{interface} \leq 50$ µm) (see Fig. 6-a) to a region where the crack driving force and energy requirements to trigger crack propagation are reportedly lower [188]. As can be seen in Fig. 5.6-a), this originated a tortuous and lengthier crack path that developed almost exclusively within the TBC, where the inter-splat cohesion is lower and compliance higher. In contrast, the reduced interfacial adhesion strength, enhanced inter-splat cohesion, and lower curvature splat morphology induced by lower tortuosity BC topographies shifted the delamination path towards the interface ($d_{interface} \leq 20$ µm). As anticipated in the previous section, this resulted in a near-horizontal and shorter delamination path that propagated in close proximity to the interface and formed a mixed failure plane with BC-TBC exposed segments, as shown in Fig. 5.6-c).

The analysis of the crack propagation behaviour also revealed that the ratio of low to high curvature splat segments incorporated into the near-interface TBC microstructure had a significant impact on the slope of the deflected crack segments (θ, see Fig. 6-d) and, by extent, with the overall degree of crack path tortuosity. As a result, the initial tilt of all crack deflections along the delamination path was determined and averaged for each specimen (Angle tool, ImageJ), as illustrated in Fig. 6-d). Results showed that the average deflection angles increased gradually with interface tortuosity, ultimately equating to an 85% difference between higher ($\theta_{av} = 38.3 \pm 12.2^{o}$) and lower ($\theta_{av} = 20.6 \pm 8.8^{o}$) tortuosity specimens. The resulting effect on fracture mechanics is investigated in section 4.2.

5.3.3 Effect of BC topography and TBC microstructure fracture behaviour

The critical strain energy release rate of each specimen group was plotted as a function of S_{sth} and E_{TBC} in Fig. 5.7-a), wherein each data point represents the average of three specimens from each group and the error bars represent the respective standard deviations. Fig. 5.7-a) shows that both the BC topography (solid black markers) and the TBC elastic modulus (dashed orange markers) have a significant impact on the critical energy release rate, albeit displaying inverse trends. Low tortuosity specimens with denser TBC microstructures displayed the highest G_C values ($G_C \geq 104.4 \pm 1.6 \text{ J}.m^{-2}$), followed by the moderate ($98.6 \pm 4.2 \leq G_C \leq 94.8 \pm 6.1 \text{ J}.m^{-2}$) and higher tortuosity specimens ($79.9 \pm 12.2 \leq G_C \leq 72.9 \pm 6.4$) with progressively lower G_C values, all within the range reported for similar bending studies [204, 212, 246]. The linear fit performed on the S_{sth} dataset (solid pattern) revealed an inverse correlation ($R^2 = 0.97$) with G_c, indicating that a 1% increase in S_{sth} led to a reduction of 12 J.m^{-2} in G_C. This translated into a substantial variation ($|\Delta G_c| = 44 \text{ J}.m^{-2} = 38\%$) between the less (Group 6) and more (Group 2) tortuous specimens. A similar ΔG_c trend was observed for the E_{TBC} dataset (stripe pattern), as the direct proportionality relationship ($R^2 = 0.76$) with G_c indicates that a variation of 23 GPa resulted in a 42 J.m^{-2} increment in G_C between the less and more compliant specimens. Nevertheless, the presence of outliers (i.e. Groups 2 and 4) in the dataset indicates that the E_{TBC} measurements could not take all microstructural factors that are relevant to fracture mechanics into account (e.g. inter-splat separation curvature).

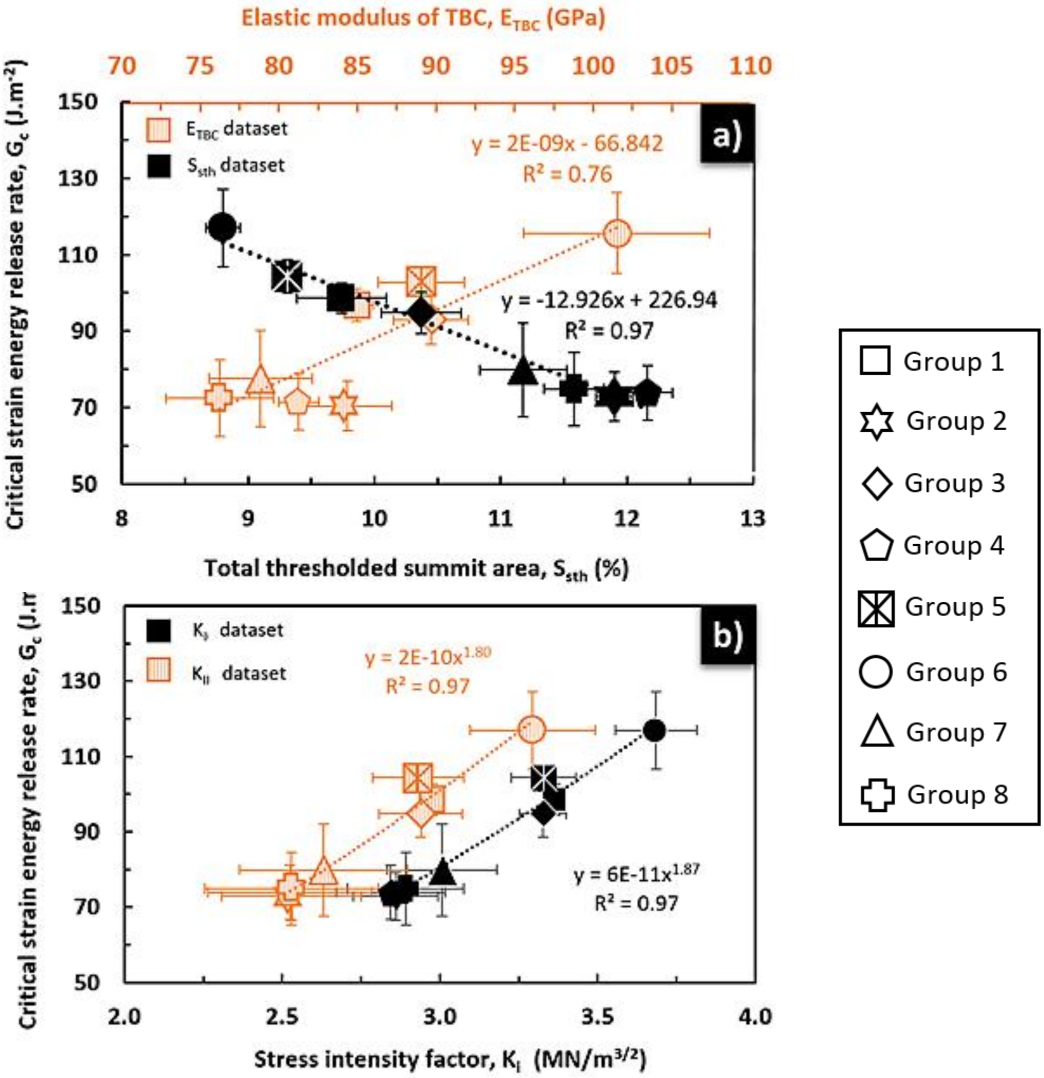

Figure 5.7 (a) Plot of the strain energy release rate as a function of the total thresholded summit area (solid black pattern) and the TBC in-plane elastic modulus in the vicinity of the interface (orange stripe pattern); (b) Plot of the critical energy release rate as a function of the tensile, (K_I) and shear (K_{II}) components of the stress intensity factor, represented by solid black and dashed orange markers respectively. It is important to note that despite gradient observed herein being indicative of an approximately constant phase angle amongst all specimens, this is only a global average based on the model assumption of the planar interface.

Fig. 5.7-b) shows a plot of the critical energy release rate as function of the tensile, (K_I) and shear (K_{II}) components of the stress intensity factor. The respective dataset trends revealed that G_c increased non-linearly with both components of the stress intensity factor, as evidenced by the least squares power law fit performed ($R^2_{K_{IC}} = 0.97$; $R^2_{K_{IIC}} = 0.97$). This signifies that the magnitude of the energy released at the onset of crack propagation is primarily dependent on the magnitude of the stress state surrounding the crack tip, as anticipated by the literature ($G_C \propto K^2$) [200, 254]. In turn, since these stresses are heavily dependent on the surrounding microstructure [203], this also means that topography-induced alterations of the near-interface TBC density should also have a significant effect on K_I and K_{II}. This relationship was effectively confirmed by the linear trends obtained for the S_{sth} and E_{TBC} datasets in Figs. 5.8-a) and b), respectively. It is also important to note that the similar magnitudes obtained for K_I and K_{II} are indicative of a heavily mixed-mode loading applied at the crack tip ($41.19 \leq \psi \leq 41.81$), similar to the ones observed during TCF testing [187]. The slightly higher K_I values ($\sim 12\%$) suggest that it might be easier for the K_{II} to surpass the critical threshold and become the predominant fracture mode. Nevertheless, it is important to consider that this is dependent on the actual loading conditions of the TBC. Overall, the results presented herein have evidenced that specimens with lower tortuosity BC topographies and denser TBC microstructures were correlated with higher fracture toughness ($K_I \geq 3.3 \pm 1.0\ MN.m^{-3/2}$; $K_{II} \geq 2.9 \pm 1.0\ MN.m^{-3/2}$) and higher energy release rates at the onset of crack propagation ($G_C \geq 104.4 \pm 1.6\ \mathrm{J}.m^{-2}$).

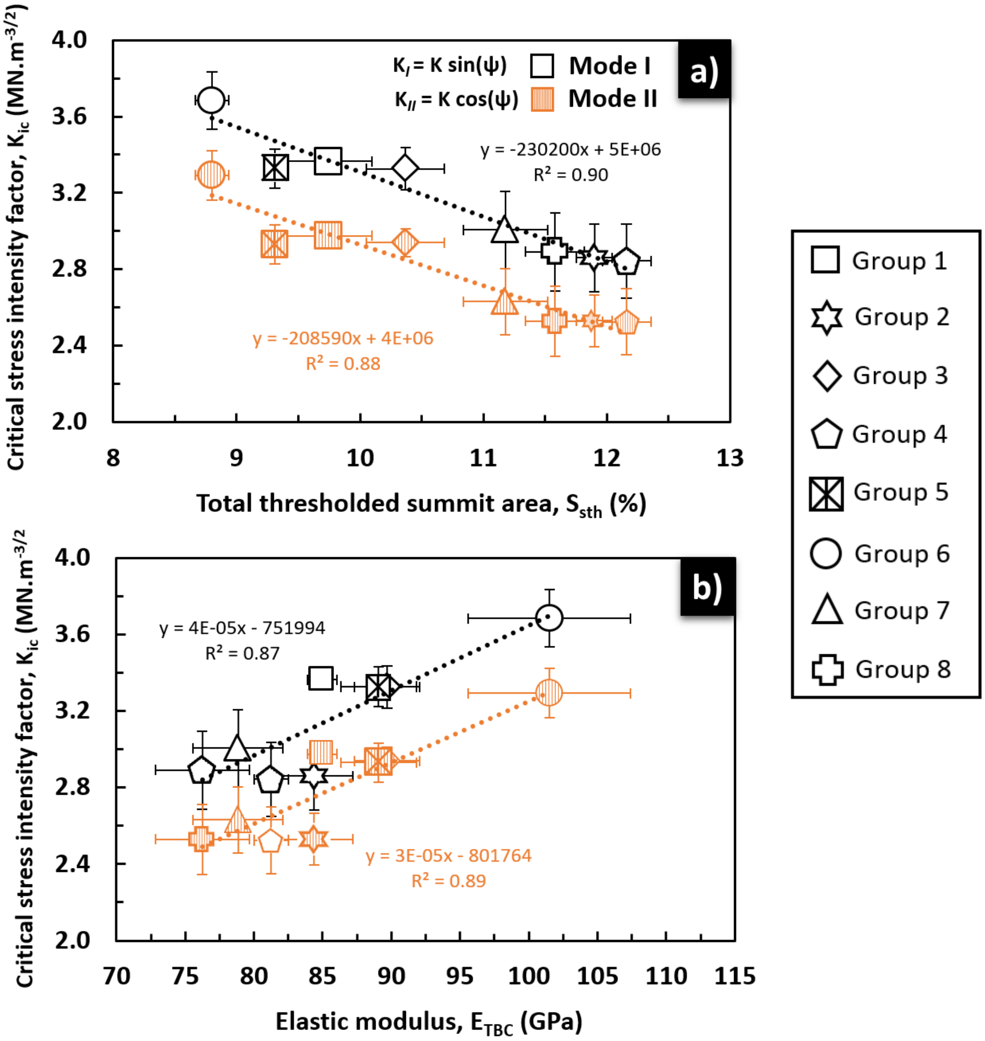

Figure 5.8 Plot of the mode I and II stress intensity factor components as a function of (a) the total thresholded summit area and (b) the TBC in-plane elastic modulus in the vicinity of the interface.

5.3.4 Crack propagation behaviour

In-situ monitoring of the crack propagation during the four-point bending experiment revealed the existence of a discrepancy in the progression velocity of the crack tip along the interfaces of low and high tortuosity specimens, as evidenced by the inversed optical frame micrographs in Fig. 5.9. These discrepancies were perceived as a burst-like crack tip advancement over small distances for the high tortuosity specimens and over longer distances for their low tortuosity counterparts. This phenomenon motivated the analytical determination of the crack propagation velocity (v_{prop}) using the methodology in section 2.3.3 and subsequent plotting as a function of G_c in Fig. 5.10-a).

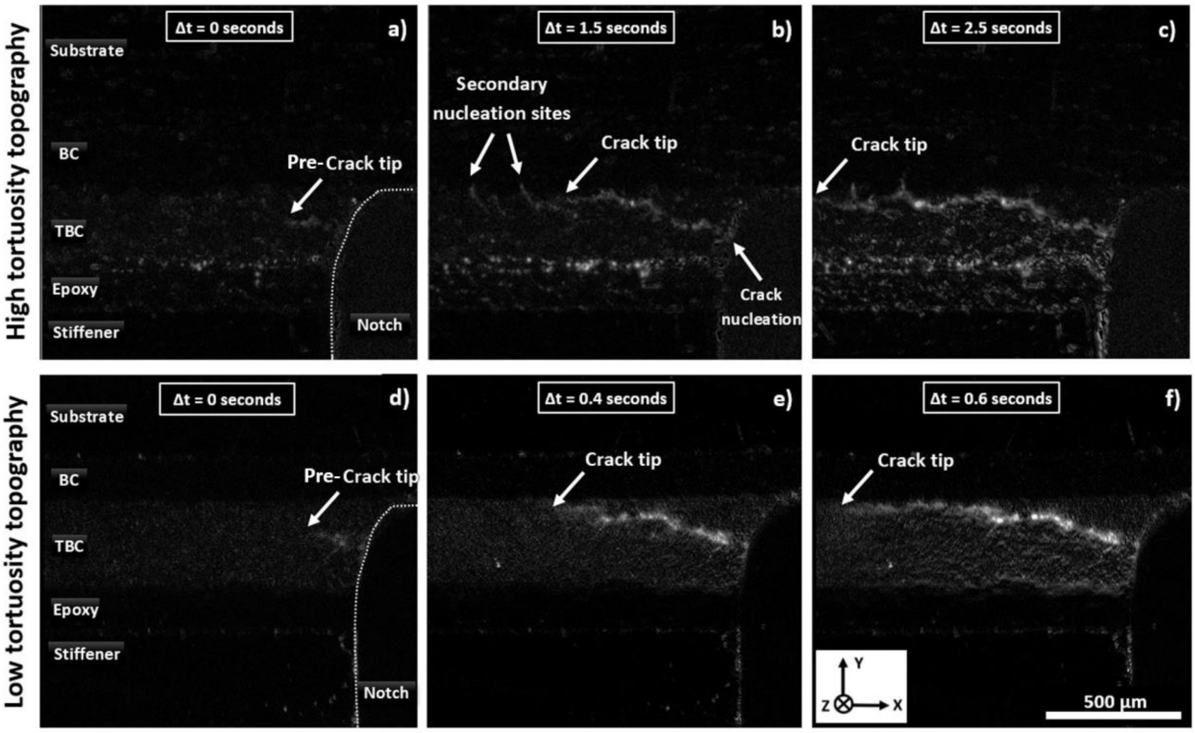
High tortuosity topography
Δt = 0 seconds
a)
Substrate
BC
Pre-Crack tip
TBC
Epoxy
Stiffener
Notch
Δt = 1.5 seconds
b)
Secondary nucleation sites
Crack tip
Crack nucleation
Δt = 2.5 seconds
c)
Crack tip
Low tortuosity topography
Δt = 0 seconds
d)
Substrate
BC
Pre-Crack tip
TBC
Epoxy
Stiffener
Notch
Δt = 0.4 seconds
e)
Crack tip
Δt = 0.6 seconds
f)
Crack tip
Y
Z
X
500 µm

Figure 5.9 Compilation of inversed optical frame micrographs depicting the crack propagation discrepancies observed during the four-point bending test for a high and low tortuosity specimen.

The results in Fig. 5.10-a) show that v_{prop} increases with G_c according to a power-law function ($R^2_{G_C} = 0.92$), with a ΔG_c of 44 J.m^{-2} between the highest and lowest tortuosity specimens resulting in a five-fold increase in crack propagation velocity. This means that the release of larger amounts of strain energy at the onset of crack propagation originated a faster progression of the crack tip along the interface. This trend is consistent with the mechanically-induced quasi-stable crack propagation behaviour reported for analogous YSZ coatings in the literature [201, 259]. The S_{Sth} and E_{TBC} datasets were also plotted as a function of v_{prop} in Fig. 5.10-b) to ascertain their impact on the crack propagation behaviour. The resulting dataset trends showed that v_{prop} varies non-linearly with both variables but according to opposite trends, as confirmed by the power-law fit performed on both datasets ($R^2_{S_{sth}} = 0.91$; $R^2_{E_{TBC}} = 0.78$). Quantitatively, this means that an increase of 3.36 % in S_{sth} amongst low and high tortuosity specimens combined with a reduction of 23 GPa in E_{TBC} were associated with a five-fold reduction in the crack propagation velocity. This behaviour is indicative that both the interface tortuosity and near-interface TBC microstructural density have affected the crack propagation behaviour in this experiment, as previously proposed by Eriksson et al. [188].

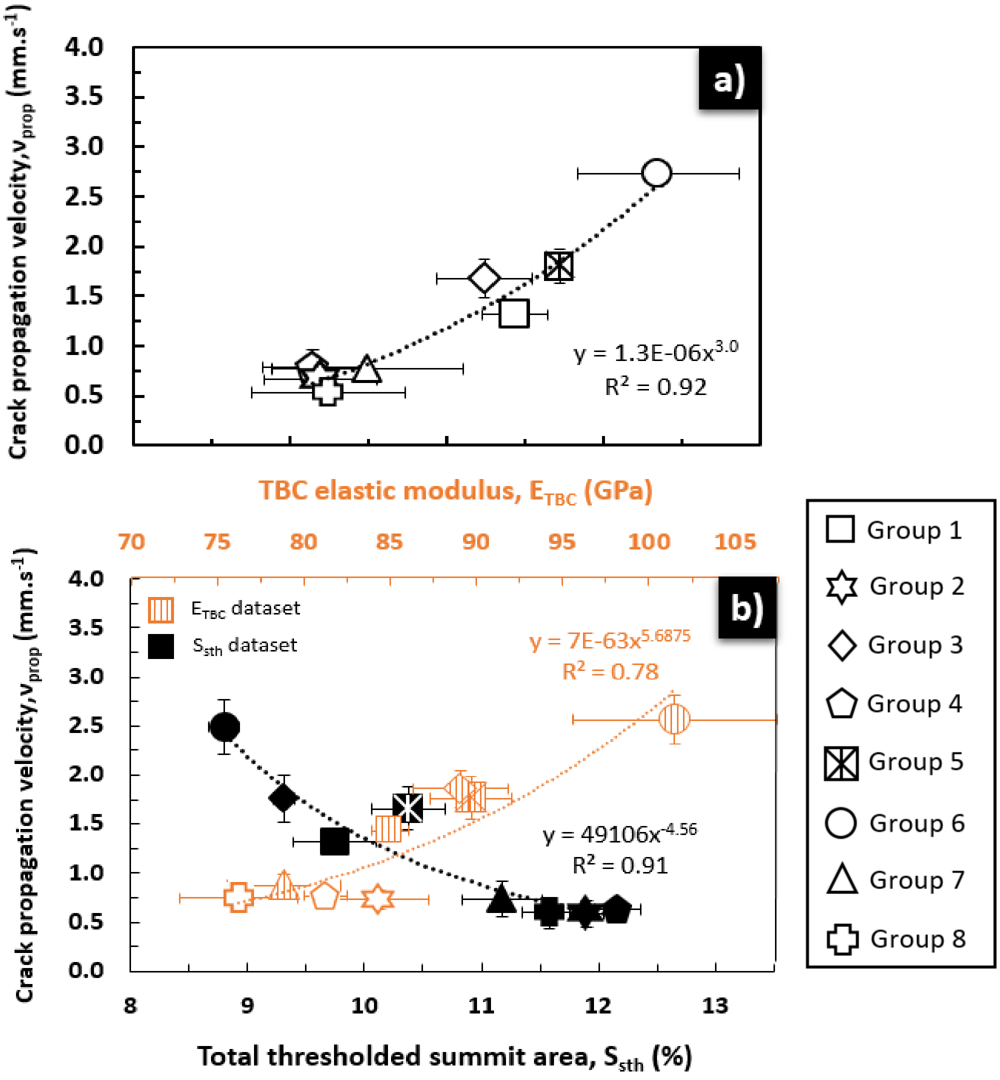

Figure 5.10 Plot of the crack propagation velocity as a function of (a) G_c and (b) the total thresholded summit area and local TBC in-plane elastic modulus.

5.3.5 Correlation with TCF lifetime results

The TCF lifetime of the button-shaped specimens (L_f) was plotted as a function of the S_{sth} parameter and G_C in Figs. 5.11-a) and b), wherein L_f was expressed as a fraction of the highest lifetime obtained. The TCF lifetime increased proportionally with the S_{sth} metric ($R^2 = 0.90$), indicating that an increase in the as-deposited interfacial tortuosity had a positive impact on TCF lifetime and by extension on the governing failure mechanisms. As such, the effect of the fracture mechanics behaviour induced by the same as-deposited topographies on TCF lifetime was assessed by plotting the latter as a function of G_c in Fig. 5.11-b). Results showed that the 70% lifetime variation observed between the lowest and highest tortuosity specimens can be matched to the 44 J.m^{-2} discrepancy in G_c obtained for the equivalent bending specimens. The datasets were correlated by an inverse linear trend (R^2=0.87), indicating that more compliant TBC microstructures are associated with less energetic fracture events (i.e. lower G_C) and are more likely to achieve higher TCF lifetimes. This is consistent with the results presented in Fig. 5.10, as it suggests that the release of lower amounts of strain energy at the onset of crack propagation have been shown to originate slower crack propagation velocities. This is consistent with the results presented in Fig. 5.10, as it suggests that the release of lower amounts of strain energy at the onset of crack propagation have been shown to originate slower crack propagation velocities [260].

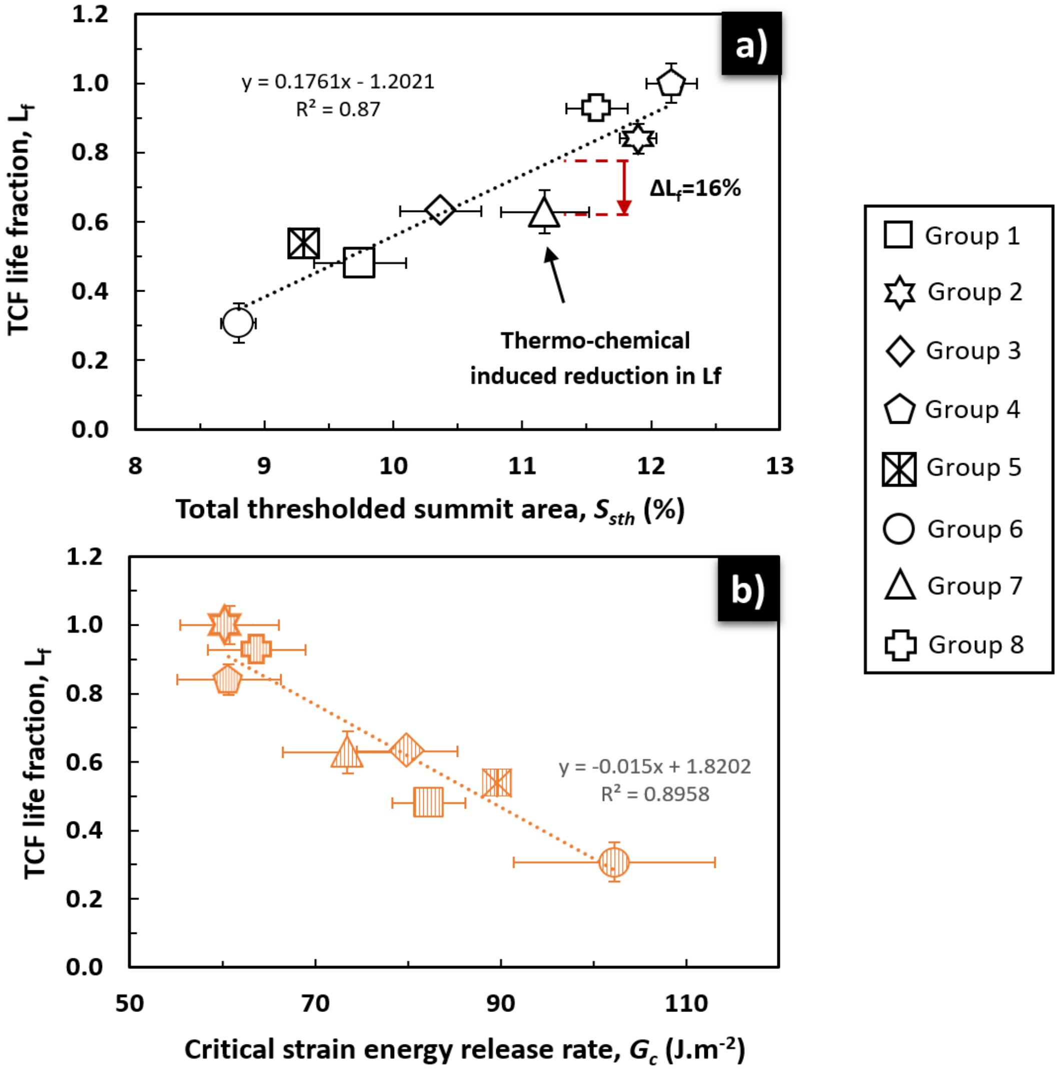

Figure 5.11 Normalised TBC lifetime for the different types of CoNiCrAlY and NiCoCrAlY-HfSi specimens as a function of (a) specimen ID and (b) critical strain energy release rate.

5.4. Discussion

5.4.1 Effect of intra-splat cohesion on fracture mechanics

The microstructural observations in section 5.3.1 have shown that TBC deposition over different interface topographies ($8.80 \pm 0.14 \leq S_{sth} \leq 11.18 \pm 0.34\%$) resulted in different degrees of splat curvature, inter-splat cohesion and intra-splat segmentation that were caused by alterations in the splat formation and packing processes. These features affected the real contact area between adjacent splats, simultaneously defining the extent of the inter-splat porosity network and the resulting inter-splat interaction dynamics for each specimen group. This was reflected by the different load-displacement behaviours and elastic moduli trend obtained during microindentation ($\Delta E_{TBC} = 23\ \mathrm{GPa}$), which evidenced distinctive levels of TBC microstructural compliance. The most conclusive evidence supporting this trend emerged from the inverse linear correlation observed between ν_{IS} and E_{TBC} in Fig. 5.5, confirming that the near-interface TBC compliance was predominantly governed by the degree of inter-splat cohesion, as previously noted by Li et al. [191] and Cocks et al. [261].

These topography-induced microstructural in the TBC also contributed significantly to the fracture mechanics behaviour during bending, as reflected by the positive correlation observed between G_C and E_{TBC} in Fig. 5.7. The fact that the amount of energy released at the onset of crack propagation increased with the TBC modulus is indicative of constrained inter-splat dynamics and intra-splat closure that have a limiting effect on the activation of local stress relaxation mechanisms (splat sliding, intra-splat closure, micro-cracking) [191, 210]. This is congruent with the higher critical loads obtained for specimens with enhanced inter-splat cohesion (i.e. low interface tortuosity), as illustrated by the load-displacement curve shown in Fig. 3.8-c) and table A1. Increasingly constrained splat dynamics are more likely to originate higher near-tip stress threshold levels in the TBC and lead to a higher strain energy density around the crack tip. These threshold levels are intrinsic to each specimen type and are represented by the K_I and K_{II} values presented in Fig. 7-b). In accordance with Freund [200] and Wiederhorn [201] theoretical framework, this meant that more energy was available for the creation of new crack surface areas upon reaching the critical point. This is consistent with the higher energy release rates ($G_C \geq 104.4 \pm 1.6\, J.m^{-2}$) and faster crack propagation velocities ($v_{prop} \geq 1.8 \pm 0.2\, mm.s^{-1}$) obtained for these specimens in Figs. 5.7 and 5.10-a), respectively.

This fracture mechanics behaviour provides strong evidence that inter-splat cohesion had a crucial impact on the magnitude of E_{TBC} and by extension on G_c, as previously suggested in the literature for porous APS ceramic coatings [191, 262]. This was effectively confirmed upon plotting G_c as a function of ν_{IS} in Fig. 5.12 and finding that the former decreased as the near-interface inter-splat separation frequency increased. Although an inverse proportionality trend is partially discernible herein, the degree of dataset scattering (Groups 2 and 4) observed indicates the existence of other unaccounted factors contributing to fracture mechanics. This is not entirely unexpected as the methodology used to determine ν_{IS} only accounts for the contributions of inter-splat and intra-splat features. However, the indent size area used for the E_{TBC} measurements was large enough to cover multiple splats ($A_{indent} \approx 450\ \mu m^2$) and therefore accounted for the microstructural contributions of intra-splat segmentation, grain size and grain morphology. Although this yielded an improved correlation with G_C in Fig. 5.7-a), the continued presence of outliers was still indicative of additional unaccounted contributions to G_c from other microstructural sources. The only major microstructural factor that still remains unaccounted is the inter-splat separation curvature and therefore its impact on fracture mechanics is addressed in the next section.

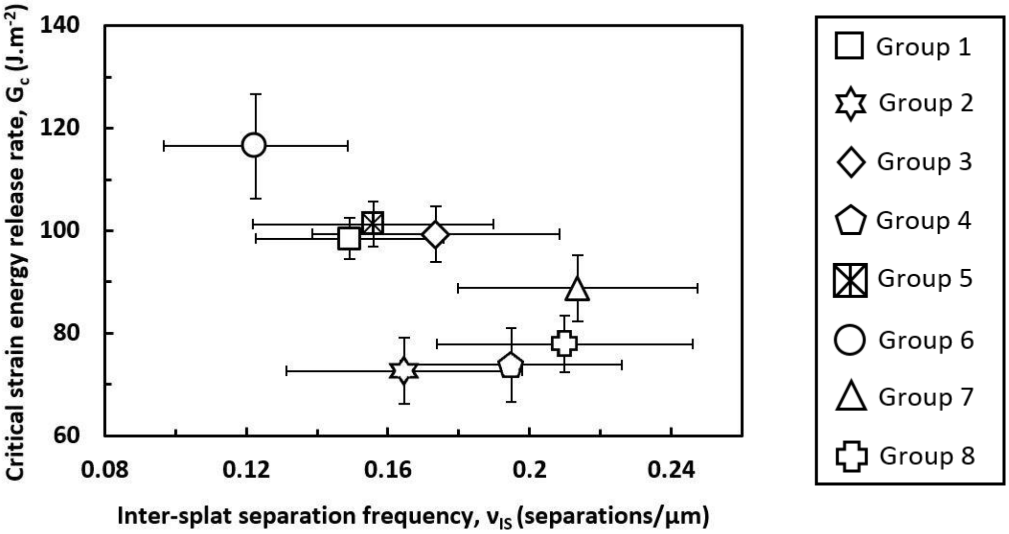

Figure 5. 12 Plot of the critical strain energy release rate as a function of the inter-splat separation frequency across the TBC thickness.

5.4.2 Impact of inter-splat separation tortuosity on fracture mechanics

As TBC crack propagation was predominantly driven by mixed-mode cohesive fracture ($\psi \approx 42^o$) along the inter-splat boundaries, the overall crack configuration was determined by the BC topography-induced variations on the splat curvature, as shown in Fig. 5.6. This was quantitatively confirmed by Fig 5.10-b), as the increasingly tortuous interface topographies were associated with a reduction in crack propagation velocity. As such, the curved segments seen consistently along the delamination paths were classified as local kinked segments that affect the near-tip slope angles and by extension the crack propagation rate. These changes in the near-tip slope angles are intrinsic to each TBC microstructure and therefore, different splat curvatures are likely to lead to alterations in the crack driving force [242] and affect the G_C magnitude. As a result, the contribution of the average slope deflection angle (θ) to the reduction of the local crack driving force along the delamination path was estimated using the theoretical framework proposed by Hussain & Pu for mixed mode conditions given by eq. 5.8 [263].

$$K_{tip} = \sqrt{\langle {k_I}^2 \rangle + \alpha {k_{II}}^2} \tag{5.8}$$

Where k_I and k_{II} are the local stress intensity factors for modes I and II and, α is a material parameter used to account for the contribution of each local stress intensity factor component in the fracture behaviour ($\alpha = 1$ for plane strain conditions). k_I and k_{II} were calculated as a function of the deflection angle (θ) in eqs. 5.9 and 5.10.

$$k_I(\theta) = \left(\frac{4}{3+\cos^2\theta}\right)\left(\frac{\pi-\theta}{\pi+\theta}\right)^{\theta/2\pi}\left(K_I\cos\theta - \frac{3}{2}K_{II}\sin\theta\right) \tag{5.9}$$

$$k_{II}(\theta) = \left(\frac{4}{3+\cos^2\theta}\right)\left(\frac{\pi-\theta}{\pi+\theta}\right)^{\theta/2\pi}\left(K_{II}\cos\theta + \frac{1}{2}K_I\sin\theta\right) \tag{5.10}$$

Where K_I and K_{II} are the applied mode I and II stress intensity factors. It is noteworthy that the $\langle\ \ \rangle$ operator represented by the Macaulay brackets is included in eq. 5.8 is used here to ensure that any negative values of K_I (i.e. crack closure) are not considered in this model, effectively disregarding any circumferential compressive stresses [264]. This parameter is defined in eq. 5.11.

$$\langle x \rangle = \begin{Bmatrix} 0 & x \leq 0 \\ x & x > 0 \end{Bmatrix} \tag{5.11}$$

The average deflection angles (θ_{av}) reported in section 3.2 for the low and high tortuosity specimens were used in eq. 5.9 and 5.10 and yielded a respective estimated average reduction of 15% and 22% in the near-tip driving force when compared to a crack propagating in parallel to the interface. This equates to a 7% difference between these specimens (ΔK_{tip}) and indicates that the K_{tip} reduction provided by the splat curvature is not sufficient to explain the 38% variation in G_c observed in Figs. 5.7-a). These calculations suggest that the degree of inter-splat separation tortuosity did have some impact on the TBC fracture mechanics ($\approx 18\%$ of ΔG_c) but the inter-splat cohesion and intra-splat segmentation contributions appear to have been the predominant factors governing interfacial crack propagation and delamination. These are consistent with the predictions made by Cotterel & Rice [263], Ritchie [203] and Pippan [265] for kinked cracks propagating under mode I loading conditions in bulk materials.

The contributions of these microstructural features to the TBC's fracture mechanics were likely reflected in the quantitative description of the BC interface by the new S_{sth} parameter, as the degree of BC interface tortuosity was shown to be influence the TBC microstructure and the critical energy release rate. This means that the BC tortuosity is closely related to the influence that each of the aforementioned microstructural features has on the overall crack path configuration and, by extension, on the TBC failure mechanisms and lifetime. This can help explain the correlations observed between the S_{sth} parameter and G_c in Fig. 5.7 and S_{sth} and TCF lifetime in Fig. 5.11-a).

5.4.3 Impact on TCF lifetime

The inverse linear trend obtained in Fig. 5.11-b) between L_f and G_c suggests that the sole contributions of the BC interface topography and resulting TBC microstructural features (i.e. inter-splat curvature and cohesion) governing the as-deposited fracture mechanics (Figs. 5.7) are still relevant in the later stages of TCF. This trend is not entirely unprecedented as the effect of the as-deposited interface roughness on the magnitude of K_I, G_C [252, 253] and TBC lifetime [118, 120] has been well documented. These results can be partially explained by the fact that the interface roughness remains mostly unaffected by the growth of a stable and homogeneous TGO scale [204], and the ΔE_{TBC} variation observed in as-deposited specimens is still present in late stage TCF specimens due to sintering being governed by a logarithmic law [59, 202]. Adding to this, the wider near-interface potential crack paths generally remain viable until the last stages of TCF due to the large interfacial tensile stresses counteracting sintering in these regions. On the other hand, it is important to note that despite the TBC sintering and TGO growth contributions were not accounted for in the G_C values of Fig. 5.11-b), they are expected to affect the TBC fracture mechanics [59, 188, 246]. However, similar four-point bending experiments conducted by Zhao et al. [204] and Yamazaki et al. [245] on as-deposited and heat treated APS TBCs have shown that sintering and TGO growth affect primarily the magnitude of K and G_c values. This behaviour suggests that the overall trend amongst specimens and crack path configurations remain mostly unaltered.

In an effort to contextualise the results presented in Fig.9 with the external loading conditions expected for a TBC undergoing TCF testing, the elastic energy per unit of TBC area (U) originating from the TCF thermal stresses that is available for release via fracture was estimated from eq. 5.12 [1].

$$U = \frac{E_{TBC} h_{TBC} (1+\nu_{TBC})}{2(1-\nu_{TBC})} (\Delta\alpha_C \Delta T)^2 \tag{5.12}$$

where the elastic modulus (E_{TBC}) and TBC thickness (h_{TBC}) used in the calculations are given in Table A1 (Appendix A), the TCF cycle maximum temperature variation ($\Delta T = 1110$°C) was obtained from TCF testing conditions, the Poisson's ratio ($\nu_C = 0.3$) and thermal expansion mismatch ($\Delta\alpha_C = 2\text{x}10^{-6} C^{-1}$) between the TBC surface and substrate were obtained from the literature [1].

Calculations showed that the estimated elastic energy available for the formation of new crack surfaces in the TCF specimens ranged from 96.9 to 137.32 $J.m^{-2}$, and are consistently higher than the G_c values obtained from the four-point bending experiment. This is even true for sintered TBC specimens, as the increase in E_{TBC} values will result in a 20 to 30% increase in fracture toughness [59, 246] and return analogously higher U values in the calculations using eq. 5.12. This means that regardless of the TBC fracture toughness, the stress conditions imposed by TCF testing are sufficiently conducive to crack propagation even during the early stages of thermal exposure. In fact, it has actually been reported that TBCs often show crack nucleation and short range propagation as early as 10 % of their total lifetime [266, 267]. This early trend for crack propagation was also confirmed in this study for the higher tortuosity specimens. The main implication here is that achieving longer TBC lifetimes by itself might not be a matter of preventing the unavoidable propagation through reaching increasingly higher fracture toughness but rather a matter of controlling and mitigating the propagation extent during thermal exposure. For instance, our results suggest that designing the BC interface to obtain more compliant TBC microstructures can affect the crack configuration to such an extent that the amount of energy released each time the crack tip advances is reduced and the area of new fracture surface along with it. These changes are ultimately reflected in a slower crack tip advancement along the interface that delay crack large scale coalescence and increase the potential for higher TBC lifetime.

It is important to note that these calculations also showed that the *U* range comprises a 29% variation between the lowest and highest tortuosity specimens(ΔU). Since eq. 5.12 only takes the as-deposited E_{TBC} into consideration and the ΔU estimated approaches the variation obtained for the as-deposited bending specimens in Fig. 7 $(\Delta G_c = 38\%)$, this suggests that the microstructural factors governing E_{TBC} (i.e. inter-splat cohesion and intra-splat segmentation) are the predominant sources of elastic strain energy storage for posterior release via fracture in both cases. Adding to this, the remaining 7 % discrepancy with ΔG_c can be explained by the contribution of crack deflection due to the inter-splat separation tortuosity. The fact that there is a good match between these two distinct results suggests that the mechanisms governing TBC system failure during bending and TCF specimens displayed enough similarity to justify the correlations seen in Fig. 9.

5.5. Conclusion

The present work has investigated the effect that the manipulation of the BC/TBC interface topographical features has on the fracture mechanics of APS TBCs via four-point bending. It was found that the novel total thresholded summit parameter (S_{sth}) described the BC interface tortuosity effectively and allowed for a correlation with the critical strain energy release rate (G_c), stress intensity factor (K_i), crack propagation velocity (v_{prop}) and TCF lifetime (L_f). These results showed that variations in the degree of BC tortuosity were associated with changes in the degree of inter-splat cohesion, intra-splat segmentation and splat curvature in the TBC. This splat arrangement created a unique splat arrangement that defined the overall crack path configuration and respective propagation behaviour.

More specifically, deposition over higher tortuosity bond coat topographies ($S_{sth} \geq 11.18\,\%$) resulted in more compliant TBC microstructures ($E_{TBC} \leq 84.9 \pm 1.1\ GPa$) with intrinsically lower fracture toughness ($K_{IC} \leq 3.0 \pm 0.2\ MN.m^{-3/2}; K_{IIC} \leq 2.6 \pm 1.7\ MN.m^{-3/2}$) due to reduced inter-splat cohesion and intra-splat segmentation. Under the mixed-mode loading applied($\psi \approx 42^o$), these features facilitated the activation of stress relaxation mechanisms that contributed to lower G_c values upon reaching the critical point ($72.9 \pm 6.1 \leq G_C \leq 79.9 \pm 12.2\,J.m^{-2}$) and slower crack propagation rates thereafter ($v_{prop} \leq 0.9 \pm 0.4\,\mathrm{mm.s^{-1}}$) . Ultimately, these conditions were associated with a higher probability of yielding higher TCF lifetimes due to enhanced strain compliance. Lastly, these results indicate that fracture mechanics of APS TBCS is primarily governed by the degree of inter-splat cohesion and intra-splat segmentation. Surprisingly, even though the inter-splat separation curvature still had a significant impact in reducing the crack driving force (K_{tip}), it displayed a more modest contribution to fracture mechanics.

Appendix A

The Suo-Hutchinson methodology [254] used to determine the critical strain energy release rate of an interfacial crack between two elastic layers is displayed in section 5.2.3.1. However, the equations used to determine the remaining parameters used in the aforementioned calculations are included below.

The compliance parameters (c_1 and c_2) and the bimaterial constant (ε) included in eq. 2 are given by:

$$c_i = \frac{\kappa_i + 1}{\mu_i} \qquad \text{and} \qquad \varepsilon = \frac{1}{2\pi} ln\left(\frac{1-\beta}{1+\beta}\right)$$

where $\kappa_i = 3 - 4\nu_i$ for plane strain, $\mu_i = \frac{E_i}{2(1+\nu_i)}$ is the shear modulus and ν_i the Poisson's ratio. The subscripts $i = 1{,}2$ refer to materials 1 and 2, as defined in section 5.2.3.1.

As material 1 is comprised of multiple layers of different materials and thicknesses, the effective elastic modulus of material 1 (E_1) was calculated according to the rule of mixture methodology employed by Vasinonta & Beuth [239] and Zhao et al. [204] for a TBC layered system. This is predicated on the fact that the constituents' layers of material 1 can be approximated as a single layer and therefore, E_1 can be calculated by:

$$E_1 = \frac{E_{TBC}h_{TBC} + E_s h_s + E_{ad}h_{ad}}{h_s + h_{TBC} + h_{ad}} \qquad (eq\ A1)$$

where $E_{TBC}, E_s\ and\ E_{ad}$ are the elastic moduli of the TBC, stiffener and adhesive; $h_{TBC}, h_s\ and\ h_{ad}$

It is important to note that the elastic modulus of material 2 was approximated as the elastic modulus of the substrate material (i.e. Nimonic alloy 263) to simplify the calculations. This decision was supported by the chemical composition similarities between the substrate and the BC and, the substrate thickness being at least one order of magnitude larger than the thickness of the bond coat (h_{subs}>>h_{BC}).

The remaining non-dimensional parameters $\gamma, \Sigma, \eta, \alpha, \beta, A, I, \Gamma\ and\ p$ found in eqs. 1 and 2 can be calculated by:

$$\Sigma = \frac{1+\alpha}{1-\alpha} \qquad \eta = \frac{h_1}{h_2} \quad \alpha = \frac{\Gamma(\kappa_2+1)-(\kappa_1+1)}{\Gamma(\kappa_2+1)+(\kappa_1+1)} \qquad \beta = \frac{\Gamma(\kappa_2-1)-(\kappa_1-1)}{\Gamma(\kappa_2+1)+(\kappa_1+1)}$$

$$A = \frac{1}{1+\Sigma(4\eta+6\eta^2+3\eta^3)} \qquad I = \frac{1}{12(1+\Sigma\eta^3)} \quad \Gamma = \frac{\mu_1}{\mu_2} \qquad p = \sqrt{\frac{1-\alpha}{1-\beta^2}}$$

where $h_1 = h_s + h_{TBC} + h_{ad}$ and h_2 is the substrate thickness.

The load per unit thickness (*P*) and moment per unit thickness (*M*) in eq. 6 are given by:

$$P = C_2 \frac{P_c(L_{out}-L_{in})}{4bh_1} \qquad \text{and} \qquad M = C_3 \frac{P_c(L_{out}-L_{in})}{4b}$$

with

$$C_1 = \frac{\Sigma}{A_0} \qquad C_2 = \frac{\Sigma}{I_0}\left(\frac{1}{\eta} - \Delta + \frac{1}{2}\right) \qquad C_3 = \frac{\Sigma}{12I_0} \qquad A_0 = \frac{1}{\eta} + \Sigma \qquad \Delta = \frac{1+2\Sigma\eta+\Sigma\eta^2}{2\eta(1+\Sigma\eta)}$$

$$I_0 = \Sigma\left[\left(\Delta - \frac{1}{\eta}\right)^2 - \left(\Delta - \frac{1}{\eta}\right) + \frac{1}{3}\right] + \frac{\Delta}{\eta}\left(\Delta - \frac{1}{\eta}\right) + \frac{1}{3\eta^3}3$$

where P_c is the critical load, b is the specimens' width, $L_{out}\, and\ L_{in}$ the outer and inner spans.

Lastly, the λ and ω parameters used in eq. 3 can be determined by:

$$\lambda = \sqrt{\frac{I}{A}\frac{Ph_1}{M}} \qquad \omega = 52.1 - 3\eta \qquad \gamma = \sin^{-1}\left[6\Sigma\eta^2(1+\eta)\sqrt{AI}\right]$$

The principles involved in the four-point bending are illustrated in Fig A1 (appendix A) to facilitate their interpretation in the context of a multi-layered beam system with a crack propagating the interface.

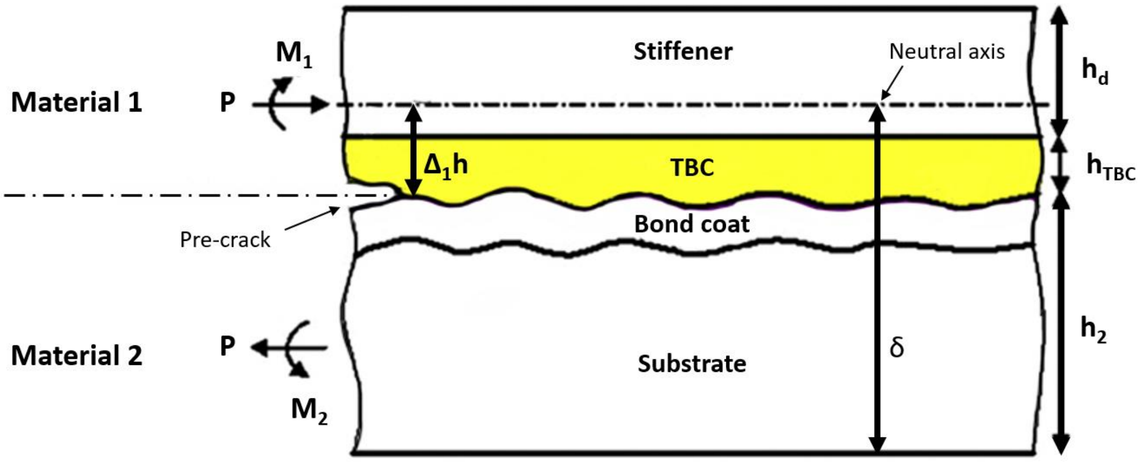

Fig. A1 A schematic illustration of the interface cracking model where the load (*P*) and moment (*M*) per unit of thickness are represented for materials 1 and 2. The location of the neutral axis (δ) is also shown here.

Table A1 Experimental data used in the calculation of the strain energy release rate and respective results for the Hofinger and the Suo-Hutchinson methods. The elastic modulus for materials 1 and 2 have been calculated according to equations A1.

Specimen ID	E_{TBC} (GPa)	E_1 (GPa)	E_2 (GPa)	h_2 (mm)	h_{TBC} (mm)	b (mm)	P_C (N)	G_C (J.m^{-2})	K_I (MN.m$^{-3/2}$)	K_{II} (MN.m$^{-3/2}$)
G1.1	85.4	174.7	209.9	3.50	0.33	2.40	455	98.6	3.37	2.97
G1.2	86.0	168.6	200.9	3.49	0.32	2.41	463	103.8	3.38	3.00
G1.3	83.5	178.6	206.1	3.61	0.35	2.40	475	93.6	3.32	2.94
G2.1	81.3	167.5	200.2	3.70	0.31	2.28	386	67.8	2.72	2.43
G2.2	83.6	176.9	213.3	3.25	0.32	2.42	371	81.9	3.10	2.72
G2.3	88.2	167.1	198.8	3.70	0.32	2.36	401	68.9	2.74	2.44
G3.1	89.2	180.2	218.2	3.25	0.37	2.39	465	100.3	3.04	3.04
G3.2	87.0	167.8	201.3	3.53	0.35	2.43	450	97.8	3.29	2.90
G3.3	96.9	181.9	220.2	3.67	0.38	2.39	493	86.3	3.21	2.87
G4.1	81.0	172.6	209.4	3.55	0.34	2.32	416	83.5	3.08	2.73
G4.2	82.9	169.1	204.4	3.71	0.35	2.34	413	71.9	2.83	2.52
G4.3	79.9	157.1	187.2	3.70	0.34	2.46	398	66.2	2.61	2.31
G5.1	90.0	167.5	200.2	3.40	0.35	2.47	469	102.9	3.36	2.98
G5.2	87.1	167.4	201.7	3.41	0.33	2.45	459	105.9	3.42	3.02
G5.3	84.3	160.3	190.5	3.71	0.35	2.46	453	95.6	3.18	2.79
G6.1	113.9	176.4	207.5	3.38	0.37	2.58	519	127.9	3.82	3.41
G6.2	102.4	180.8	213.4	3.60	0.32	2.37	488	103.3	3.47	3.11
G6.3	117.5	180.5	214.8	3.45	0.33	2.38	502	119.6	3.75	3.35
G7.1	74.5	175.6	213.9	3.39	0.35	2.46	399	79.8	3.07	2.68
G7.2	79.4	162.6	198.2	3.33	0.38	2.45	406	94.8	3.21	2.81
G7.3	82.5	172.5	208.7	3.74	0.36	2.40	413	64.9	2.73	2.39
G8.1	81.1	179.5	217.4	3.36	0.34	2.51	406	80.7	3.11	2.72
G8.2	73.4	156.7	190.2	3.38	0.35	2.54	395	82.8	2.94	2.58
G8.3	74.3	166.1	203.8	3.73	0.38	2.45	402	61.2	2.62	2.28

Appendix B

The python script used to perform all fracture mechanics calculations

```
import xlrd
import xlwt
import math
import numpy as np
sheet=2 #Read sheet No. from 0(The first sheet is 0)
def catch(y): #Get values in list, replace null to int '1' & data strings to float.
    x=table.col_values(y)
    for j in range(0,len(label)):
        if label[j]==1:
            if x[j]=='':
                x[j]=1
            else: x[j]=float(x[j])
        else:x[j]=1
    return x
def Suo_Hutchinson(E1,E2,v1,v2,h,H,P0,b): # Implementation of Suo-Hutchinson equations
    mu1=E1/(2*(1+v1))
    mu2=E2/(2*(1+v2))
    k1=3-4*v1
    k2=3-4*v2
    c1=(k1+1)/mu1
    c2=(k2+1)/mu2
    eta=h/H
    _Gamma_=mu1/mu2
    alpha=(_Gamma_*(k2+1)-(k1+1))/(_Gamma_*(k2+1)+(k1+1))
    _Sigma_=(1+alpha)/(1-alpha)
    beta=(_Gamma_*(k2-1)-(k1-1))/(_Gamma_*(k2+1)+(k1+1))
    epsilon=(1/(2*np.pi))*np.log((1-beta)/(1+beta))
    Delta=(1+2*_Sigma_*eta+_Sigma_*eta**2)/(2*eta*(1+_Sigma_*eta))
    I0=_Sigma_*((Delta-1/eta)**2-(Delta-1/eta)+1/3)+(Delta/eta)*(Delta-1/eta)+1/(3*eta**3)
    C2=(_Sigma_/I0)*(1/eta-Delta+1/2)
    C3=_Sigma_/(12*I0)
    P=C2*((P0*(L1-L))/(4*b*h))
    M=C3*((P0*(L1-L))/(4*b))
    I=1/(12*(1+_Sigma_*eta**3))
    A=1/(1+_Sigma_*(4*eta+6*eta**2+3*eta**3))
    Lambda=math.sqrt(I/A)*(P*h/M)
    omega=52.1-3*eta
    R_omega=omega*np.pi/180
    R_gamma=math.asin(6*_Sigma_*eta**2*(1+eta)*math.sqrt(A*I))
    gamma=R_gamma*180/np.pi
    Psi=math.atan((Lambda*math.sin(R_omega)-
math.cos(R_omega+R_gamma))/(Lambda*math.cos(R_omega)+math.sin(R_omega+R_gamma)))
    G=(c1/16)*((P**2)/(A*h)+(M**2)/(I*h**3)+(2*P*M)/(math.sqrt(A*I)*h**2)*math.sin(R_gamma))
    K=(4*math.cosh(np.pi*epsilon)/(math.sqrt(c1+c2)))*math.sqrt(G)
    KI=K*math.cos(Psi)
    KII=K*math.sin(Psi)
    PA=180*np.arctan(KII/KI)/np.pi
    print (epsilon)
    return K,G,KI,KII,PA
data=xlrd.open_workbook('C:/Users/ Documents/calculations.xlsx') #Your file location
table=data.sheets()[sheet] #Save extracted sheet into memory
group=table.col_values(0) #Get sample ID info
label=table.col_values(1) #Get the label '1'
sample=table.col_values(2) #Get the Sample labels
for i in range(0,len(label)): #Convert label list to array
    if label[i]=='':label[i]=0
    else:label[i]=1

L1=table.cell(2,3).value #Outer span distance
L=table.cell(2,4).value #Inner span distance
v1=table.cell(2,6).value #TBC Poisson’s ratio
v2=table.cell(2,7).value #Substrate Poisson’s ratio
vd=v2 # StiffenerPoisson’s ratio
nrows=table.nrows
Pc=catch(3) #Critical Load
h1=catch(10) #TBC thickness
h2=catch(9) #Sub thickness
hd=catch(8) #Stiffener thickness
E1=catch(4) #Material 1 elastic modulus
E2=catch(6) # Material 2 elastic modulus
b=catch(13) #Beam width
Ed=E2
G=np.zeros(nrows)
K=np.zeros(nrows)
G_Suo=np.zeros(nrows)
KI=np.zeros(nrows)
KII=np.zeros(nrows)
PA=np.zeros(nrows)

for i in range(0,nrows): #Function running
    K[i],G_Suo[i],KI[i],KII[i],PA[i]=Suo_Hutchinson(E1[i],E2[i],v1,v2,h1[i]+hd[i]+0.0003,h2[i],Pc[i],b[i]
for i in range(0,nrows): #Output
    if label[i]==1:
        print(group[i],'\n',sample[i],'\n' ,G[i],'\n','G_Suo_Hutchinson =',G_Suo[i])
        print('K =',K[i],'KI =',KI[i],'KII =',KII[i],'Phase angle =',PA[i])
```

Chapter 6. Effect of bond coat microstructure of CoNiCrAlY coatings on the oxide scale formation

Credit authorship contribution: **João P. Martins, Zhaohe Gao, Shying Qin, Ying Chen, Ping Xiao**

6.1. Introduction

MCrAlY (M=Ni, Co or both) overlay coatings have been widely used in gas-turbine engines with the purpose of providing efficient oxidation and corrosion protection to the underlying components at high temperatures [12, 81, 133]. Their effectiveness is primarily reliant on the ability to promote the formation of a continuous, dense, adherent, slow-growing and thermodynamically stable α-Al_2O_3 oxide scale upon exposure to high-temperatures [83, 143]. However, the thermally grown oxide (TGO) formation is a complex process influenced by multiple concurrent factors such as the BC chemical composition and internal microstructure, bond coat surface topography (i.e. roughness, curvature and distance between asperities [60]) and thermal exposure conditions (i.e. oxygen partial pressure and temperature) [140].

The study of the oxidation behaviour of MCrAlY coatings has been the focus of extensive research over the past decades due to the central role of oxidation on protection provided by the coatings. This research has provided a good insight into how the bond coat microstructure and composition affect the formation of the oxide scale and its evolution with oxidation time [133, 135, 142, 146, 268]. The Co-rich MCrAlY chemistries (i.e. CoNiCrAlY) have been of particular interest since their intrinsic oxidation kinetics behaviour still presents some challenges in terms of thermo-chemical degradation of the protective oxide scale. A large number of oxidation studies conducted on CoNiCrAlY coatings have reported that the oxide scales formed over these bond coat compositions show a great microstructural and compositional diversity that can affect the TBC system performance. In fact, a significant number of these studies have reported that the gradual formation of a continuous and persistent duplex oxide scale with a mixed oxide-rich outer scale primarily comprised of $CoCr_2O_4$ and Cr_2O_3 is fairly common [151, 154, 202, 269-271]. Some of these studies have also noted that the outer scale shows an inhomogeneous morphology comprised of small equiaxed grain morphology, persistent presence of porosity at the inner/outer scale boundaries and formation of large heterogeneities at the surface [151, 269]. FEM simulations conducted by Ni et al. [154] have demonstrated that the formation of dual-layer oxide scale with a mixed oxide-rich outer layer results in higher residual stresses and can lead to premature failure. A recent study by Doolabi et al. [270] has moved on to explore the effects of BC microstructure on the formation of the outer scale and found that a dual-phase microstructure with coarse grain size and low dislocation density increased the probability of outer scale formation due to reduced Al^{3+} diffusion flux profiles. On the other hand, Saeidi et al. [108] followed a preventive approach focused on inhibiting the formation of a Cr-rich spinel outer layer by conducting a vacuum heat treatment (3h at 1100°C) on the BC surface prior to the TBC deposition. Although this procedure was able to mitigate the formation of the outer scale to a certain extent and slow down the TGO growth rate, the formation of a mixed oxide outer scale that has a significant effect on the TBC system performance can still be observed [202, 272, 273]. This highlights the importance of improving the mechanistic understanding of the formation process of the outer scale and its impact on the oxide scale failure to develop new methodologies to prevent its formation, as this is still not fully understood.

The main aim of the current study is to provide a comprehensive characterisation and mechanistic understanding of the formation, evolution and thermo-chemical degradation of oxide scales forming over HVOF CoNiCrAlY coatings at high temperatures. Multiple specimens of similar microstructure and nominal composition specimens were isothermally heat treated for different intervals of time to facilitate the microstructural and compositional study of the oxide scale during different stages of oxidation. The oxide scales were characterised by conducting a correlative microscopy approach that combined the microstructural, compositional and topographical results obtained from scanning electron microscopy (SEM), transmission electron microscopy (TEM) and 3-D laser confocal microscopy (CLSM). These measurements were complemented by photoluminescence piezospectroscopy (PLPS) to perform the phase identification of the oxide scale in the initial stages of oxidation and the evolution of the residual stress thereafter. The impact of the BC microstructure on the formation process of the outer scale and subsequent evolution with oxidation time is then described in terms of oxidation kinetics, focusing on the γ/β grain boundary (i.e. phase boundaries) diffusion relationship with mixed oxide formation in the outer scale. The effects associated with the incorporation and diffusion of Cr^{3+} across the oxide scale are also addressed in terms of its impact on the transient oxidation regime and residual stresses throughout the oxidation.

6.2. Materials and methods

6.2.1 Sample fabrication and preparation

The bare MCrAlY bond coat specimens were fabricated via HVOF deposition of CoNiCrAlY powder (Bal. Co, 31-33% Ni, 20-22% Cr, 7-9% Al, 0.35-0.65% Y, H.C. Stark, AMPERIT® 405.072) onto the surface of a polycrystalline Nimonic Alloy 263 substrate (Ø=25 mm, height=6mm). The average thickness achieved for these coatings (~165 μm) was helpful in minimising the effect of substrate inter-diffusion on the formation of the oxide scale during the initial stages of oxidation. The specimens were then annealed for 1 hour at 1100°C in an Argon atmosphere ($p_{O^{2-}}$=1.7x10^{-1} mbar) to promote the homogenisation of the BC internal microstructure (i.e. increase β–phase grain size and promote an interspersed distribution) and relax the residual stresses arising from deposition. The coated superalloy specimen was then sectioned into a parallelepiped shape (5x5x6 mm^3) and the BC top surface polished to a 0.25 µm surface finish according to the metallographic procedure described in section 3.1. This process generated a smooth surface with very low surface roughness ($S_a = 0.016 \pm 0.002\ \mu\text{m}$) that mitigated any contributions of BC surface heterogeneities to the formation of the oxide scale. Several Vickers micro-indentations were made on the BC top surface and used as markers to correlate the as-polished BC microstructure with the oxide formations growing atop. The subsequent isothermal thermal exposure was performed under atmospheric conditions in a CM^{TM} furnace following the specifications in section 3.2 until spallation of more than 50% of the oxide scale was observed.

6.2.2 Sample characterisation

The as-polished BC surface was characterised by 3-D laser scanning confocal microscopy (VK-X200K, Keyence) and SEM (Tescan Mira3 LC) equipped with EDS elemental analysis (X-Max 150 mm^2, Oxford Instruments) according to the procedures described in sections 3.3.1 and 3.3.2, respectively. EBSD mapping (Nordlys Nano, Oxford Instruments) was also conducted on the BC surface following the experimental methodology described in section 3.3.2 to acquire additional information regarding the grain size and distribution.

After oxidation, the oxide scale phase identification and residual stresses measurements were carried out on a Renishaw InVia Raman microscope equipped with a He-Ne laser source (λ=633 nm) according to the experimental photoluminescence piezospectroscopy (PLPS) methodology described in section 3.3.5 and reference [274]. The oxide scale surface topography, morphology and composition were then investigated using a combination of laser scanning confocal microscopy and SEM/EDS. The surface texture parameter selected to characterise the evolution of the oxide scale topography with oxidation time (t_O) was the arithmetic mean roughness (S_a) defined in section 4.2.2.1.The heat-treated specimens were then cross-sectioned using a focused ion-beam-scanning electron microscope (FIB-SEM, FEI Helios Nanolab 660) coupled with a X-Max 150 mm^2 EDS system in order to study the oxide scale morphology and respective chemical composition without introducing any mechanical damage in the specimen. The equivalent thickness of the oxide scale (δ_{eq}) was determined from five different FIB cross-sections (ImageJ, Area tool) in accordance with the procedure described in section 4.2.1. Cross-sectional thin lamellae ($\sim$100 nm) were subsequently prepared by FIB milling according to the methodology described by Langford and Long [275] and analysed via scanning transmission electron microscope (STEM, FEI $Tecnai^{TM}$ G2 200kV) equipped with an EDS system X-maxN 80T (Oxford instruments). The main purpose of using this technique was to confirm that the degradation of the outer scale is associated with outward diffusion of non-Al elements along the grain boundaries the oxide scale.

6.3. Results

6.3.1 Pre-oxidation microstructure

Fig. 6.1 shows a low-magnification cross-sectional overview (a) and high-magnification top surface view (b-) of the as-polished HVOF BC microstructure prior to oxidation alongside the respective phase (c) and composition (-d, -e) analyses results. The HVOF coatings displayed a dense and homogeneous dual-phase microstructure comprised of a γ-Co phase (lighter contrast) and a β–phase (darker contrast), primarily differentiated by the BSD contrast variation in Fig. 6.1-b) and EDS spectra in Figs. 6.1-d) and -e). The EBSD map conducted on the BC top surface shown in Fig. 6.1-c) has provided additional information regarding the average grain morphology, size and distribution of each phase. The resulting grain size, aspect ratio and phase fraction results were determined via image analysis of the phase contrast map in Fig. 6.1-c) (HKL Tango software, Oxford instruments) and compiled in table 6.1. Results showed that both phases displayed similar sub-micron average grain areas ($A_{G\gamma} = 0.64 \pm 0.41\ \mu m^2$; $A_{G\beta} = 0.41 \pm 0.27\ \mu m^2$) and aspect ratios ($AR_\gamma = 2.05 \pm 0.88$; $AR_{G\beta} = 1.84 \pm 0.68$), indicating a predominant formation of slightly elongated nanocrystalline grains in the BC microstructure. This is relevant to the early oxidation behaviour of the coating as sub-micron elongated grains are known to affect the oxide scale formation process [146].

The EBSD map analysis also revealed a larger presence of γ-phase grains in the BC microstructure that translated into an approximate γ/β phase ratio of 3:1, in accordance with previous thermodynamic calculations of phase equilibrium for CoNiCrAlY coatings with 8 wt.% Al in the literature (see table 6.1) [276]. The resulting inhomogeneous distribution of β grains across the coating led to a phase segregated microstructure consisting of partially connected clusters of Al-rich β-phase regions (~28.4 at.%) surrounded by Al-poor γ–phase regions (~9 at.%) (see Fig. 6.1-c). The compositional analysis in Figs. 6.1-d) and e) also revealed that the Ni and Al contents in the β-phase were well below those of stoichiometric β-NiAl and indicated a significant presence of Co (18.7 at.%) and Cr (18 at.%) in the β-phase. This is a strong indication that Co and Cr have occupied the Ni and Al sublattices respectively, as previous research has shown that both sublattices must always be fully occupied [277, 278]. All these microstructural and compositional changes combined have significant implications on the subscale Al distribution and subsequent diffusion to the interface during the early stages of oxidation, leading to alterations in the rate of formation, structure and composition of the oxide scale.

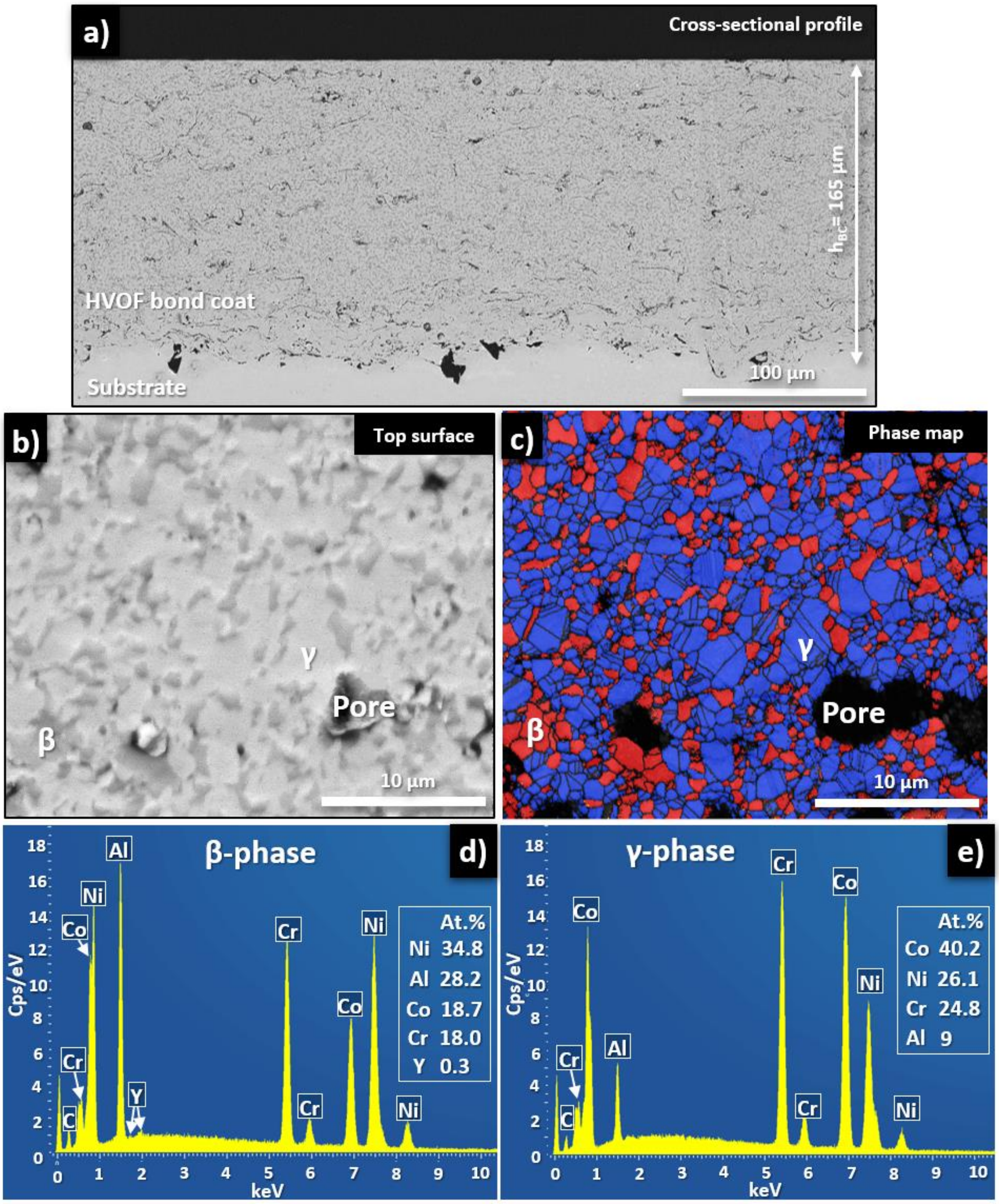

Figure 6.1 (a) Cross-sectional and (b) top view surface BSE micrographs depicting the as-polished microstructure of the HVOF coatings; (c) EBSD phase map contrast map of the same region represented in the (b), where the red areas were indexed as β-phase, the blue areas as γ-phase and black areas as unindexed; Representative EDS spectra and chemical composition of the (d) β and (f) γ-phases obtained from area analysis.

Other less prominent microstructural features like the occasional presence of oxide inclusions and low porosity content (~2%) were also observed in the microstructure, albeit exclusively located at the inter-splat boundaries. These features were originated by the minimal in-flight oxidation of the powder feedstock and post-impact cohesive arrangement of the melted particles promoted by the

HVOF low processing temperatures and high particle velocities. Although Cr-rich oxide formations formed over these regions and contribute to the local de-stabilisation of the oxide scale, the infrequent presence in the coating did not produce a meaningful impact on the overall oxidation behaviour.

Table 6. 1 Representative average grain size, aspect ratio and phase fractions of the as-polished HVOF BC specimens.

Phase	**Grain area, A_G (μm^2)**	**Aspect ratio, AR**	**Experimental phase fraction (%)**	**Predicted phase fraction**
γ	0.64±0.41	2.05±0.88	68.99	76 [276]
β	0.41±0.27	1.84±0.68	26.90	24 [276]

6.3.2 Oxide growth correlation with the BC microstructure

Fig. 6.2 depicts the surface morphology of the same region of the HVOF coating before (-a) and after 10 min oxidation (-b,-c), alongside the respective chemical element distribution in the EDS map overlay (-d). The initial distribution and size of the β grains within the region of interest are shown by the BSD micrograph of the as-polished BC surface presented in Fig. 6.2-a). The correlation with the respective oxide scale surface in Fig. 6.2-b) revealed the formation of oxides with distinct morphologies and topographies over each phase, a clear indication of site-specific oxidation behaviour. The oxides forming over the β grains displayed a convex semi-hemispherical morphology that originated a significant topographical variation in relation to the surrounding oxides forming over γ grains. Although this behaviour is indicative of a faster growth rate and suggests the formation of metastable alumina at some point during the initial stages of oxidation (i.e. γ-Al_2O_3, θ-Al_2O_3) [81, 146], no evidence was found in the PLPS spectra of the Al_2O_3 scales (see section 6.3.6). The reason why metastable alumina has not been detected is discussed in section 6.4.3. On the other hand, the oxide scale segments growing over γ grains displayed a notably smaller and more homogenous grain morphology that is presumably correlated with a slower growth rate and formation of α-Al_2O_3. This was effectively confirmed by the aforementioned PLPS analysis in section 6.3.6.

The BSE micrograph of the oxide scale surface displayed in Fig. 6.2-c) showed significant variations in the oxide scale contrast across the surface, thus indicating that oxides with higher atomic number are predominantly forming over the edges of β grains. The respective EDS map overlay in Fig. 6.2-d) revealed that although the oxide scale was predominantly comprised of Al and O (darker contrast), some regions contained significantly higher quantities of Co and Ni (brighter contrast). The distribution of these mixed oxide (MO) formations over the β grains was found to vary with grain size and distance between γ/β grain boundaries, as evidenced by the correlation of the regions highlighted in Figs. 6.2-a) and –b) (dashed box areas). This was further supported by the fact that the MO formations were found primarily along the γ/β grain boundaries in larger β grains (green dashed area) and over most of the grain surface in smaller grains (yellow dashed area). It is noteworthy that MO formations were also found to be growing over γ grain boundaries (red dashed area), although with less frequency and smaller sizes.

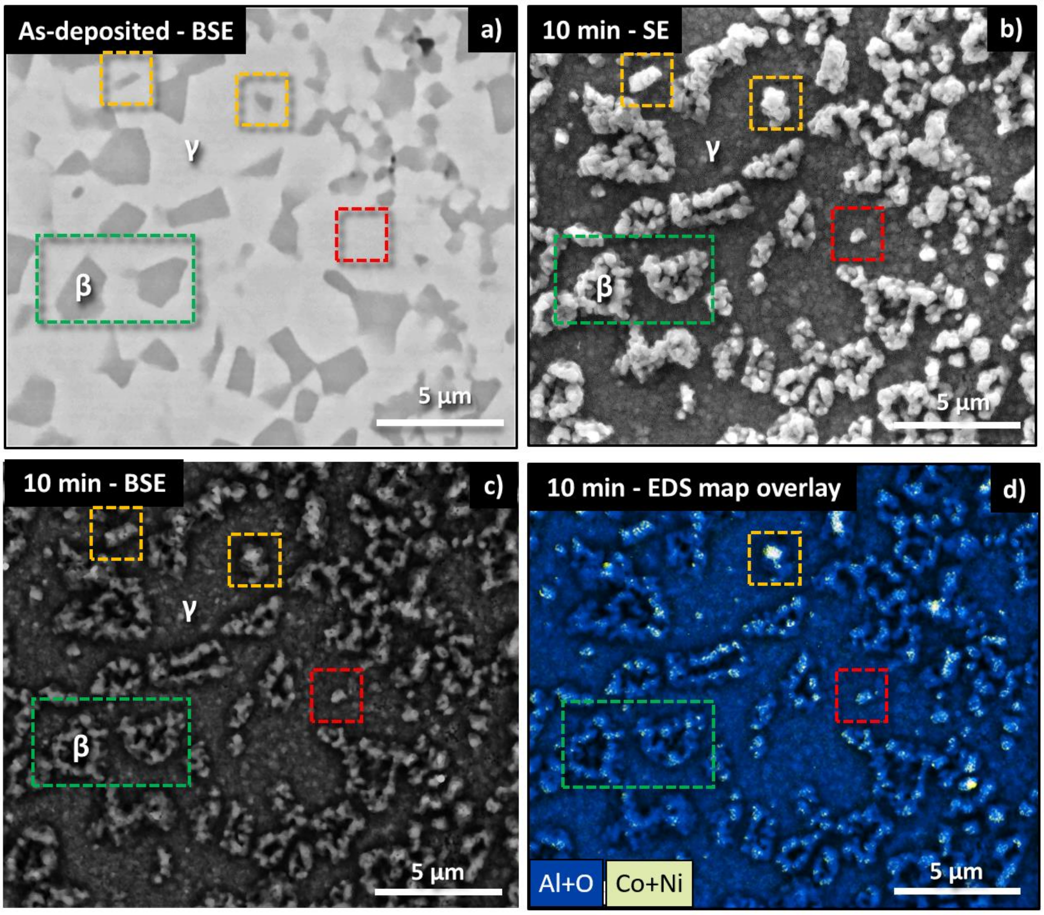

Figure 6.2 (a) BSE micrograph displaying the as-polished BC surface morphology and the respective (b) SE and (c) BSE mode imagery of the oxide scale growing atop; (d) EDS map overlay displaying the distribution of Al+O and Co+Ni ($EHT = 10keV$). The green, yellow and red areas delineated by a dashed line indicate regions of the BC where larger, small and no β grains are found.

6.3.3 Oxide scale structure and composition

The oxide scale structure and composition analysis was performed on a more mature oxide scale (i.e. 120 min oxidation) and the results are displayed in Fig 6.3. This scale was purposefully selected for this analysis since its cross-sectional equivalent thickness (~ 0.98 ± 0.11 µm) surpasses the maximum photon generation depth in Al_2O_3 (0.7 µm, calculated from eq. 3.1 for a 10 keV EHT) and mitigates any

BC contributions to the BSD and EDS signals. Nevertheless, it is important to note that the absolute atomic fraction values provided herein may have been slightly affected by the geometry and depth of the microstructural features as well as by the respective electron beam interaction volume and/or different atomic numbers of its constituents. However, the results obtained can be considered illustrative of the elements presence in certain microstructural features and respective main compositional trends.

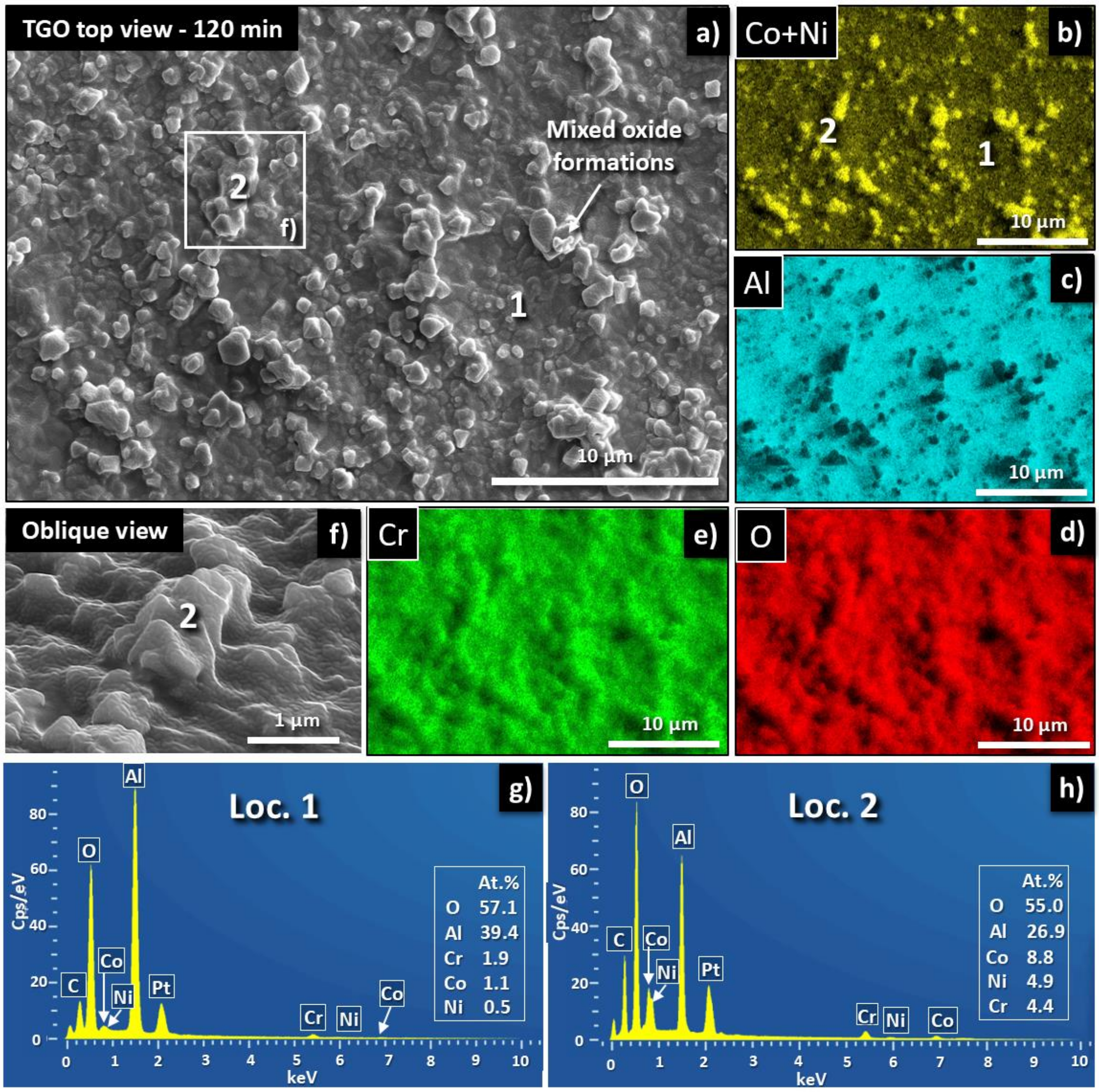
TGO top view - 120 min
a)
2
f)
Mixed oxide formations
1
10 µm
Co+Ni
b)
2
1
10 µm
Al
c)
10 µm
Oblique view
f)
2
1 µm
Cr
e)
10 µm
O
d)
10 µm
Loc. 1
g)
Cps/eV
keV
Al
O
C
Co
Ni
Pt
Cr
Ni
Co
At.%
O 57.1
Al 39.4
Cr 1.9
Co 1.1
Ni 0.5
Loc. 2
h)
O
Al
C
Co
Ni
Pt
Cr
Ni
Co
At.%
O 55.0
Al 26.9
Co 8.8
Ni 4.9
Cr 4.4

Figure 6.3 (a) Top view SE micrograph ($EHT = 10keV$) of an oxide scale formed after 120 min of isothermal thermal exposure and (b-e) respective EDS maps alongside a (f) high magnification oblique view of a mixed oxide ridge formation; EDS spectra obtained from area analysis of (g) the inner scale (region 1) and (h) mixed oxide formations (region 2).

Fig. 6.3-a) displays an overview of the irregular oxide scale surface morphology formed after 120 min of oxidation where two types of oxide formations were identified, smaller homogeneous grains (region 1) and convex semi-hemispherical outward growing heterogeneities (region 2). The respective

EDS maps and area analysis spectra presented in Figs. 6.3-b) to –g) showed that region 1 is predominantly comprised of a continuous Al_2O_3 layer with minor incorporation of other metallic elements such as Cr (~2 at.%), Co(~1.1 at.%) and Ni (~2 at.%). These maps also showed that whilst Cr incorporated the oxide scale homogeneously, Co and Ni displayed a sparser presence that resulted in a clustered distribution. This suggests that some regions of the oxide scale are more prone to the nucleation of MO formations than others, as noted in the previous section. The incorporation of Cr in the oxide scale was effectively confirmed by the results of the FIB/EDS cross-sectional analysis in Fig. 6.4, as the Cr map (-d) and linescan analysis across the scale (-g) showed a larger concentration along the TGO scale segment of region 1. The same analysis also revealed that Co and Ni were mostly distributed at the surface of the oxide scale in this region, as evidenced by the contour-like effect observed in the Co+Ni EDS map and linescan in Figs. 6.4-e) and –h), respectively. This suggests the existence of a continuous thin outer scale that covers the whole oxide scale surface. The outer scale existence was effectively confirmed by high magnification STEM-HAADF analysis, as illustrated in Fig. 6.4-b) and previously noted in the literature [108, 269, 270]. The boundary between the inner and outer scales was defined as the region where the grain morphology shifted from columnar to an equiaxed morphology.

In contrast, the mixed oxide formations observed in region 2 formed extensive ridge-like structures across the surface, as depicted in Figs. 6.3-a) and -f). This ridge network morphology has been previously identified by Brumm & Grabke in NiAl coatings [279], thereby contextualising their preferential formation over β grains in this study. The resulting semi-hemispherical convex morphology observed and the interspersed distribution along the oxide scale grain boundaries are suggestive of a diffusion-based formation mechanism driven by outward diffusion of metallic elements along the oxide scale grain boundaries. The respective EDS maps and area analysis spectrum presented in Figs. 6.3-b) to -e) and –h) showed that these oxide formations are comprised of a mixture of Al (at.% 26.9) with other metallic elements such as Co (at.% 8.8), Ni (at.% 4.9) and Cr (at.% 4.4) after 120 min of oxidation. The cross-sectional analysis in Figs. 6.4-a) and -b) has additionally revealed that these formations are well integrated into the outer scale and the resulting boundary region formed with the inner scale is usually populated by a considerable amount of small-scale voids. The formation of these voids can be explained either by the volumetric shrinkage associated with a solid state reaction between Al_2O_3 and transient MO formations (NiO, CoO, Cr_2O_3) to form spinel [12], and/or vacancy injection and coalescence mechanism (Kirkendall effect) due to the different diffusivity of the elements present in this region at the inner/outer scale interface [146].

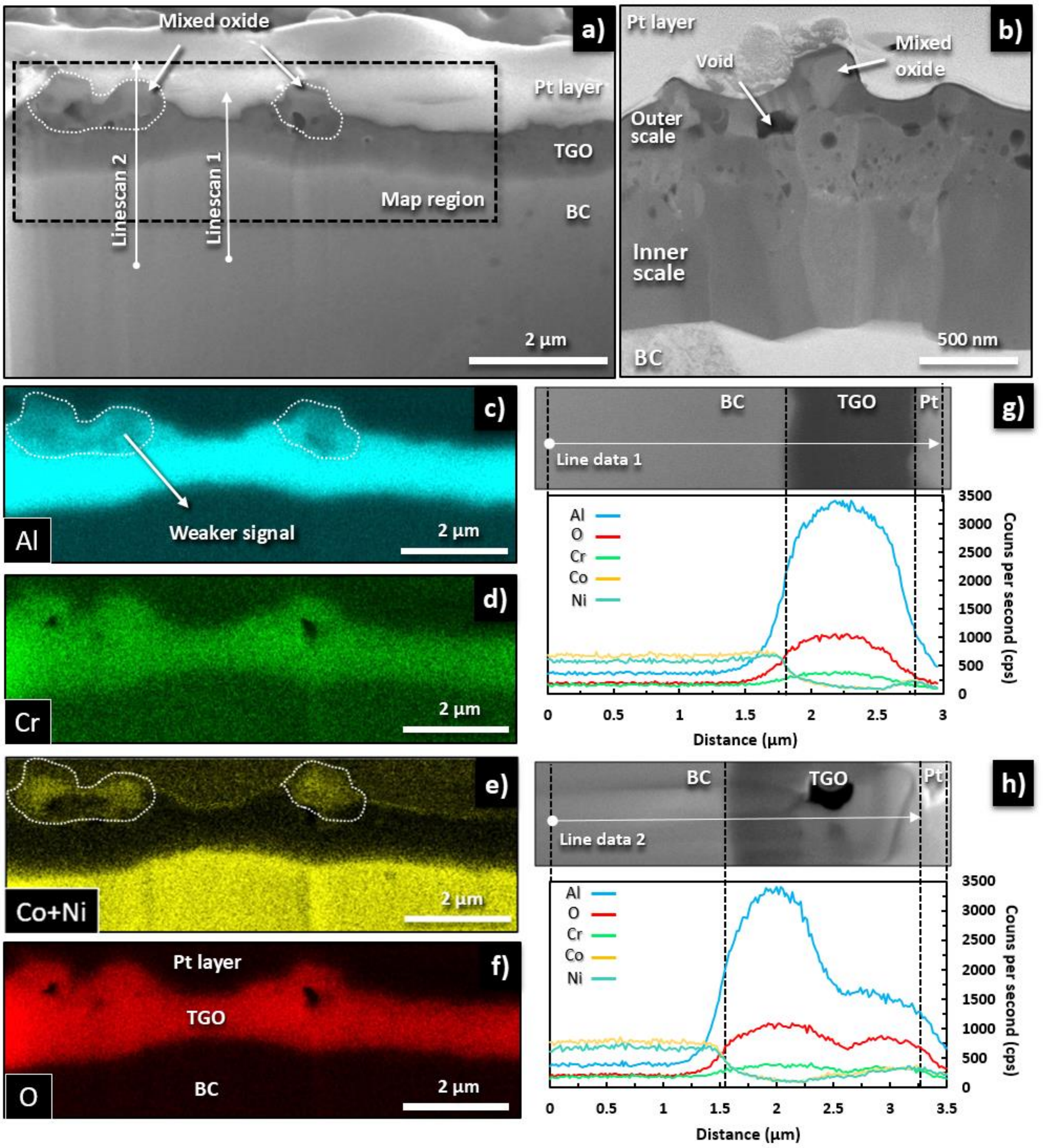

Figure 6.4 (a) FIB cross-section of the TGO scale after 120 min oxidation and (b) representative depiction of the microstructural features found at the inner/outer scale boundary obtained from STEM-HAADF; EDS map analysis of the framed area (c-f) and linescan analysis displaying the element across the near-interface BC and TGO segments in regions (g) 1 and (h) 2.

A similar analysis was also conducted on the remaining heat treated specimens to investigate how the oxide scale microstructure and composition evolved with oxidation time. The concentration of Co, Cr and Ni in the oxide scale was quantified by EDS point analysis at 10 keV to enhance surface sensitivity, and plotted as a function of oxidation time in Figs. 6.5-a) and –b) for specimens with thicker oxide scales (> 60 min oxidation). The results in Fig. 6.5-a) confirmed that the incorporation of Cr in the oxide scale was persistent during the whole thermal exposure but varied significantly with oxidation time and location in the scale (i.e. inner or outer layer). The plot showed that Cr concentration in the inner scale was higher during the initial stages of oxidation (i.e. < 60 min) but quickly decreased and stabilised around 1 at.% after 240 min. In contrast, the Cr concentration in the outer scale was only determined for thicker oxide scale specimens (> 60 min) due to thickness limitations but the results showed a sub-parabolic increasing trend from ∼3 at.% to ∼10 at% after 3000 min. These results indicate a slow but consistent Cr segregation in the outer scale. Fig. 6.5-b) also showed that Co and Ni concentrations in the outer scale increased with oxidation time according to a power-law trend (R_{Co}^2= 0.93), respectively reaching ∼7 at.% and 10 at.% after 3000 min. These results suggest that Co, Cr and Ni are not only incorporating the oxide scale since the initial stages of oxidation but are also segregating to the outermost section of the scale. This is further asserted by the fact that their combined concentration in the outer scale already amounted to ∼26 at.% after 3000 min, slightly below the Al concentration (∼28 at.%). These results are relevant to the early stage formation, as the evolution of the oxide scale with thermal exposure is already showing a transformational tendency towards the formation of the MO-rich outer layer commonly reported in the literature for CoNiCrAlY coatings. This topic is further explored in the next section.

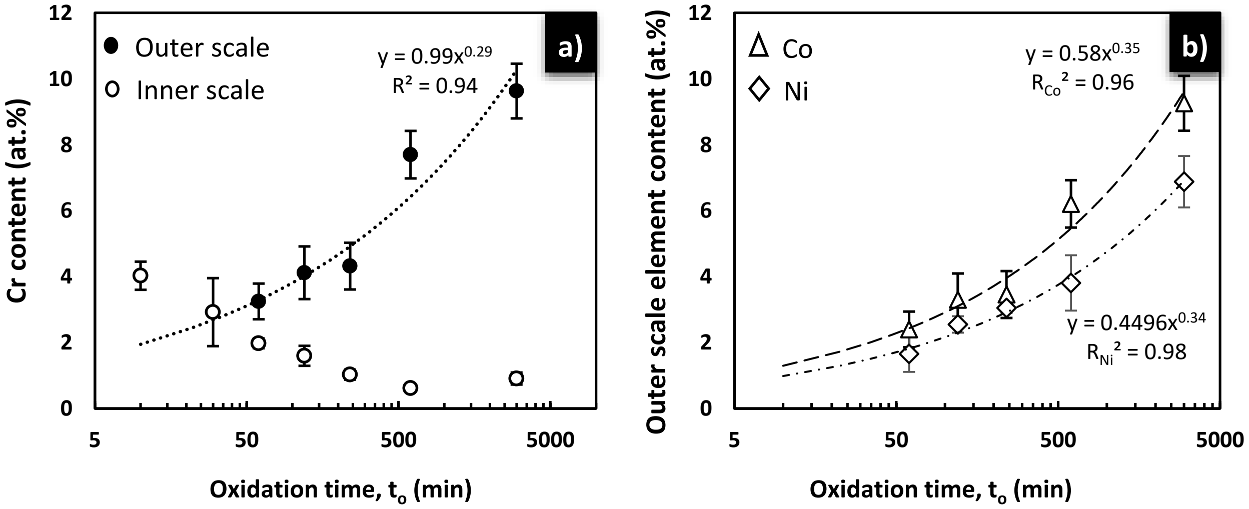

Figure 6. 5 Evolution of the atomic fraction of (a) Cr in the inner and outer scales and (b) Co and Ni in the outer scale, obtained from EDS point analysis at 10 keV. Each data point corresponds to the average of 10 measurements performed in three different FIB cross-sections. The abscissa axis of both plots is shown in a logarithmic scale of base 10 to improve the visual perception of the overall trend.

6.3.4 Evolution of the oxide scale with oxidation time

Figs. 6.6 is a compilation of SEM micrographs obtained at low EHT (i.e. 5keV) depicting the evolution of the oxide scale surface morphology with oxidation time from a top view perspective. Each row of micrographs represents a specific oxidation time and includes a lower magnification overview of the surface morphology (left column) alongside higher magnification SE (middle column) and BSD (right column) imagery of the main oxide formations identified. The continuous Al_2O_3 inner scale (region 1) and mixed oxide ridge formations (region 2) identified in the previous section are also identified herein to contextualise their distribution across the oxide scale surface and morphological evolution with oxidation time.

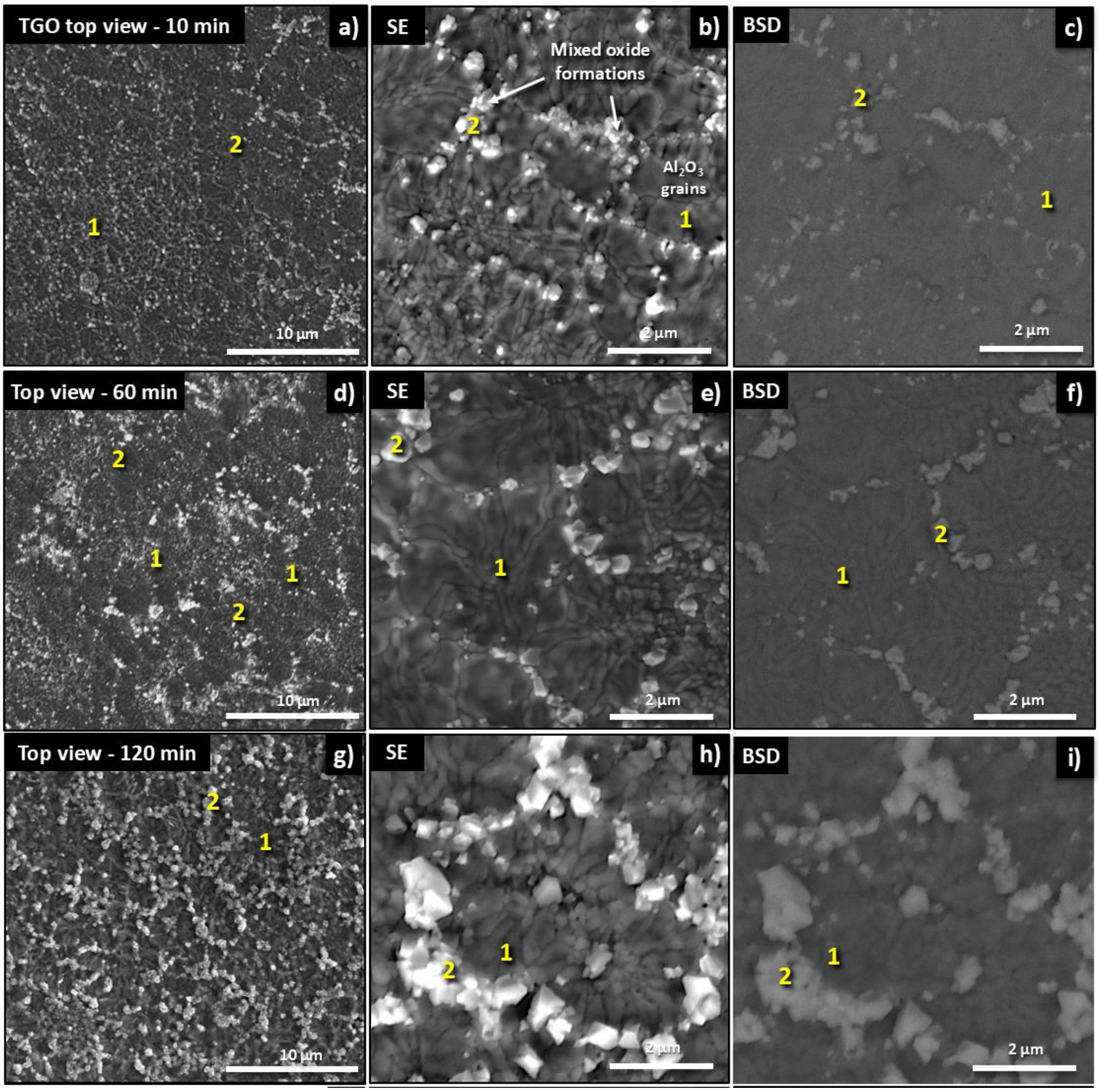
TGO top view - 10 min
a)
2
1
10 µm
SE
b)
Mixed oxide formations
2
Al_2O_3 grains
1
2 µm
BSD
c)
2
1
2 µm
Top view - 60 min
d)
2
1
1
2
10 µm
SE
e)
2
1
2 µm
BSD
f)
2
1
2 µm
Top view - 120 min
g)
2
1
10 µm
SE
h)
1
2
2 µm
BSD
i)
1
2
2 µm

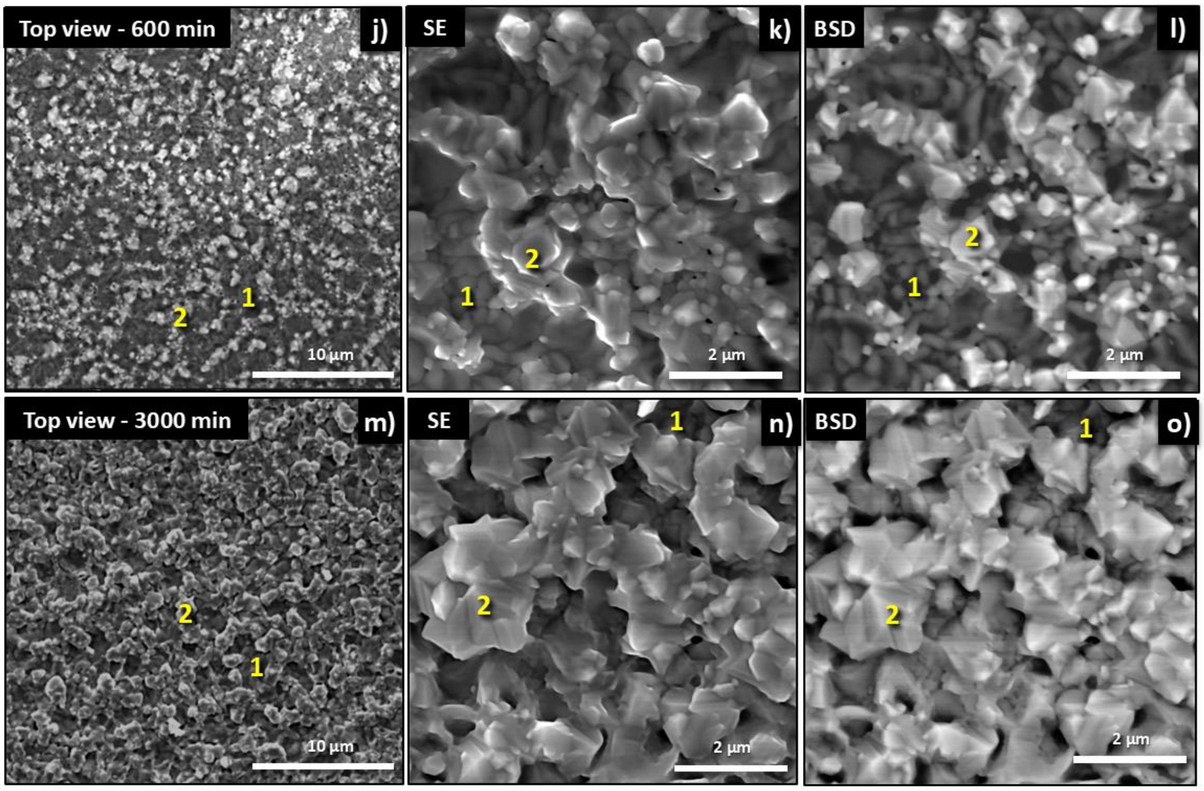

Figure 6.6 Evolution of the oxide scale morphology from a top view perspective for isothermally heat treated specimens after (a-c) 10, (d-f) 60, (g-i) 240, (j-l) 600 and (m-o) 3000 min. The left column includes a low magnification overview of the oxide scale depicting the overall frequency and distribution of the mixed oxide formations (region 2) with increasing oxidation time. The high magnification SE and BSD micrographs included in the middle and right columns, respectively, illustrate the growth location and morphology of the mixed oxide formations.

Analysis of the oxide scale surface morphology after 10 min oxidation shown in Figs. 6.6-a) to –c) has revealed that a significant quantity of MO formations (region 2) are already present in the initial stages of oxidation, equating to a 7.5% coverage of the top surface area of the oxide scale. As oxidation time progressed, the surface of the oxide scale underwent significant morphological, topographical and compositional changes that led to a gradual increase of mixed oxide coverage over the underlying Al_2O_3 scale and eventual establishment of a continuous mixed oxide outer layer. This process is qualitatively illustrated by descending sequence of the rows of micrographs in Fig. 6.6. The two major processes driving this transformation were the outward growth of new mixed oxide formations over TGO grain boundary regions (i.e. nucleation effect) and the volumetric expansion of the pre-existent mixed oxide formations (i.e. coarsening effect). The concomitant effect of these processes was quantified by plotting the top-view projected area of mixed oxide surface coverage as a function of oxidation time in Fig. 6.7-a). Each data point corresponds to the average mixed oxide formation area coverage obtained from three top view thresholded BSD micrographs (Threshold and area wand tools, Imagej) covering a representative area of 3 mm^2. This plot showed that the mixed oxide area coverage increased from an initial 6 % after just 5 min of oxidation to approximately 16 % coverage after 240 min and 48.7 % at the time of failure (i.e. 3000 min). It also revealed that the outer scale coverage followed two distinct behaviours, one that can be described by a logarithmic function (R_A^2=0.99) during the initial stages of oxidation (< 60 min) and the other by a sub-parabolic function thereafter (R_A^2=0.98) ($60 < t < 3000$ min). This is consistent with the oxide scale surface morphology changes observed before and after 60 min oxidation in Fig. 6.6, as the nucleation of new mixed oxide formations appears to be predominant during the initial stages of oxidation and the coarsening effect in stages of oxidation thereafter. The oxide scale surface roughness (S_a) was also determined for all heat treated specimens and plotted in Fig. 6.7-b) as a function of oxidation time. The main dataset trend revealed a very similar trend to the one seen in Fig. 6.7-a) for the mixed oxide coverage analysis. This can only be possible if the oxide scale surface roughening observed with the progression of oxidation time is also driven by the nucleation of new MO and isotropic volumetric growth of the mixed oxides in the outer layer.

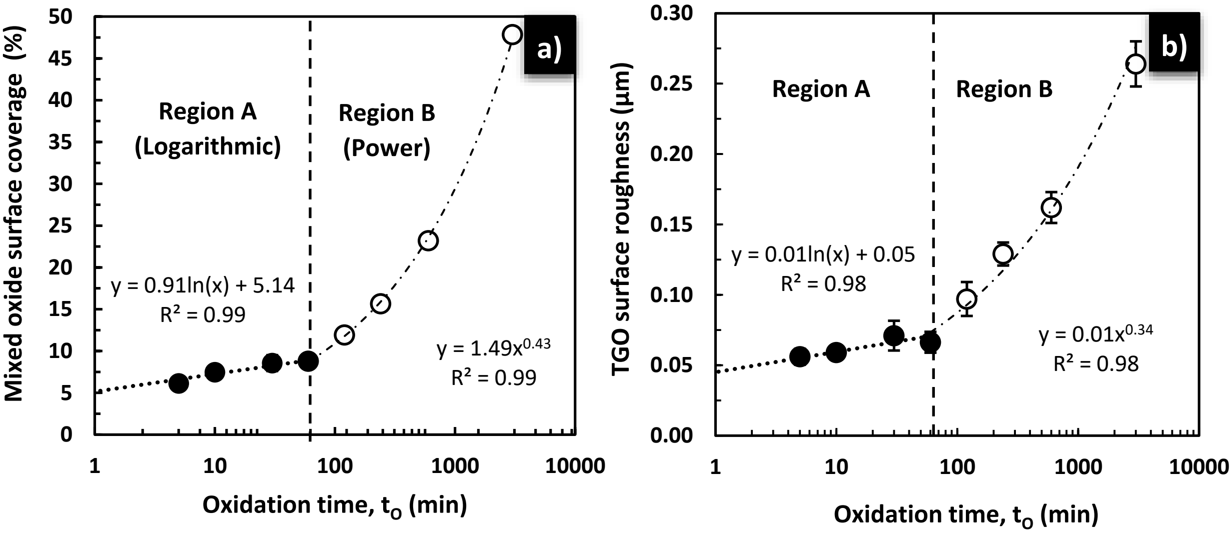

Figure 6.7 Plots of the (a) percentage of area covered by mixed oxide formations and (b) oxide scale surface roughness as a function of the oxidation time (t_o). It is noteworthy that the abscissa axis of both plots is shown in a logarithmic scale of base 10 to improve the visual perception of the overall trend.

6.3.5 Cationic diffusion across the oxide scale

The results obtained in the previous sections suggest that the nucleation and growth of the MO formations driving the transformation of the outer scale is controlled by diffusional processes along the TGO grain boundaries. In order to investigate this phenomenon, a thin cross-sectional lamella of an oxide scale formed after 240 min oxidation was prepared by FIB milling and analysed via STEM-

HAADF. A SE micrograph of the resulting lamella is presented in Fig. 6.8-a) alongside a high magnification STEM-HAADF image of the highlighted segment analysed (white dashed area) in Figs. 6.8-b). This region was intentionally selected since it was representative of the oxide scale structure and contained an adequate size MO formation.

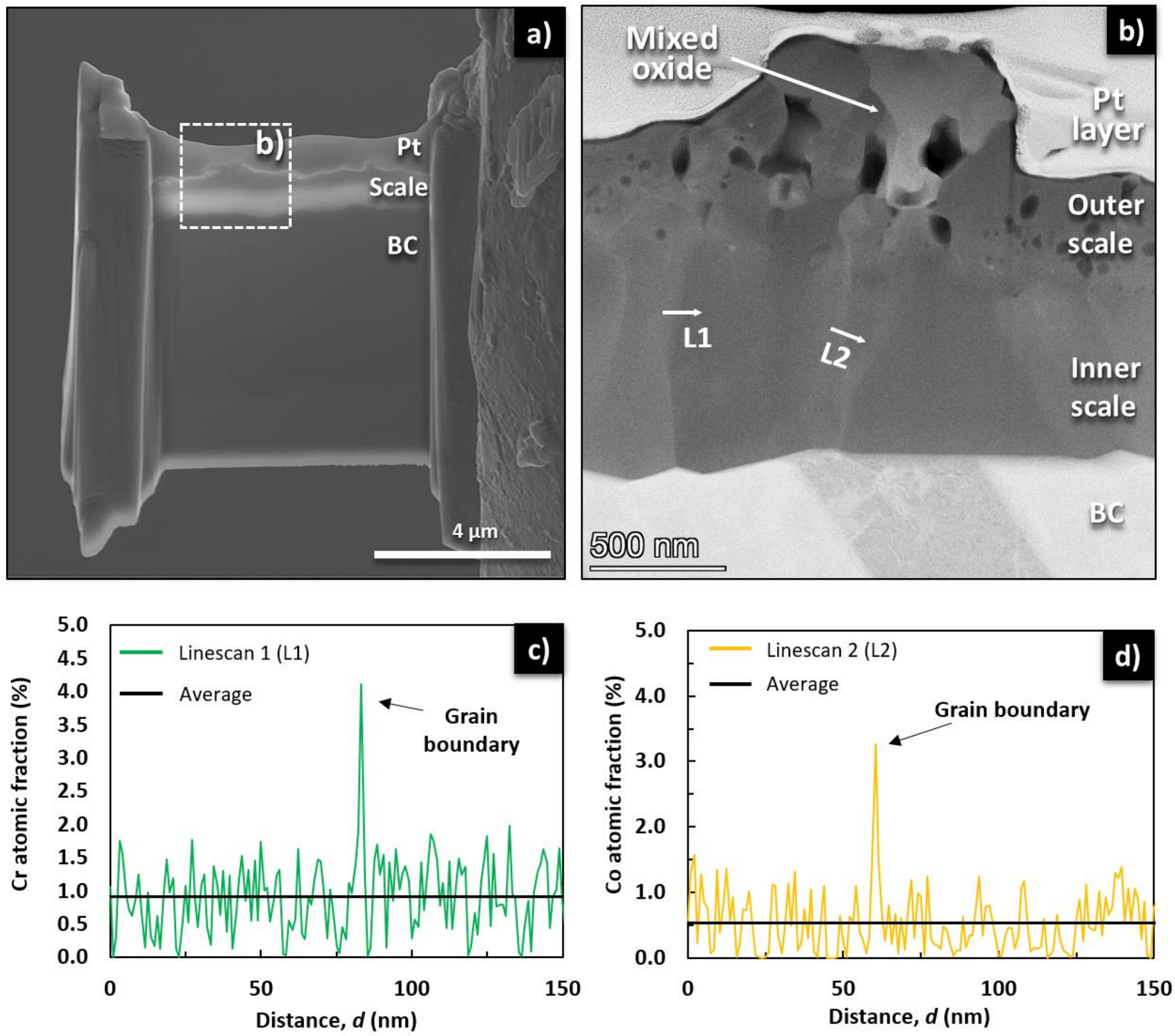

Figure 6.8 (a) SE micrograph of a cross-sectional lamella of an oxide scale prepared by FIB milling after 240 min oxidation and (b) a STEM-HAADF micrograph of the highlighted segment (white dashed area) containing a mixed oxide formation; Linescan compositional analysis across grain boundary segments of inner scale columnar grains confirming the segregation of (c) Cr and (d) Co.

Multiple EDS linescans were performed across the inner scale grain boundaries directly beneath the MO formations to ensure that Cr and Co concentration profiles as a function of distance presented in Figs. 6.8-c) and –d) were representative of the observations. Both plots contain an abnormally high amplitude peak that signalled a relevant increase in the Cr ($\sim 4\ at.\%$) and Co ($\sim 3.1\ at.\%$) atomic fractions across the grain boundary region in relation to the average Cr ($\sim 1\ at.\%$) and Co ($\sim 0.5\ at.\%$) concentrations in relation to the adjacent grain regions. The sharp and narrow shape of these peaks translated into a full width at half maximum (FWHM) of ~1 nm, effectively providing a good degree of confidence that the highly localised concentration spikes are indicative of a larger presence of Co and Cr along the grain boundaries. The consistent detection of these elements along various sections of different grain boundaries constitute solid evidence in favour of outward diffusion of Co and Cr.

6.3.6 PLPS analysis of the oxide scale

Phase identification of the Al_2O_3 polymorphs present in the heat treated specimens was carried out by analysis of the experimental luminescence spectra obtained from PLPS and plotted in Fig. 6.9. The resulting line plot shows the luminescence spectra of four analogous specimens that have been oxidised for 5 (black), 30 (green), 120 (blue) and 3000 (red) min. The resulting spectra revealed that α-Al_2O_3 was the only polymorph found in any stage of oxidation, as the R-line doublet were the only luminescence peaks detected. The absence of the characteristic T-lines indicated that θ-Al_2O_3 was not present in the oxide scale even at the time of the earliest measurement conducted (5 min). These results suggest that either no metastable alumina polymorphs have formed during oxidation or the θ → α phase transition occurred at an earlier point in time before the first measurement. The latter is more consistent with the topography of the oxide formations seen over the β-phase grains in Fig. 6.2, as a similar growth rate to the one seen over γ grains (α-Al_2O_3) is unlikely to originate such different features. This argument can be supported by Liu et al. [150] observations on similar scales forming over NiAl alloys, as they showed that the θ → α phase transition can be finished within 2 min oxidation.

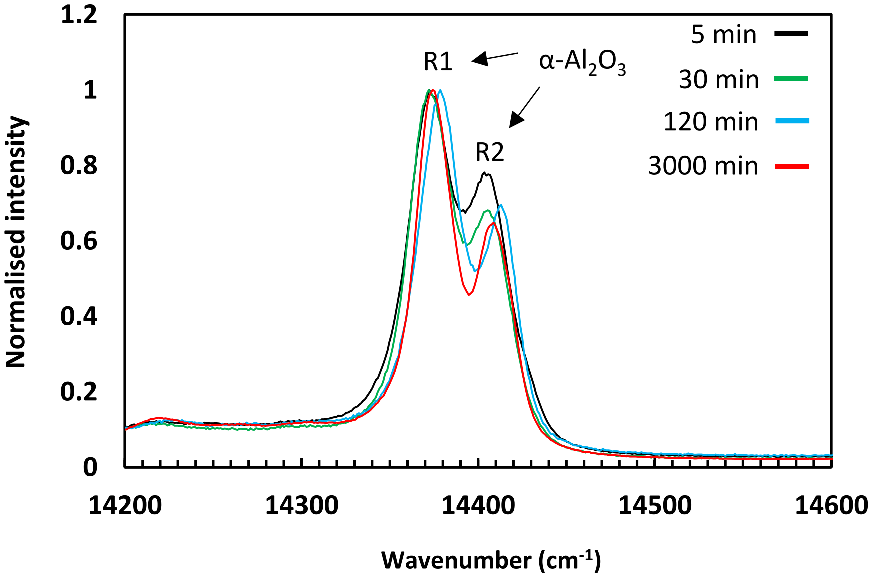

Figure 6. 9 PLPS spectra of the oxide scale obtained after 5 (black), 30 (green), 120 (blue) and 3000 (red) min of oxidation. The only peaks observed in the spectra are the R-lines associated with the presence of α-Al_2O_3.

The position of the R2 luminescence peaks of these spectra were then used to calculate the residual stress for each specimen (eq. 3.6, see section 3.3.5) and plot it as a function of oxidation time in Fig. 6.10. Results showed that the oxide scale growing over the CoNiCrAlY coating displayed an overall high stress magnitude during the whole thermal exposure, ranging from approximately - 5.7 GPa in the early stages of oxidation (5 min) to 5.3 GPa at time of failure (3000 min). These values are in good agreement with some of the theoretical predictions ($-5.6\ GPa \leq \sigma \leq -5.2\ GPa$ [154, 280]) and experimental values (σ= - 5.2 GPa) reported in the literature for MCrAlY coatings at 1100°C [280, 281]. However, it is important to note that these magnitudes are indicative of an exacerbated stress state as most scales forming over similar coatings show values in the range of 1 to 4 GPa [12, 150]. Another important aspect of the stress evolution in the oxide scale is the temporary reduction of 0.8 GPa observed between 30 and 240 min of oxidation. Such a significant deviation from the apparent slow descending trend perceived in Fig. 6.10 is a strong indication of an event-triggered abnormal behaviour in the scale. The fact that this phenomenon was observed during the same period of time of an abrupt reduction in Cr concentration in the inner scale (see Fig. 6.5) might suggest a possible correlation. This is further explored in section 6.4.4.

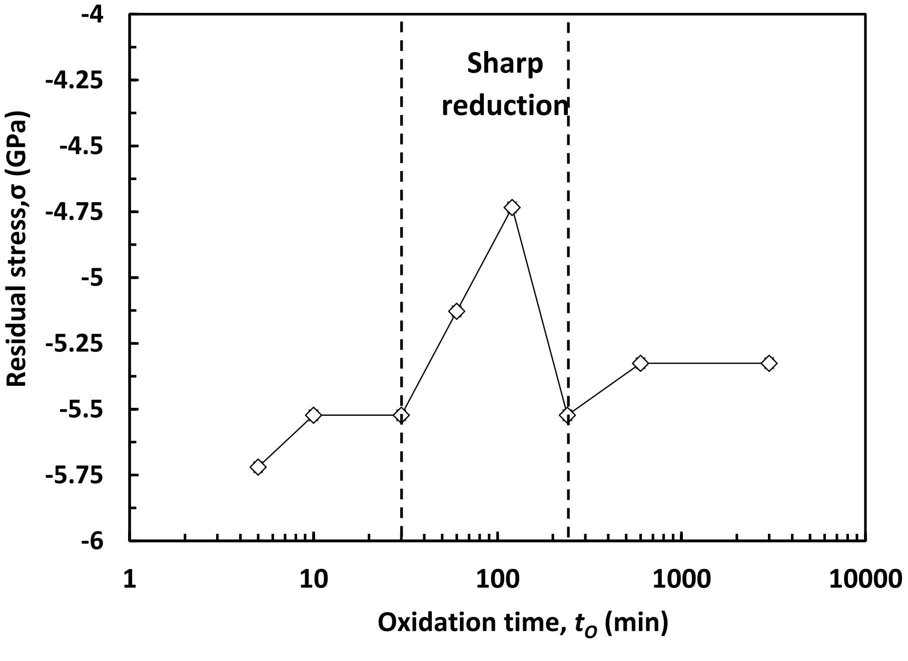

Figure 6. 10 Evolution of the residual stress as a function of oxidation time. The abscissa axis is shown in a logarithmic scale of base 10 to improve the visual perception of the overall trend.

6.3.7 Oxide scale failure

Spallation of the oxide scale was observed after 3000 min of oxidation when the oxide scale thickness reached a value of 3.2 ± 0.2 µm. This value is within the range reported in the literature for analogous oxide scales (i.e. 3 to 10 µm [12]), although the proximity to the lower end of the range is an indication of premature failure. This is consistent with the residual stress results in the previous section, as the large compressive stresses measured and characteristic low creep rate reported for these scales [172] can lead to a critically high strain energy density within the oxide scale at an earlier point in oxidation time. In turn, this would accelerate the crack nucleation and propagation mechanisms.

The analysis of the failure plane showed that spallation was not homogeneous across the specimen, as the failure plane was a combination of spalled (~61%) and non-spalled segments (~39%). The analysis of non-spalled oxide scale segment shown in Fig. 6.11-a) revealed a fracture pattern that is consistent with a small-scale buckling (SSB) failure mode. A schematic illustration of the perceived failure mechanism driving spallation of the oxide scale is shown in Fig. 6.11-b). This assessment is primarily based on the fact that the average radius of the buckled segments observed across the failure plane suggest a critical flaw length (L_c) in the order of 40 to 60 µm. This value can be validated by using eq. 6.1, where an the oxide scale thickness of h_c=3.2 µm and residual stress σ_C=5.3 GPa at time of failure were used along with an oxide scale elastic modulus of E_{OX}=400 GPa [12] , Poisson's ratio of υ=0.25 [156] and a critical buckling index of Π_C=1.223 [12]. The estimated critical flaw length obtained from the calculations (~32 µm) was found to be similar to the experimental observations, indicating that the interfacial de-cohesion responsible for spallation is consistent with SSB. This can be further supported by the fact that the buckled segments also showed a characteristic centre-point fracture across the oxide scale surface that is consistent with the inward lateral movement of the compressed plates. Even the exposed inner scale surface segments seen around the perimeter of the buckled segment (dashed area) can be explained by a SSB failure mode, as the collision of the fractured plates at the centre-point can originate shear stresses at the inner/outer scale interface.

$$L_c = \frac{h_c}{\sqrt{\frac{\sigma_C(1-\upsilon^2)}{\Pi_C E}}} \qquad \text{(eq. 6.1)}$$

An oblique view of a spalled segment of the failure plane is presented in Fig. 6.11-c), wherein the two main cracking mechanisms leading to spallation were identified, interfacial delamination at the BC/inner scale interface (type I crack) and intra-scale cracking at the inner/outer scale boundary. A larger presence of exposed BC segments was found at the failure plane, indicating that spallation was primarily driven by delamination at the BC/inner scale interface. However, the additional presence of Al_2O_3 inner scale exposed segments at the failure plane (~7%) was demonstrative of delamination along the inner/outer scale boundary, as shown in Figs. 6.11-c) and -d). This indicates that intra-scale cracking was relevant to the oxide scale failure, likely due to the fact that the compositional (i.e. Co,Cr and Ni concentration) and microstructural (i.e. void formation, grain morphology) differences observed for the inner and outer scale.

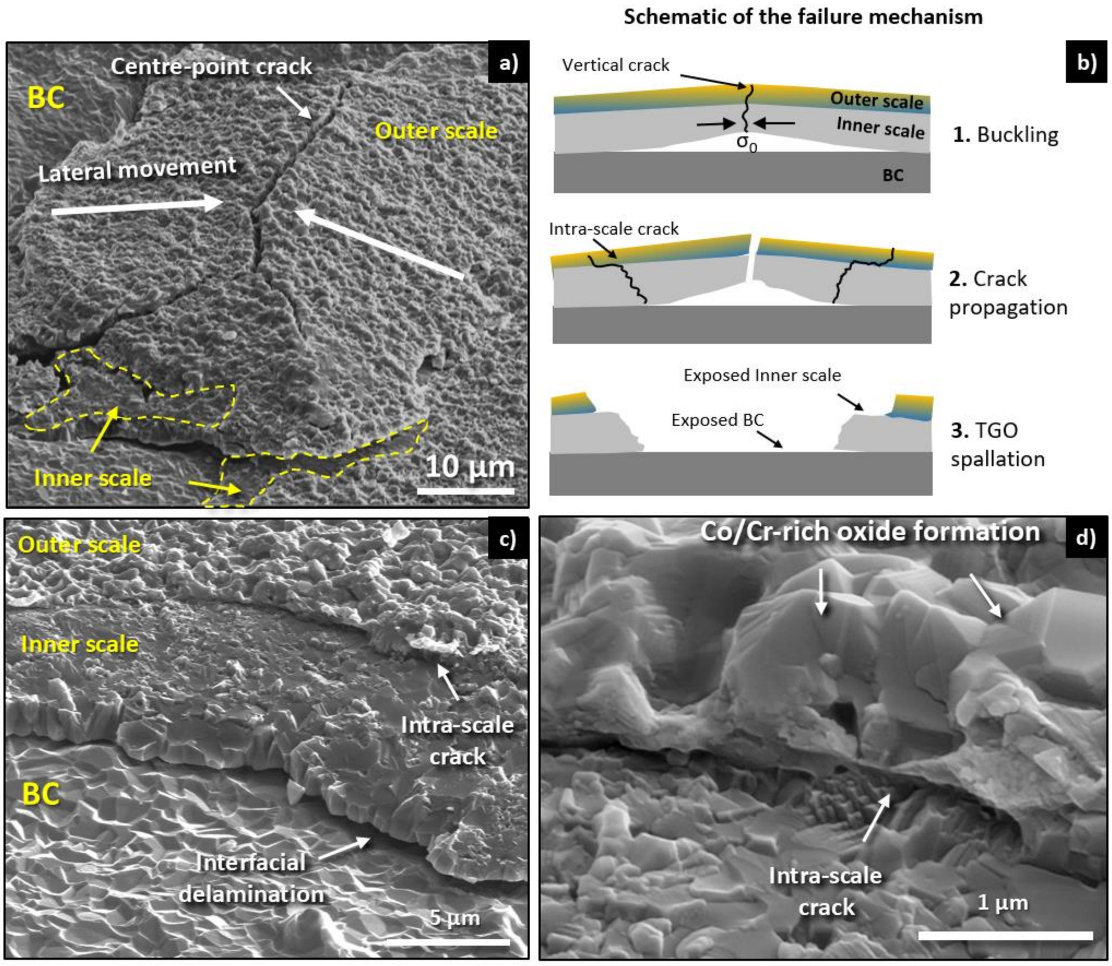
Schematic of the failure mechanism
a)
Centre-point crack
BC
Outer scale
Lateral movement
Inner scale
10 µm
b)
Vertical crack
Outer scale
Inner scale
σ_0
BC
1. Buckling
Intra-scale crack
2. Crack propagation
Exposed Inner scale
Exposed BC
3. TGO spallation
c)
Outer scale
Inner scale
Intra-scale crack
BC
Interfacial delamination
5 µm
d)
Co/Cr-rich oxide formation
Intra-scale crack
1 µm

Figure 6.11 (a) Depiction of a non-spalled segment of the oxide scale displaying the characteristic features of small-scale bucking (SSB) and (b) a schematic illustration of the respective failure mechanisms; (c) Oblique view of the failure plane of a 3000 min specimen where the two main cracking mechanisms are highlighted (i.e. BC interface and intra-scale cracking) alongside (b) a higher magnification of the inner/outer scale delamination boundary;

6.4. Discussion

The results obtained in this work have shown that the BC microstructure and respective composition had a substantial impact on the oxide scale formation process during the early stages of oxidation. The dual-phase BC microstructure promoted a site-specific oxidation behaviour that led to the formation of a layered oxide scale with inhomogeneous surface morphology, topography and composition, as previously noted by Doolabi et al. [270]. This phenomenon was associated with the selective oxidation of Al observed in the β-phase and subsequent formation of MO heterogeneities along the surface of the oxide scale. As oxidation progressed, the continuous segregation of multiple non-Al elements across the oxide scale induced a gradual microstructural and compositional transformation of the outer section that led to the establishment of a continuous mixed oxide scale.

This behaviour affected the overall magnitude of the residual stress within the oxide scale and contributed to a premature failure. These findings are explored in greater detail over the following sections by focusing on the mechanistic understanding of oxide scale formation and relationship with the BC microstructure.

6.4.1 Current understanding of the outer scale formation mechanism

The analysis of the oxide scale formation and evolution with oxidation time conducted in section 6.3 revealed that the dual-layered structure with an external MO-rich layer can be traced back to the initial stages of oxidation. These findings have facilitated an improved mechanistic understanding of the outer scale formation process and transformation process, leading to the development of the schematic illustration presented in Fig. 6.12.

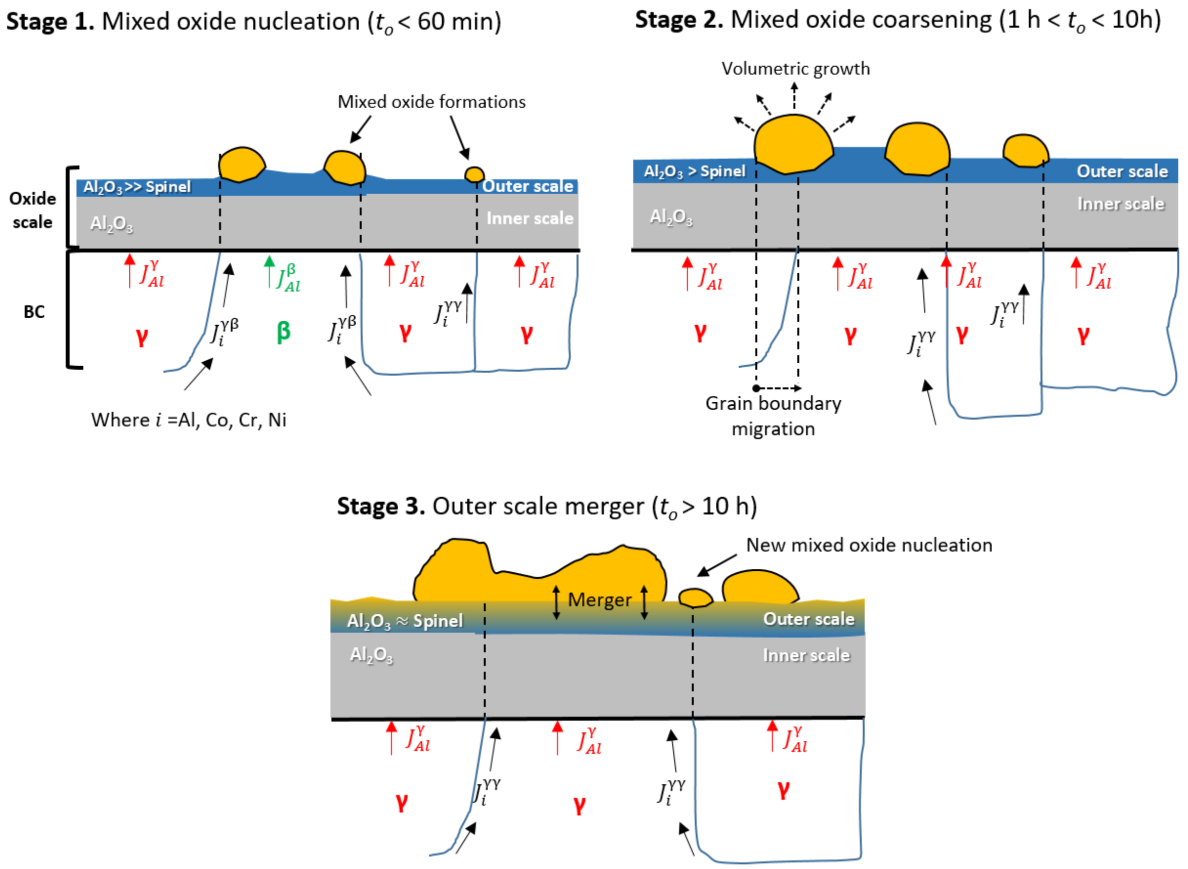
Stage 1. Mixed oxide nucleation (t_o < 60 min)
Mixed oxide formations
Oxide scale
Al_2O_3 >> Spinel
Al_2O_3
Outer scale
Inner scale
BC
J_{Al}^{γ}
J_{Al}^{β}
$J_i^{\gamma\beta}$
$J_i^{\gamma\gamma}$
γ
β
Where i =Al, Co, Cr, Ni
Stage 2. Mixed oxide coarsening (1 h < t_o < 10h)
Volumetric growth
Al_2O_3 > Spinel
Al_2O_3
Outer scale
Inner scale
J_{Al}^{γ}
$J_i^{\gamma\gamma}$
γ
Grain boundary migration
Stage 3. Outer scale merger (t_o > 10 h)
New mixed oxide nucleation
Merger
$Al_2O_3 \approx$ Spinel
Al_2O_3
Outer scale
Inner scale
J_{Al}^{γ}
$J_i^{\gamma\gamma}$
γ

Figure 6.12 Schematic illustration of the outer scale formation mechanism presented in three stages, mixed oxide nucleation (stage 1), mixed oxide coarsening (stage 2) and outer scale merger (stage 3). The relevant diffusion fluxes ($J_i^{\gamma}, J_i^{\beta}, J_i^{\gamma\beta}$ and $J_i^{\gamma\gamma}$ where i=Al, Co, Cr, Ni) and microstructural features that impact the outer scale formation are included.

The outer scale formation process can be divided into three representative stages according to its microstructural/compositional evolution with oxidation time, mixed oxide nucleation (stage 1), mixed oxide coarsening (stage 2) and outer scale merger (stage 3). The first stage takes place within the first 60 min of oxidation and is characterised by an initial period of rapid nucleation of MO formations at the oxide scale/gas interface. These oxides formed predominantly over grain boundary segments that were directly located above the β grains, suggesting a correlation between γ/β grain boundaries and accelerated outward diffusion rate of non-Al elements. Nucleation of MO over γ grain regions was also observed but the reduced frequency and size is consistent with a reduced growth rate limited by the already known diffusional impositions of cationic transport rate along the γ/γ and α-Al_2O_3 scale grain boundaries [140]. The mechanistic interpretations of these phenomena are further explored in the next section.

The second stage takes place between 60 and 600 min and is characterised by the predominant volumetric growth of the pre-existent MO formations, reduced nucleation rate of new MO formations and gradual enrichment of the outer scale with Cr. This pattern of behaviour indicates that cationic diffusion is the main mechanism responsible for the transformation of the outer scale, as confirmed by the TEM analysis in section 6.3.5. These findings are consistent with diffusion studies conducted on Al_2O_3 oxide scales [282, 283] which demonstrated that outward cationic diffusion is predominant under higher O_2^- partial pressures. The fact that MO coarsening is predominant in this stage also suggests that cationic diffusion is primarily occurring along the same oxide scale pathways of the previous stage. One possible explanation is that favoured MO nucleation regions in the BC surface do not change location significantly during this interval of time due to slower grain growth and related grain boundary migration [284]. Sub-scale depletion of the β–phase was also observed at the early instances of this stage, indicating that after this point in time all diffusion across the scale is dictated by the diffusion rates along the path comprised of γ/γ and α-Al_2O_3 grain boundaries.

The third stage occurs after 600 min of oxidation and is defined by the gradual merger of the Cr-rich outer scale with the embedded Co-rich MO formations to form the MO-rich external layer typically reported in the literature [108, 269, 270]. This transformation is caused by the gradual compositional changes in the MO formations and surrounding outer scale arising from the continuous cationic diffusion across the inner scale and segregation of Cr within the oxide scale, respectively. As the outer scale transformation process relies heavily on the Cr presence, this topic is further explored in section 6.4.3. The predominant mechanism driving the transformation of the outer scale is still MO coarsening, although a significant increase in MO nucleation was seen at the oxide scale surface between 600 and 3000 min of oxidation. This can be explained by a combination of grain boundary migration at the BC/oxide interface that results from γ-phase grain growth, BC creep rate and reduced sub-scale Al concentration measured ($1.9 \leq$ Al wt.% ≤ 3.2) [285]. Adding the resulting shift in the physical location of the γ grain boundaries to the diffusional range of other α-Al_2O_3 grain boundary segments can create new diffusion paths and facilitate the nucleation of new MO formation across the surface.

6.4.2 Effect of BC microstructure on the early oxidation behaviour

The correlation of the oxide scale morphology with the underlying BC microstructure in section 6.3.2 revealed that the β grain size and respective phase boundary distance (x_{PB}) had an instrumental role on the early oxide scale growth rate and composition. This was especially noticeable over smaller β grains, as the increased phase boundary (PB) proximity promotes the formation of a thicker oxide scale segment where MO formations rich in non-Al elements can be observed. This effect is clearly illustrated from a cross-sectional perspective in Figs. 6.13-a) and –b) for β grains with smaller and larger PB distance, respectively. These findings suggest that there might be a critical PB distance threshold $\left(x_{PB}^{crit}\right)$ beyond which the interaction between the diffusion fluxes of neighbouring grain boundaries has a crucial effect on the oxide scale formation and growth processes. It can then be hypothesised that this interaction accelerates Al consumption at the surface of the bare alloy and leads to significant alterations on the oxide morphology and composition, as highlighted in sections 6.3.2, 6.3.3 and 6.3.4.

In order to investigate this hypothesis, an analytical model that evaluates the effect of PB distance in the overall Al diffusion flux across the BC surface was developed. This model assumes that each PB has an adjacent region of influence within the grains (d_{RI}) from where Al^{3+} and other metallic elements can migrate. A schematic illustration of the diffusion flux towards the BC surface and respective oxide formation during the initial stages of oxide scale formation was developed to support this model. These schematics are presented in depicted in Fig. 6.13-c) and d) and comprise a dual-layer oxide scale growing atop of a dual-phase BC microstructure with variable β–phase grain size for the cases of smaller and larger PB distances. As the oxide scale growing on these coatings is predominantly comprised of Al_2O_3, the Al^{3+} diffusion flux across the surface of the γ grains $\left(J_{Al}^{\gamma}\right)$, β grains $\left(J_{Al}^{\beta}\right)$ and α/β phase boundaries$\left(J_{Al}^{\gamma\beta}\right)$ were represented. This is supported by previous fundamental diffusion studies on bare MCrAlY coatings that showed that the initial stages of the oxide scale growth are dominated by outward diffusion of metallic elements towards the interface (i.e. Al, Cr, Co, Ni and Y) due to higher partial pressure at the BC surface[140]. Although the quantitative relationship between the magnitude of these fluxes in MCrAlY coatings is not known, it is well accepted that they vary by a few orders of magnitude ($J_{Al}^{\gamma} < J_{Al}^{\beta} << J_{Al}^{\gamma\beta}$) and lead to significant morphological/compositional changes in the oxide scale [133, 146]. Taking these findings and the classical 1-D grain boundary diffusion framework into consideration [286, 287], it was possible to construct an approximation of the instantaneous Al diffusion flux profile along the interface (red line). The shape of the resulting diffusion flux profile is similar to a normal distribution function [286, 287], displaying a maxima along the y axis over the PB segment and a decreasing trend in the adjacent regions (Figs. 6.13-c) and d).

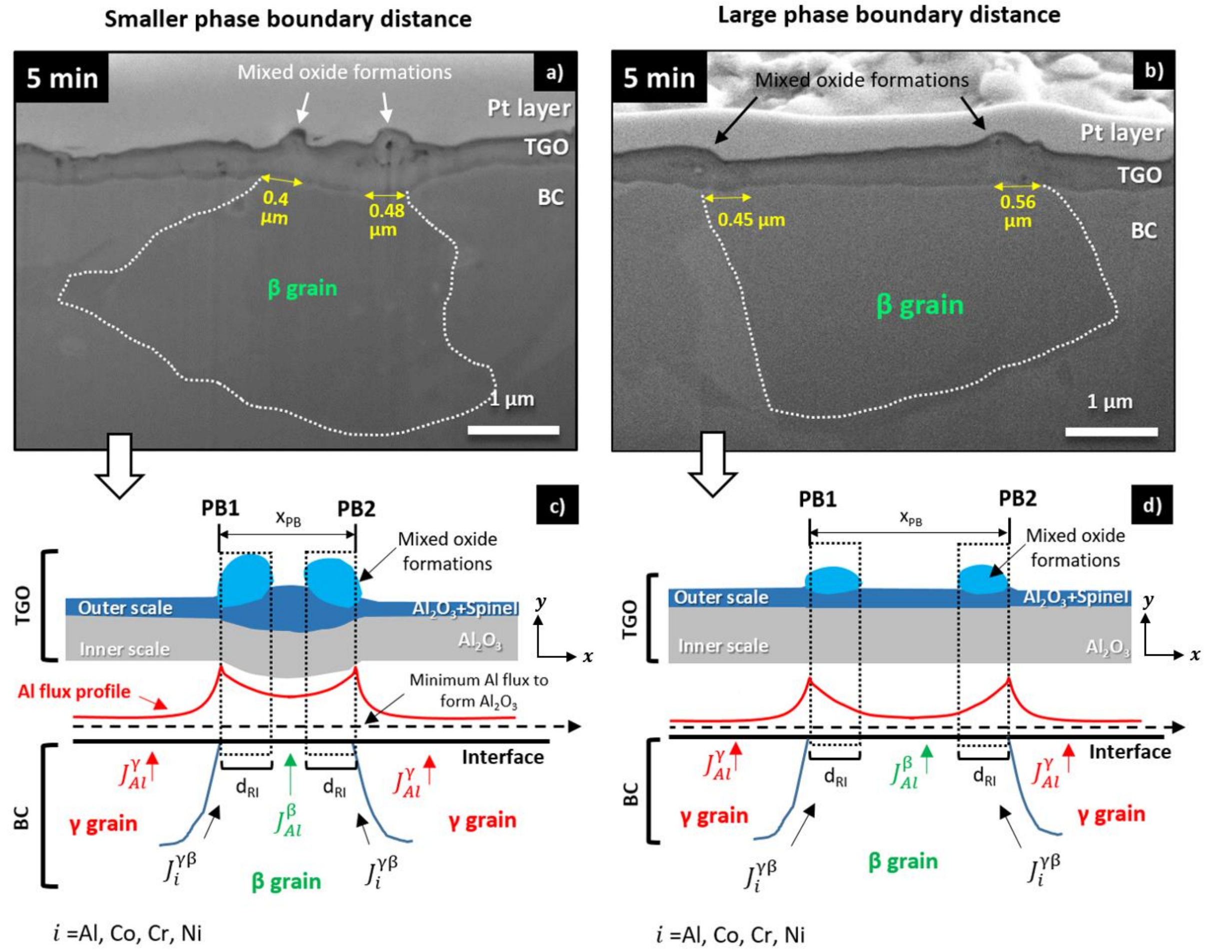
Smaller phase boundary distance
Large phase boundary distance
5 min
Mixed oxide formations
a)
Pt layer
TGO
0.4 µm
0.48 µm
BC
β grain
1 µm
5 min
Mixed oxide formations
b)
Pt layer
TGO
0.45 µm
0.56 µm
BC
β grain
1 µm
PB1
x_{PB}
PB2
c)
Mixed oxide formations
TGO
Outer scale
Al_2O_3+Spinel
Inner scale
Al_2O_3
y
x
Al flux profile
Minimum Al flux to form Al_2O_3
Interface
BC
J_{Al}^{γ}
d_{RI}
J_{Al}^{β}
γ grain
β grain
$J_i^{\gamma\beta}$
i =Al, Co, Cr, Ni
PB1
x_{PB}
PB2
d)
Mixed oxide formations
TGO
Outer scale
Al_2O_3+Spinel
Inner scale
Al_2O_3
y
x
Interface
BC
J_{Al}^{γ}
d_{RI}
J_{Al}^{β}
γ grain
β grain
$J_i^{\gamma\beta}$
i =Al, Co, Cr, Ni

Figure 6.13 Cross-sectional FIB micrographs and respective schematic illustration of Al flux across the interface during oxidation for a β grain with (a,c) smaller and (b,d) larger phase boundary distance. The BC and oxide scale microstructure and compositions are superimposed on the schematic. The representative Al flux profile over each surface (red line) and the minimum Al flux to maintain the exclusive formation of Al_2O_3 are also represented.

The diffusion flux of metallic elements towards the BC surface can be described by Fick's first law (eq. 6.2), as the diffusion flux is directly proportional to the product of the diffusion coefficient and the concentration gradient of the diffusing species across the y axis.

$$J = -D\left(\frac{d\varphi}{dy}\right) \qquad \text{(eq. 6.2)}$$

Where J is the diffusion flux, D the diffusion coefficient, φ is the concentration of and y is the position across the thickness of the BC.

However, the previous equation had to be re-written (eq. 6.3) in order to reflect the experimental conditions depicted in Figs. 6.13-c) and d) and provide a description of the diffusion flux across the x axis (i.e. surface of the BC). The first term was modified to include the overall diffusion coefficient of any metallic elements diffusing towards the BC surface. An exponential function was then added as a second term to account for the contribution of PB position (x_{PB}) and width of the regions of influence (d_{RI}) to the diffusion flux. It is noteworthy that the effects of x_{PB} and d_{RI} were decoupled from the effects of the concentration gradient and the diffusion flux results normalised by attributing a fixed unitary value to the first term of eq. 6.3, $J_i^{PB} = 1$.

$$J_i^{PB}(x) = \underbrace{-\left(D_i^{PB}\frac{d\varphi}{dy}\right)}_{1^{st}\text{ term}} \underbrace{e^{\left(-\frac{\left(x-x_{PB}\right)^2}{2d_{RI}^2}\right)}}_{2^{nd}\text{ term}} = J_i^{PB} e^{\left(-\frac{\left(x-x_{PB}\right)^2}{2d_{RI}^2}\right)} \qquad \text{(eq. 6.3)}$$

Where $i = Al, Co, Cr, Ni$ and D_i^{PB} and J_i^{PB} are the diffusion coefficient and flux along the phase boundaries.

The effect of the distance between two neighbouring phase boundaries on the overall diffusion flux of a BC segment was then be simulated by considering the additional contribution of an additional PB located at a distance of x_{PB}, where $x_{PB} = x_{PB2}$ -x_{PB1}. This can be achieved by adding another term to eq. 6.4 to account for the diffusion flux of the neighbouring PB and plotting the resulting overlap diffusion flux (J_i^{ov}) as a function of the x position along the interface, as shown in Fig. 6.14.

$$J_i^{ov}(x) = \underbrace{J_i^{PB1} e^{\left(-\frac{\left(x-x_{PB1}\right)^2}{2d_{RI}^2}\right)}}_{\text{Phase boundary 1}} + \underbrace{J_i^{PB2} e^{\left(-\frac{\left(x-x_{PB2}\right)^2}{2d_{RI}^2}\right)}}_{\text{Phase boundary 2}} \qquad \text{(eq. 6.4)}$$

where the subscript 1 and 2 refer to phase boundaries 1 and 2.

An example of such plot is shown in Fig. 6.14 for a x_{PB}=1 µm and d_{RI}=0.35 µm, wherein the green and red dashed profiles represent the normalised Al diffusion flux across PB1 and PB2, and the solid blue profile represents the overlap profile of both phase boundaries. A null diffusion flux at the centre-point distance between grain boundaries $\left(x_{cp} = \frac{x_{PB}}{2}\right)$ signifies the absence of an interaction between the individual PB fluxes whereas values between 1 and 2 mean that the flux is larger than the one of the individual profiles (J_{Al}^{ov}). Fig. 6.14 shows that the overlap profile resulting from the interaction between the Al diffusion flux of both phase boundaries at x_{cp} translates to a normalised diffusion flux of $\sim$0.7. Physically, this means that the proximity between PB1 and PB2 leads to an Al diffusion flux in the x_{cp} position by two-fold in relation to the individual PB1 and PB2 profiles.

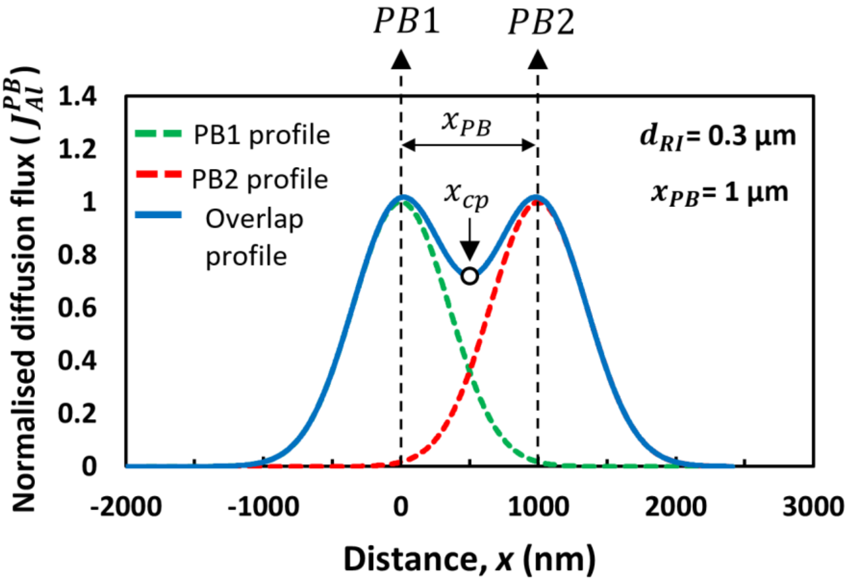

Figure 6.14 Plot of the normalised diffusion flux as a function of the position along the bare BC surface for a phase boundary distance of 1 µm and 0.3 µm region of influence. The green and red dashed line represent the normalised Al diffusion flux of across phase boundary 1 $\left(J_{Al}^{PB1}\right)$ and 2 $\left(J_{Al}^{PB2}\right)$, respectively, whereas the solid blue profile represents the overlap profile of both phase boundaries (J_{Al}^{ov}).

In order to evaluate this impact in a systematic manner, the normalised overlap diffusion flux at $x = x_{cp}$ was plotted as a function of the PB region of influence in Fig. 6.15 for different PB distances. These results were microstructurally contextualised by assuming PB distances and regions of influence analogous to the ones observed in the BC microstructure. Our experimental observations suggest that d_{RI} ranges between 350 to 450 nm, as the vast majority of the MO formations can be found within that distance from the phase boundaries (see Fig. 6.13). This interval was defined as the region of interest for the evaluation of the diffusion flux overlap analysis and highlighted by the dashed vertical lines in Fig 6.13. This is in good agreement with the estimated value proposed in literature by Chen et al. [146] for NiCoCrAlY coatings (350 nm). Fig. 6.15 showed that the degree of diffusion flux overlap between neighbouring PBs is significant within the pre-selected range highlighted by the vertical dashed lines and becomes increasingly more relevant as the PB distance is reduced. It also shows that there is still some degree of overlap diffusion flux even for larger x_{PB} values, although the predominance of the overlap flux is defined for J_{Al}^{ov} values above 1. Taking into consideration that the average β grain size obtained for these HVOF coatings is ~ 0.41± 0.27 µm^2 (see section 6.3.1), these results indicate that a significant fraction of the β grains should display some degree of overlap diffusion flux. In regions where this flux is sufficiently high to induce periodic and momentary reductions in the Al concentration within the region of influence, outward diffusion of other elements such as Co^{2+}, Cr^{3+}

and Ni^{2+} becomes favoured. This has major implications on the oxide formation process in the vicinity of the grain boundary region, increasing the likelihood of MO formation and growth below a critical phase boundary distance $\left(x_{PB}^{crit}\right)$. These predictions are consistent with the existent literature on NiCoCrAlY coatings, as accelerated diffusion along the PBs within the region of influence has been shown to affect the oxide morphology and composition [146].

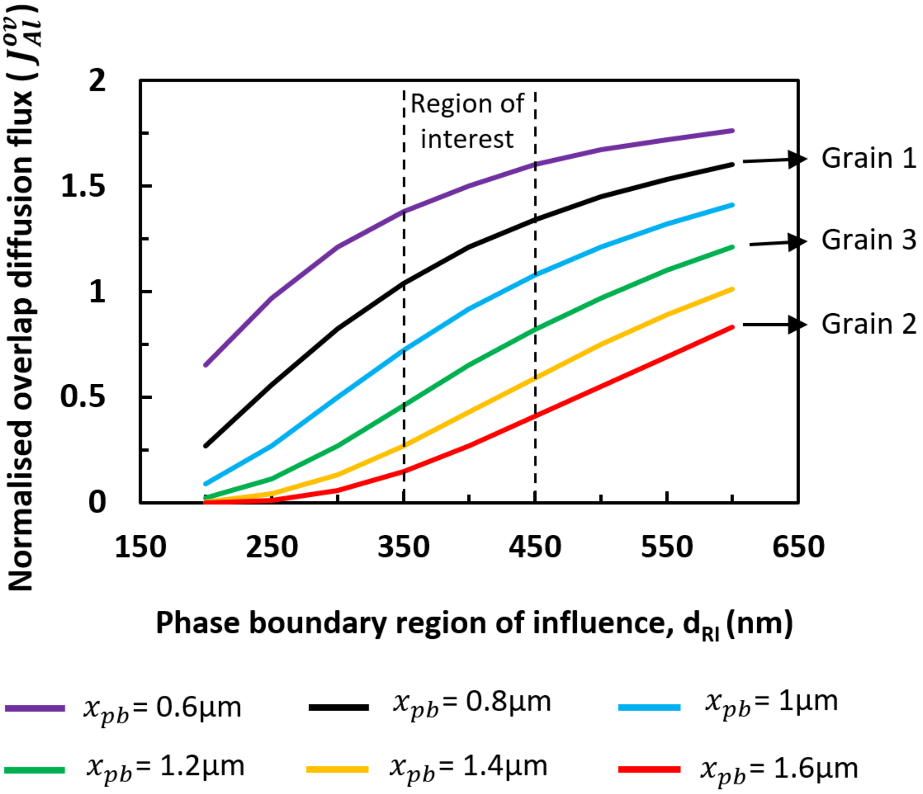

Figure 6.15 Plot of the normalised overlap diffusion flux as a function of the phase boundary region of influence measured. Each colour line profile represents a different phase boundary distance, ranging from 0.6 to 1.6 µm.

The results of the analytical model can be validated experimentally by establishing a comparison between the oxidation behaviour observed for β grains with PB distances similar to the ones given by the profiles in Fig. 6.15. Fig. 6.16 shows higher magnification micrographs of an as-polished BC surface segment (6.16-a) and resulting surface morphology after 10 min oxidation imaged under SE (6.16-b) and BSD (6.16-c) modes. Three grains with PB distances ranging from 0.8 µm (grain 1) to 1.2 µm (grain 2) and 1.6 µm (grain 3) can be discerned and the respective MO presence across the surface matched to the brighter contrast regions of Fig. 6.16-c). A concentrated presence of MO formations can be seen along the perimeter of grains with PB distances over ~1.2 µm and a single MO formation over grains with PB distances below ~0.8 µm. It is noteworthy that larger MO formations were also observed in the vicinity of vertices of larger grains (e.g. grains 2 and 3) where PB distances are smaller. These oxide distributions are indicative of a predominant flux overlap ($J_{Al}^{ov} > 1$) in grain segments with reduced PB distance and of the opposite in larger grains ($J_{Al}^{ov} < 1$). Combining these observations with the predictions in Fig. 6.14, it can be ascertained that the x_{PB}^{crit} required to trigger the predominant PB overlap interaction must be within the 0.8 < x_{PB}^{crit} < 1.2 µm interval and d_{RI} within the 400 to 450 nm range.

The main implication here is that the Al diffusion flux over a β grain is greatly accelerated by the proximity of neighbouring phase boundaries, reasserting the importance of the initial grain size on the oxidation behaviour. This means that the β-phase refinement of β grains in dual-phase HVOF CoNiCrAlY coatings might only be beneficial down to a certain grain size where the PB distance is greater than the equivalent length of their regions of influence (i.e. x_{PB} > $2d_{RI}$). Below this threshold, the combination of low Al content in the β grains with the PB flux overlap can increase the probability of MO formation and accelerate the detrimental transformation of the outer scale. This can be partially addressed by conducting a post-deposition annealing in a vacuum or O_2^- poor atmosphere to promote the coarsening of the β grains and formation of a thin protective oxide scale, as suggested by Saeidi et al. [108].

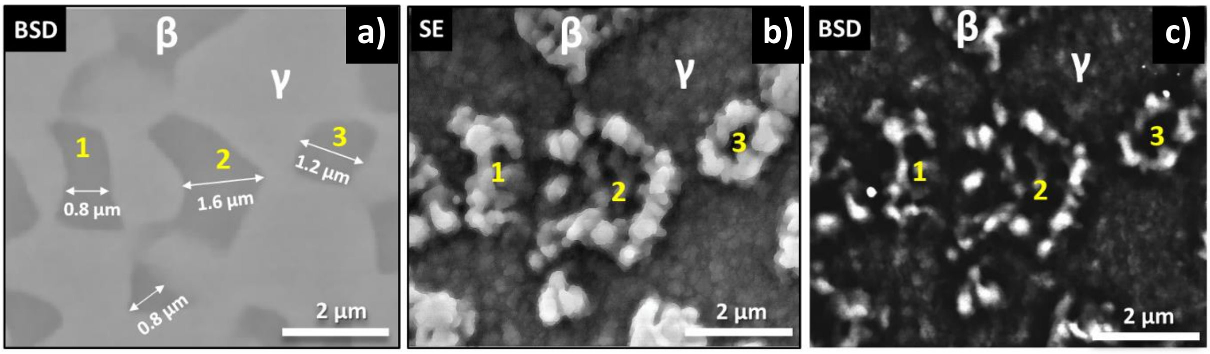

Figure 6.16 High magnification BSE micrograph of the as-polished BC microstructure and respective oxide alongside the respective (b) SE and (c) BSE mode images of the oxide scale growing atop where brighter contrast indicates the presence of mixed oxide formations.

The same reasoning can also be used to analyse the overlap diffusion flux along the γ/γ grain boundaries and explain why the mixed oxide formation was less pronounced in these regions during the initial stages of oxidation. Firstly, the diffusion flux along the γ grain surface is orders of magnitude lower than along the γ/γ grain boundaries [146, 287]. As a consequence, the majority of BC surface does not allow for sufficiently high diffusion fluxes $\left(J_{Al}^{\gamma}\right)$ that favour the diffusion of other cations across the scale periodically for very brief periods of time [146]. This establishes the γ/γ grain boundaries as the most effective nucleation points for the mixed oxide formations, especially in locations where multiple grain boundaries converge (i.e. grain vertices). However, the larger average grain size obtained for the γ-phase in this study (0.64±0.41 µm, see section 6.3.1) translates to longer distances between γ/γ grain boundaries and decreases the occurrence of significant overlap contributions to the Al flux so frequently. This probability is further reduced by the fact that the aforementioned elongated sub-micron γ grain morphology accelerates the formation of α-Al_2O_3 and suppresses the formation of mixed oxides after the initial oxide scale has been established [81, 146, 270]. This introduces significant limitations on the cation transport across the oxide scale from the onset [81, 140] and further decreases the probability of MO formation in comparison to regions where β grains are found. Although these factors were decisive in limiting MO formation over γ grain regions during the earlier stages of oxidation, the grain boundary migration and sub-scale Al depletion mechanisms described in section 6.4.1 appear to have been able to counteract these factors and gradually enable the outer scale transformation.

6.4.3 Effect of Cr^{3+} incorporation in the oxide scale

The compositional analysis of the oxide scale and respective evolution with oxidation has revealed that Cr incorporates the oxide scale homogeneously since the early stages of formation in significant quantities (~4 at.%) and eventually segregates to the outer scale as oxidation time progresses. The incorporation of Cr^{3+} in the Al_2O_3 lattice at high temperatures is expected for CoNiCrAlY compositions since Al^{3+} and Cr^{3+} are cations with similar charge and ionic radii that form highly stable sesquioxides (i.e. Al_2O_3 and Cr_2O_3) with similar crystal structures (hexagonal, space group $R_{\bar{3}C}$) [288, 289]. The direct substitution of Al^{3+} by Cr^{3+} in the Al_2O_3 lattice promotes the formation of a substitutional solid solution at temperatures between 1000 and 1200°C [289, 290]. In fact, TEM studies conducted by Doychak and Rühle [291] on α-Al_2O_3 scales grown over NiAl coatings confirmed the Cr presence within the scale as embedded Cr_2O_3 oxides. These observations can be used to explain the outer scale gradual merger process described in section 6.4.1. Firstly, the large presence of Cr^{3+} in the oxide scale and the continuous segregation to the outer scale has likely originated an increased concentration of Cr_2O_3, as this oxide displays the lowest Gibbs free energy after Al_2O_3 (see table 6.2) and similar lattice parameters. When the Cr_2O_3 concentration in the outer scale is high enough to become the predominant species to react with other non-Al elements or oxides, a mixture of spinel (e.g. $CoAl_2O_4$, $AlCo_2O_4$, $NiCr_2O_4$ $NiAl_2O_4$, $CoCr_2O_4$) or a substitutional solid solution $(Ni,Co)(Al,Cr)_2O_4$ is bound to form [108, 270, 292]. However, the formation of Co/Cr-rich oxides like $CoCr_2O_4$ and Cr_2O_3 is likely preferred for the HVOF coatings studied, as Co^{2+} and Cr^{3+} are the predominant non-Al chemical elements found in the outer scale during thermal exposure (see Fig. 6.5) and are amongst the species with lowest Gibbs free energy in MCrAlY systems, apart from Al_2O_3. In fact, it has been reported in several studies that predominant oxide species found in the external layer of the TGO forming over CoNiCrAlY coatings is $CoCr_2O_4$ and Cr_2O_3 [81, 202, 293, 294].

Table 6. 2 Gibbs free energy of formation (ΔG_0) for the most common oxide and spinel formations in MCrAlY systems at 727 °C and 1227 °C [292].

Oxide	$-\Delta \boldsymbol{G_0}\ (\boldsymbol{kJ.mol^{-1}})$	
	727°C	1227°C
Al_2O_3	1362.4	1146.9
Cr_2O_3	861.6	731
CoO	163.3	127.7
NiO	150.7	108.4
$CoCr_2O_4$	52.6	48.9
$CoAl_2O_4$	29.1	26.9
$NiCr_2O_4$	18.6	21.1
$NiAl_2O_4$	15.3	19.9

Another implication of Cr incorporation in oxide scale for the present study is that the $Cr^{3+} \rightarrow Al^{3+}$ substitution induces a severe lattice strain due to the ionic radius of Cr^{3+} (0.62 Å) being 15% larger than Al^{3+} (0.53 Å) [295, 296]. The resulting volumetric expansion of the α-Al_2O_3 lattice originates a pronounced shift in the R-line frequency that is reflected in the residual stresses magnitude. As this shift becomes increasingly more relevant with higher Cr concentrations in the scale [288, 297] and Cr had an active role on the oxidation behaviour studied herein, its impact on the residual stresses are discussed below. The residual stress results shown in section 6.3.6 indicated that the oxide scale stress magnitude is higher during the initial stages of oxidation ($\sigma \sim 5.9$ GPa for t_O<30 min) when the Cr concentration in the inner scale is at the highest point ($3 \leq \mathrm{Cr\ at.\%} \leq 4$) and the outer scale is still very thin (i.e. negligible contribution). This relationship was investigated by using the linear relationship between the Cr concentration in the oxide scale and the R2 line frequency shift reported by Yu and Clarke [297]. The R2 peak shift originated by each specific concentration was estimated using eq. 6.5 and was then input into eq. 3.5 to provide an estimation of the residual stress. A peak shift of 5.2 cm^{-1} was obtained for a concentration of 4 at.% (i.e. 6.3 wt.%) of Cr in the oxide scale after 5 min of oxidation, effectively translating into an estimated residual stress contribution of 1 GPa. This estimation constitutes approximately 18% of the absolute stress value measured for the same specimen and suggests that the substitutional presence of Cr in the oxide scale is notably relevant during the early stages. This argument was further supported by the fact that the 0.8 GPa residual stress reduction observed between 30 and 240 min of oxidation in Fig. 6.10 can be mostly explained by the 2 at.% (i.e. 3.1 wt.%) reduction of Cr concentration in the inner scale reported in Fig. 6.7-a). The same methodology was employed in this case, originating an estimated R2 peak shift of 2.5 cm^{-1} for a

3.1 wt.% Cr concentration reduction in the inner scale that equated to a residual stress value of 0.5 GPa. Although this value only accounts for 65% of the experimental reduction observed in Fig. 6.10, it is a good indication that this variation was predominantly caused by compositional changes in the inner scale arising from the segregation of Cr to the outer scale. These results also indicate that Cr had a more active role on the overall stress state of the oxide scale during the initial stages of oxidation than previously believed.

$$\Delta\nu^{Cr} = 0.827x_{Cr} \qquad \text{(eq. 6.5)}$$

where $\Delta\nu^{Cr}$ is the luminescence peak shift of the R2 line and x_{Cr} is the Cr concentration in the oxide scale in wt.% at room temperature.

Another effect of Cr incorporation in the oxide scale that has been reported in the literature is the impact on oxidation kinetics, especially during the initial stages of the oxide scale formation [279, 298]. Brumm & Grabke [279] reported that the presence of Cr in the α-Al_2O_3 scale accelerates the θ → α phase transformation and originates higher k_p values for the final growth of α-Al_2O_3 scale afterwards when compared with homologous Cr-free scales. This is facilitated by formation of hexagonal $(Al,Cr)_2O_3$ crystals that arise from the reaction between θ or γ-Al_2O_3 polymorphs with Cr_2O_3 and act as premature nucleation points for the formation of hexagonal α-Al_2O_3 [279]. Adding this to the fact that the θ → α phase transformation in Cr-free NiAl compositions is already fast (≤ 2 min of oxidation at 1000°C [150]), it seems reasonable than no obvious θ-Al_2O_3 peaks were detected in the PLPS spectrum in Fig 6.8. Nevertheless, the oxide growth rate discrepancy seen between oxide formations over γ and β grains in Fig. 6.2 are significant and can only be explained by the formation of a transient oxide species with significantly higher k_p values than the α-Al_2O_3 polymorph at some point before the first measurement after 5 min of oxidation. In fact, the 50°C/min heating up rate used in the experiment supports this possibility, as the formation of alumina polymorphs is thermodynamically favoured during the 5 min interval that the specimens were exposed to the 750 and 1000°C temperature range, as indicated by the schematic below [279, 299]. Since the diffusion coefficients of the γ, δ, and θ- Al_2O_3 polymorphs are two order of magnitude higher than α-Al_2O_3 [279], this means that the diffusion rates during this time can be 100 times faster over the β grains and adjacent γ/β phase boundaries, thereby explaining the morphology and topography seen over the β grains. However, the present data is not sufficient to quantify the individual contributions of each metastable polymorph to the oxide scale formation process.

$$\gamma - Al_2O_3 \xrightarrow{750^oC} \delta - Al_2O_3 \xrightarrow{900^oC} \theta - Al_2O_3 \xrightarrow{1000^oC} \alpha - Al_2O_3$$

6.5. Conclusion

The effect of the BC microstructure on the oxidation behaviour of HVOF CoNiCrAlY coatings has been investigated by using a combination of correlative microscopy and spectroscopy techniques. The dual-phase BC microstructure has revealed a site-specific oxidation behaviour that had significant implications on diffusion behaviour along the γ/β grain boundaries and subsequent oxide formation. The resulting oxide scale displayed a dual-layer microstructure with an outer scale displaying an inhomogeneous surface morphology, topography and composition. The evolution of the oxidation scale with oxidation time revealed that the initial outer scale undergoes a slow and gradual transformation that contributes to an overall high stress state and premature failure. It was also found that smaller grain size and reduced γ/β grain boundary distance has a detrimental effect on oxidation, as it promotes the segregation of non-Al elements to the outer scale and contributes to the formation of undesirable mixed oxide formation. It was also found that the incorporation of Cr in the oxide scale is detrimental to the residual stress magnitude and thermo-chemical degradation of the oxide scale.

Chapter 7. Conclusions and future work

7.1. Conclusions

The role of the bond coat microstructure, composition and surface topography on the oxidation, mechanical and performance behaviour of the TBC systems has been studied in this thesis. The main conclusions drawn are highlighted below:

1) The BC interface topography has a significant impact on TBC lifetime due to the alterations induced on the ceramic topcoat microstructure and mechanical properties. The topographical features responsible for these alterations can be better described by employing a multi-parameter characterisation approach. A newly formulated metric, S_{sth}, was proposed to quantify the contribution of the individual summit morphology to the overall BC topography tortuosity. The resulting correlation with TBC lifetime evidenced that this parameter was more effective than the others ISO 25178 surface texture parameters in predicting the overall lifetime trend for different specimens. This suggested that it could be used as a potential lifetime prediction tool under non-extreme oxidation kinetics oxidation. BC topographies with high roughness, lower summit density, lower peak curvature and high total thresholded summit area were associated with more compliant TBC microstructures and higher TBC lifetimes.
2) The degree of BC interface tortuosity affects the TBC microstructure via alteration of the splat formation process and lead to variations in the degree of inter-splat cohesion, intra-splat segmentation and splat curvature. These microstructural features originate a unique splat arrangement in the vicinity of the interface that define the local mechanical properties and the crack path configuration. Specimens with higher tortuosity bond coat topographies originated more compliant TBC microstructures with lower fracture toughness due to reduced inter-splat cohesion and intra-splat segmentation. These features facilitated the activation of stress relaxation mechanisms during loading and contributed to lower critical energy release and crack propagation rates. It was then proposed that although higher tortuosity specimens show a premature tendency for crack nucleation, the lower strain energy release rates induce a slower crack propagation rate. In mechanistic terms, it was also suggested that the failure of APS TBCS is primarily governed by the degree of inter-splat cohesion and intra-splat segmentation. It is noteworthy to mention that the inter-splat separation curvature still had a significant contribution, albeit more modest. TCF testing of these specimens also revealed that more compliant microstructures displayed longer lifetimes.

3) The dual-phase BC microstructure observed in CoNiCrAlY coatings has a significant impact on the formation and evolution of the oxide scale. The site-specific oxidation behaviour observed was primarily caused by microstructurally-induced variations in the diffusion flux across the BC surface that led to the formation of a layered oxide scale. Regions with smaller β-phase grain size and phase boundary distance show accelerated diffusion flux along the γ/β grain boundaries and contribute to the enrichment of outer scale with non-Al cations in the early stages of oxidation. A new analytical model has been proposed to describe the diffusion flux interaction between neighbouring grain boundaries and explain the oxide formation during the initial stages of oxidation. As oxidation progresses, the outer scale undergoes a gradual thermo-chemical transformation due to continuous cationic diffusion of non-Al cations across the oxide scale. All the experimental observations suggest that this transformation is a major contributor for the higher residual stresses leading to premature failure.

All these findings have provided a deeper insight into how the BC microstructure, composition and topography can have dramatic effects in the formation of the oxide scale and in the alteration of the intrinsic properties of the adjacent TBC layer. As the extent of their influence was assessed by their impact on the fundamental properties and lifetime of the TBC system, they can be considered in conjunction with the established literature to provide improved guidelines for the design of TBC systems. The S_{sth} metric can be used in conjunction with multiple processing techniques to develop a comprehensive set of new BC topographies that are more likely to generate more compliant TBC microstructures that can yield longer TBC lifetimes. The β-phase grain size impositions suggested to avoid critical diffusion flux overlap between neighbouring grain boundaries can also be used to mitigate the formation and growth of mixed oxides during the early stages of oxidation.

7.2. Future work

(1) Optimisation of the BC topography via further validation of the S_{sth} metric

Chapter 4 has demonstrated that the BC interface topography has a crucial impact on the durability of TBC systems, further reasserting the importance of obtaining an accurate description of this surface. Although the current study has shown a good correlation of the newly proposed S_{sth} metric with TBC lifetime, this has only been shown for the HVOF and APS techniques and a limited number of BC topographies. Future studies are needed to further validate the applicability of this metric for a wider range of interface topographies and processing techniques. The resulting data could then be used to manufacture microstructurally tailored BC surfaces with laser-ablation techniques to further narrow down the optimal range of BC interfacial features (i.e. summit distance, roughness, summit curvature and overall tortuosity).

(2) Investigation of the influence of stress relaxation mechanisms in APS TBCs fracture mechanics

Chapter 5 has showed that the overall tortuosity of the BC interface has a significant impact on the crack propagation due to the microstructural alterations induced in the TBC. Although it has been shown that the TBC compliance plays a predominant role in governing the fracture behaviour, the influence that each stress relaxation mechanism (i.e. inter-splat sliding, intra-splat crack closure, microcracking) has on TBC compliance is still not fully understood. It would be highly beneficial for the understanding of APS TBC fracture mechanics to conduct a high-resolution in-situ SEM study focused on the observation of these phenomena and respective quantification of their influence in the energy dissipation mechanisms.

(3) Study of the oxide scale formation process for CoNiCrAlY coatings fabricated by other plasma-spraying techniques

Chapter 6 has shown that the oxide scale formation and evolution process is dependent on the initial microstructure and composition of HVOF bond coats. As these properties are fairly sensitive to the fabrication techniques (e.g. APS, CGDS), it is anticipated that the respective oxidation behaviours will affect the oxide scale formation process in different ways. As a result, it would be beneficial to expand the current study to encompass a comprehensive evaluation and comparison of these oxidation behaviours. The enhanced mechanistic understanding arising from this could lead to the development of more advanced techniques that are more effective in mitigating the thermo-chemical degradation processes of the oxide scale.

References

1. Levi, C.G., J.W. Hutchinson, M.-H. Vidal-Sétif, and C.A. Johnson, *Environmental degradation of thermal-barrier coatings by molten deposits.* MRS bulletin, 2012. **37**(10): p. 932-941.
2. Association, I.A.T., *20 year passenger forecast.* Press release 2017. **62**.
3. International, F., *Aviation gas turbine forecast.* 2019.
4. Clarke, D.R., M. Oechsner, and N.P. Padture, *Thermal-barrier coatings for more efficient gas-turbine engines.* MRS bulletin, 2012. **37**(10): p. 891-898.
5. Bathie, W.W., *Fundamentals of gas turbines.* 1984.
6. Perepezko, J.H., *The hotter the engine, the better.* Science, 2009. **326**(5956): p. 1068-1069.
7. Kumar, V. and K. Balasubramanian, *Progress update on failure mechanisms of advanced thermal barrier coatings: A review.* Progress in Organic Coatings, 2016. **90**: p. 54-82.
8. Pollock, T.M. and S. Tin, *Nickel-based superalloys for advanced turbine engines: chemistry, microstructure and properties.* Journal of propulsion and power, 2006. **22**(2): p. 361-374.
9. Clarke, D. and C. Levi, *Materials design for the next generation thermal barrier coatings.* Annual review of materials research, 2003. **33**(1): p. 383-417.
10. Pomeroy, M., *Coatings for gas turbine materials and long term stability issues.* Materials & design, 2005. **26**(3): p. 223-231.
11. Nowotnik, A., *Nickel-based superalloys.* 2016.
12. Evans, A.G., D. Mumm, J. Hutchinson, G. Meier, and F. Pettit, *Mechanisms controlling the durability of thermal barrier coatings.* Progress in materials science, 2001. **46**(5): p. 505-553.
13. Wright, P. and A.G. Evans, *Mechanisms governing the performance of thermal barrier coatings.* Current Opinion in Solid State and Materials Science, 1999. **4**(3): p. 255-265.
14. Miller, R.A., *Thermal barrier coatings for aircraft engines: history and directions.* Journal of thermal spray technology, 1997. **6**(1): p. 35.
15. Harrison, W., D. Moore, and J. Richmond, *Review of an investigation of ceramic coatings for metallic turbine parts and other high-temperature applications.* 1947.
16. Morrell, P., D. Rickerby, and D. Derby, *Advantages/disadvantages of various TBC systems as perceived by the engine manufacturer.* ROLLS ROYCE PLC-REPORT-PNR, 1998.
17. Dennis, P., *Plasma jet technology*. Vol. 5033. 1965: National Aeronautics and Space Administration.
18. Stecura, S., *Effects of compositional changes on the performance of a thermal barrier coating system.[yttria-stabilized zirconia coatings on gas turbine engine blades].* 1978.
19. Sumner, I. and D. Ruckle. *Development of improved-durability plasma sprayed ceramic coatings for gas turbine engines*. in *16th Joint Propulsion Conference*. 1980.
20. Wellman, R. and J. Nicholls, *A review of the erosion of thermal barrier coatings.* Journal of Physics D: Applied Physics, 2007. **40**(16): p. R293.
21. Clarke, D.R. and S.R. Phillpot, *Thermal barrier coating materials.* Materials today, 2005. **8**(6): p. 22-29.
22. Levi, C.G., *Emerging materials and processes for thermal barrier systems.* Current Opinion in Solid State and Materials Science, 2004. **8**(1): p. 77-91.
23. Padture, N.P., M. Gell, and E.H. Jordan, *Thermal barrier coatings for gas-turbine engine applications.* Science, 2002. **296**(5566): p. 280-284.
24. Pan, W., S.R. Phillpot, C. Wan, A. Chernatynskiy, and Z. Qu, *Low thermal conductivity oxides.* MRS bulletin, 2012. **37**(10): p. 917-922.
25. Bakan, E. and R. Vaßen, *Ceramic top coats of plasma-sprayed thermal barrier coatings: materials, processes, and properties.* Journal of Thermal Spray Technology, 2017. **26**(6): p. 992-1010.
26. Tzimas, E., H. Müllejans, S. Peteves, J. Bressers, and W. Stamm, *Failure of thermal barrier coating systems under cyclic thermomechanical loading.* Acta materialia, 2000. **48**(18-19): p. 4699-4707.

27. Vaßen, R., Y. Kagawa, R. Subramanian, P. Zombo, and D. Zhu, *Testing and evaluation of thermal-barrier coatings.* MRS bulletin, 2012. **37**(10): p. 911-916.
28. Scardi, P., M. Leoni, and L. Bertamini, *Influence of phase stability on the residual stress in partially stabilized zirconia TBC produced by plasma spray.* Surface and Coatings Technology, 1995. **76**: p. 106-112.
29. Miller, R.A., J.L. Smialek, and R.G. Garlick, *Phase stability in plasma-sprayed, partially stabilized zirconia-yttria.* 1981.
30. Witz, G., V. Shklover, W. Steurer, S. Bachegowda, and H.P. Bossmann, *Phase evolution in yttria‐stabilized zirconia thermal barrier coatings studied by rietveld refinement of X‐ray powder diffraction patterns.* Journal of the American Ceramic Society, 2007. **90**(9): p. 2935-2940.
31. Nicholls, J.R., Y. Jaslier, and D. Rickerby. *Erosion and foreign object damage of thermal barrier coatings*. in *Materials science forum*. 1997. Trans Tech Publ.
32. Jin, X.-J., *Martensitic transformation in zirconia containing ceramics and its applications.* Current Opinion in Solid State and Materials Science, 2005. **9**(6): p. 313-318.
33. Kelly, P.M. and L.F. Rose, *The martensitic transformation in ceramics—its role in transformation toughening.* Progress in Materials Science, 2002. **47**(5): p. 463-557.
34. Sampath, S., U. Schulz, M.O. Jarligo, and S. Kuroda, *Processing science of advanced thermal-barrier systems.* MRS bulletin, 2012. **37**(10): p. 903-910.
35. Goff, J., W. Hayes, S. Hull, M. Hutchings, and K.N. Clausen, *Defect structure of yttria-stabilized zirconia and its influence on the ionic conductivity at elevated temperatures.* Physical Review B, 1999. **59**(22): p. 14202.
36. Varga, A., S. Mounsey, and D. Fray, https://www.doitpoms.ac.uk/tlplib/fuel-cells/printall.php. University of Cambridge, 2020.
37. Virkar, A.V. and R.L. Matsumoto, *Ferroelastic domain switching as a toughening mechanism in tetragonal zirconia.* Journal of the American Ceramic Society, 1986. **69**(10): p. C‐224-C‐226.
38. Mercer, C., J. Williams, D. Clarke, and A. Evans, *On a ferroelastic mechanism governing the toughness of metastable tetragonal-prime (t′) yttria-stabilized zirconia.* Proceedings of the Royal Society A: Mathematical, Physical and Engineering Sciences, 2007. **463**(2081): p. 1393-1408.
39. Nowak, W., D. Naumenko, G. Mor, F. Mor, D.E. Mack, R. Vassen, L. Singheiser, and W. Quadakkers, *Effect of processing parameters on MCrAlY bondcoat roughness and lifetime of APS–TBC systems.* Surface and coatings technology, 2014. **260**: p. 82-89.
40. Dwivedi, G., V. Viswanathan, S. Sampath, A. Shyam, and E. Lara‐Curzio, *Fracture toughness of plasma‐sprayed thermal barrier ceramics: influence of processing, microstructure, and thermal aging.* Journal of the American Ceramic Society, 2014. **97**(9): p. 2736-2744.
41. Chen, Y., X. Zhang, X. Zhao, N. Markocsan, P. Nylén, and P. Xiao, *Measurements of elastic modulus and fracture toughness of an air plasma sprayed thermal barrier coating using micro-cantilever bending.* Surface and Coatings Technology, 2019. **374**: p. 12-20.
42. Vaßen, R., M.O. Jarligo, T. Steinke, D.E. Mack, and D. Stöver, *Overview on advanced thermal barrier coatings.* Surface and Coatings Technology, 2010. **205**(4): p. 938-942.
43. Kulkarni, A., Z. Wang, T. Nakamura, S. Sampath, A. Goland, H. Herman, J. Allen, J. Ilavsky, G. Long, and J. Frahm, *Comprehensive microstructural characterization and predictive property modeling of plasma-sprayed zirconia coatings.* Acta Materialia, 2003. **51**(9): p. 2457-2475.
44. Brandon, J. and R. Taylor, *Phase stability of zirconia-based thermal barrier coatings part I. Zirconia-yttria alloys.* Surface and Coatings Technology, 1991. **46**(1): p. 75-90.
45. VanValzah, J. and H. Eaton, *Cooling rate effects on the tetragonal to monoclinic phase transformation in aged plasma-sprayed yttria partially stabilized zirconia.* Surface and coatings technology, 1991. **46**(3): p. 289-300.

46. Thompson, J., W. Ji, T. Klocker, and T. Clyne, *Sintering of the top coat in thermal spray TBC systems under service conditions.* Superalloys 2000, 2000: p. 685-692.
47. Sasaki, K., A. Suzuki, N. Akasaka, and T. Terai, *Influence of microstructure on the thermal diffusivity of sintered porous YSZ.* International Journal of Applied Ceramic Technology, 2011. **8**(2): p. 455-466.
48. Ma, W., M. Jarligo, D. Mack, D. Pitzer, J. Malzbender, R. Vaßen, and D. Stöver, *New generation perovskite thermal barrier coating materials.* Journal of thermal spray technology, 2008. **17**(5-6): p. 831-837.
49. Vaßen, R., F. Traeger, and D. Stöver, *New thermal barrier coatings based on pyrochlore/YSZ double‐layer systems.* International Journal of Applied Ceramic Technology, 2004. **1**(4): p. 351-361.
50. Leckie, R., S. Krämer, M. Rühle, and C. Levi, *Thermochemical compatibility between alumina and ZrO2–GdO3/2 thermal barrier coatings.* Acta materialia, 2005. **53**(11): p. 3281-3292.
51. Vaßen, R., E. Bakan, D. Mack, S. Schwartz-Lückge, D. Sebold, Y.J. Sohn, D. Zhou, and O. Guillon, *Performance of YSZ and Gd2Zr2O7/YSZ double layer thermal barrier coatings in burner rig tests.* Journal of the European Ceramic Society, 2020. **40**(2): p. 480-490.
52. McPherson, R., *A review of microstructure and properties of plasma sprayed ceramic coatings.* Surface and Coatings Technology, 1989. **39**: p. 173-181.
53. Wei, P., Z. Wei, S. Li, C. Tan, and J. Du, *Splat formation during plasma spraying for 8 mol% yttria-stabilized zirconia droplets impacting on stainless steel substrate.* Applied surface science, 2014. **321**: p. 538-547.
54. Chraska, T. and A.H. King, *Transmission electron microscopy study of rapid solidification of plasma sprayed zirconia—part I. First splat solidification.* Thin Solid Films, 2001. **397**(1-2): p. 30-39.
55. Cedelle, J., M. Vardelle, and P. Fauchais, *Influence of stainless steel substrate preheating on surface topography and on millimeter-and micrometer-sized splat formation.* Surface and Coatings Technology, 2006. **201**(3-4): p. 1373-1382.
56. Chraska, T. and A.H. King, *Transmission electron microscopy study of rapid solidification of plasma sprayed zirconia–part II. Interfaces and subsequent splat solidification.* Thin Solid Films, 2001. **397**(1-2): p. 40-48.
57. Zhu, D. and R.A. Miller, *Thermal conductivity and elastic modulus evolution of thermal barrier coatings under high heat flux conditions.* Journal of Thermal Spray Technology, 2000. **9**(2): p. 175-180.
58. Nicholls, J.R., K. Lawson, A. Johnstone, and D. Rickerby, *Methods to reduce the thermal conductivity of EB-PVD TBCs.* Surface and Coatings Technology, 2002. **151**: p. 383-391.
59. Choi, S.R., D. Zhu, and R.A. Miller, *Effect of sintering on mechanical properties of plasma‐sprayed zirconia‐based thermal barrier coatings.* Journal of the American Ceramic Society, 2005. **88**(10): p. 2859-2867.
60. Martins, J.P., Y. Chen, G. Brewster, R. McIntyre, and P. Xiao, *Investigation of the bond coat interface topography effect on lifetime, microstructure and mechanical properties of air-plasma sprayed thermal barrier coatings.* Journal of the European Ceramic Society, 2020.
61. Li, C., A. Ohmori, and R. McPherson, *The relationship between microstructure and Young's modulus of thermally sprayed ceramic coatings.* Journal of materials Science, 1997. **32**(4): p. 997-1004.
62. Hadad, M., G. Marot, P. Démarécaux, J. Lesage, J. Michler, and S. Siegmann. *Adhesion tests for thermal spray coatings: Application range of tensile, shear and interfacial indentation methods*. in *Proceedings of ITSC*. 2005.
63. Lima, C. and J. Guilemany, *Adhesion improvements of thermal barrier coatings with HVOF thermally sprayed bond coats.* Surface and Coatings Technology, 2007. **201**(8): p. 4694-4701.
64. Sobolev, V., J. Guilemany, J. Nutting, and J. Miquel, *Development of substrate-coating adhesion in thermal spraying.* International materials reviews, 1997. **42**(3): p. 117-136.

65. Eriksson, R., H. Brodin, S. Johansson, L. Östergren, and X.-H. Li, *Influence of isothermal and cyclic heat treatments on the adhesion of plasma sprayed thermal barrier coatings.* Surface and Coatings Technology, 2011. **205**(23-24): p. 5422-5429.
66. Vaidya, A., V. Srinivasan, T. Streibl, M. Friis, W. Chi, and S. Sampath, *Process maps for plasma spraying of yttria-stabilized zirconia: An integrated approach to design, optimization and reliability.* Materials Science and Engineering: A, 2008. **497**(1-2): p. 239-253.
67. Sobolev, V., J. Guilemany, and A. Martin, *Influence of surface roughness on the flattening of powder particles during thermal spraying.* Journal of Thermal Spray Technology, 1996. **5**(2): p. 207-214.
68. Sobolev, V. and J. Guilemany, *Flattening of droplets and formation of splats in thermal spraying: a review of recent work—part 1.* Journal of Thermal Spray Technology, 1999. **8**(1): p. 87-101.
69. Mutter, M., G. Mauer, R. Mücke, O. Guillon, and R. Vaßen, *Correlation of splat morphologies with porosity and residual stress in plasma-sprayed YSZ coatings.* Surface and Coatings Technology, 2017. **318**: p. 157-169.
70. Griekspoor, *https://www.griekspoorthermalcoatings.com/plasma-spraying.* 2020.
71. Chrome, A., *http://www.amphardchrome.co.uk/plasma-spraying.php.* 2020.
72. Cipitria, A., I. Golosnoy, and T. Clyne, *A sintering model for plasma-sprayed zirconia TBCs. Part I: Free-standing coatings.* Acta Materialia, 2009. **57**(4): p. 980-992.
73. Schulz, U., B. Saruhan, K. Fritscher, and C. Leyens, *Review on advanced EB‐PVD ceramic topcoats for TBC applications.* International journal of applied ceramic technology, 2004. **1**(4): p. 302-315.
74. Gell, M., J. Eric, V. Krishnakumar, K. McCarron, B. Barber, Y.-H. Sohn, and V.K. Tolpygo, *Bond strength, bond stress and spallation mechanisms of thermal barrier coatings.* Surface and Coatings Technology, 1999. **120**: p. 53-60.
75. Wu, L., R. Wu, X. Zhao, and P. Xiao, *Microstructure parameters affecting interfacial adhesion of thermal barrier coatings by the EB-PVD method.* Materials Science and Engineering: A, 2014. **594**: p. 193-202.
76. Singheiser, L., R. Steinbrech, W. Quadakkers, and R. Herzog, *Failure aspects of thermal barrier coatings.* Materials at High Temperatures, 2001. **18**(4): p. 249-259.
77. Clarke, D.R., *Stress generation during high-temperature oxidation of metallic alloys.* Current opinion in solid state and materials science, 2002. **6**(3): p. 237-244.
78. Kawagishi, K., H. Harada, A. Sato, A. Sato, and T. Kobayashi, *The oxidation properties of fourth generation single-crystal nickel-based superalloys.* Jom, 2006. **58**(1): p. 43-46.
79. Reed, R.C., *The superalloys: fundamentals and applications*. 2008: Cambridge university press.
80. Pollock, T., D. Lipkin, and K. Hemker, *Multifunctional coating interlayers for thermal-barrier systems.* Mrs Bulletin, 2012. **37**(10): p. 923-931.
81. Sloof, W. and T. Nijdam, *On the high-temperature oxidation of MCrAlY coatings.* International Journal of Materials Research, 2009. **100**(10): p. 1318-1330.
82. Hindam, H. and D. Whittle, *Microstructure, adhesion and growth kinetics of protective scales on metals and alloys.* Oxidation of metals, 1982. **18**(5-6): p. 245-284.
83. Prescott, R. and M. Graham, *The formation of aluminum oxide scales on high-temperature alloys.* Oxidation of metals, 1992. **38**(3-4): p. 233-254.
84. Naumenko, D., V. Shemet, L. Singheiser, and W.J. Quadakkers, *Failure mechanisms of thermal barrier coatings on MCrAlY-type bondcoats associated with the formation of the thermally grown oxide.* Journal of materials science, 2009. **44**(7): p. 1687-1703.
85. Taylor, M., H.E. Evans, S. Gray, and J.R. Nicholls, *A chromia forming thermal barrier coating system.* Materials and corrosion, 2011. **62**(7): p. 668-673.
86. Hayashi, S., S. Ford, D. Young, D. Sordelet, M. Besser, and B. Gleeson, *α-NiPt (Al) and phase equilibria in the Ni–Al–Pt system at 1150 C.* Acta Materialia, 2005. **53**(11): p. 3319-3328.

87. Achar, D., R. Munoz-Arroyo, L. Singheiser, and W. Quadakkers, *Modelling of phase equilibria in MCrAlY coating systems.* Surface and Coatings Technology, 2004. **187**(2-3): p. 272-283.
88. Pint, B.A., J.A. Haynes, and T.M. Besmann, *Effect of Hf and Y alloy additions on aluminide coating performance.* Surface and Coatings Technology, 2010. **204**(20): p. 3287-3293.
89. Goward, G. and L. Cannon, *Pack cementation coatings for superalloys: a review of history, theory, and practice.* 1988.
90. Goward, G. and D. Boone, *Mechanisms of formation of diffusion aluminide coatings on nickel-base superalloys.* Oxidation of metals, 1971. **3**(5): p. 475-495.
91. Das, D., *Microstructure and high temperature oxidation behavior of Pt-modified aluminide bond coats on Ni-base superalloys.* Progress in Materials Science, 2013. **58**(2): p. 151-182.
92. Busso, E. and F. McClintock, *Mechanisms of cyclic deformation of NiAl single crystals at high temperatures.* Acta metallurgica et materialia, 1994. **42**(10): p. 3263-3275.
93. Dey, G.K., *Physical metallurgy of nickel aluminides.* Sadhana, 2003. **28**(1-2): p. 247-262.
94. Zhang, Y., J. Haynes, B. Pint, I. Wright, and W. Lee, *Martensitic transformation in CVD NiAl and (Ni, Pt) Al bond coatings.* Surface and Coatings Technology, 2003. **163**: p. 19-24.
95. Pan, D., M. Chen, P. Wright, and K. Hemker, *Evolution of a diffusion aluminide bond coat for thermal barrier coatings during thermal cycling.* Acta Materialia, 2003. **51**(8): p. 2205-2217.
96. Evans, A.G., D.R. Clarke, and C.G. Levi, *The influence of oxides on the performance of advanced gas turbines.* Journal of the European Ceramic Society, 2008. **28**(7): p. 1405-1419.
97. Hamadi, S., M.-P. Bacos, M. Poulain, S. Zanna, A. Seyeux, V. Maurice, and P. Marcus, *Oxidation of a Zr-doped NiAl bondcoat thermochemically deposited on a nickel-based superalloy.* Materials at High Temperatures, 2009. **26**(2): p. 195-198.
98. Barrett, C.A., *Effect of 0.1 at.% zirconium on the cyclic oxidation resistance ofβ-NiAl.* Oxidation of Metals, 1988. **30**(5-6): p. 361-390.
99. Pint, B., M. Treska, and L. Hobbs, *The effect of various oxide dispersions on the phase composition and morphology of Al 2 O 3 scales grown on β-NiAl.* Oxidation of Metals, 1997. **47**(1-2): p. 1-20.
100. Zhang, Y., J.A. Haynes, G. Wright, B. Pint, K. Cooley, W. Lee, and P. Liaw, *Effects of Pt incorporation on the isothermal oxidation behavior of chemical vapor deposition aluminide coatings.* Metallurgical and Materials Transactions A, 2001. **32**(7): p. 1727-1741.
101. Tolpygo, V., K. Murphy, and D. Clarke, *Effect of Hf, Y and C in the underlying superalloy on the rumpling of diffusion aluminide coatings.* Acta Materialia, 2008. **56**(3): p. 489-499.
102. Rickerby, D.S. and R.G. Wing, *Thermal barrier coating for a superalloy article and a method of application thereof*. 1999, Google Patents.
103. Rickerby, D.S., S.R. Bell, and R.G. Wing, *Method of applying a thermal barrier coating to a superalloy article and a thermal barrier coating*. 1997, Google Patents.
104. Zhang, Y., J. Stacy, B.A. Pint, J.A. Haynes, B.T. Hazel, and B. Nagaraj, *Interdiffusion behavior of Pt-diffused $\gamma+\gamma'$ coatings on Ni-based superalloys.* Surface and Coatings Technology, 2008. **203**(5-7): p. 417-421.
105. Zhao, X., B. Cernik, C. Tang, S. Thompson, and P. Xiao, *Stress evolution in a Pt-diffused γ/γ' bond coat after oxidation.* Surface and Coatings Technology, 2014. **247**: p. 48-54.
106. Gleeson, B., W. Wang, S. Hayashi, and D.J. Sordelet. *Effects of platinum on the interdiffusion and oxidation behavior of Ni-Al-based alloys*. in *Materials Science Forum*. 2004. Trans Tech Publ.
107. Hayashi, S., D.J. Sordelet, L.R. Walker, and B. Gleeson, *Interdiffusion in Pt-Containing γ-Ni and γ'-Ni3Al alloys at 1150 C.* Materials transactions, 2008: p. 0805260433-0805260433.
108. Saeidi, S., K. Voisey, and D. McCartney, *Mechanical properties and microstructure of VPS and HVOF CoNiCrAlY coatings.* Journal of thermal spray technology, 2011. **20**(6): p. 1231-1243.
109. Mauer, G., D. Sebold, and R. Vaßen, *MCrAlY bondcoats by high-velocity atmospheric plasma spraying.* Journal of thermal spray technology, 2014. **23**(1-2): p. 140-146.

110. Patterson, T., A. Leon, B. Jayaraj, J. Liu, and Y. Sohn, *Thermal cyclic lifetime and oxidation behavior of air plasma sprayed CoNiCrAlY bond coats for thermal barrier coatings.* Surface and Coatings Technology, 2008. **203**(5-7): p. 437-441.
111. Wood, G.C., *High-temperature oxidation of alloys.* Oxidation of Metals, 1970. **2**(1): p. 11-57.
112. Busso, E., H. Evans, Z. Qian, and M. Taylor, *Effects of breakaway oxidation on local stresses in thermal barrier coatings.* Acta materialia, 2010. **58**(4): p. 1242-1251.
113. Weman, K., *Welding processes handbook*. 2011: Elsevier.
114. Karthikeyan, J., *The advantages and disadvantages of the cold spray coating process*, in *The cold spray materials deposition process*. 2007, Elsevier. p. 62-71.
115. Rajasekaran, B., G. Mauer, and R. Vaßen, *Enhanced characteristics of HVOF-sprayed MCrAlY bond coats for TBC applications.* Journal of thermal spray technology, 2011. **20**(6): p. 1209-1216.
116. Fauchais, P., J. Heberlein, and M. Boulos, *Thermal Spray Fundamentals from Powder to Part, Ilustrada.* 2012.
117. technologies, F.s., *High velocity oxygen fuel (HVOF) schematic*. 2020. p. https://www.fst.nl/systems/hvof.
118. Eriksson, R., S. Sjöström, H. Brodin, S. Johansson, L. Östergren, and X.-H. Li, *TBC bond coat–top coat interface roughness: Influence on fatigue life and modelling aspects.* Surface and Coatings Technology, 2013. **236**: p. 230-238.
119. Yuan, K., Y. Yu, and J.-F. Wen, *A study on the thermal cyclic behavior of thermal barrier coatings with different MCrAlY roughness.* Vacuum, 2017. **137**: p. 72-80.
120. Weeks, M.D., R. Subramanian, A. Vaidya, and D.R. Mumm, *Defining optimal morphology of the bond coat–thermal barrier coating interface of air-plasma sprayed thermal barrier coating systems.* Surface and Coatings Technology, 2015. **273**: p. 50-59.
121. VV, E.J.G., V. Viswanathan, M.J. Lance, J.A. Haynes, B.A. Pint, and S. Sampath, *Role of bond coat processing methods on the durability of plasma sprayed thermal barrier systems.* Surface and Coatings Technology, 2019. **375**: p. 782-792.
122. Gupta, D. and D. Duvall, *A silicon and hafnium modified plasma sprayed MCrAlY coating.* Superalloys 1984, 1984: p. 711.
123. Nicholls, J., N.J. Simms, W. Chan, and H. Evans, *Smart overlay coatings—concept and practice.* Surface and Coatings Technology, 2002. **149**(2-3): p. 236-244.
124. Jarvis, E.A. and E.A. Carter, *The role of reactive elements in thermal barrier coatings.* Computing in Science & Engineering, 2002. **4**(2): p. 33-41.
125. Hou, P.Y. *The reactive element effect–past, present and future*. in *Materials Science Forum*. 2011. Trans Tech Publ.
126. Lu, J., Y. Chen, C. Zhao, H. Zhang, L. Luo, B. Xu, X. Zhao, F. Guo, and P. Xiao, *Significantly improving the oxidation and spallation resistance of a MCrAlY alloy by controlling the distribution of yttrium.* Corrosion Science, 2019. **153**: p. 178-190.
127. Nijdam, T. and W. Sloof, *Effect of Y distribution on the oxidation kinetics of NiCoCrAlY bond coat alloys.* Oxidation of metals, 2008. **69**(1-2): p. 1-12.
128. Wu, Q., H.M. Chan, J.M. Rickman, and M.P. Harmer, *Effect of Hf 4+ Concentration on Oxygen Grain ‐ Boundary Diffusion in Alumina.* Journal of the American Ceramic Society, 2015. **98**(10): p. 3346-3351.
129. Christensen, R., V. Tolpygo, and D. Clarke, *The influence of the reactive element yttrium on the stress in alumina scales formed by oxidation.* Acta Materialia, 1997. **45**(4): p. 1761-1766.
130. Chevalier, J., C. Olagnon, and G. Fantozzi, *Subcritical crack propagation in 3Y ‐ TZP ceramics: static and cyclic fatigue.* Journal of the American Ceramic Society, 1999. **82**(11): p. 3129-3138.
131. Baufeld, B. and M. Schmücker, *Microstructural evolution of a NiCoCrAlY coating on an IN100 substrate.* Surface and Coatings Technology, 2005. **199**(1): p. 49-56.
132. Czech, N., F. Schmitz, and W. Stamm, *Microstructural analysis of the role of rhenium in advanced MCrAlY coatings.* Surface and Coatings Technology, 1995. **76**: p. 28-33.

133. Brandl, W., H. Grabke, D. Toma, and J. Krüger, *The oxidation behaviour of sprayed MCrAlY coatings.* Surface and Coatings Technology, 1996. **86**: p. 41-47.
134. Mendis, B., B. Tryon, T. Pollock, and K. Hemker, *Microstructural observations of as-prepared and thermal cycled NiCoCrAlY bond coats.* Surface and Coatings Technology, 2006. **201**(7): p. 3918-3925.
135. Chen, Y., X. Zhao, and P. Xiao, *Effect of surface curvature on oxidation of a MCrAlY coating.* Corrosion Science, 2020. **163**: p. 108256.
136. Weng, W.-X., Y.-M. Wang, Y.-M. Liao, C.-C. Li, and Q. Li, *Comparison of microstructural evolution and oxidation behaviour of NiCoCrAlY and CoNiCrAlY as bond coats used for thermal barrier coatings.* Surface and Coatings Technology, 2018. **352**: p. 285-294.
137. Eriksson, R., M. Gupta, E. Broitman, K.P. Jonnalagadda, P. Nylén, and R.L. Peng, *Stresses and cracking during chromia-spinel-NiO cluster formation in TBC systems.* Journal of Thermal Spray Technology, 2015. **24**(6): p. 1002-1014.
138. Hemker, K., B. Mendis, and C. Eberl, *Characterizing the microstructure and mechanical behavior of a two-phase NiCoCrAlY bond coat for thermal barrier systems.* Materials Science and Engineering: A, 2008. **483**: p. 727-730.
139. Chia, C., K. Khor, Y. Gu, and F. Boey, *Viscoelastic properties of plasma sprayed NiCoCrAlY coatings.* Thin solid films, 2002. **405**(1-2): p. 146-152.
140. Heuer, A., T. Nakagawa, M. Azar, D. Hovis, J. Smialek, B. Gleeson, N. Hine, H. Guhl, H.-S. Lee, and P. Tangney, *On the growth of Al2O3 scales.* Acta Materialia, 2013. **61**(18): p. 6670-6683.
141. Liu, X., T. Wang, C. Li, Z. Zheng, and Q. Li, *Microstructural evolution and growth kinetics of thermally grown oxides in plasma sprayed thermal barrier coatings.* Progress in Natural Science: Materials International, 2016. **26**(1): p. 103-111.
142. Toma, D., W. Brandl, and U. Köster, *Studies on the transient stage of oxidation of VPS and HVOF sprayed MCrAlY coatings.* Surface and Coatings Technology, 1999. **120**: p. 8-15.
143. Stott, F. and G. Wood, *Growth and adhesion of oxide scales on Al2O3-forming alloys and coatings.* Materials Science and Engineering, 1987. **87**: p. 267-274.
144. Nijdam, T. and W. Sloof, *The role of transient oxides during deposition and thermal cycling of thermal barrier coatings.* Materials at High Temperatures, 2005. **22**(3-4): p. 551-559.
145. Zhang, W.X., Y.L. Sun, and T.J. Wang. *Effect Of Spinel Growth On The Delamination Of Thermal Barrier Coatings*. in *Key Engineering Materials*. 2011. Trans Tech Publ.
146. Chen, Y., X. Zhao, and P. Xiao, *Effect of microstructure on early oxidation of MCrAlY coatings.* Acta Materialia, 2018. **159**: p. 150-162.
147. Haynes, J.A., M. Ferber, and W. Porter, *Thermal cycling behavior of plasma-sprayed thermal barrier coatings with various MCrAlX bond coats.* Journal of Thermal Spray Technology, 2000. **9**(1): p. 38.
148. Matsumoto, M., T. Kato, K. Hayakawa, N. Yamaguchi, S. Kitaoka, and H. Matsubara, *The effect of pre-oxidation atmosphere on the durability of EB-PVD thermal barrier coatings with CoNiCrAlY bond coats.* Surface and Coatings Technology, 2008. **202**(12): p. 2743-2748.
149. Matsumoto, M., K. Hayakawa, S. Kitaoka, H. Matsubara, H. Takayama, Y. Kagiya, and Y. Sugita, *The effect of preoxidation atmosphere on oxidation behavior and thermal cycle life of thermal barrier coatings.* Materials Science and Engineering: A, 2006. **441**(1-2): p. 119-125.
150. Chen, L., C. Ying, A.S. Eggeman, G. Brewster, and X. Ping, *Pt effect on early stage oxidation behaviour of Pt-diffused γ-Ni/γ'-Ni3Al coatings.* Acta Materialia, 2020.
151. Lelait, L., S. Alperine, and R. Mevrel, *Alumina scale growth at zirconia-MCrAlY interface: a microstructural study.* Journal of materials science, 1992. **27**(1): p. 5-12.
152. Taniguchi, S. and A. Andoh, *Improvement in the oxidation resistance of an Al-deposited Fe–Cr–Al foil by preoxidation.* Oxidation of Metals, 2002. **58**(5-6): p. 545-562.
153. Evans, H. and M. Taylor, *Diffusion cells and chemical failure of MCrAlY bond coats in thermal-barrier coating systems.* Oxidation of metals, 2001. **55**(1-2): p. 17-34.

154. Ni, L., C. Liu, H. Huang, and C. Zhou, *Thermal cycling behavior of thermal barrier coatings with HVOF NiCrAlY bond coat.* Journal of thermal spray technology, 2011. **20**(5): p. 1133.
155. Tomimatsu, T., S. Zhu, and Y. Kagawa, *Effect of thermal exposure on stress distribution in TGO layer of EB-PVD TBC.* Acta Materialia, 2003. **51**(8): p. 2397-2405.
156. Tolpygo, V., J. Dryden, and D. Clarke, *Determination of the growth stress and strain in α-Al2O3 scales during the oxidation of Fe–22Cr–4.8 Al–0.3 Y alloy.* Acta Materialia, 1998. **46**(3): p. 927-937.
157. Mennicke, C., D. Clarke, and M. Rühle, *Stress relaxation in thermally grown alumina scales on heating and cooling FeCrAl and FeCrAlY alloys.* Oxidation of metals, 2001. **55**(5-6): p. 551-569.
158. Martena, M., D. Botto, P. Fino, S. Sabbadini, M. Gola, and C. Badini, *Modelling of TBC system failure: Stress distribution as a function of TGO thickness and thermal expansion mismatch.* Engineering Failure Analysis, 2006. **13**(3): p. 409-426.
159. Gupta, M., K. Skogsberg, and P. Nylén, *Influence of topcoat-bondcoat interface roughness on stresses and lifetime in thermal barrier coatings.* Journal of thermal spray technology, 2014. **23**(1-2): p. 170-181.
160. Evans, A., M. He, and J. Hutchinson, *Effect of interface undulations on the thermal fatigue of thin films and scales on metal substrates.* Acta Materialia, 1997. **45**(9): p. 3543-3554.
161. Clarke, D.R., *The lateral growth strain accompanying the formation of a thermally grown oxide.* Acta materialia, 2003. **51**(5): p. 1393-1407.
162. Evans, A., M. He, and J. Hutchinson, *Mechanics-based scaling laws for the durability of thermal barrier coatings.* Progress in materials science, 2001. **46**(3-4): p. 249-271.
163. Lipkin, D.a. and D. Clarke, *Measurement of the stress in oxide scales formed by oxidation of alumina-forming alloys.* Oxidation of Metals, 1996. **45**(3-4): p. 267-280.
164. Yang, L., L. Zheng, and H. Guo, *The residual stress of oxide scales grown on Ni-Al alloys doped with minor Dy and Y.* Corrosion Science, 2016. **112**: p. 542-551.
165. He, M., A. Evans, and J. Hutchinson, *The ratcheting of compressed thermally grown thin films on ductile substrates.* Acta Materialia, 2000. **48**(10): p. 2593-2601.
166. Hsueh, C., P.F. Becher, E.R. Fuller, S. Langer, and W. Carter. *Surface-roughness induced residual stresses in thermal barrier coatings: computer simulations*. in *Materials science forum*. 1999. Trans Tech Publ.
167. Krishnasamy, J., S.A. Ponnusami, S. Turteltaub, and S. van der Zwaag, *Computational investigation of porosity effects on fracture behavior of thermal barrier coatings.* Ceramics International, 2019. **45**(16): p. 20518-20527.
168. Evans, H., *Oxidation failure of TBC systems: An assessment of mechanisms.* Surface and Coatings Technology, 2011. **206**(7): p. 1512-1521.
169. Arai, M., Y. Okajima, and K. Kishimoto, *Mixed-mode interfacial fracture toughness for thermal barrier coating.* Engineering Fracture Mechanics, 2007. **74**(13): p. 2055-2069.
170. Wessel, E. and R.W. Steinbrech. *Crack propagation in plasma-sprayed thermal barrier coatings*. in *Key Engineering Materials*. 2002. Trans Tech Publ.
171. Gupta, M., R. Eriksson, U. Sand, and P. Nylén, *A diffusion-based oxide layer growth model using real interface roughness in thermal barrier coatings for lifetime assessment.* Surface and Coatings Technology, 2015. **271**: p. 181-191.
172. Schwarzer, J., D. Löhe, and O. Vöhringer, *Influence of the TGO creep behavior on delamination stress development in thermal barrier coating systems.* Materials Science and Engineering: A, 2004. **387**: p. 692-695.
173. Kyaw, S., A. Jones, and T. Hyde, *Predicting failure within TBC system: Finite element simulation of stress within TBC system as affected by sintering of APS TBC, geometry of substrate and creep of TGO.* Engineering Failure Analysis, 2013. **27**: p. 150-164.
174. Busso, E.P., L. Wright, H. Evans, L. McCartney, S. Saunders, S. Osgerby, and J. Nunn, *A physics-based life prediction methodology for thermal barrier coating systems.* Acta materialia, 2007. **55**(5): p. 1491-1503.

175. Hillery, R., B. Pilsner, R. McKnight, T. Cook, and M. Hartle, *Thermal barrier coating life prediction model development.* 1988.
176. Théry, P.-Y., M. Poulain, M. Dupeux, and M. Braccini, *Spallation of two thermal barrier coating systems: experimental study of adhesion and energetic approach to lifetime during cyclic oxidation.* Journal of Materials Science, 2009. **44**(7): p. 1726-1733.
177. Dong, H., G.J. Yang, C.X. Li, X.T. Luo, and C.J. Li, *Effect of TGO thickness on thermal cyclic lifetime and failure mode of plasma‐sprayed TBC s.* Journal of the American Ceramic Society, 2014. **97**(4): p. 1226-1232.
178. Vaßen, R., S. Giesen, and D. Stöver, *Lifetime of plasma-sprayed thermal barrier coatings: comparison of numerical and experimental results.* Journal of thermal spray technology, 2009. **18**(5-6): p. 835.
179. Tolpygo, V., D. Clarke, and K. Murphy, *Oxidation-induced failure of EB-PVD thermal barrier coatings.* Surface and coatings technology, 2001. **146**: p. 124-131.
180. Jackson, R., M. Taylor, H. Evans, and X.-H. Li, *Oxidation study of an EB-PVD MCrAlY thermal barrier coating system.* Oxidation of metals, 2011. **76**(3-4): p. 259-271.
181. Cheng, B., Z.-Y. Wei, L. Chen, G.-J. Yang, C.-X. Li, and C.-J. Li, *Prolong the durability of La2Zr2O7/YSZ TBCs by decreasing the cracking driving force in ceramic coatings.* Journal of the European Ceramic Society, 2018. **38**(16): p. 5482-5488.
182. Taylor, M., W. Pragnell, and H. Evans, *The influence of bond coat surface roughness on chemical failure and delamination in TBC systems.* Materials and corrosion, 2008. **59**(6): p. 508-513.
183. Vaßen, R., G. Kerkhoff, and D. Stöver, *Development of a micromechanical life prediction model for plasma sprayed thermal barrier coatings.* Materials Science and Engineering: A, 2001. **303**(1-2): p. 100-109.
184. Choi, S.R., J.W. Hutchinson, and A. Evans, *Delamination of multilayer thermal barrier coatings.* Mechanics of materials, 1999. **31**(7): p. 431-447.
185. Hutchinson, J., M. He, and A. Evans, *The influence of imperfections on the nucleation and propagation of buckling driven delaminations.* Journal of the Mechanics and Physics of Solids, 2000. **48**(4): p. 709-734.
186. Kim, D.-J., I.-H. Shin, J.-M. Koo, C.-S. Seok, and T.-W. Lee, *Failure mechanisms of coin-type plasma-sprayed thermal barrier coatings with thermal fatigue.* Surface and Coatings Technology, 2010. **205**: p. S451-S458.
187. Ping-wei, C., W. Shao-ming, and W. Feng-Hui, *Fracture analysis of thermal barrier coating delamination under thermal shock.* Procedia Engineering, 2015. **99**: p. 344-348.
188. Eriksson, R. and K.P. Jonnalagadda. *A study on crack configurations in thermal barrier coatings*. in *ASME Turbo Expo 2017: Turbomachinery Technical Conference and Exposition*. 2017. American Society of Mechanical Engineers Digital Collection.
189. Evans, A. and J. Hutchinson, *The mechanics of coating delamination in thermal gradients.* Surface and Coatings Technology, 2007. **201**(18): p. 7905-7916.
190. Hutchinson, J. and A. Evans, *On the delamination of thermal barrier coatings in a thermal gradient.* Surface and Coatings Technology, 2002. **149**(2-3): p. 179-184.
191. Li, G.-R., B.-W. Lv, G.-J. Yang, W.-X. Zhang, C.-X. Li, and C.-J. Li, *Relationship between lamellar structure and elastic modulus of thermally sprayed thermal barrier coatings with intra-splat cracks.* Journal of Thermal Spray Technology, 2015. **24**(8): p. 1355-1367.
192. Huang, J., W. Wang, X. Lu, S. Liu, and C. Li, *Influence of lamellar interface morphology on cracking resistance of plasma-sprayed YSZ coatings.* Coatings, 2018. **8**(5): p. 187.
193. Krishnasamy, J., S.A. Ponnusami, S. Turteltaub, and S. van der Zwaag, *Numerical Investigation into the Effect of Splats and Pores on the Thermal Fracture of Air Plasma-Sprayed Thermal Barrier Coatings.* Journal of Thermal Spray Technology, 2019. **28**(8): p. 1881-1892.

194. Strauss, D., G. Müller, G. Schumacher, V. Engelko, W. Stamm, D. Clemens, and W. Quaddakers, *Oxide scale growth on MCrAlY bond coatings after pulsed electron beam treatment and deposition of EBPVD-TBC.* Surface and coatings Technology, 2001. **135**(2-3): p. 196-201.
195. Zhang, D., S. Gong, H. Xu, and Z. Wu, *Effect of bond coat surface roughness on the thermal cyclic behavior of thermal barrier coatings.* Surface and Coatings Technology, 2006. **201**(3-4): p. 649-653.
196. Mumm, D., A. Evans, and I. Spitsberg, *Characterization of a cyclic displacement instability for a thermally grown oxide in a thermal barrier system.* Acta Materialia, 2001. **49**(12): p. 2329-2340.
197. Mumm, D. and A. Evans, *On the role of imperfections in the failure of a thermal barrier coating made by electron beam deposition.* Acta materialia, 2000. **48**(8): p. 1815-1827.
198. Xu, T., M. He, and A. Evans, *A numerical assessment of the propagation and coalescence of delamination cracks in thermal barrier systems.* Interface Science, 2003. **11**(3): p. 349-358.
199. Schlichting, K.W., N. Padture, E. Jordan, and M. Gell, *Failure modes in plasma-sprayed thermal barrier coatings.* Materials Science and Engineering: A, 2003. **342**(1-2): p. 120-130.
200. Freund, L., *Energy flux into the tip of an extending crack in an elastic solid.* Journal of Elasticity, 1972. **2**(4): p. 341-349.
201. Wiederhorn, S., *Subcritical crack growth in ceramics*, in *Fracture mechanics of ceramics*. 1974, Springer. p. 613-646.
202. Martins, J.P., Y. Chen, G. Brewster, R. McIntyre, and P. Xiao, *Investigation of the bond coat interface topography effect on lifetime, microstructure and mechanical properties of air-plasma sprayed thermal barrier coatings.* Journal of the European Ceramic Society, 2020. **40**(15): p. 5719-5730.
203. Ritchie, R., *Mechanisms of fatigue crack propagation in metals, ceramics and composites: role of crack tip shielding.* Materials Science and Engineering: A, 1988. **103**(1): p. 15-28.
204. Zhao, Y., A. Shinmi, X. Zhao, P. Withers, S. Van Boxel, N. Markocsan, P. Nylen, and P. Xiao, *Investigation of interfacial properties of atmospheric plasma sprayed thermal barrier coatings with four-point bending and computed tomography technique.* Surface and Coatings Technology, 2012. **206**(23): p. 4922-4929.
205. Schütze, M. and M. Malessa, *Standardisation of thermal cycling exposure testing*. Vol. 53. 2014: Elsevier.
206. Egerton, R.F., *Physical principles of electron microscopy*. Vol. 56. 2005: Springer.
207. Ul-Hamid, A., *Characterization of a thin film of Al2O3 by SEM/EDS analysis.* Corrosion prevention & control, 2002. **49**(3): p. 93-98.
208. Joy, D.C. and C.S. Joy, *Low voltage scanning electron microscopy.* Micron, 1996. **27**(3-4): p. 247-263.
209. Oliver, W.C. and G.M. Pharr, *An improved technique for determining hardness and elastic modulus using load and displacement sensing indentation experiments.* Journal of materials research, 1992. **7**(6): p. 1564-1583.
210. Chen, Y., C. Li, X. Zhao, and P. Xiao, *Measurements and understanding of the stiffness of an air plasma sprayed thermal barrier coating using three-point bending.* Surface and Coatings Technology, 2020: p. 125678.
211. Wang, X., S. Tint, M. Chiu, and A. Atkinson, *Stiffness of free-standing thermal barrier coating top coats measured by bending tests.* Acta materialia, 2012. **60**(8): p. 3247-3258.
212. Hofinger, I., M. Oechsner, H.-A. Bahr, and M.V. Swain, *Modified four-point bending specimen for determining the interface fracture energy for thin, brittle layers.* International Journal of Fracture, 1998. **92**(3): p. 213-220.
213. Standard, A., *C1161-13 (2013) Standard test method for flexural strength of advanced ceramics at ambient temperature.* ASTM International, West Conshohocken, 2013.
214. Qian, G., T. Nakamura, C. Berndt, and S. Leigh, *Tensile toughness test and high temperature fracture analysis of thermal barrier coatings.* Acta materialia, 1997. **45**(4): p. 1767-1784.

215. Segmüller, A., *Characterization of epitaxial films by grazing-incidence X-ray diffraction.* Thin Solid Films, 1987. **154**(1-2): p. 33-42.
216. Lee, M., *X-Ray diffraction for materials research: from fundamentals to applications*. 2017: CRC Press.
217. Hejrani, E., D. Sebold, W. Nowak, G. Mauer, D. Naumenko, R. Vaßen, and W. Quadakkers, *Isothermal and cyclic oxidation behavior of free standing MCrAlY coatings manufactured by high-velocity atmospheric plasma spraying.* Surface and Coatings Technology, 2017. **313**: p. 191-201.
218. Bose, S., *High temperature coatings*. 2017: Butterworth-Heinemann.
219. Wang, Y., A.S. Özcan, G. Özaydin, K.F. Ludwig Jr, A. Bhattacharyya, T.D. Moustakas, H. Zhou, R.L. Headrick, and D.P. Siddons, *Real-time synchrotron x-ray studies of low-and high-temperature nitridation of c-plane sapphire.* Physical Review B, 2006. **74**(23): p. 235304.
220. He, J. and D.R. Clarke, *Determination of the piezospectroscopic coefficients for chromium‐doped sapphire.* Journal of the American Ceramic Society, 1995. **78**(5): p. 1347-1353.
221. Peng, X. and D.R. Clarke, *Piezospectroscopic analysis of interface debonding in thermal barrier coatings.* Journal of the American Ceramic Society, 2000. **83**(5): p. 1165-1170.
222. Busso, E., J. Lin, S. Sakurai, and M. Nakayama, *A mechanistic study of oxidation-induced degradation in a plasma-sprayed thermal barrier coating system.: Part I: model formulation.* Acta materialia, 2001. **49**(9): p. 1515-1528.
223. Jinnestrand, M. and S. Sjöström, *Investigation by 3D FE simulations of delamination crack initiation in TBC caused by alumina growth.* Surface and Coatings Technology, 2001. **135**(2-3): p. 188-195.
224. Schwingel, D., R. Taylor, T. Haubold, J. Wigren, and C. Gualco, *Mechanical and thermophysical properties of thick PYSZ thermal barrier coatings: correlation with microstructure and spraying parameters.* Surface and Coatings Technology, 1998. **108**: p. 99-106.
225. Salimijazi, H., L. Pershin, T. Coyle, J. Mostaghimi, S. Chandra, Y. Lau, L. Rosenzweig, and E. Moran, *Effect of droplet characteristics and substrate surface topography on the final morphology of plasma-sprayed zirconia single splats.* Journal of thermal spray technology, 2007. **16**(2): p. 291-299.
226. Lima, R., A. Kucuk, and C. Berndt, *Evaluation of microhardness and elastic modulus of thermally sprayed nanostructured zirconia coatings.* Surface and Coatings Technology, 2001. **135**(2-3): p. 166-172.
227. Unocic, K.A. and B.A. Pint, *Characterization of the alumina scale formed on a commercial MCrAlYHfSi coating.* Surface and Coatings Technology, 2010. **205**(5): p. 1178-1182.
228. Ahrens, M., R. Vaßen, D. Stöver, and S. Lampenscherf, *Sintering and creep processes in plasma-sprayed thermal barrier coatings.* Journal of thermal spray technology, 2004. **13**(3): p. 432-442.
229. Keyvani, A., M. Bahamirian, and A. Kobayashi, *Effect of sintering rate on the porous microstructural, mechanical and thermomechanical properties of YSZ and CSZ TBC coatings undergoing thermal cycling.* Journal of Alloys and Compounds, 2017. **727**: p. 1057-1066.
230. Lv, B., R. Mücke, X. Fan, T. Wang, O. Guillon, and R. Vaßen, *Sintering resistance of advanced plasma-sprayed thermal barrier coatings with strain-tolerant microstructures.* Journal of the European Ceramic Society, 2018. **38**(15): p. 5092-5100.
231. Thompson, J. and T. Clyne, *The effect of heat treatment on the stiffness of zirconia top coats in plasma-sprayed TBCs.* Acta Materialia, 2001. **49**(9): p. 1565-1575.
232. Tang, F. and J.M. Schoenung, *Evolution of Young's modulus of air plasma sprayed yttria-stabilized zirconia in thermally cycled thermal barrier coatings.* Scripta Materialia, 2006. **54**(9): p. 1587-1592.
233. Choi, S.R., D. Zhu, and R.A. Miller, *Mechanical Properties/Database of Plasma‐Sprayed ZrO2‐8wt% Y2O3 Thermal Barrier Coatings.* International Journal of Applied Ceramic Technology, 2004. **1**(4): p. 330-342.

234. Eldridge, J.I., D. Zhu, and R.A. Miller, *Mesoscopic nonlinear elastic modulus of thermal barrier coatings determined by cylindrical punch indentation.* Journal of the American Ceramic Society, 2001. **84**(11): p. 2737-2739.
235. Beck, T., R. Herzog, O. Trunova, M. Offermann, R.W. Steinbrech, and L. Singheiser, *Damage mechanisms and lifetime behavior of plasma-sprayed thermal barrier coating systems for gas turbines—Part II: Modeling.* Surface and coatings technology, 2008. **202**(24): p. 5901-5908.
236. Kuroda, S. and T. Clyne, *The quenching stress in thermally sprayed coatings.* Thin solid films, 1991. **200**(1): p. 49-66.
237. Zhao, X., J. Liu, D. Rickerby, R. Jones, and P. Xiao, *Evolution of interfacial toughness of a thermal barrier system with a Pt-diffused γ/γ' bond coat.* Acta materialia, 2011. **59**(16): p. 6401-6411.
238. Wang, J.-S. and A. Evans, *Measurement and analysis of buckling and buckle propagation in compressed oxide layers on superalloy substrates.* Acta Materialia, 1998. **46**(14): p. 4993-5005.
239. Vasinonta, A. and J.L. Beuth, *Measurement of interfacial toughness in thermal barrier coating systems by indentation.* Engineering Fracture Mechanics, 2001. **68**(7): p. 843-860.
240. Guo, S., D. Mumm, A.M. Karlsson, and Y. Kagawa, *Measurement of interfacial shear mechanical properties in thermal barrier coating systems by a barb pullout method.* Scripta Materialia, 2005. **53**(9): p. 1043-1048.
241. Liu, Y.-F., Y. Kagawa, and A. Evans, *Analysis of a "barb test" for measuring the mixed-mode delamination toughness of coatings.* Acta materialia, 2008. **56**(1): p. 43-49.
242. Choi, S., D. Zhu, and R. Miller, *Fracture behavior under mixed-mode loading of ceramic plasma-sprayed thermal barrier coatings at ambient and elevated temperatures.* Engineering fracture mechanics, 2005. **72**(13): p. 2144-2158.
243. Bahr, H.-A., H. Balke, T. Fett, I. Hofinger, G. Kirchhoff, D. Munz, A. Neubrand, A. Semenov, H.-J. Weiss, and Y. Yang, *Cracks in functionally graded materials.* Materials Science and Engineering: A, 2003. **362**(1-2): p. 2-16.
244. Hirakata, H., M. Kitazawa, and T. Kitamura, *Fatigue crack growth along interface between metal and ceramics submicron-thick films in inert environment.* Acta Materialia, 2006. **54**(1): p. 89-97.
245. Yamazaki, Y., A. Schmidt, and A. Scholz, *The determination of the delamination resistance in thermal barrier coating system by four-point bending tests.* Surface and Coatings Technology, 2006. **201**(3-4): p. 744-754.
246. Zhao, P., C. Sun, X. Zhu, F. Shang, and C. Li, *Fracture toughness measurements of plasma-sprayed thermal barrier coatings using a modified four-point bending method.* Surface and Coatings Technology, 2010. **204**(24): p. 4066-4074.
247. Zhu, Q., W. He, J. Zhu, Y. Zhou, and L. Chen, *Investigation on interfacial fracture toughness of plasma-sprayed TBCs using a three-point bending method.* Surface and Coatings Technology, 2018. **353**: p. 75-83.
248. Charalambides, P., J. Lund, A. Evans, and R. McMeeking, *A test specimen for determining the fracture resistance of bimaterial interfaces.* 1989.
249. Charalambides, P., H. Cao, J. Lund, and A. Evans, *Development of a test method for measuring the mixed mode fracture resistance of bimaterial interfaces.* Mechanics of materials, 1990. **8**(4): p. 269-283.
250. Yamazaki, Y., H. Fukanuma, and N. Ohno, *Effect of interfacial roughness of bond coat on the residual adhesion strength of a plasma sprayed TBC system after thermal cycle fatigue.* Journal of Solid Mechanics and Materials Engineering, 2010. **4**(2): p. 196-207.
251. Ebrahimi, H. and S. Nakhodchi, *Thermal fatigue testing and simulation of an APS TBC system in presence of a constant bending load.* International Journal of Fatigue, 2017. **96**: p. 1-9.
252. Aktaa, J., K. Sfar, and D. Munz, *Assessment of TBC systems failure mechanisms using a fracture mechanics approach.* Acta materialia, 2005. **53**(16): p. 4399-4413.

253. Zhang, W., X. Fan, and T. Wang, *The surface cracking behavior in air plasma sprayed thermal barrier coating system incorporating interface roughness effect.* Applied surface science, 2011. **258**(2): p. 811-817.

254. Suo, Z. and J.W. Hutchinson, *Interface crack between two elastic layers.* International Journal of Fracture, 1990. **43**(1): p. 1-18.

255. Rice, J., *Elastic fracture mechanics concepts for interfacial cracks.* 1988.

256. Hutchinson, J.W., M. Mear, and J.R. Rice, *Crack paralleling an interface between dissimilar materials.* 1987.

257. Sobolev, V. and J. Guilemany, *Flattening of droplets and formation of splats in thermal spraying: A review of recent work—Part 2.* Journal of thermal spray technology, 1999. **8**(2): p. 301-314.

258. Li, G.-R., G.-J. Yang, C.-X. Li, and C.-J. Li, *Strain-induced multiscale structural changes in lamellar thermal barrier coatings.* Ceramics International, 2017. **43**(2): p. 2252-2266.

259. Kumar, A.N. and B.F. Sørensen, *Fracture Resistance and Stable Crack‐Growth Behavior of 8‐mol%‐Yttria‐Stabilized Zirconia.* Journal of the American Ceramic Society, 2000. **83**(5): p. 1199-1206.

260. Olagnon, C., J. Chevalier, and V. Pauchard, *Global description of crack propagation in ceramics.* Journal of the European Ceramic Society, 2006. **26**(15): p. 3051-3059.

261. Cocks, A., N. Fleck, and S. Lampenscherf, *A brick model for asperity sintering and creep of APS TBCs.* Journal of the Mechanics and Physics of Solids, 2014. **63**: p. 412-431.

262. Li, C.-J., W.-Z. Wang, and Y. He, *Dependency of fracture toughness of plasma sprayed Al 2 O 3 coatings on lamellar structure.* Journal of thermal spray technology, 2004. **13**(3): p. 425-431.

263. Hussain, M., S. Pu, and J. Underwood. *Strain energy release rate for a crack under combined mode I and mode II*. in *Fracture analysis: Proceedings of the 1973 national symposium on fracture mechanics, part II*. 1974. ASTM International.

264. Salimi-Majd, D., F. Shahabi, and B. Mohammadi, *Effective local stress intensity factor criterion for prediction of crack growth trajectory under mixed mode fracture conditions.* Theoretical and Applied Fracture Mechanics, 2016. **85**: p. 207-216.

265. Pippan, R., *The crack driving force for fatigue crack propagation.* Engineering fracture mechanics, 1993. **44**(5): p. 821-829.

266. Herzog, R., P. Bednarz, E. Trunova, V. Shemet, and L. Singheiser, *Simulation of stress development and crack formation in APS-TBCs for cyclic oxidation loading and comparison with experimental observations.* Advanced Ceramic Coatings and Interfaces, 2009. **306**: p. 103.

267. Wu, X., *The crack number density theory on air-plasma-sprayed thermal barrier coating.* Surface and Coatings Technology, 2019. **358**: p. 347-352.

268. Brandl, W., D. Toma, and H. Grabke, *The characteristics of alumina scales formed on HVOF-sprayed MCrAlY coatings.* Surface and Coatings Technology, 1998. **108**: p. 10-15.

269. Di Girolamo, G., M. Alfano, L. Pagnotta, A. Taurino, J. Zekonyte, and R. Wood, *On the early stage isothermal oxidation of APS CoNiCrAlY coatings.* Journal of materials engineering and performance, 2012. **21**(9): p. 1989-1997.

270. Doolabi, D.S., M. Rahimipour, M. Alizadeh, S. Pouladi, S. Hadavi, and M. Vaezi, *Effect of high vacuum heat treatment on microstructure and cyclic oxidation resistance of HVOF-CoNiCrAlY coatings.* Vacuum, 2017. **135**: p. 22-33.

271. Mercier, D., C. Kaplin, G. Goodall, G. Kim, and M. Brochu, *Parameters influencing the oxidation behavior of cryomilled CoNiCrAlY.* Surface and Coatings Technology, 2010. **205**(7): p. 2546-2553.

272. Ghadami, F., A. Sabour Rouh Aghdam, S. Ghadami, and Q. Zeng, *Effect of vacuum heat treatment on the oxidation kinetics of freestanding nanostructured NiCoCrAlY coatings deposited by high-velocity oxy-fuel spraying.* Journal of Vacuum Science & Technology A: Vacuum, Surfaces, and Films, 2020. **38**(2): p. 022601.

273. Puetz, P., X. Huang, R. Lima, Q. Yang, and L. Zhao, *Characterization of transient oxide formation on CoNiCrAlY after heat treatment in vacuum and air.* Surface and Coatings Technology, 2010. **205**(2): p. 647-657.

274. Tolpygo, V. and D. Clarke, *Microstructural study of the theta-alpha transformation in alumina scales formed on nickel-aluminides.* Materials at High Temperatures, 2000. **17**(1): p. 59-70.

275. Langford, R. and A. Petford-Long, *Preparation of transmission electron microscopy cross-section specimens using focused ion beam milling.* Journal of Vacuum Science & Technology A: Vacuum, Surfaces, and Films, 2001. **19**(5): p. 2186-2193.

276. Chen, H. and T. Barman, *Thermo-Calc and DICTRA modelling of the β-phase depletion behaviour in CoNiCrAlY coating alloys at different Al contents.* Computational Materials Science, 2018. **147**: p. 103-114.

277. Song, Y., Z. Guo, R. Yang, and D. Li, *First principles study of site substitution of ternary elements in NiAl.* Acta Materialia, 2001. **49**(9): p. 1647-1654.

278. Noebe, R., R. Bowman, and M. Nathal, *Physical and mechanical properties of the B2 compound NiAl.* International Materials Reviews, 1993. **38**(4): p. 193-232.

279. Brumm, M. and H. Grabke, *The oxidation behaviour of NiAl-I. Phase transformations in the alumina scale during oxidation of NiAl and NiAl-Cr alloys.* Corrosion science, 1992. **33**(11): p. 1677-1690.

280. Huntz, A., *Stresses in NiO, Cr2O3 and Al2O3 oxide scales.* Materials Science and Engineering: A, 1995. **201**(1-2): p. 211-228.

281. Diot, C., P. Choquet, and R. Mevrel. *Simultaneous determination of residual stresses in a thin alumina layer grown by oxidation on a NiCoCrAlY alloy and in this alloy*. in *International Conference on Residual Stresses*. 1989. Springer.

282. Messaoudi, K., A. Huntz, and B. Lesage, *Diffusion and growth mechanism of Al2O3 scales on ferritic Fe-Cr-Al alloys.* Materials Science and Engineering: A, 1998. **247**(1-2): p. 248-262.

283. Heuer, A.H., D.B. Hovis, J.L. Smialek, and B. Gleeson, *Alumina scale formation: a new perspective.* Journal of the American Ceramic Society, 2011. **94**: p. s146-s153.

284. Hasegawa, M., M. Iwashita, Y. Kubota, P. Dymáček, and F. Dobeš, *Microstructure evolution under high temperature deformation of CoNiCrAlY bond coat alloy.* Materials Science and Engineering: A, 2019. **756**: p. 237-247.

285. Chen, Y., X. Zhao, Y. Dang, P. Xiao, N. Curry, N. Markocsan, and P. Nylen, *Characterization and understanding of residual stresses in a NiCoCrAlY bond coat for thermal barrier coating application.* Acta Materialia, 2015. **94**: p. 1-14.

286. Ohring, M. and M. Ohring, *Chapter 11—interdiffusion, reactions, and transformations in thin films.* Materials Science of Thin Films, 2002: p. 641-710.

287. Fisher, J.C., *Calculation of diffusion penetration curves for surface and grain boundary diffusion.* Journal of Applied Physics, 1951. **22**(1): p. 74-77.

288. Kislenko, S.A., M.S. Vlaskin, and A.Z. Zhuk, *Diffusion of cation impurities by vacancy mechanism in α-Al2O3: Effect of cation size and valence.* Solid State Ionics, 2016. **293**: p. 1-6.

289. Zhao, P., H. Zhao, J. Yu, H. Zhang, H. Gao, and Q. Chen, *Crystal structure and properties of Al2O3-Cr2O3 solid solutions with different Cr2O3 contents.* Ceramics International, 2018. **44**(2): p. 1356-1361.

290. Naramoto, H., C. White, J. Williams, C.J. McHargue, O. Holland, M. Abraham, and B. Appleton, *Ion implantation and thermal annealing of α - Al2O3 single crystals.* Journal of Applied Physics, 1983. **54**(2): p. 683-698.

291. Doychak, J. and M. Rühle, *TEM studies of oxidized NiAl and Ni 3 Al cross sections.* Oxidation of metals, 1989. **31**(5): p. 431-452.

292. Tang, F., L. Ajdelsztajn, and J.M. Schoenung, *Influence of cryomilling on the morphology and composition of the oxide scales formed on HVOF CoNiCrAlY coatings.* Oxidation of Metals, 2004. **61**(3): p. 219-238.

293. Rathod, W., A. Khanna, J. Karthikeyan, and R. Rathod, *Effect of N 2 and He Carrier Gases on Oxidation Behavior of Cold Sprayed CoNiCrAlY Powder to Deposit Bond Coats.* Transactions of the Indian Institute of Metals, 2014. **67**(2): p. 247-262.

294. Liu, C.-B., Z.-M. Zhang, X.-L. Jiang, L. Min, and Z.-H. Zhu, *Comparison of thermal shock behaviors between plasma-sprayed nanostructured and conventional zirconia thermal barrier coatings.* Transactions of Nonferrous Metals Society of China, 2009. **19**(1): p. 99-107.

295. Emura, S., H. Maeda, Y. Kuroda, and T. Murata, *Coordination of Cr3+ Ion in α-Al2O3.* Japanese Journal of Applied Physics, 1993. **32**(S2): p. 734.

296. Moya, E., F. Moya, A. Sami, D. Juve, D. Treheux, and C. Grattepain, *Diffusion of chromium in alumina single crystals.* Philosophical Magazine A, 1995. **72**(4): p. 861-870.

297. Yu, H. and D.R. Clarke, *Effect of Codoping on the R ‐ Line Luminescence of Cr3+ ‐ Doped Alumina.* Journal of the American Ceramic Society, 2002. **85**(8): p. 1966-1970.

298. Bye, G. and G. Simpkin, *Influence of Cr and Fe on Formation of α ‐ Al2O3 from γ ‐ Al2O3.* Journal of the American Ceramic Society, 1974. **57**(8): p. 367-371.

299. Moseley, P., K. Hyde, B. Bellamy, and G. Tappin, *The microstructure of the scale formed during the high temperature oxidation of a Fecralloy steel.* Corrosion science, 1984. **24**(6): p. 547-565.